Kinetics and Decomposition Mechanisms of Selected Nitrogen-Containing Species

A Thesis Submitted for the Degree of

Doctor of Philosophy in Chemical Engineering

Kamal Siddique

B.Sc. Chemical Engineering

School of Engineering and Information Technology,

Murdoch University

April, 2018

Declaration

I hereby declare that this thesis is the result of original research and encompasses, as its main content, work which has not previously been submitted for a higher degree or diploma at any university or institution.

……..

Kamal Siddique

April, 2018

Supervisory Statement

We, the undersigned, attest that Research Higher Degree candidate, Kamal Siddique, has designed and performed the experiments, analysed the results, executed the computational mechanical calculations, and written all the chapters of this thesis. He has also written several related papers. Dr Mohammednoor ALTARAWNEH and Professor Bodgdan Z. DLUGOGORSKI provided necessary advice on the experimental task and project direction, and assisted with editing of the papers and thesis, as per normal supervisor-candidate relations.

Dr Mohammednoor ALTARAWNEH

April, 2018

Professor Bogdan Z. DLUGOGORSKI

April, 2018

Dedication

To my parents, wife and beautiful daughter

The reason of what I become today.

Thanks for your support and continuous care…..

Acknowledgements

It is a humbling experience to acknowledge those people who have, mostly out of kindness, helped me along the journey of my PhD. I am indebted to so many for encouragement and support.

Firstly, I would like to express my sincere gratitude to my advisors, Dr Mohammednoor Altarawneh and Professor Bogdan Z. Dlugogorski, for their continuous support of my Ph.D. study and related research, and for their patience, motivation and immense knowledge. Their guidance helped me throughout the research and writing of this thesis. I genuinely appreciate their mentorship and their contributions of time, ideas and funding, which have made my research inspiring and productive.

I would also like to thank Murdoch University, Australia, for awarding me a postgraduate research scholarship. Moreover, I acknowledge the support provided by the Australian Research Council (ARC), Dyno Nobel Asia Pacific, the computing time granted by the National Computational Infrastructure (NCI), Australia, and the Pawsey Supercomputing Centre in Perth.

Special thanks to Dr Jeff Gore of Dyno Nobel Asia Pacific Pty Limited and Senior Lecturer Dr David Ralph for their effective suggestions. Very special gratitude goes out to all the admin and technical staff of the School of Engineering and IT, as well as the postgraduate office personnel for their technical and professional assistance. I am truly grateful to Dr Juita, Dr Anam Saeed, Dr Ibukun Oluwoye, Dr Jakub Skut and Dr Zhe Zeng for their assistance and useful suggestions for my research work. The members of the Fire Safety and

Combustion Kinetics group have been a source of insightful discussions related to my project. It was a joyous and friendly atmosphere.

I am grateful to my siblings (Bilal, Waqas, Jamal and Zahra) and their families who gave me moral and emotional support in my life. I would also like to acknowledge Zubair Aziz's family and Mir Rehan Farid's family for their unconditional support, encouragement and love. Thanks also to Samreen Hameed who has provided me moral support. I give my regards to all my teachers, from school until now, for their knowledge and best wishes.

A bundle of thanks to my parents, Mirza Mohammed Siddique and Shahida Siddique, for their faith in me and for allowing me to be as ambitious as I wanted. It was under their watchful eye that I gained my drive and ability to tackle challenges head-on, and they made countless sacrifices to help me get to this point. A special thanks to my daughter Hoorain for her patience and love. The last words of acknowledgment I have saved for my beloved wife Anam Saeed, who has been with me all these years and has made them the best years of my life. Her encouragement, support, quiet patience and firm love were irrefutably the backbone upon which the past three years of my life have been built.

Abstract

This thesis calculates the rate of hydrogen abstraction reactions and the mechanisms of nitrogen oxides (NO_x and N_2O) reduction, especially those relevant to the oxidation and pyrolysis of nitrogen-rich fuels such as biomass. The dissertation firstly focuses on the interaction of hydrocarbons with the amidogen radical (NH_2) and nitrogen dioxide (NO_2), before analysing in detail the decomposition of ammonium nitrate (AN) both in gas and liquid media. In addition to this, the moderation of nitrous oxide (N_2O) and nitrogen oxides (NO_x) via their reaction with a biomass surrogate of catechol was also studied. The underlying aims of the study were to report the mechanisms and kinetic factors controlling the interaction of NH_2 and NO_2 radicals with a wide array of hydrocarbons, then to map out the prominent reaction pathways prevailing in the decomposition of ammonium nitrate (AN) and conversion of N_2O into N_2 via dissociative adsorption onto a catechol moiety.

Accurate quantum-mechanical calculations probed the hydrogen abstraction reactions from small aliphatic and aromatic hydrocarbons by NH_2 and NO_2 radicals. Reaction and activation energies for all plausible hydrogen abstraction channels were executed with the accurate chemistry model of CBS-QB3. Reaction rate parameters were obtained based on conventional transition-state theory, accounting for a plausible contribution from tunnelling effects and treating internal rotations as hindered rotors. We established that a linear correlation existed between the strength of the C-H bonds (i.e., primary, secondary, vinylic, and benzylic) and the activation energies for H abstraction channels operated by NH_2 and NO_2 radicals. Moreover, the meta-hybrid Density Functional Theory (DFT) of M05-2X/6-311+G(d,p) levels elucidated viable systematic conversion routes of N_2O into N_2 via interaction with a catechol molecule. Two theoretical methodologies were applied to study

thermal decomposition of AN in gas and liquid phases. A continuum solvation model density-polarisable continuum model (SMD-PCM) expounds the catalysing effect of water on AN thermal cracking. The solvation model systematically predicts lower activation energies when contrasted with analogous gas phase values.

An important part of the thesis investigates the potential of biomass constituents for the so-called selective non-catalytic reduction of NO_x into nitrogen molecules. The laboratory-scale rig offers a continuous supply of carrier and reaction gases which run through a tubular reactor coupled with FTIR spectroscopy, micro-GC and a chemiluminescence NO_x analyser. The consumption of the biomass surrogate (catechol) is analysed using a triple quadruple mass spectrometer (QQQ-MS) at temperatures starting from 400 °C. Fine-tuning of experimental conditions encompasses residence time and inlet reactant mixing ratios. Above 800 °C, we report more than 80 % NO_x reduction efficiency. In summary, our findings throughout the thesis present previously unreported data and new insights pertinent to the combustion chemistry of several selected N-species.

Table of contents

Contribution towards Publication

1. A critical review on NO_x mitigation and their intermediate reaction kinetics.

Siddique, K.; Altarawneh, M.; Gore, J.; Dlugogorski, B. Z., (In preparation)

2. Hydrogen Abstraction from Hydrocarbons by NH_2.

Siddique, K.; Altarawneh, M.; Gore, J.; Westmoreland, P. R.; Dlugogorski, B. Z.,

The Journal of Physical Chemistry A **2017**, *121*, 2221-2231. **DOI:**10.1021/acs.jpca.6b12890

3. Interaction of NH_2 radical with Alkylbenzenes

Siddique, K.; Altarawneh, M.; Gore, J.; Dlugogorski, B. Z.,

Combustion and Flame (Under review)

4. Reaction Kinetics of Hydrocarbons + NO_2

Siddique, K.; Altarawneh, M.; Gore, J.; Dlugogorski, B. Z. (In preparation)

Target Journal: *Combustion and Flame*

Contribution towards conferences

1. **Systematic Study for H Abstraction from Alkanes by Amine Radical (NH_2)**

Siddique, K.; Altarawneh, M.; Gore, J.; Dlugogorski, B. Z., Proceedings of the Australian Combustion Symposium, 2015, 272-275, Melbourne (2015).

http://www.anz-combustioninstitute.org/local/papers/ACS2015-Proceedings.pdf

2. Theoretical investigation of the ethylbenzene with NH_2 radical: H abstraction and addition reactions pathways

Siddique, K.; Altarawneh, M.; Saeed, A.; Gore, J.; Dlugogorski, B. Z.,

11th Asia-Pacific Conference on Combustion, 2017, Sydney (2017).

The list below itemises the publications to which I have contributed during the course of the PhD study, but which fall outside the scope of this thesis.

Journal paper

1. Photodecomposition Properties of Brominated Flame Retardants (BFRs)

Saeed, A.; Altarawneh, M.; **Siddique, K.**; Dlugogorski BZ., (Ready to submit)

Target Journal: *Chemosphere*

Conference paper

1. Toxic Species from Oxidation of Tetrabromobisphenol A

Saeed, A.; Dlugogorski BZ.; **Siddique, K.**; Altarawneh, M.;

Organohalogen compound, 2017 (accepted). Will be available online soon.

Glossary of abbreviations and technical terms

AN	Ammonium nitrate
ANFO	Ammonium nitrate fuel oil
BDH	Bond dissociation enthalpy
CBS	Complete basis set
DFT	Density functional theory
FBC	Fluidised bed combustion
FTIR	Fourier transforms infrared
GC-MS	Gas chromatography mass spectrometer
GGA	Generalised gradient approximation
G2M	Gaussian-2 method
HCN	Hydrogen cyanide
HF	Hartree-Fock
HEG	Homogeneous electron gas
ICPs	Incomplete combustion products
IR	Infrared
IRC	Intrinsic reaction coordinates
KiSThelP	Kinetic and statistical-thermodynamic program
KS	Kohn-sham
LDA	Local density approximation
µ-GC	Micro-gas chromatography
NH_2	Amidogen radical
NO_x	Oxides of nitrogen
N_2O	Nitrous oxide
OB	Oxygen balance
PCM	Polarisable continuum models
PES	Potential energy surface
PFC	Pulverised fuel combustion
QCI	Quadratic Configuration Interaction

TF	Thomas-Fermi
SCRF	Self-consistent reaction field
SCR	Selective catalytic reduction
SNCR	Selective non catalytic reduction
SMD-PCM	Solvation model density-polarizable continuum model
TS	Transition state
TS	Transition state theory
VOCs	Volatile organic compounds
VTS	Variational transition state theory
ZPVE	Zero-point vibrational energy

Chapter 1

Introduction

This chapter elucidates the thesis proposal, highlighting relevant research background followed by the research motivation, its significance and existing gaps in literature. This chapter also demonstrates the research goals and overall structure of the thesis.

1.1. Background

Fossil fuels such as oil, gas, and coal constitute more than ~80 % of the current world energy usage. Figure 1.1 demonstrates the annual consumption of various available resources globally.

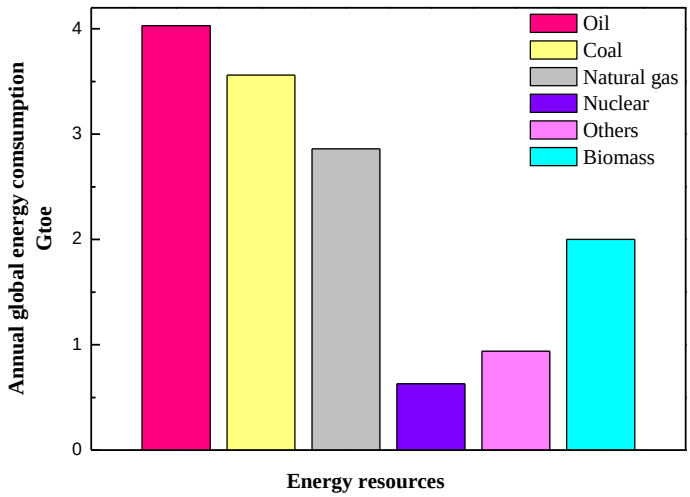

Figure 1.1. Global use of energy annually. Unit of energy is one billion tonne of oil equivalent (Gtoe). Reproduced from Williams et al.[1]

The use of solid fuels during combustion supplements energy demands at the expense of environmental contamination and becomes a source of airborne pollutants, especially of nitrogen-bearing compounds. The most important pollutants are particulate matter, unburned hydrocarbons, carbon monoxide (CO), sulfur oxides (SO_2), nitric oxide (NO) nitrogen dioxide (NO_2), ammonia (NH_3), nitrous oxide (N_2O) and amines (R-NH_2). Figure 1.2 provides an overview of the N-containing pollutants and their possible sources. The use of

ammonium nitrate (NH_4NO_3) in mining activity generates NO and NO_2 (collectively called NO_x). It is predicted that mining-related operations emit 5.0×10^4 t N of NO_x gases annually, as compared to the accumulative anthropogenic release of 41.3×10^4 t N of NO_x per year.[2] NO_x is a potential cause of prominent environmental phenomena including photochemical smog, acid rain, and ozone layer depletion. Likewise, N_2O is a potent contributing factor of global warming. Exposure to an elevated level of these gases causes serious health concerns for humans, as well as damaging the environment.[3] An additional dimension to the adverse effect of NO_x stems from the reactions of NO_2 with olefins in the atmosphere, producing a variety of secondary hazardous compounds.[4] NO_2 is formed through the oxidation of NO, the decomposition of peroxynitrite, the reaction of nitric acid with hydroxyl radicals, and the reaction of NO with ozone.[5] NO_x gases, in general, are generated from the decomposition of nitro-containing explosives[6] and from the combustion of nitrogen-containing solid fuels.[1, 7] N_2O emissions arise from both natural and anthropogenic sources.[8]

The so-called selective non-catalytic reduction (SNCR) of NO_x (NO_xOUT, RapreNO_x)[9] also contributes to the overall inventory N_2O formation. As chapter 2 will elaborate in further detail, NH_3 is a major product from the fragmentation of N-constituents in coal. Central to the SNCR process are NH_2 radicals, which are produced from the decomposition of hydrazine and all classes of amines triggered via radiolysis, photolysis, microwave discharge, pyrolysis, and combustion. SNCR utilises NH_2 to convert NO into nitrogen molecules.[10] So it is very insightful to follow the combustion chemistry of NH_2 radicals because they act as principal chemical agents in nearly all SNCR processes. From the above discussion, it becomes apparent that NH_2/NO_2 radicals coexist with hydrocarbons.

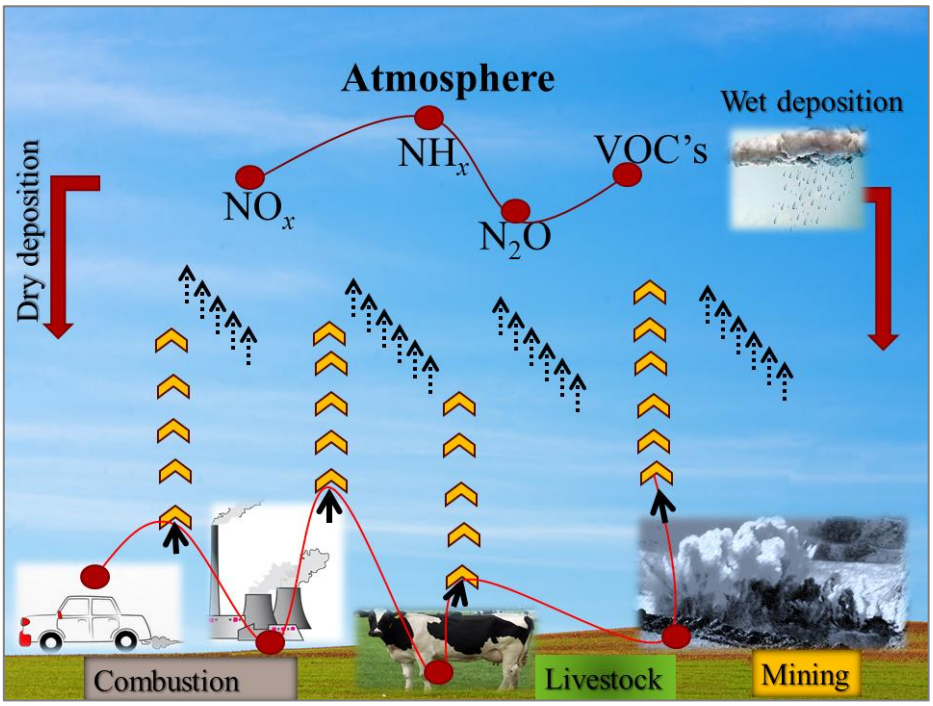

Figure 1.2. Overview of nitrogenous pollutant sources

1.2. Research motivation

The underlying motivation behind the work in this thesis is the necessity to develop accurate thermochemical and kinetics accounts for chemical events pertinent to the reactions of $NH_2/NO_x/N_2O$ in thermal systems. These operations encompass their reactions with hydrocarbons and their potential conversion into N_2 via dissociative adsorption on selected surrogate molecules. The most relevant thermal systems to the emission of N-bearing entities are the pyrolysis of biomass[1, 11] and explosions.[12-15] The extensive use of NH_4NO_3 in mining operations[16] has resulted in appreciable concentrations of NO with relatively lower amounts of NO_2, and N_2O.[14] In fluidized bed combustion,[17] N_2O generation generally exceeds that of NO.[18-20]

The chemical reactions of NO_x formed by combustion[21-22] and high energy density material[23] systems have been an area of intensive study for more than half a century. Conversely, the reaction kinetics of NH_2 and NO_2 has received generally less attention compared with other nitrogenous species such as NH_3 and HCN. In this regard, the reactions of NH_2 and NO_2 with hydrocarbon species occur largely through H abstraction channels rather than through addition at all temperatures. The literature provides rather limited kinetic data that were restricted to a narrow range of operational temperatures and pressures. The formation of a substantial level of N_2O in NO_xOUT processes has overshadowed the overall environmental merit of this NO_x abatement technology. The use of a biomass surrogate in the diminution of NO_x was rendered to be effective as it readily reduces N_2O into nitrogen in a facile non-catalytic reaction. Decomposition of emulsion-based explosives occurs both in the gas phase and liquid phase (i.e., prior to detonation). The reaction kinetics of the degradation of NH_4NO_3 in a liquid medium remains poorly understood, with the energy requirements for several key steps still not accurately determined.

Figure 1.3 depicts the linkage of current dissertation goals with the respective thesis chapters.

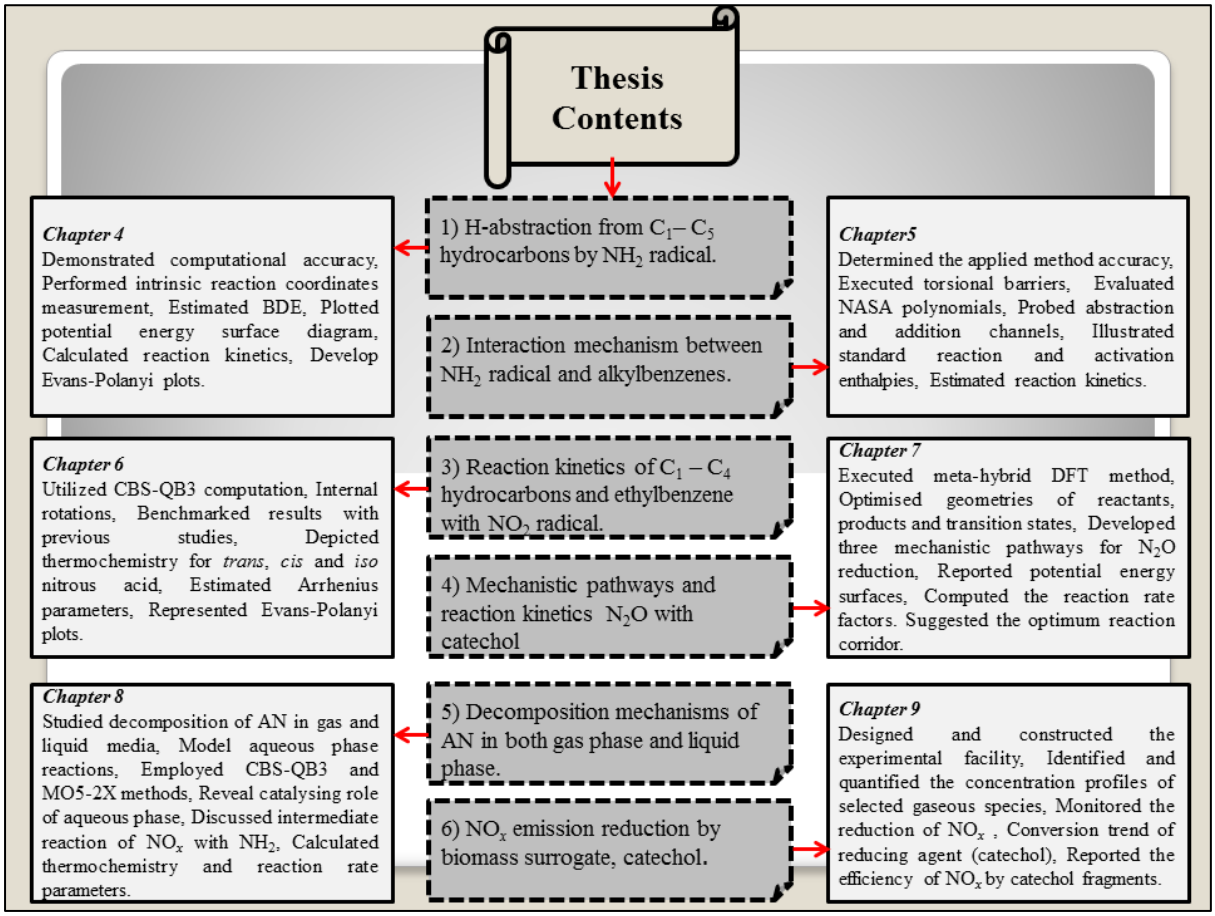

Figure 1.3. Correlation of thesis aims with relating chapters.

1.3. Research aims

The transformation chemistry of nitrogenous reacting species in the relevant chemical system and their underlying environmental implications can only be completely described when the underpinning reaction kinetics and mechanisms are well known and precisely calculated. Accordingly, this dissertation endeavours to:

1. Conduct accurate quantum chemistry calculations to improve reaction energies and energy barrier values involving H abstraction from C_1–C_5 hydrocarbons by NH_2 radicals.
2. Develop an interaction mechanism between NH_2 radical and alkylbenzenes; a major fraction of commonly deployed transportation fuels such as diesel.
3. Report kinetics of H abstraction by NO_2 radicals from selected C_1–C_4 hydrocarbons, toluene, and ethylbenzene.
4. Propose the mechanistic pathways and reaction kinetics for the conversion of N_2O into N_2, mediated by the biomass surrogate of catechol ($C_6H_5(OH)_2$).
5. Elucidate the decomposition mechanisms of NH_4NO_3 in both gas and liquid phases to map out reaction corridors and kinetics related under the conditions encountered during emulsion explosive decomposition.
6. Investigate the potential reduction in NO_x emissions initiated by its adsorption over catechol oxidative fragments using an experimental approach.

1.4. Thesis framework

This thesis analyses in detail the interaction of hydrocarbons with NH_2 and NO_2 radicals coexisting in combustion and explosion processes, and the reduction of unwanted pollutants such as NO_x and N_2O with biomass representative compounds.

Chapter 2 contains a comprehensive literature review pertinent to 1) the contribution of solid fuel combustion and mining-based NH_4NO_3 explosives to anthropogenic NO_x formation; 2) the mechanism of NO_x formation during combustion and detonation of NH_4NO_3, and

sensitisation of emulsion explosives; 3) currently deployed NO_x mitigation technologies and their efficiencies; 4) the reaction kinetics of hydrocarbons with NH_2 and NO_2 radicals prevailing in combustion, and an overview based on the available kinetics data for these reactions; and 5) the reaction pathway for the decomposition of NH_4NO_3 in the gas phase.

Chapter 3 describes the research methodology applied and the theoretical background forming the basis of the quantum chemical calculations throughout the thesis. In the second section, experimental setup and analytical instruments highlight the experimental approach utilised in chapter 9.

Chapter 4 presents a systematic CBS-QB3 evaluation of the thermochemistry and reaction kinetics of direct H abstraction from C_1–C_5 hydrocarbons by NH_2 radicals forming hydrocarbon radicals and NH_3 as products. We report an accuracy benchmark of the developed methodology by contrasting our calculated bond dissociation energies (BDE) with their analogous experimental values and by comparing computed standard reaction ($\Delta_r H^o_{298}$) and standard activation enthalpies ($\Delta^{\ddagger} H^o_{298}$) for three selected reactions, with corresponding values estimated using composite chemistry models. The obtained standard activation enthalpies display a linear correlation with bond dissociation enthalpies of the target C-H bond, mimicking an Evans–Polanyi trend. The average ratio of $k_{calculated}/k_{experimental}$ (k = reaction rate constant) for methane, ethane and *n*-butane remains between 1.1–1.5, within the temperature range of experimental measurements.

Chapter 5 reports thermodynamic values and reaction rate parameters for the interaction of alkylbenzenes with the NH_2 radicals present during pyrolysis of biomass. We map out energy profiles for H removal from the alkyl side chains in toluene, ethylbenzene and *n*-

propylbenzene, in addition to attachment of NH_2 at the four available positions of the phenyl ring in toluene and ethylbenzene. Abstraction of benzylic H from alkylbenzene is the favourable reaction pathway as it has the weakest C–H site at all temperatures except for benzylic H in ethylbenzene. The abstraction reaction overrides the additional channels for toluene and ethylbenzene at all temperatures. We observe a minimal influence of the length of the hydrocarbon chain on the computed activation and reaction enthalpies.

Chapter 6 describes the formation of three different types of nitrous acid isomers (*trans*-HONO, *cis*-HONO, and *iso*-HNO_2) from the removal of H from hydrocarbons with NO_2 radicals. A precise computational method (CBS-QB3) gauges the thermodynamic and reaction kinetics of H abstraction from C_1–C_4 aliphatic saturated and unsaturated hydrocarbons and aromatic hydrocarbons (ethylbenzene) with NO_2 radicals. We found that *cis*-HONO production is more kinetically feasible in reference to *iso*-HNO_2 and *trans*-HONO isomers based on lower $\Delta^{\ddagger}H^{o}_{298}$ values. The investigated sites included H abstraction of the tertiary C–H site in *iso*-butane, the allylic C–H bond in propene and the benzylic C–H site in ethylbenzene.

Chapter 7 investigates the non-catalytic reduction of N_2O using a biomass representative compound, catechol. In this chapter, we develop implicit reaction mechanisms for all channels involved in the interaction between a catechol molecules and N_2O. We propose three initial reaction corridors for N_2O: (1) 1,2-cycloaddition of N_2O to the aromatic ring; (2) abstraction of an O atom from N_2O by catechol; and (3) the removal of hydroxyl's H atoms from catechol by N_2O. The reaction channel (1) was found to be the dominant reaction pathway.

Chapter 8 investigates the thermal decomposition of NH_4NO_3 appearing concurrently in gas and liquid phases similar to the real scenarios encountered in explosive emulsions. We report kinetic rate parameters for all reactions leading to the formation of nitrogen molecules from thermal decomposition of NH_4NO_3 in the gas and aqueous phases, using very accurate theoretical frameworks. We employed the solvation model and explicitly added water molecules to present aqueous medium reactions. Additionally, we attempt to identify the catalysing effect of water molecules on the decomposition of NH_4NO_3. Our findings reveal that NH_4NO_3 decomposition in an aqueous medium systematically requires lower activation enthalpies compared to its decomposition in the gas phase.

Chapter 9 reveals the mitigation of NO under conditions relevant to fuel reburning processes using biomass surrogate (catechol), elucidating the N-conversion profiles, and NO_x reduction efficiency as compared to conventional hydrocarbon fuels. The results indicate that hydrocarbons from catechol oxidation convert NO into N_2 via the formation of hydrogen cyanide.

Chapter 10 presents some concluding remarks and highlights suggestions and recommendations for future investigations.

Finally, Chapter 11 provides all necessary supplementary information.

1.5. References

1. Williams, A.; Jones, J.; Ma, L.; Pourkashanian, M., Pollutants from the Combustion of Solid Biomass Fuels. *Prog. Energy Combust. Sci.* **2012**, *38*, 113-137.

2. Oluwoye, I.; Dlugogorski, B. Z.; Gore, J.; Oskierski, H. C.; Altarawneh, M., Atmospheric Emission of NO_x from Mining Explosives: A Critical Review. *Atmos. Environ* **2017**, *167*, 81-96.

3. Skalska, K.; Miller, J. S.; Ledakowicz, S., Trends in NO_x Abatement: A Review. *Sci. Total Environ.* **2010**, *408*, 3976-3989.

4. Giamalva, D. H.; Kenion, G. B.; Church, D. F.; Pryor, W. A., Rates and Mechanisms of Reactions of Nitrogen Dioxide with Alkenes in Solution. *J. Am. Chem. Soc.* **1987**, *109*, 7059-7063.

5. Huie, R. E., The Reaction Kinetics of NO_2. *Toxicology* **1994**, *89*, 193-216.

6. Zhang, J.-D.; Kang, L.-H.; Cheng, X.-L., Theoretical Study of the Reaction Mechanism of CH_3NO_2 with NO_2, NO and CO: The Bimolecular Reactions That Cannot Be Ignored. *J. Mol. Model.* **2015**, *21*, 13.

7. Chen, J., et al., A Review of Biomass Burning: Emissions and Impacts on Air Quality, Health and Climate in China. *Sci. Total Environ.* **2017**, *579*, 1000-1034.

8. Wójtowicz, M. A.; Pels, J. R.; Moulijn, J. A., Combustion of Coal as a Source of N_2O Emission. *Fuel Process. Technol.* **1993**, *34*, 1-71.

9. Tayyeb Javed, M.; Irfan, N.; Gibbs, B. M., Control of Combustion-Generated Nitrogen Oxides by Selective Non-Catalytic Reduction. *J. Environ. Econ. Manag.* **2007**, *83*, 251-289.

10. Lesclaux, R., Reactivity and Kinetic Properties of the NH_2 Radical in the Gas Phase. *Res. Chem. Intermed.* **1984**, *5*, 347-392.

11. Ren, Q.; Zhao, C., Evolution of Fuel-N in Gas Phase During Biomass Pyrolysis. *Renew. Sustainable Energy Rev.* **2015**, *50*, 408-418.

12. Weng, Z.; Mudd, G. M.; Martin, T.; Boyle, C. A., Pollutant Loads from Coal Mining in Australia: Discerning Trends from the National Pollutant Inventory (NPI). *Environ. Sci. Policy* **2012**, *19*, 78-89.

13. Higginbotham, N.; Freeman, S.; Connor, L.; Albrecht, G., Environmental Injustice and Air Pollution in Coal Affected Communities, Hunter Valley, Australia. *Health Place* **2010**, *16*, 259-266.

14. Bian, Z.; Inyang, H. I.; Daniels, J. L.; Otto, F.; Struthers, S., Environmental Issues from Coal Mining and Their Solutions. *Min. Sci. Technol.* **2010**, *20*, 215-223.

15. Morrice, E.; Colagiuri, R., Coal Mining, Social Injustice and Health: A Universal Conflict of Power and Priorities. *Health Place* **2013**, *19*, 74-79.

16. Finkelman, R. B.; Tian, L., The Health Impacts of Coal Use in China. *Int. Geol. Rev.* **2017**, 1-11.

17. Kilpinen, P.; Hupa, M., Homogeneous N_2O Chemistry at Fluidized Bed Combustion Conditions: A Kinetic Modeling Study. *Combust. Flame* **1991**, *85*, 94-104.

18. Armesto, L.; Boerrigter, H.; Bahillo, A.; Otero, J., N_2O Emissions from Fluidised Bed Combustion. The Effect of Fuel Characteristics and Operating Conditions. *Fuel* **2003**, *82*, 1845-1850.

19. Chen, Z.; Lin, M.; Ignowski, J.; Kelly, B.; Linjewile, T. M.; Agarwal, P. K., Mathematical Modeling of Fluidized Bed Combustion. 4: N_2O and NO_x Emissions from the Combustion of Char. *Fuel* **2001**, *80*, 1259-1272.

20. Chyang, C.-S.; Qian, F.-P.; Lin, Y.-C.; Yang, S.-H., NO and N_2O Emission Characteristics from a Pilot Scale Vortexing Fluidized Bed Combustor Firing Different Fuels. *Energy Fuels* **2008**, *22*, 1004-1011.

21. Miller, J. A.; Bowman, C. T., Mechanism and Modeling of Nitrogen Chemistry in Combustion. *Prog. Energy Combust. Sci.* **1989**, *15*, 287-338.

22. Peck, R.; Altenkirch, R.; Midkiff, K., Fuel • Nitrogen Transformations in One-Dimensional Coal-Dust Flames. *Combust. Flame* **1984**, *55*, 331-340.

23. Xu, Z.-X.; Liu, D.-B.; Hu, Y.-T., Investigation of Ammonium Nitrate Based Emulsion Ignition Characteristic. *J. L. Prevent Proc.* **2013**, *26*, 994-1001.

Chapter 2

Literature Review

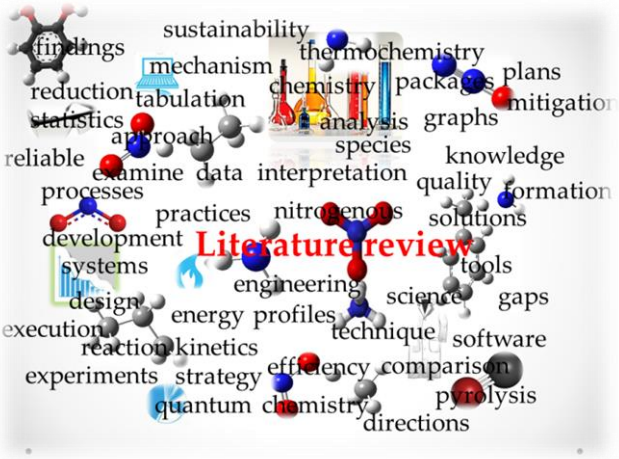

This chapter presents a comprehensive overview of the formation of NO_x, HCN, NH_3 and N_2O and its mitigation, as well as the energetics and reaction kinetics of the intermediate radical (NH_2) and NO_2 radical formed during combustion of solid duels and AN.

2.0. Abstract

Energy generation from fossil fuels and the ever-increasing utilisation of high energy density materials for mining operations have some severe environmental implications. The environmental burden of these thermal processes is mainly characterised by the emission of a wide array of pollutants, most notably nitrogen-bearing gases such as nitrogen oxide (NO) and dinitrogen oxide (NO_2) – collectively called NO_x – and the potent greenhouse gas, N_2O.

This review analyses the sources contributing to the emission of nitrogen-containing pollutants, mainly NO_x, N_2O, ammonia (NH_3), hydrogen cyanide (HCN), and the intermediate amidogen radical (NH_2), from solid fuel (coal and biomass) pyrolysis and combustion, as well as from the decomposition of ammonium nitrate (NH_4NO_3) – an important chemical gassing agent of emulsion explosives.

We reiterate the kinetics and mechanistic parameters pertinent to the formation of reactive nitrogenated intermediates and stable-end products from the combustion of coal/biomass and detonation of NH_4NO_3. We review the mitigation technologies for NO_x with a focus on selective catalytic and selective non-catalytic operations, as well as subsequent N_2O generation from chemical reactions that function to abate NO_x gases. Here, we present a comprehensive account of the reaction kinetics and energy profiles of the NH_2 and NO_2 reactions with co-existing hydrocarbons which prevail in the combustion of coal/biomass and in the course of the fragmentation of ammonium nitrate fuel oil (ANFO) explosives.

2.1. Background

The anticipated depletion of fossil fuels and environmental pollution associated with combustion has, in general, stemmed a global interest in renewable and alternative energy resources. Nitrogen oxide (NO) and nitrogen dioxide (NO_2), collectively called NO_x gases, have been identified as acid rain contributors as well as global warming gases that impose hazards on the environment. Thermal treatment of coal/biomass is the chief anthropogenic contributor to the emission of NO_x.[1-2] NO_x evolves majorly from fuel-bearing nitrogen (fuel-N) in the coal matrix, with minor participation from molecular nitrogen in air.[3] Similarly, the combustion and pyrolysis of biomass fuel forms NO_x through thermal reactions from the fragmentation of N-constituents in biomass structural entities.[4] While biomass generally contains a lesser amount of fuel-N, the wide use of biomass as a renewable source of energy via gasification reactions has resulted in significant NO_x pollution.[5]

High energy matrices, such as ammonium nitrate as emulsion, slurries and blend of ammonium nitrate with fuel-oil, are used extensively in mining, tunneling and several other civil infrastructure processes. Ideally, detonation of these commercial nitrogen-bearing energy materials forms carbon dioxide (CO_2), nitrogen (N_2) and water vapors (H_2O);[6-7] however, poor mixing conditions and turbulent flow regimes during detonation facilitates the formation of incomplete combustion products, most notably carbon monoxide (CO), NO and NO_2, as well as the potent greenhouse gas, N_2O.[6-11] The release of toxic gases in the vicinity of populated areas requires immediate approaches for abatement; for example, NO_2 reacts with water vapour to form nitric acid, which seeps through soil into ground the water making it more acidic. The aforementioned gases pose serious health effects for mine workers. Mining operations in Australia pose particular health and environmental risks due to the

generation of NO_2 gases (often in visible orange clouds) immediately after blasts. NO_2 is relatively resistant to atmospheric oxidation, resulting in its travel through the air to nearby communities.[10-11]

Here, we describe the nitrogenous compounds formed from biomass and coal combustion and NH_4NO_3 decomposition and detonation. We summarise the combustion systems of coal and biomass fuels, with a focus on the chemical reactions that lead to NO_x and N_2O formation from the nitrogen present in these fuels. We report the literature on levels of NO_x, N_2O, NH_2, NH_3, HCN, NH_4NO_3 and HNO_2 in combustion and atmospheric media under various operational conditions. Next, the mechanism of NO_x formation is discussed in detail. Moving on, the NO_x mitigation technologies efficiency is illustrated, focusing on the mechanism of NO_x reduction. In the subsequent section, the NH_4NO_3 decomposition and detonation chemistry is elaborated to reveal chemical phenomena contributing to the formation of NO_x, N_2O and NH_2 radicals. This is followed by a survey of currently deployed technologies that aim to reduce emissions of NO_x from the detonation of NH_4NO_3 -materials. Finally, we present reaction kinetics of NH_2 and NO_2 radicals with selected hydrocarbons.

2.2. Combustion technologies

Solid fuel combustion systems mainly encompass fluidised bed combustion (FBC), pulverised fuel combustion (PFC) and combustion on grates (GC). Table 2.1 exemplifies the commonly used energy sources in combustion processes. Pulverised fuel combustion is the most widely used combustion technology due to high levels of reliability and its ability to operate on all coal ranks; however, production of NO_x and particulate emissions compromise

its advantages. Fluidised bed combustion is favoured over PFC due to its high heat transfer, increased combustion performance and low NO_x generation. Contrarily, increased levels of N_2O and solid residue emissions are the primary concerns of the FBC combustion method. Biomass energy sources are burned in GC furnaces. Over the last decade or so, substantial research has focused on gaining a better understanding of nitrogenous pollutants and their mitigation from PFC systems by selective catalytic and selective non-catalytic methodologies.[12]

Table 2.1. Amount of nitrogen in commonly deployed solid fuels.[13]

Energy sources	% w of nitrogen
Coal	0.5-2.5
Peat	0.5-2.5
Wood	0.03-1.0
Straw	0.3-1.5
Paper	0.1-0.2
Tires	0.3
Household waste	0.1-1.0
Sewage sludge	2.5-6.5
Other agricultural residue	0.4-3.5

Attempts to reduce emission of harmful NO_x gases in combustion systems require detailed understanding of the chemical events that dictate their transformations, destruction and formation under the conditions encountered in real combustion scenarios. A great deal of fundamental and applied research has provided comprehensive mechanisms of NO_x

formation and decomposition, with a focus on various factors that underpin their final yields in thermal systems. In this review, we focus on the formation pathways of NO_x gases from several structural precursors. A special emphasis is placed on NO_x reduction methodologies focusing on the nitrogen chemistry and related unwanted by-products.

2.3. Nitrogenous combustion and atmospheric pollutants

Apart from NO_x gases, combustion processes lead to the formation of a wide array of incomplete combustion products (ICPs); mostly CO, unburned hydrocarbons and volatile organic compounds (VOCs)[14-17] that are deposited into the atmosphere at an alarming rate. The participation of these pollutants towards forming acid rain and photochemical smog, and stratospheric ozone destruction, is one of the motives for the extensive focus on NO_x and VOCs. In addition, these chemical moieties have explicit adverse effects on human health because of their existence in the tropospheric ozone and adsorption on fine particulate matter.[18] Atmospheric concentrations of nitrate and ammonium have been studied broadly at the global level.[19] Table 2.2 illustrates the trace amounts of NO_x, N_2O, NH_3, HCN, NH_4NO_3 and nitrous acid (HNO_2) in a typical atmospheric environment.

Table 2.2. Trace gaseous nitrogen species in the atmosphere. Value reported from Kramlich and Linak.[20] (Further adapted from Levine)[21-22]

Species	Concentration level
NO_x	0–1 ppb, Tropospheric 0.02 ppm, Stratospheric
N_2O	310 ppb
NH_3	0.1–1.0 ppm
HCN	200 ppt
HNO_2	0.1 ppt
NH_4NO_3	10 ppt

Anthropogenic NO_x emissions – according to United State (US) emissions – is 23 million tonnes, where 45 % and 55 % stem from mobile and stationary sources, respectively. The typical atmospheric NO_x concentration resulting from gas, coal and oil combustion resides between 25–150 ppm, 200–1000 ppm and 60–1000 ppm, respectively.[23] Considering the nitrogenous pollutants, NH_3 is the most copious alkaline atmospheric gas that neutralises acidic gases (SO_2 and NO_x) and forms atmospheric aerosols (ammonium sulphate, etc.).[24-25] The most commonly discussed sources of NH_3 are biomass burning, fossil fuel combustion, agricultural crops, synthetic fertilisers and volatilisation from animal waste.[26-28] Synthetic fertilisers and agricultural crops contribute significantly to the inventory of NH_3, up to 9 Tg NH_3-N per year into the atmosphere globally.[29] The dominant natural and anthropogenic contribution is from domestic animals (40 %), at 32 Tg NH_3-N per year.[30-31] The contribution of biomass burning and fossil fuel combustion is 5 Tg NH_3-N per year and 2 Tg NH_3-N per year, respectively.[29, 32] Ammonia released from anthropogenic and natural

sources participates in atmospheric reactions (e.g. gas-to-particle conversion) and is ultimately deposited in soil via wet and dry deposition processes.[33]

Among the atmospheric organic compounds, alkaline gases are volatile amines (R-NH_2). In particular, the gaseous aliphatic amines have the potential to progress acid-base reactions to form salt particulates in the presence of atmospheric acids.[34] The concentration of amines reaches as high as 14–23 % of the total NH_3 content in the atmosphere.[35] These amines can undergo reactions with atmospheric NO_x to produce secondary organic aerosols; for example, carcinogenic nitroso-amines results from the photo-oxidation of amines by NO_x.[36] The origin of amines in the atmosphere is linked with combustion and biomass burning, geological sources, vegetation, oceans, pesticides, indoor textiles, automobiles, tobacco smoke, sewage, cooking and biodegradation of organic material.[37] Biomass burning produces C_1–C_5 amines[38-39] and may also generate large molecules of alkyl-amide.[40] The standard level of atmospheric amines is nearly 1–2 orders of magnitude lower than that of NH_3.[41] Concentration levels of amines in the atmosphere depend on varying parameters, making it very difficult to acquire accurate and consistent measurements. The contribution of global emissions of total alkylamines (methylamine, diethyl amine and triethylamine) in the atmosphere amounts to 285 ± 78 Gg N per year. Biomass burning accounts for 60 ± 28 Gg N per year of global emissions of total methylamines.[42]

As elaborated above, NO_x formation has been the subject of several laboratory-scale, pilot-scale and full-scale combustion systems experiments.[43-44] These studies have reported temperature history profiles for the emission of nitrogenated pollutants in the form of NO, N_2O, NO_2, NH_3, HCN and *iso*-cyanic acid (HCNO) from the combustion of biomass and coal.[5, 45-48] As coal and biomass incur different fuel-bound nitrogen speciation, the

underlying formation methods for HCN and NH_3 are distinct and depend on the fuel type, heating rate, pyrolysis, and temperature; for instance, NH_3[49] is produced from the pyrolytic decomposition of biomass, while only a small amount of NH_3 is generated from the combustion of coal.[44, 50] Pyrolysis of bituminous coals under a high rate of heating produces mainly HCN, while pyrolysis of low-ranking coals, peat and bark yields significant amounts of NH_3. Ammonia results from coal and biomass under a low heating rate. The formation of NH_3 is also linked with the source of nitrogen. In biomass, NH_3 is released from amino groups and amides while quaternary nitrogen (especially in low-rank coal) generate NH_3.[13] Thermal cracking of biomass[49] and coal[50] result in the formation of HCN from their volatile components. Table 2.3 itemises the emission factors of selected N-containing gaseous species from different types of biomass burning and charcoal burning.

Table 2.3. Emission factors of selected N-containing gaseous species from different kinds of biomass burning.[51] Values are reported in gram species per kilogram of dry biomass burned.

	NO_x	N_2O	NH_3	HCN
Savanna and Grassland	3.9	0.21	0.6–1.5	0.03
Tropical forest	1.6	0.20	1.30	0.15
Extra tropical forest	3.0	0.26	1.4	0.15
Biofuel burning	1.1	0.06	1.30	0.15
Charcoal making	0.04	0.03	0.09	0.15
Charcoal burning	3.9	0.20	1.30	0.15
Agricultural residue	2.5	0.07	1.30	0.15

Combustion region conditions, such as the fuel/oxygen ratio and temperature, primarily determine the extent of the formation of the abovementioned nitrogen moieties; for example, NO_2 signifies 10 % of the total NO_x content in typical CH_4/air flames, while the amount rises to a significant level of 90 % of the total NO_x at a low temperature.[52] Pre-mixed flames cause NO_2 formation which describes purely the fluid dynamic behavior of NO_2 in the flame zone. Also, the transformation of NO into NO_2 occurs in the mixing region, where combustion gases at high temperature mix with the inlet air.[53-54] In conventional combustion processes at elevated temperature, N_2O is released in the early stages of flame from fuel-N and is subsequently reduced or destroyed. In fluidised bed combustion, along with injection of NH_3 in off-gases, formation of N_2O is observed under medium temperature regions.[20] More details of the N_2O formation are given in section 2.6.

2.4. Sources and formation mechanism of NO_x

The key channels operating in NO_x release during combustion fall into three main categories: 1) thermal, 2) prompt, and 3) fuel NO_x mechanisms. The contribution of NO_x in biomass combustion is linked to the transformation of fuel-N.[4] Thermal and prompt NO_x mechanisms are relevant at an elevated temperature, and this temperature is rarely achieved in biomass combustion.[13] The thermal NO mechanism denotes the formation of NO from the oxidation of molecular nitrogen at a high temperature. Intuitively, the contribution of NO in the low NO_x burner is insignificant.

2.4.1. Thermal NO

Thermal NO is released from the oxidation of atmospheric nitrogen at a high temperature under fuel lean conditions. Significant formation of thermal NO is observed at temperatures above 1500 ^{o}C. The strong triple N≡N in nitrogen molecule (945.2 kJ mol^{-1}) [55] demands a high operating temperature for nitrogen atoms that are further oxidized into NO. Zeldovich[56] explained the formation of so-called thermal NO based on the following sequence of reactions:

$$O + 2N \rightleftharpoons NO + N \qquad \text{R2.1}$$

$$N + O_2 \rightleftharpoons NO + O \qquad \text{R2.2}$$

Under fuel-rich flame conditions,[57] the reaction of atomic nitrogen with hydroxyl groups via the so-called Zeldovich mechanism assumes critical importance.

$$N + OH \rightleftharpoons NO + H \qquad \text{R2.3}$$

The above reaction pathway accounts for the effect of O_2 and OH radicals on NO formation. Owing to the presence of these radicals, thermodynamic equilibrium calculations predict an NO concentration that underestimates the actual NO concentration.[58-59] The adjustment of the equilibrium concentration of radicals for the estimation of actual concentration displays good correlation.[58, 60]

2.4.2. Prompt NO

The rapid formation of NO in the combustion zone from the reaction of hydrocarbons with atmospheric nitrogen is termed the prompt NO pathway. The most prevailing reaction is R2.4, with a negligible contribution from reaction R2.5. Depending on the experimental conditions, the formed HCN can be oxidised to form NO and N_2. Unlike the thermal NO pathway, the NO_x yield from the prompt NO pathway depends on the N_2 concentration and fuel rich conditions.[61-62]

$CH + N_2 \rightleftharpoons HCN + N$ R2.4

$CH_2 + N_2 \rightleftharpoons HCN + NH$ R2.5

$N + OH \rightleftharpoons NO + H$ R2.3

Numerous experimental studies have shown that NO production rates in the combustion zone were inconsistent with NO formation in the post combustion zone. In fact, the rate of NO production in the combustion zone exceeded the NO production rate in the post combustion area.[63-64] Fenimore[63, 65] and other studies[64, 66] support the conclusion of an increased rate of NO formation in the combustion flame compared to the post combustion zone. This noticeable increase was attributed to the prompt NO pathway. The prompt NO pathway is more favorable in fuel-rich combustion zones (staged coal combustion) and contributes minimally to overall NO_x formation under the fuel-lean conditions of the practical combustion systems. Overall, the favorable parameters for prompt NO formation are cooler and cleaner hydrocarbon flames; i.e., those without a nitrogen-containing fuel source.[67]

2.4.3. Fuel-NO_x

Fuel NO_x is the dominant (~80 %) formation pathway in flames containing fuel-N. For coal, the major contribution of NO_x comes from char combustion, while devolatilisation of biomass contributes majorly to NO_x release from fuel-N. In stationary combustion, the emission of NO from fuel-bound nitrogen signifies an important source of NO_x emission. [68-69] The abundant N–H and N–C bonds in nitrogen-containing fuels account for the ready formation of fuel NO compared to thermal NO that comes from the thermal breakdown of the triple bond in molecular nitrogen.[70] For bituminous coals at high temperatures, HCN or soot nitrogen stems from tarry volatile-N compounds. Conversely, biomass and low-rank coal releases small nitrogenous moieties (HCN, HNCO and NH_3) directly into the combustion environment. NO formed from the homogenous oxidation of HCN through intermediary reaction pathways may be transformed into N_2 depending on the NO concentration. Figure 2.1 portrays the conversion of HCN (from fuel-N) into NO and N_2.

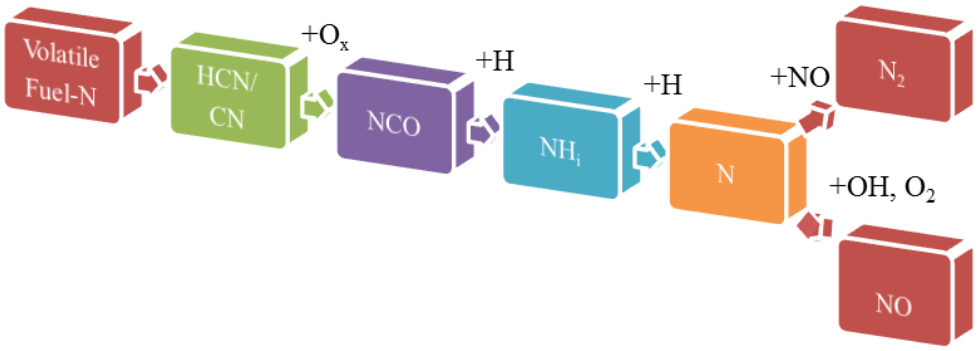

Figure 2.1. Reaction scheme for the conversion of HCN (from fuel-N) into NO and N_2.

Heterogeneous oxidation of char-N and soot-N produces NO and N_2. Subsequently, the formed NO is converted back to HCN and N_2 by hydrocarbon radicals positioned on char or soot surfaces.[13, 71]

For fuel-lean conditions (more air than fuel, $\lambda > 1.0$):

$HCN + O_2 \rightarrow NO + \ldots$ R2.7

$NH_3 + O_2 \rightarrow NO + \ldots.$ R2.8

For fuel-rich conditions (more fuel than air, $\lambda < 1.0$):

$NO + HCN \rightarrow N_2 + \ldots$ R2.9

$NO + NH_3 \rightarrow N_2 + \ldots$ R2.10

Experimental results have shown that the formation of NO from fuel nitrogen is rapid in the flame zone and decreases in the post flame region (flame rich). This result indicated that, the oxidation reactions of nitrogen-containing compounds, forming NO, are comparable to combustion reactions .[72] A Pioneering study by Fenimore et al.[73] on NH_3 oxidation revealed that, NO is formed through irreversible reactions of oxygen and NH_3, assuming a faster reaction rate constant compared to the reaction of oxygen with hydrogen. Furthermore, in jet stirred combustion, the rapid conversion of NO more than the equilibrium concentration was reported during the investigation of numerous nitrogen-bearing compounds in NO generation.[74] Moreover, excess NO was formed during coal combustion when different nitrogenous organic compounds were added to the CO flame at atmospheric pressure.[75]

The above experimental studies confirmed the formation of rapid NO from nitrogen-containing fuel; i.e., NO formed by the reaction of oxygen with nitrogen-containing fragments of parent compounds. This results in a non-equilibrium concentration of NO in the combustion region due to non-equilibrium radical concentrations (O and NO) in the combustion zone.

2.4.4. Nitrogenous compounds conversion in coal and biomass combustion

The amount of chemically-bound nitrogen in coal resides between 0.2 and 2.5% by dry weight. As explained above, combustion leads to the formation of NO from the oxidation of fuel nitrogen. The type of coal and temperature determine the total volatile nitrogen contents; for example, due to the fast release of water and light components in early stages of devolatilisation, the fractional nitrogen release is slower than the fraction mass release and the initial release of carbon.[76] For the medium rank coal, the rate of nitrogen and mass fractions are equivalent.[77] For high rank bituminous and anthracite, the fractional release of nitrogen is higher than the mass release. The temperature variation during combustion, char chemistry and the chemical structure of the coal are the main contributing factors towards the rates of nitrogen release. It is generally anticipated that the rate of nitrogen release is proportional to the overall weight loss.[78]

The transformation of nitrogen-containing compounds during coal and biomass pyrolysis has been addressed in detail. For coal, at a higher temperature, nitrogenous compounds are readily converted into pyridinic-N and quaternary-N.[79] Volatiles from pyrolysis of coal containing intermediate N-species generate HCN, and stable Char-N forms NH_3.[44]

Figure 2.2 depicts the general pathways in combustion processes where nitrogen-containing pollutants originate from fuel-N conversion. Biomass and coal contain different nitrogen species. In coal, hetero-atomic rings such as pyrolic and pyridinic nitrogen are major nitrogen functionalities. In biomass (cellulose, hemi-cellulose and lignin), nitrogen majorly exists in proteins[80] and is partitioned into alkaloids, porphyrin and chlorophyll.[81] During pyrolysis, some of the fuel-N evaporates and becomes part of the volatile gases; the rest is retained in the solid char that is subsequently emitted during combustion or gasification.[82] The distribution of fuel-bound nitrogen during pyrolysis displays sensitivity to many factors; most notably, temperature,[83] fuel type[83] and particle size,[84] while the heating rate[85] contributes only minimally. Kelemen et al.[79] studied the pyrolysis of coal and suggested that at higher temperatures, nitrogenous compounds are converted into pyridinic-N and quaternary-N compounds. Tan et al.[44] explained that the volatiles from pyrolysis of coal contain intermediate N-species that generate HCN and stable Char-N form NH_3. Choi et al.[86] reported the nitrogen-containing heterocyclic species from the pyrolysis of amino acid monomers. Biomass constituents have pronounced analogous effects on the release of nitrogenated species during pyrolysis. For instance, Chen et al.[5] conducted co-pyrolysis of amino acids with lignin and proposed the conversion of nitrogen compounds from lignin. Similarly, it was found that cellulose enhances the conversion of nitrogenous moieties into bio-oil. Hemicellulose impeded NH_3 production from co-pyrolysis of hemicellulose with amino acids – the work done by Ren et al.[87-88]

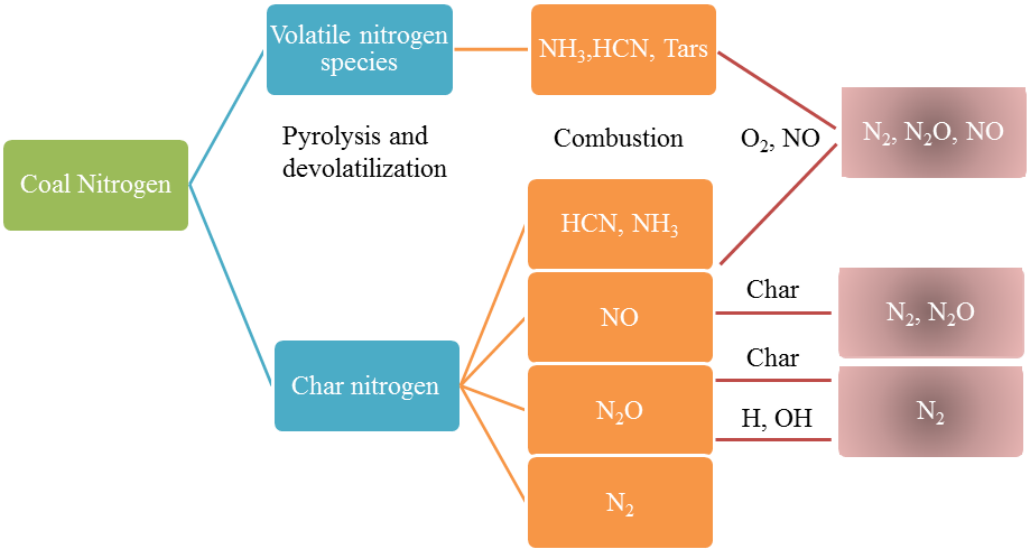

Figure 2.2. Simplified reaction scheme for the production of nitrogen-bearing pollutants in coal combustion.

2.4.5. Volatile nitrogenous species

2.4.5.1. Coal

Volatile nitrogen is primarily released as HCN and NH_3 species during devolatilisation. Under pulverised coal combustion, nearly 20–40 % of coal nitrogen is converted to NO while the remainder is eventually transformed into N_2.[89-90] The higher concentration of NH_3 is detected under more oxidative environments, such as the oxidation of char or during high temperature gasification of low rank coals[91-92]. The amount of HCN and NH_3 formed

depends on the local stoichiometry.[93] Combustion of coal may evolve small amount of HCN from the total nitrogen compounds but in the absence of oxygen, other nitrogen compounds are converted to HCN.[94] Under the presence of fuel-rich and nitrogenous compounds, HCN emerges as a major product. Furthermore, fuel-N primarily exists as HCN near the combustion zone.[89-90, 95-96] In an attempt to simulate fuel-N, nitrogenous compounds were added into combustion gases. It was found that the conversion of fuel-N to NO at elevated temperatures of 147–2027 ^{o}C does not depend on the type of compound added; rather, the combustion environment plays a major role. The foremost and imperative intermediates during the transformation of fuel-N are HCN, NH, NH_2, and NH_3.[62, 97] Hydrogen cyanide decays to form NH_i, which oxidises to form NO or N_2.

De Sotee[71] highlights the importance of HCN as an intermediate, while Fenimore[65] and Haynes[96] have illustrated the series of reactions of NH_2 that leads to the formation of NO and N_2. In a system with stoichiometry ratios higher than 0.70, HCN was reported to decay from high to low concentrations under stoichiometry ratios less than 0.70. HCN was found to have formed, presumably according to the reaction (NO + C_xH_y= HCN + …).[98-99] Under fuel-lean conditions, the amount of NO exceeds that of NH_3 and HCN. An opposite trend prevails under fuel-rich conditions.[94-95, 100-101] In addition, a higher amount of HCN is linked to bituminous coals, while more NH_3 formation is associated with lignite coals.[81]

2.4.5.2. Biomass

Thermal treatment of biomass drives increased O and OH radical pools and more volatiles compared to coal, due to higher O/N ratios. The most important biomass pyrolytic N-fragments are NH_3, HCN and HCNO, which serve as potent precursors for the formation of

NO_x.[4] Parameters such as final temperature, heating rate, fuel type and particle size govern the branching of biomass fuel-N degradation into volatiles (homogenous reactions) and char-N (heterogeneous reactions). The volatile formation takes place via a complex series of reactions that encompasses decomposition, substitution and hydrogen transfer reactions.[102-103] Figure 2.3 portrays the temperature windows for the synthesis of the dominant volatile species (HCN or NH_3) from biomass burning.

The yield of nitrogen-containing fragments seems to depend on the morphology of biomass particles in which relatively large biomass particles give small ratios of HCN/NH_3 and HNCO/HCN. High temperatures promote increased HCN during biomass pyrolysis.[47, 104] The cracking of heterocyclic and nitrogen ring molecules is enhanced in the presence of oxygen. The largest fraction of nitrogen in this scenario is converted into HCN. In pyrolysis of biomass-N, carbon dioxide reduces the formation of HCN and HNCO while enhancing the formation of NH_3.[81, 104-106] Hydrogen chloride (in agriculture biomass) promotes the formation of HCN and HNCO, and reduces NH_3 formation. The product distribution characterisation from biomass pyrolysis is also influenced by the minerals present in biomass.[107-108] For example, potassium increases the formation of HCN, NH_3, NO and HCNO at relatively low temperatures. Conversely, the inclusion of calcium retards the formation of HCN, NH_3, NO and HCNO at 330 ^oC but favours their formation at high temperatures.[103] Iron, silicon and aluminium display a similar influence on nitrogen transformation during biomass pyrolysis.[109]

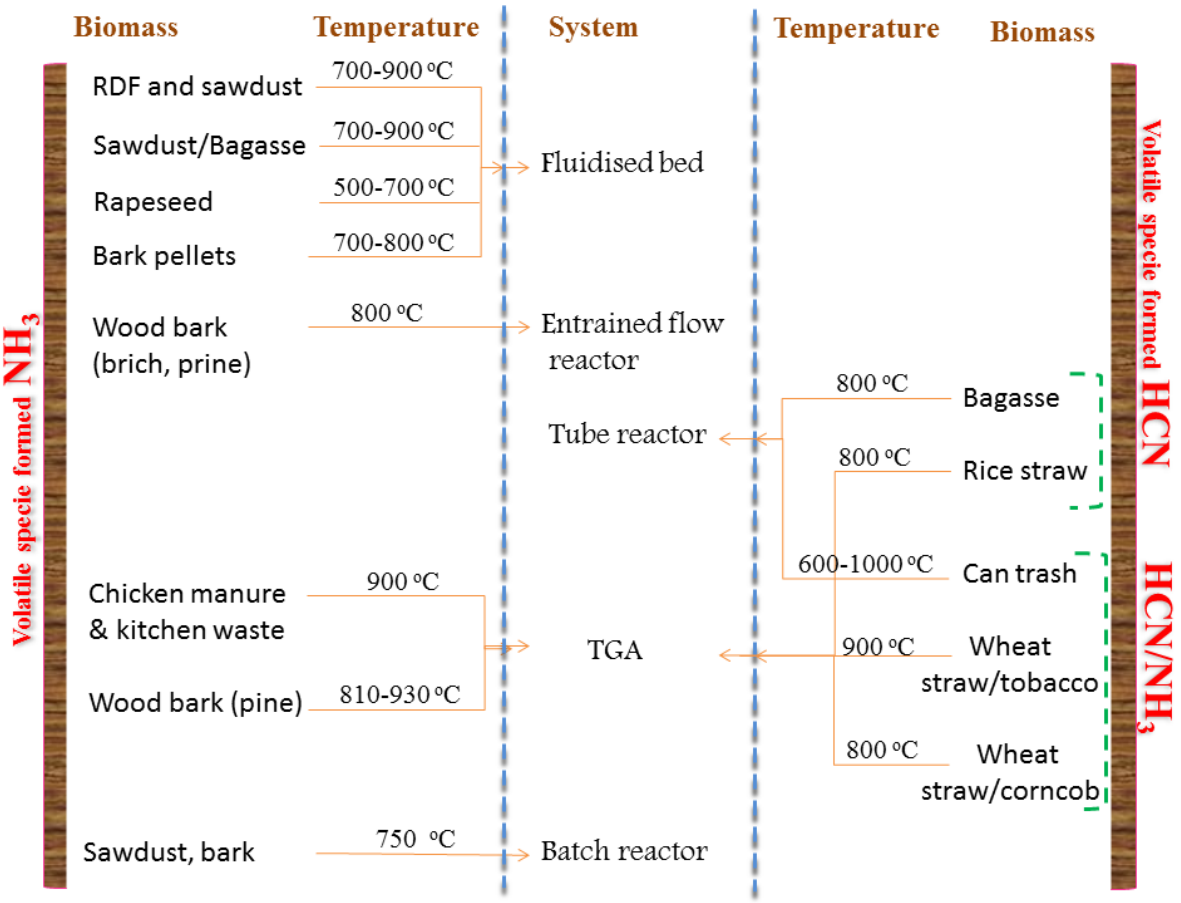

Figure 2.3. Nitrogen transformation from thermal degradation of notable categories of biomass into HCN and NH_3. (Reproduced from Ren et al.)[48]

2.5. NO_x control and reduction methods

Conventional NO_x control technologies are classified into pre-combustion strategies and post-combustion techniques. Pre-combustion methods incorporate burner design, flue gas recirculation, air-staging, over-fire air, fuel-staging, reburning, and advanced reburning. In total, combustion modifications and over-fire air can reduce ~23 % (average basis) of NO_x formation. Furthermore, the use of a low NO_x burner and natural gas reburning showed a ~51 % reduction efficiency. For post combustion treatment of NO_x, selective catalytic reduction

(SCR) and selective non-catalytic reduction (SNCR) are the most commonly deployed technologies. The combination of both these methods is also in use. SNCR is generally viewed as a cost effective method of NO_x reduction compared to the SCR method. The reduction proficiency of SNCR attains a value of 43 % while SCR displays up to 78 % NO_x reduction performance.[110-111] Advanced reburning technologies account for 70–90 % reduction of NO_x.[112]

NO can also be reduced to N_2 by both heterogeneous and homogeneous reactions.[113] The low-NO_x burner aimed to provide a fuel-rich zone that favours homogenous NO reduction.[71] Under fuel-rich conditions and more nitrogenous species conditions, a deficient oxygen concentration generally produces less NO release.

2.5.1. Reburning

The process of NO emission reduction by the addition of hydrocarbon fuel into the exit of the combustion chamber operated at a lower temperature is termed as "reburning". Wendt et al. [114] pioneered the reburning technology. This technology provides a fuel-rich region which promotes the formation of CH_i radicals that react with NO_x to form nitrogen molecules through HCN[115-118], as depicted in Figure 2.4. The effective yield of energy from fuel in the primary region also generates NO through the enrichment of OH and O radicals. The reburning region basically operates to reduce NO concentrations: under excess fuel conditions, it forms short chain hydrocarbons (open and closed shell species) that promote NO mitigation via reactions R2.11 and R2.12.[62, 118-120]

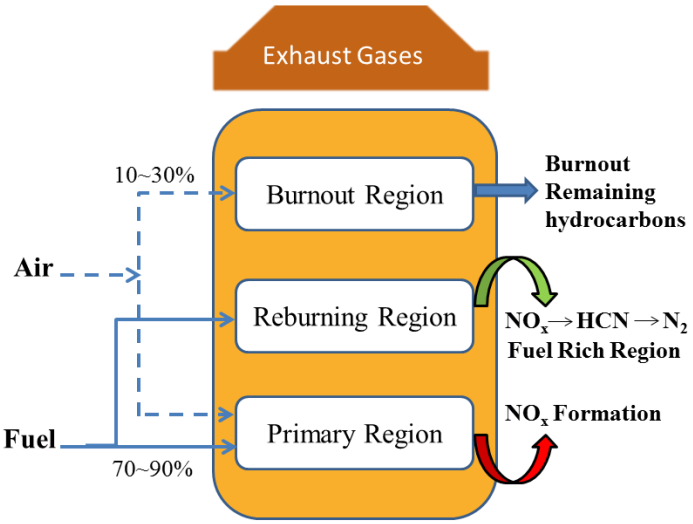

Figure 2.4. Overview of reburning technology for NO_x diminution.

At the exit of the combustion region, the burnout process ensures the complete combustion process and lessens the formation of nitrogen pollutants and NO release:

$NO + C_xH_y \rightarrow HCN + ...$ R2.11

$HCN + O/OH \rightarrow N_2 + ...$ R2.12

Wendt considered the below reaction (R2.13) as a crucial pathway for NO_x destruction:[121]

$NO + NH_i \rightarrow N_2 + ……$ R2.13

The efficiency of the reburning technology primarily depends on the temperature-profiles of the chemical species (N-compounds, carbon monoxide and hydrocarbons) as well as the process conditions (temperature, pressure, time and stoichiometry). The reduction of NO is optimum in a narrow range of temperatures (just below 1200 ^oC to well above 1300 ^oC).[62, 116, 118-119, 122-126]

The literature reports several reburning additive fuels, such as natural gas, oil, gasified biomass, micronised coal, polymers, pulverised coal and reburn fuel, the same as primary fuel. At high temperature reburning (above 1300 ^{o}C), surrogates of fossil fuel (for example, methane, ethane and a mixture of small hydrocarbons) have been employed for the reduction of NO, while for low temperature reburning, C_1–C_4 hydrocarbons have been tested. It has been generally shown that reburn fuel carrying higher concentrations of hydrocarbons promote higher amounts of HCN that are further oxidised back to NO before the burnout region.[93, 117, 127-129]. Natural gas (15–25 %) displayed a NO_x reduction efficiency of up to 67 %.[121] It has been shown that hydrocarbons, N-compounds and carbon monoxide are important agents of NO reduction during reburning, and natural gas is found to be an effective reburn fuel in most studies.[130-131] The fuel reburning mechanism for NO reduction is explained comprehensively in section 2.5.5.

2.5.2. Air staging

Another method for the reduction of NO is air staging, which divides the combustion air into:

- A primary zone that runs with a deficiency of air; and
- A second burnout zone that runs under excess air; this method tends to minimise NO_x formation by decreasing the concentration of O_2, O and OH (promoters of NO formation).

Several investigations show the strong influence of stoichiometry and residence time (1 s–2 s) depending on the type of coal. In a deficiency of air, NO concentrations are reduced and NH_3 and HCN are typically formed. In the case of a bituminous coal, both NH_3 and HCN were measured under fuel-rich conditions, revealing HCN in higher concentrations; in the

case of brown coal, NH_3 is much more predominant than HCN. As is the case in reburning, air staging leads to lower HCN production, which usually prevails under fuel-rich conditions.[132-136]

In both reburning and air staging, gas-phase hydrocarbon reactions with NO append the formation of HCN in the fuel-rich region. Hydrocarbon radicals (CH_i) and amine (NH_i) radicals play key roles in the mechanism of NO diminution in the fuel-rich region of reburning and air staging technology via the following two reactions:

$NO + NH_i \rightarrow N_2 + \text{products}$ $i = 0, 1, 2$ R2.14

$NO + CH_i \rightarrow HCN + \text{products}$ $i = 0. 1, 2$ R2.15

2.5.3. Selective non-catalytic reduction of NO_x

The selective non-catalytic reduction technique incorporates the injection of selective reagents into flue gases in the post combustion chamber between the temperature ranges of 875–1175 ^oC for the reduction of NO_x. Figure 2.5 displays a general overview of the SNCR NO_x mitigation operation. This technology is catalyst-free and can be coupled with other NO_x emission technologies. The ease of installation, and lower capital and operating cost renders it a more cost-effective option as compared to SCR. The majorly deployed chemical-injected species include ammonia ($DeNO_x$), urea (NO_xOUT)[137] and cyanuric acid ($RapereNO_x$).[138]

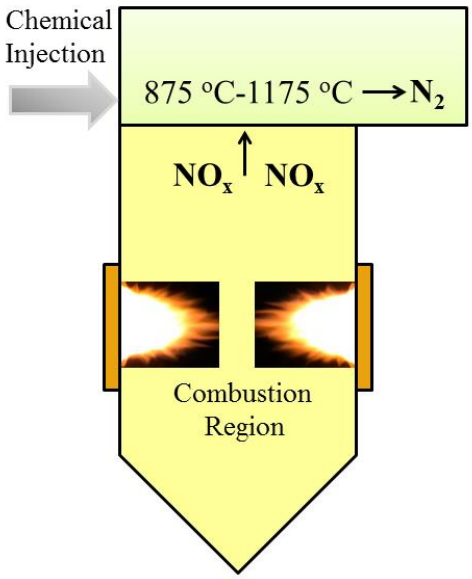

Figure 2.5. General representation of the selective non-catalytic reduction of NO_x.

2.5.3.1. Thermal DeNO$_x$

Thermal DeNO$_x$ signifies the homogeneous reduction of NO[139]. In this technology, NH_3 is injected into combustion systems that supply a nitrogen species for the reduction of NO. The injection of NH_3 in SNCR techniques operates in a narrow temperature window (800–1200 ^oC) in a process that is very sensitive to system operating conditions, such as mixing of the added reagent with flue gas and flue gas chemical species. The literature describes in detail the effect of temperature on NO_x reduction in specific combustion systems. The reduction of NO_x proceeds slowly below 800 °C and most of the added NH_3 remains un-reacted (i.e., NH_3 slip), while NH_3 oxidises to NO at temperatures higher than 1200 °C rather than reducing it.[62, 140-146]

The reaction mechanisms operating during the reduction of NO, through NH_3-SNCR, involve the following elementary reactions:

$NH_3 + OH \rightleftharpoons NH_2 + H_2O$ R2.16

$NH_3 + O \rightleftharpoons NH_2 + OH$ R2.17

$NH_2 + NO \rightleftharpoons N_2 + H_2O$ R2.18

$NH_2 + NO \rightleftharpoons NNH + OH$ R2.19

$NNH + NO \rightleftharpoons N_2 + HNO$ R2.20

$HNO + M \rightleftharpoons H + NO + M$ R2.21

$H + O_2 \rightleftharpoons OH + O$ R2.22

$O + H_2O \rightleftharpoons OH + OH$ R2.23

The NH_2 radical formed reduces NO under optimum conditions of temperature (730–1000 ^oC) in an oxidative environment. The formation of NH_2 radicals is mainly carried out by OH and O radicals through reactions R2.16 and R2.17. The success of the SNCR relies on the chain branching production of O and OH radicals. This result shows that, the reduction of NO by the NH_2 reaction is self-sustained via the regeneration of O and OH radicals which readily convert NH_3 to NH_2 radicals.

Atmospheric oxygen plays a central role in the reduction of NO via the SNCR process. The inclusion of O_2 minimises NH_3 slip and causes the formation of N_2O. Also, the presence of O_2 helps propagate the self-sustained (NH_2 + NO) reaction through steps R2.22, R2.17 and R2.18.[141, 147-149]. In short, under poor combustion conditions, admitting O_2 entails a twofold functionality: 1) generating the hydroxyl radicals necessary for the formation of NH_2 from NH_3; and 2) converting abundant hydrogen atoms into hydroxyl groups. While the presence

of trace water vapour facilitates the formation of hydroxyl groups (as in the reaction R2.23);[62, 144, 146, 150] it has been shown that even in its absence, such as in the experiments of Lyon and Benn, oxygen atoms produced by R2.22 react directly with NH_3 via R2.16, producing both NH_2 and OH radicals.[150] Figure 2.6 shows the effect of oxygen on NO reduction at different (NH_3/NO_o) ratios, in which NO_o denotes the initial concentration of NO.[140]

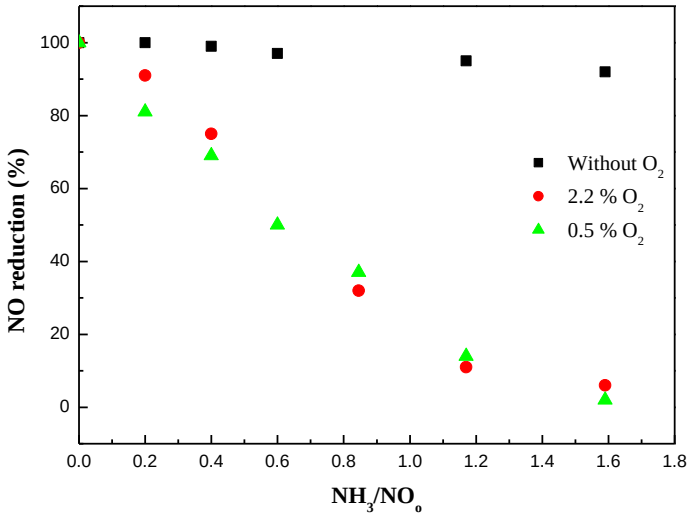

Figure 2.6. NO reduction at variable NH_3/NO_o concentrations.; the experimental conditions are (T = 982 ^oC, reaction time = 0.075 s, initial concentrations are NO_o = 1020 ppm and NH_3 level = 1400 ppm).[140]

Figure 2.7 presents the work of Lodder and Leffers[151] in which they tested the reduction of NO_x, using NH_3 in the presence of O_2 from an oil fired boiler. The reduction efficiency of NO_x increased with the increase of NH_3 loads. The NH_3 slip was notable for a NH_3 /NO_x ratio of more than 20. The effect of average flue gas temperature on the mitigation of NO_x is displayed in Figure 2.8.

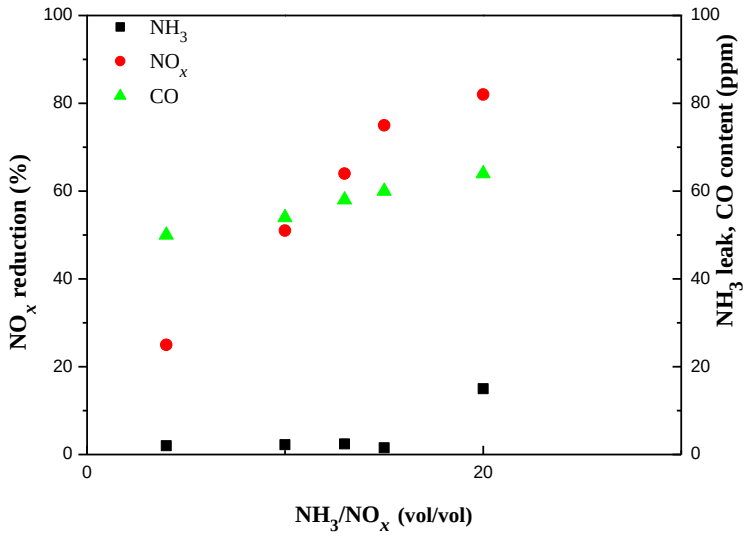

Figure 2.7. Reduction of NO_x with NH_3 at T = 1040 ^oC , O_2 level = 1 vol %, initial NO_x = 345 ppm.[151]

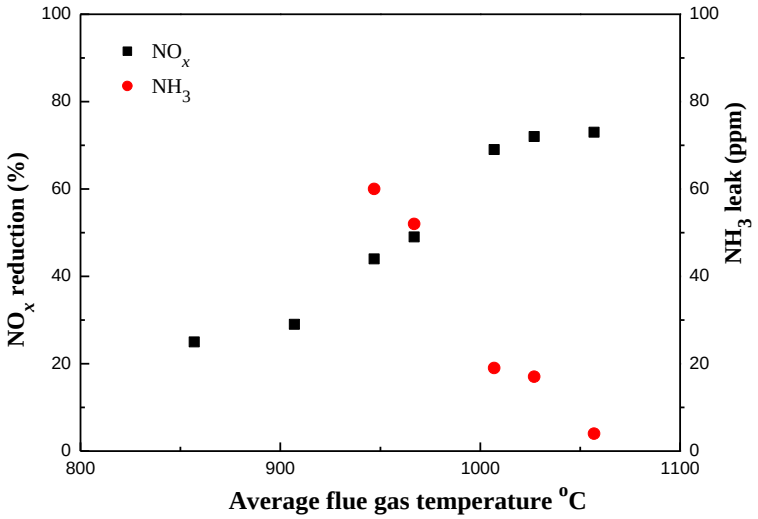

Figure 2.8. NO_x reduction at NH_3/NO_x molar ratio = 1.5, O_2 level = 1 vol % against various average flue gas temperatures.[151]

The addition of various types of agents plays a critical role in NO_x abatement. The addition of hydrogen with NH_3 decreases the NO_x reduction temperature. Conversely, excess addition of hydrogen might affect the NO_x reduction efficiency as NH_3 is oxidised into NO.[139-140, 150, 152] The inclusion of hydrogen with NH_3 in SNCR of NO enhances generation of OH radicals through the following sequence of reactions:[62, 153]

$H_2 + OH \rightleftharpoons H + H_2O$ R2.24

$H + O_2 \rightleftharpoons OH + O$ R2.22

$O + H_2O \rightleftharpoons OH + OH$ R2.26

As a result, the oxidation of NH_3 to NH_2 increases at the low temperature of 650 ^{o}C.[140] The effect of the co-existence of hydrogen peroxide (H_2O_2) with NH_3 in SNCR processes has been addressed in number of studies. H_2O_2 serves as a potent source for the active OH

radicals.[62, 154] Researchers observed enhanced mitigation of NO using H_2O_2 with NH_3 at temperature of 500 ^oC. The presence of OH radicals influenced the net reduction of NO. The key NH_2 radical readily forms by H abstraction of NH_3 by OH, thereby promoting NO reduction (R.218):

$H_2O_2 + OH \rightleftharpoons H_2O + HO_2$ R2.27

$NH_2 + NO \rightleftharpoons N_2 + H_2O$ R2.18

$HO_2 + NO \rightleftharpoons NO_2 + OH$ R2.28

Hydrocarbon addition in conjunction with NH_3 was found to lower the NO reduction temperature by 150-200 ^oC. It was revealed that ethane is more effective in reducing NO_x in comparison to similar concentrations of methane or carbon monoxide.[151] Wenli et al. found that C_2H_6 has a greater impact on removing NO as compared to CH_4, C_4H_{10} and C_2H_4 for the same carbon contents[155]. Previous studies[148, 151, 155-156] have reported a fall in the NO reduction temperature window due to ignition of combustible hydrocarbons with a minimal decrease of NO reduction efficiency. Furthermore, in combustion processes, alkyl radicals and hydro-peroxy radicals formed from hydrocarbons initiate the formation of OH and subsequently oxidise NH_3 into NH_2, thereby reducing the temperature region for NO reduction; however, it was shown that the increase of hydrocarbon concentrations shifts the optimum temperature window at the expense of NO removal efficiency.[151, 157] In addition to the shift in temperature window in the presence of hydrocarbons and ammonia (200 ppm), the ammonia slip was less than 5 ppm.[156] Figure 2.9 (a) and (b) present the work of the Lodders and Leffers[151], who studied the effect of CH_4 and C_2H_6 addition in conjunction with NH_3.

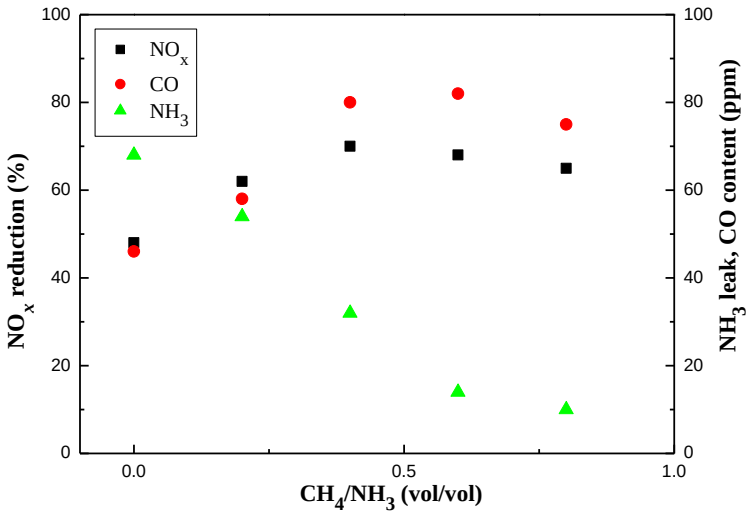

(a)

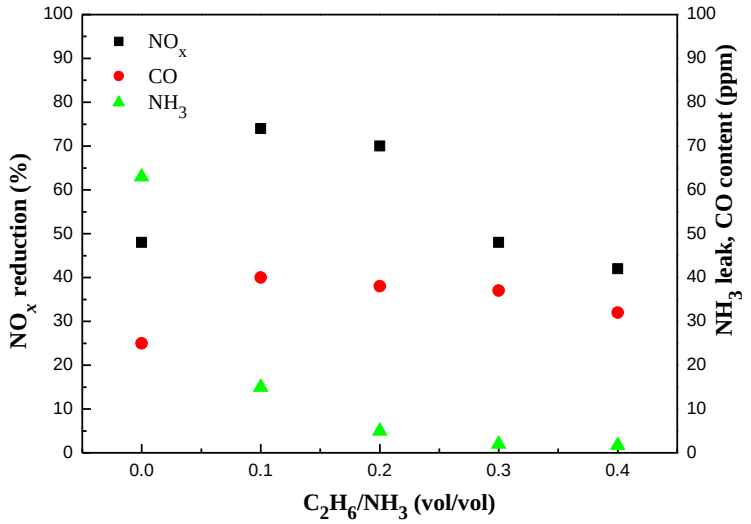

(b)

Figure 2.9. NO_x reduction versus a) CH_4/NH_3 and b) C_2H_6/NH_3, at T = 937 ^oC, initial NO_x level = 255 ppm, $[NH_3]/[NO_x]$ = 1.5 and under an oxygen level of 1 % by volume.[151]

During selective injection of NH_3 for NO reduction, the CO concentration increases through the inhibition of CO oxidation into CO_2 by NO.[151, 158] Wenli et al.[155] describe the role of CO in NO reduction and reported a shift of NO reduction temperature by 50 ^oC. Along the same line of enquiry, Lodder and Leffers'[151] findings support the fact that the decrease in the NO mitigation temperature window between 40–80 ^oC stems from an increase in OH concentrations. In their experiments, they utilise dry gas to report the oxidation of CO in the presence of NH_2. These results are comparable to those of Lyon and Hardy who add moisture (up to 11 %) and report an inhibition of CO conversion into CO_2. The higher initial CO level decreases the NH_3 slip.[159] Lyon and Hardy[140] present detailed kinetic accounts to explain the formation of more CO in the presence of NH_3. Carbon monoxide enhances the reaction of NH_3 with O_2, forming more NO rather than reducing it. Carbon monoxide is oxidised according to:

$$CO + OH \rightleftharpoons CO_2 + H \qquad \text{R2.29}$$

The generated H atoms in the above reaction react with oxygen as follows:

$$H + O_2 \rightleftharpoons OH + O \qquad \text{R2.22}$$

$$O + H_2O \rightleftharpoons OH + OH \qquad \text{R2.26}$$

Enhancement of the H/O radical's pool increases consumption of NO by ammonia via:

$$NH_2 + O \rightleftharpoons NH + OH \qquad \text{R2.32}$$

Chan et al.[160] found that, in staging, if a reducing agent is injected into a fuel-rich region of a rich/fuel staged combustor, significant NO can be reduced after the poor region. They illustrated a comprehensive mechanism for the production of NH_2 and reduction of NO by CO, and suggested that the primary source of CO is the rich zone in the combustion chamber. The transition from poor to rich regions leads to the production of more OH radicals through R2.29 and R2.22:

$CO + OH \rightleftharpoons CO_2 + H$ R2.29

$H + O_2 \rightleftharpoons OH + O$ R2.22

$O + H_2O \rightleftharpoons OH + OH$ R2.26

As explained earlier, OH reacts with NH_3 to form NH_2 radicals that reduce NO into N_2:

$NH_3 + OH \rightleftharpoons NH_2 + H_2O$ R2.16

2.5.3.2. NO_xOUT process

Since the reduction of NO_x is dominated by the intermediate species of NH_2 and OH radicals, the agents in the NO_xOUT process, such as urea, should be capable of serving as a facile source for NH_2 radicals. Salimian and Hanson[142] modelled the reduction of NO using urea as a source of NH_2 radicals. In natural gas-fired furnaces, the injection of urea reduces the NO_x in a temperature window of 1015–1060 ^oC.[161] NO_xOUT technology has been used for a variety of fuels, such as oil, coal and gas.[157] Table 2.4 gives the reported efficiency values of the NO_xOUT process for NO_x emission under variable combustion conditions. Ammonia slip can compromise the NO_xOUT process, but injection of the correct urea concentration into the optimum reaction zone (1040 ^oC) can reduce the potential for NH_3 slip.[162]

Table 2.4. NO_xOUT performance of numerous combustion systems.

System	Temperature	NO reduction	NH_i/NO	References
Pulverised coal boiler	1000 °C	40-45 %	1.5	Chen et al.[160]
Pilot scale reactor	1000 °C	70 %	1.3	Jodal et al.[137]
KVA Bessel municipal incineration solid waste plant	945–1000 °C	65 %		Jones et al.[163]
Cement kiln systems		45–50 %		Lin and Knenlein[164]
Pulverised coal combustion		50 %	1	Higgins and Douglas [165]
LPG gas fired furnace	1000 °C	40–60 %	1-1.5	Lee et al 1996[166]
Brown coal-fired boiler		30 %	0.3	Negrea et al.[167]
Pilot-scale combustor aired with natural gas	1000 °C	50–55 %	2	Muzio et al.[168]
116 KW flow reactor combustion	1025–1100 °C	58 %	1	Irfan and Gibbs[169]
Pilot-scale diesel fired tunnel furnace	855 °C	54 %		Hossain et al.[170]
Utility fired boiler		30 %	2	Abele et al.[171]
Gas- and oil-fired boiler	980-1040 °C	40 %	2	Nylander et al.[172]

At an NH_2/NO ratio of 1, the maximum reduction of NO_x is ~58 % over a temperature range of 1025–1100 °C, while for the NH_2/NO ratio of 2, NO_x reduction efficiency resides at 78 % at a temperature of 1100 °C.[173] The use of an additive with urea solutions, such as furfural derivatives and alcohols, displays a positive impact on NO_x mitigation.[157]

2.5.3.3. NO_x reduction mechanism in NO_xOUT process

The initial main decomposition products of urea are NH_3 or NH_2 and HNCO or NCO. The mechanism of the NO_xOUT process takes place in three steps: 1) Urea decomposition; 2) reactions of NH_3/NH_2 with NO [174]; and 3) reactions of HCNO/NCO with NO.[175] Urea breaks down into NH_3 and HCNO at around 300 °C. The amidogen radical is formed via H abstraction from ammonia. This reaction assumes a critical importance in the NO_x abatement through the NO_xOUT operation.[176-177] Formation of NCO from HNCO + OH (via the H abstraction channel), and further reaction with NO, predominantly gives N_2 and N_2O.[178] Figure 10 shows the reaction channels for the gas phase reaction of urea in a rich NO_x atmosphere.

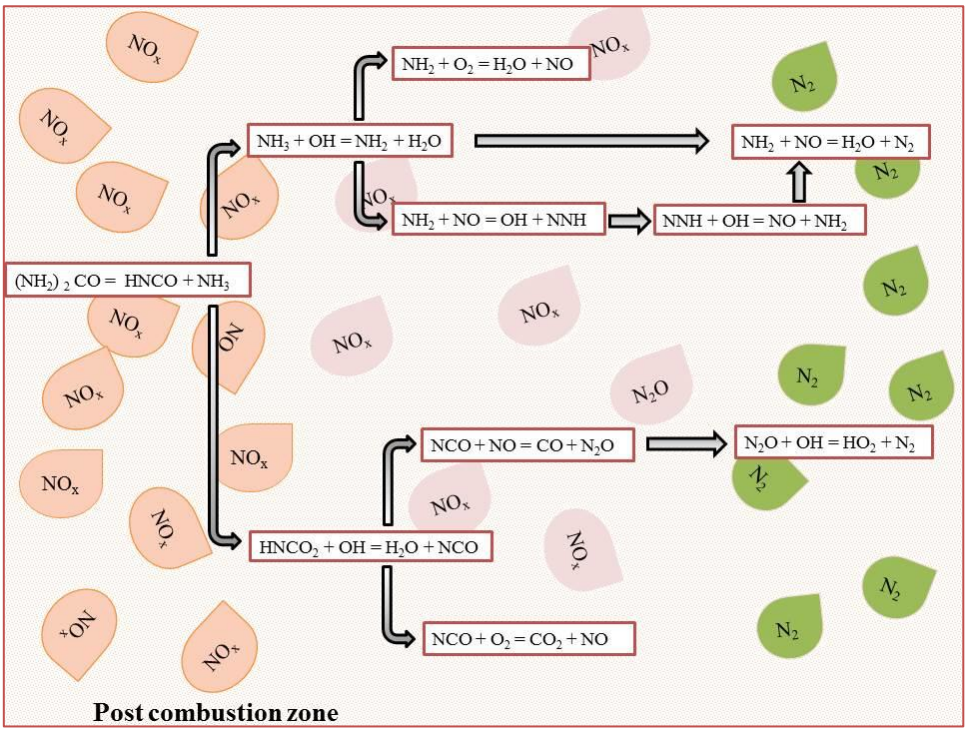

Figure 10. Reaction pathways illustrating the NO_xOUT process, $(NH_2)_2CO$ + NO.

2.5.4. Biomass as a reburn fuel

Many efforts have been made to enhance the reduction of NO_x using liquefied petroleum gas, coal water slurry, superfine pulverised coal and biomass. These efforts have also targeted the implementation of new advanced reburning technologies that combine basic reburning with SNCR methods. Mostly, biomass fuels contain less nitrogen content compared to coal. Agricultural-based biomass generally contains more nitrogen (based on % dry basis) compared to other categories of biomass.[179] In addition, sulphur contents in biomass are also very low and do not pose an effect from SO_2 formation. The emission of CO_2 from biomass usage is also significantly low compared to coal and other reburn fuels. Furthermore, the low total heat input (10–20 %) for the reduction of NO_x makes it a better choice as a reburn fuel. [157, 180]

Li et al.[181] demonstrated an NO_x reduction efficiency of 50–70 % using biomass-based reburning fuels such as wood, rice husks and orange peel. Adams and Harding[182] investigated NO_x reduction in cyclone-fired boilers using wood as a source of reburn fuel. Their study revealed a 45–55 % NO_x reduction using optimised parameters and conditions such as suitable carrier gases, optimum stoichiometry values and the proper design of the fuel injector. In another experimental study by Adams and Harding[183], they reported 70 % NO_x reduction efficiency using hardwood and softwood at a stoichiometry ratio of 0.85. They strongly emphasise the stoichiometry ratio of reburn fuels and residence time in the reburn region as the most important variables controlling NO_x mitigation. Recently, Zhuang et al.[184] used sawdust, corn straw and cotton straw in a lab-scale, self-heating, drop tune furnace for NO_x removal. They reported maximum NO_x reduction efficiency at 1100 ^{o}C temperature, based on a stoichiometry ratio of 0.6–0.7 and residence time of 1.88 s.

Shu et al.[185] used a horizontal fixed-bed quartz reactor to investigate the diminution of NO_x utilizing rice husk, sawdust and corncob as biomass samples. The fine-tuned experimental conditions were a 800–1200 ^{o}C temperature interval, a 200–1200 ppm NO initial concentration, a residence time of 0.6 s, and a 0–6 volume % of inlet oxygen concentration. The maximum NO_x removal efficiency was obtained by sawdust at inlet 800 ppm of NO, 0–1 volume % O_2, and particle size of 160–370 μm. Casaca and Costa[186] evaluated the effect of rice husk particle size distribution on the reburning process to remove NO_x formation from a large-scale laboratory furnace. The maximum removal efficiency obtained was 60 % from an intermediate size distribution of rice husk at a residence time of 0.70 s and stoichiometry ratio of 0.90. Wang et al.[187] performed kinetic modelling to analyse the effects of biogas fragments, reburning fuel ratio, stoichiometry, temperature, residence time and initial NO concentration on the reduction efficiency of NO. They concluded a maximum NO reduction

from biogas reburning fuel using a higher fuel ratio at 0.6 stoichiometry ratio and reburning temperature of 927–1127 °C. At the low initial concentration of NO, the reduction efficiency was shown to be independent of residence time and initial NO value. Vilas et al. [188] conducted pilot-scale experiments using straw and poplar wood as biomass reburning fuels and Gottelborn coal as a primary fuel. They found reasonable agreement between the modelled and experimental results. An NO reduction efficiency of 15 % was attained at a residence time of 1.2 s and temperature of 1264 °C. Luan et al.[189] described comprehensively the factors (stoichiometry ratio, fuel type and reburning distance) influencing NO reduction using the experimental setup of a drop tube furnace. Biomass fuel set a strong reducing environment in the reburning zone through the formation of high C_xH_y, H, H_2 and CO concentrations and a low O_2 concentration that converts NO into N_2.

Efficient NO removal is possible with a high ratio of carbon conversion in the reaction zone. The optimal conditions are 15–20 % biofuel reburning ratio, NH_3/HCN ratio of 1.6–2.5 and stoichiometry ratio of 0.6–0.8. Under equivalent experimental conditions (NO = 500 ppm, residence time 1 s, stoichiometry of 0.7 and at 1200 °C temperature), corn straw achieved a higher NO reduction efficiency as compared to the rice husk, attaining an efficiency value of more than 80 %. Under the same conditions, the analogous reduction efficiency by rice husk peaked at 70 % NO reduction. In another study, Casaca and Costa[190] analysed the ability of biomass (rice husk) for NO_x reduction in a reburning process.; they conclude that rice husk performance, a 60 % NO_x reduction, was comparable to that of natural gas reburning at a higher added fuel fraction (20–30 %), low stoichiometry ratio and a high initial NO_x concentration (700 ppm). Ballester et al.[191] illustrated a broad experimental depiction of biomass reburning under propane and pulverised coal flames. The study was conducted in a semi-industrial-scale furnace using natural gas and sawdust as reburn fuels at residence times

(0.41–1.44 s) and variable stoichiometry ratios (0.85–1.05) in the reburn zone. Lu et al.[192] controlled the optimum conditions to maximise NO_x reduction through the reburning of biomasses (cotton stalk, wheat straw, rice husk and rice straw) using an entrained flow reactor. NO reduction efficiency with cotton stalk reburning (SR = 0.77), wheat straw reburning (SR2 = 0.73), rice husk reburning (SR = 0.77), and rice straw reburning (SR = 0.75) was 66.4 %, 63.6 %, 56.0 %, and 52.0 %, respectively. NO reduction efficiency of biomass reburning follows a pattern of first increasing and then decreasing efficiency for varying stoichiometry ratios from 0.68 to 1.03. NO removal efficiency peaks at 1373 K and 20-25 % reburn fuel fraction. In summary, greater than 50 % NO reduction capacity can be obtained at a stoichiometry of 0.7–0.8, or fuel reburn fraction at 20–25 %. Table 2.5 elaborates the comprehensive use of biomass as a reburn fuel for NO_x diminution.

Table 2.5. Efficiency of NO_x control using biomass.

Biomass Compound	Reduction efficiency	Temperature **°C**	System	SR	**Residence time**	Initial NO
Sawdust[184] Corn Straw Cotton stalk	25–52 % 24–42 % 22–50 %	800–1100	Lab-scale and self-heating drop-tube furnace	0.70	1.88 s	
Sawdust[185] Rice Husk Corncob	55 % 43 % 44 %	800–1200	Horizontal fixed-bed quartz reactor	0–1% vol O_2 6 % H_2O	0.6 s	800 ppm
Rice Husk[186]	60 %	Thermal input 33 kW	Instituto Superior	0.90	0.7 s	350 ppm

			Técnico large-scale laboratory furnace			
Biogas[187]	82–90 %	927	Kinetic modelling	0.60	1.0–3.0 s	1000 ppm
Sawdust Rice husk Sludge reburning	68 % 58 % 45 %		Semi-industrial pulverised-coal single-burner furnace	0.89–1.02	0.62 s	
biomass char[188]	15 %	1200	Entrained flow reactor	<0.1% of O_2 0.8	1.2 s	365 ppm
Corn straw[189] Rice husk	81 % 70 %	1000	Drop Tube Furnace	0.7	1.0 s 0.84 s	~500 ppm
Rice Husk[190]	60 %	Total thermal input 130-186 kW	large-scale laboratory furnace	0.8–1.1	0.7 s	700 ppm
Oak sawdust[191]	58–83 %	1200	Semi-industrial-	0.91	0.41–1.44 s	190 ppm

			scale furnace			
Cotton stalk[192] Wheat straw Rice husk Rice straw	40–68 % 35–60 % 33–45 % 30–50 %	900–1100	Entrained flow reactor	0.68–1.03	0.8 s	800 ppm
Phenol	20–86 %	1100–1300	Tubular flow reactor system	0.58–3.3	0.13 s	1000 ppm

2.5.5. NO reduction mechanism in fuel reburning

Comprehensive studies[193-197] have been carried out to discover the NO reduction mechanism through reburning. Figure 2.11 depicts an overview of NO_x reduction mechanisms by hydrocarbon fragments.

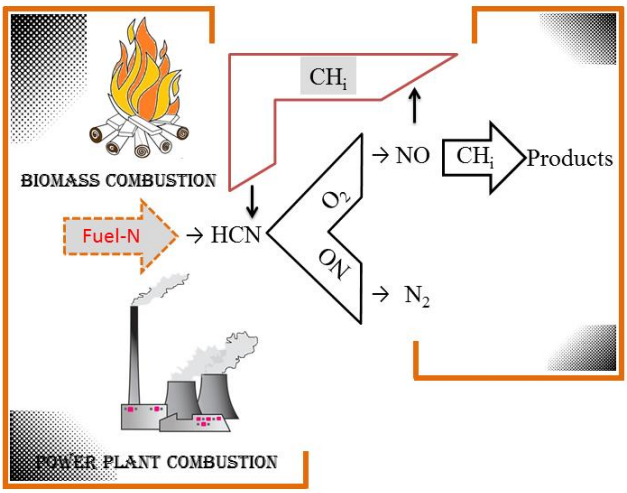

Figure 2.11. Global NO_x formation and mitigation pathways

A bottleneck for the overall process is impeded in the initial transformation of NO to HCN accomplished via the reaction of NO with hydrocarbon fragments:

$C + NO \rightarrow CN + O$ R2.37

$CH + NO \rightarrow HCN + O$ R2.38

$CH_2 + NO \rightarrow HCNO + H$ R2.39

The dominant channel is R2.38, which depends on the concentration of hydrocarbon radicals present in the reburning zone. Chan et al.[198] found that the end product of the interaction hydrocarbon and NO is HCN sourced from the potent CN and HCNO intermediates. HCN consumes OH and O radicals via the following subset of reactions:

$HCN + OH \rightarrow HOCN + H$ R2.40

$HCN + OH \rightarrow HNCO + H$ R2.41

$HCN + O \rightarrow NCO + H$ R2.42

$HCN + O \rightarrow NH + CO$ R2.43

The existence of the reducing species near stoichiometry is too low to reduce NO. In the fuel-rich region, the concentration of oxidising compounds starts decreasing and the reducing species start accumulating, enabling them to react with NO.

Wendt[121] described the mechanisms of NO reduction and formation. Specific to reburning technology, NO reduction normally occurs through a series of elementary reactions of HCN and NO. Hydrocarbon radicals present in fuel-rich conditions convert NO into HCN through

the reaction R2.15. In subsequent reactions, HCN is oxidised to NCO with the generation of H radicals via reaction R2.42, which eventually affords N_2 (R2.46-R2.48):

$CH_i + NO \rightarrow HCN + \ldots$ R2.15

$HCN + O \rightarrow NCO + H$ R2.42

$NCO + H \rightarrow NH + CO$ R2.46

$NH + H \rightarrow N + H_2$ R2.47

$N + NO \rightarrow N_2 + O$ R2.48

Contrary to fuel-rich conditions, hydrocarbon reacts with oxygen and hydroxyl radicals under fuel-lean conditions via reaction R2.49. The efficacy of the reburning method's success strongly depends on the interaction of CH_i radicals with NO.

$CH_i + O/OH \rightarrow CO + H + \ldots..$ R2.49

To improve the kinetic mechanism, a global reaction rate for the reburning methods was developed[71, 199-200] for premixed, laminar hydrocarbon-containing flames using the CHEMKIN code.[201] For the global reaction mechanism[200] in reburning regions, calculating the reaction rate of $NO + C_iH_j$ is as follows:

$\sum C_iH_j + NO \rightarrow HCN + \ldots..$ R2.50

Development of reburning NO was an important step towards the exact determination of formation and destruction of NO, especially in hydrogen-rich flames; otherwise, the concentration profiles of NO, HCN and NH_3 were inaccurate without accounting for the NO-

reburning mechanism during the formation of NO in hydrogen-rich flames.[112] Recently, Ibukun et al.[129] investigated the recycled plastic for probable NO_x reduction. They were able to reduce 80 % of the NO_x with the use of polyethylene. The literature reports a safe, recycled polymer for NO_x reduction.[129, 202]

2.5.6. Catalytic conversion of NO_x into N_2

Selective catalytic reduction (SCR) incorporated NH_3 as the reducing agent and has been proved an effective and preferred choice for the mitigation of NO_x at a modest temperature of 250–500 ^oC, especially for mobile emission sources.[203] Catalytic surfaces employed in SCR can be arranged in three sub-categories: 1) noble metals like Pt, Pd, Ag, etc.; 2) transition metal ions, mainly Fe and Cu, transition metals nitrides and oxides such as Mn, Fe, V, Cu, Cr, Co; and 3) exchanged zeolite surfaces.[204] Transition metal oxide catalytic surfaces have acquired outstanding low-temperature SCR activity. Mn-based catalysts (pure nano-MnO_x), Mn-based metal oxide mixture (MnO_xCeO_2, MnO_xFeO_x) and MnO_x are typically loaded on various supports (Al_2O_3, TiO_2, carbon materials, ceramic monolith).[205] Further research in this area was conducted by Fu et al.[206] In their review, they summarise the use of catalytic surfaces with and without carriers, reaction kinetics, mechanism of NO_x diminution MnO_x catalysts, as well as the effect of reaction conditions. For efficient low temperature catalytic surfaces, Mn-doped materials (MnO_x/TiO_2 and MnO_x) exhibit high activity for NH_3-SCR.[207] The reactivity of Cr-MnO_x mixed-oxide surfaces are very effective over a temperature window of 120–220 °C.[208]

Li et al.[209] provided a review on the SCR performances of Mn-based metal oxide and Fe, Cu exchanged zeolite catalysts. They showed that MnO_x molecules are the dynamic gears for

NH_3-SCR of NO across a range of low temperatures (100–300 ˚C). Among Cu and Fe based exchanged zeolite surfaces, the Cu–zeolite catalyst offered superior activity at the lower temperatures, while Fe/beta shows enhanced activity among all the Fe-based exchanged zeolite catalysts; however, exposure to SO_2 and H_2O induces catalyst poisoning as well as the formation of N_2O. Shan and Song[210] urged a review of low temperature catalytic surfaces for NH_3-SCR, focusing on carbon-loaded V_2O_5 and Cu-bearing tiny pore zeolites. They pointed out that V_2O_5 doped on carbon material offers high activity and SO_2 resistance at low temperatures, counting as an appropriate choice for high sulphur-containing fuels. The hydrothermal stability and elevated activity is noted in Cu-based small pore zeolites.

SCR reduces NO_x levels through the reaction of NH_3 with NO over catalytic surfaces (frequently used V_2O_5-$WO_3(MoO_3)/TiO_2$)[211] to produce N_2 and H_2O without consuming excess O_2 and upholding ~95 % conversion efficiency.[212] Under NH_3-SCR operation, Ce-doped surfaces claim excellent NO_x reduction proficiency due to the greater O_2 capturing capacity and effective redox ability of CeO_2. Furthermore, the literature provides a variety of Ce-based catalytic surface, such as Ce-Mn, Ce-Ti, Ce-W, Ce-Sn , Ce-Cu, Ce-V, Ce-Mo, Ce-Nb, Ce-Ta, Ce-W-Ti, Ce-Cu-Ti, Ce-Mn-Ti and Ce-Sn-Ti.[213]

Besides NH_3, the N-containing compound like urea[214], and other reducing agents such as H_2,[215] CO[216] , ethanol [217]and hydrocarbons[218], are used for the remedy of NO_x emission over catalytic surfaces. Various hydrocarbons such as methane, propane, and propylene can function as effective carrier gases/reducing agents for NO_x conversion into N_2, as reducers. Table 2.6 presents various Mn-based NH_3-SCR and zeolite catalysts HC-SCR of NO conversion and N_2 selectivity.

Table 2.6. NO mitigation efficiency of selected Mn-based NH_3-SCR and zeolite based HC-SCR surfaces.

Catalyst	Reducing agents	Reaction condition	NO conversion %	N_2 selectivity %	Sources
		Mn-based NH_3-SCR			
MnO_x-CeO_2	0.1 % NH_3,	0.1 % NO, 2 % O_2, 150 °C	95	98	Qi et al.[219]
MnO_x-Fe-CeO_2	0.1 % NH_3,	0.1 % NO, 2 % O_2, 180 °C	93	92	Qi et al.[219]
MnO_x-Cu-CeO_2			90	89	
MnO_x-Pr-CeO_2			75	94	
MnO_x-Zr-CeO_2			95	88	
MnO_x-SnO_2	0.05 % NH_3	0.05 % NO, 3 %O_2, 120–200 °C	100		Tang et al.[220]
MnO_x-FeO_x-TiO_2	0.05 % NH_3,	0.05 % NO, 5 %O_2, 200–300 °C	100	>90 %	Liu et al.[221]
MnO_x/Al_2O_3	0.05 % NH_3	0.05 % NO, 2% O_2	95	>65	Singoredjo et al.[222]

		150–250 °C			
MnO_x/TiO_2	0.04 % NH_3,	0.04 % NO, 2% O_2, 170 ^oC	95	72	Simirnioti s et al.[223]
		Zeolite based HC-SCR			
CuSiBEA	0.1 % C_2H_6O	0.1% NO, 2 % O_2, 380 °C	40	78-90	Dzwigaj et al.[224]
Pd-SBA-Imp	0.15 % CH_4	0.015 % NO, 7 % O_2, 300 °C	98%	NA	Boutros et al.[225]
Ag/Al-SBA-15	0.25% C_2H_6O	0.05 % NO, 10 % O_2, 350 °C	35	100	Boutros et al.[226]
2% Pt/MPS	1 % C_3H_6	0.1 % NO, 14 % O_2, 160 °C	100	na	Komatsu et al.[227]
2% Pt/B-MPS	0.3 % C_3H_6	0.1 % NO, 1 % O_2, 400 °C	100	na	Komatsu et al.[227]
Co-Pd-ZSM-5	0.25 % CH_4	0.05 % NO, 5 % O_2, 450 °C	90	na	Pieterse et al.[228]
Co- Ba/ZSM-5	0.1 % C_3H_8	0.09 % NO, 2 % O_2, 500 °C	76	na	Stakheev et al.[229]

Recently, Altarawneh et al.[230] computationally tested the catalytic activity of cubic molybdenum nitride (γ-Mo_2N) for the reduction of NO into N_2 via its adsorption on γ-Mo_2N surfaces. Based on the experimental study of He et al.,[231] they developed a reaction mechanism for the conversion of NO into N_2 over γ-Mo_2N(100) and γ-Mo_2N(111) surfaces. The catalytic ability of γ-Mo_2N triggered dissociative adsorption of ^{15}NO molecules over γ-

$Mo_2N(100)$ and γ-$Mo_2N(111)$ surfaces, through accessible reaction barriers of 24.1 and 117.6 kJ mol^{-1}, respectively. NO dissociation on these surfaces leads to the formation of an oxynitride configuration, $Mo_2O_xN_y$. Subsequent desorption of N_2 takes place via the Langmuir–Hinshelwood mechanism. Figure 2.12 reproduces He et al.'s[231] reported conversion efficiency of NO by passivated and H_2-treated γ-Mo_2N surfaces over the temperature range of 100–400 °C. The reduction efficiency at 200 °C of passivated γ-Mo_2N (3.9 %) was reported to reside below that of H_2 treated γ-Mo_2N (13.6 %); however, near 450 °C, both these surfaces show 100 % mitigation of NO with an N_2 selectivity of 98 %.

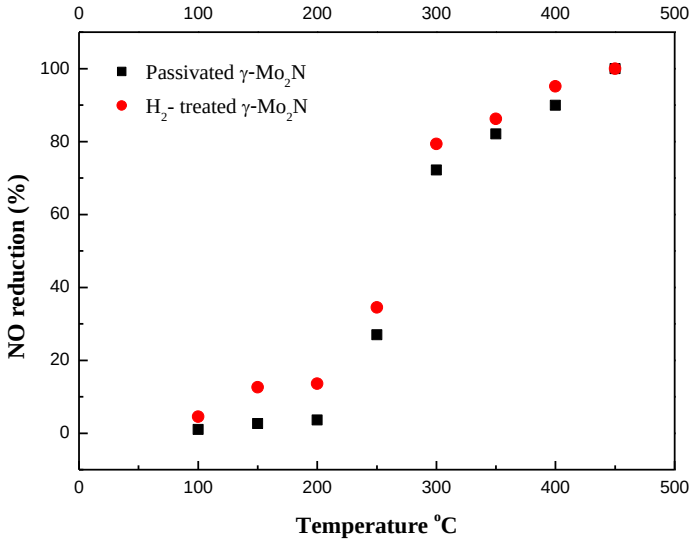

Figure 2.12. Reduction efficiency of NO over H_2-treated and passivated γ-Mo_2N.

2.6. Formation of N_2O: A greenhouse gas

Figure 2.13 (a) and (b) display the contribution of N_2O to overall greenhouse gas budgets and emissions of N_2O from various emission sources, respectively. The level of N_2O gas is

increasing (0.26 % per year) in the atmosphere over time, which ultimately diffuses into the stratosphere region causing ozone depletion.[232] N_2O has a major role in global warming potential (~300 times CO_2) due to its effective property as an infrared radiation absorber.[233-235] The major input of anthropogenic N_2O is the agricultural sector based on a million tonnes of nitrogen bearing fertilisers.[236-238] The total N_2O emissions from natural and anthropogenic endpoints combined is approximately 17.7 Tg N $year^{-1}$. The estimation of N_2O from industrial biomass burning and industrial energy production systems is about 2 Tg N $year^{-1}$.[232]

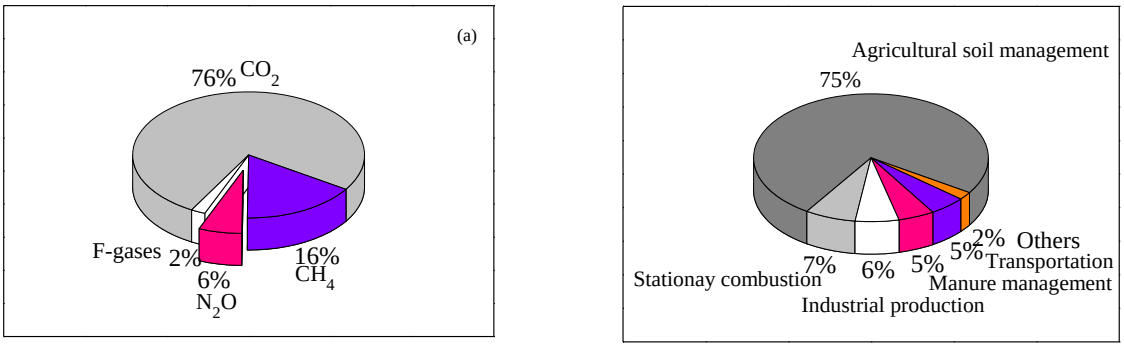

Figure 2.13. a) Global emission of greenhouse gases into the atmosphere;[239] b) contribution of N_2O from different sources into the atmosphere.[240-241]

A great deal of work has been conducted on N_2O release from combustion fuels (solid and liquid based) as these sources contain fuel-N.[20, 242-243]. N_2O is generated from combustion systems as well as from NO_x abatement technologies (thermal $DeNO_x$ and NO_xOUT) alike.[157] Table 2.7 summarises N_2O release from some widely used combustion systems and NO_x mitigation activities. Coal fired combustion and oil burning are major contributors to N_2O formation, with an observed level of ~25 ppmdv (parts per million dry volume).[244-245] Fluidised bed combustion is a particularly potent source of N_2O due to the lower temperature operating condition, typically releasing 20–400 ppm [246] N_2O.

Table 2.7. Emission sources of N_2O and their reported concentrations.[20]

Combustion Sources	N_2O release	NO_x mitigation technology	N_2O release
Conventional stationary combustion	1–5 ppm	Fuel staging in conventional stationary combustion	10-15 ppm
Fluidised bed combustion	20–150 ppm	Thermal DeNO$_x$ Ammonia addition Urea or cyanuric addition	3–5 % of NO_x reduction 10–15 % of NO_x reduction
Diesel engines	0.03 g N per km		
Gasoline engines	0.01–0.03 g N per km	Three-way catalyst for gasoline engines	0.03–0.15 g N per km

The formation of N_2O is mainly derived from two reactions: NCO + NO → N_2O + CO and NH + NO → N_2O + H. In most conventional combustion systems operating between 900 – 1250 °C, N_2O forms from fuel-bound nitrogen.[243, 247] In fluidised bed reactors and SNCR operations which typically operate at low temperatures, N_2O is not reduced into nitrogen.[20, 248]

Due to the lower operation temperature of FBC, N_2O is formed in higher yields compared to other systems.[249] Few studies have investigated the emission of N_2O and its potential reduction strategies in FBC. The controlling factors that influence the reduction of N_2O[242, 250] include the operating temperature and pressure, excess combustion air, char, coal type and particle size, additives in coal combustion, reburning, air staging and catalysts. In pressurised FBC, an increase in temperature often decreases N_2O concentrations, while the formation of N_2O is seen to peak at 0.4 MPa. The release of N_2O increases with the increase of excess

combustion air. Reburning (fuel-rich conditions) reverses air staging, causing a reduction in N_2O. Surfaces of catalysts (up to 80 %) and char (up to 20 %) can significantly reduce N_2O, as the higher particle size of coal and more porous char releases less N_2O. [251-260]

2.6.1. Reaction routes leading to N_2O

The release of N_2O is strongly related to the fuel-bound nitrogen (amine or other N-compounds) present in fossil fuels. Nitrogen in biomass mainly exists in the form of amino acid proteins. Fuel-bound nitrogen dissociates into volatile-N and char-N. N_2O arises from the homogeneous and heterogeneous reaction pathways.[47, 261-263] The formation and reduction mechanism of N_2O is portrayed in Figure 2.14.

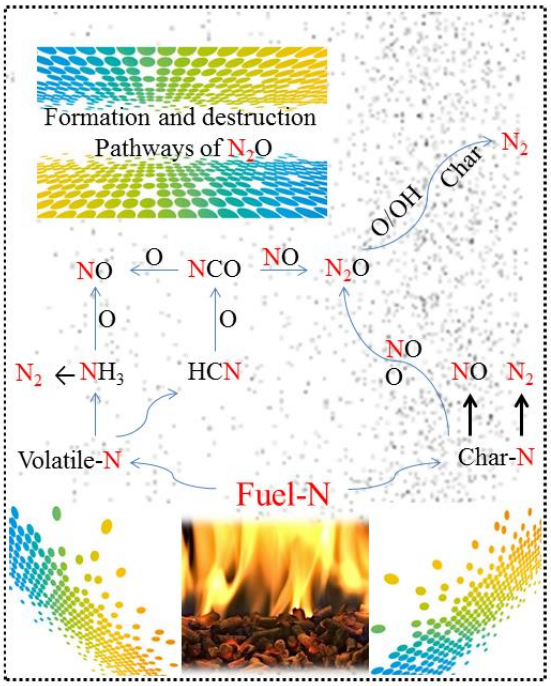

Figure 2.14. N_2O formation and destruction mechanism from fuel-N.[264]

Kramlich et al.[245] confirmed that the precursors of N_2O formation in solid fuels are HCN and NH_3. They noted a substantial rise in N_2O generation when they added NH_3, HCN and acetonitrile (CH_3CN) as a nitrogenous prototype to gas flames in the temperature range 775–1125 °C. Hayhurst and Lawrence[265] also demonstrated how N_2O release ensues via homogenous gas-phase reaction through R2.53 and R2.42 reactions. The homogeneous reaction pathways pertinent to N_2O are essentially R2.52 in real combustion systems and, to a minor level, the reaction R2.53. The mechanism of N_2O formation proceeds through a series of reactions:[71, 266-267]

Homogeneous pathways

$HCN + O \rightarrow NCO + H$ R2.42

$NCO + NO \rightarrow N_2O + CO$ R2.52

$NH + NO \rightarrow N_2O + H$ R2.53

$N_2O + O \rightarrow NO + NO$ R2.54

Heterogeneous pathways

$N(C) + O \rightarrow NCO(C)$ R2.55

$NCO(C) + NO \rightarrow N_2O + CO + C$ R2.56

$N_2O + M \rightarrow N_2 + O_2 + M$ R2.57

2.6.2. Formation of N_2O from thermal DeNO$_x$ and NO$_x$OUT

A pilot-scale, natural gas fired combustor is used to execute the NO$_x$OUT process[168]. Researchers were able to achieve the desired NO reduction performance (50–55 %), but at the same time they observed an increased level of N_2O ($NCO + NO \rightarrow CO + N_2O$). Miller

and Glarborg[268] expounded a comprehensive study focusing on N_2O formation from the thermal DeNO$_x$ process ($NH_2 + NO_2 \rightleftharpoons N_2O + H_2O$ and $NH + NO \rightleftharpoons N_2O + H$).

2.7. Nitrogen conversion in explosives

Ammonium nitrate (AN)-based high density energy materials (HDEM) are frequently used in coal mine blasting. The detonation of AN causes the generation of unwanted post-blast NO_x gases that appear in the form of yellow, orange and purple fumes.[269] Mining companies, explosives manufacturers and monitoring authorities joined hands to develop a safe code of conduct and procedures through management and engineering control measures. Although these strategies have helped in the reduction of NO_x fumes, they didn't account for the elimination of post blast toxic gases made from nitrogen.[270]

The increased number of coal mines and the adverse effects of post-blast toxic fumes on nearby living communities have drawn much concern from regulatory authorities, the media and the public.[271] The National Pollutant Inventory (NPI) measures the emission factors of NO_x (8 kg t^{-1}), CO (34 kg t^{-1}) and SO_2 (1 kg t^{-1})[272]; exposure to these toxic gases can have a range of negative effects on the health and safety of exposed persons and on the surrounding environment, in many cases having a catastrophic impact.

2.7.1. Formation of NO_x

Nitrogen-containing oxidisers used in mining, infrastructure and aviation industries are potent source of NO_x formation and deflagration of NH_4NO_3. Chemical gassing of NH_4NO_3 emulsions and unbalanced stoichiometry blasting contribute towards NO_x formation.[273] Figure 2.15 presents a schematic of NO_x formation in the abovementioned three processes.

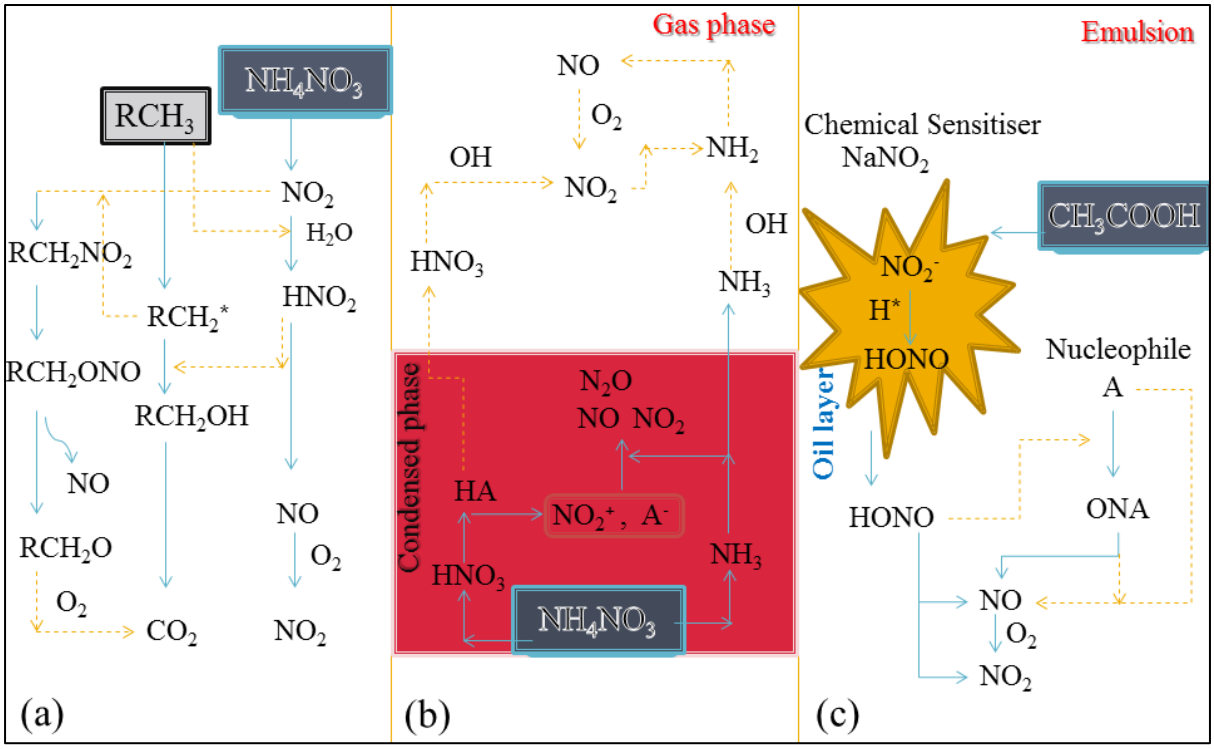

Figure 2.15. NO_x formation during (a) NH_4NO_3 stoichiometrically unbalanced detonation; (b) N transformation in NH_4NO_3 deflagration during blasting of bulk explosive mixtures; and (c) sensitisation of emulsion explosives. (Acquired with author's permission).[273]

On an ideal basis, NH_4NO_3 should follow the explosive reaction shown below, based on stoichiometric conditions:

$$(3x+1)NH_4NO_3 + C_xH(2x+2) \rightarrow (3x+1)\,N_2 + (7x+3)H_2O + xCO_2 \qquad 2.58$$

In the presence of fuel oil and carbon content in emulsions (ANFO), the above generic equation can be written as R2.59 and R2.60, respectively.[7, 274-278]

$3NH_4NO_3 + CH_2 \rightarrow 3N_2 + CO_2 + 7H_2O$ 2.59

$2NH_4NO_3 + C \rightarrow 2N_2 + CO_2 + 4H_2O$ 2.60

Numerous factors can alter the stoichiometry of nitrate blasting agents and, hence, the products formed as a result of blasts or explosions; for example, the extraction of fuel by surrounding rocks, wet conditions in the blast hole, and inorganic compounds present in the bulk matter resulting in toxic carbon monoxide (CO) and NO. ANFO particle size distribution may influence the formation of NO_x. ANFO consisting of fine grains releases more NO_x when compared with the coarse sized ANFO, due to better surface interaction of small sized grains with oxygen which leads to increased NO_x generation.[279] Conversely, many researchers demonstrated the low NO_x level from pulverised ANFO. It has been shown that through effective mixing of nitrate with fuel, a complete detonation reaction can be attained.[10, 280-281] Oxygen balance (OB) defines the reaction stoichiometry of the explosive mixture. The OB value of the contents of the explosive matter represents the amount of oxygen per unit mass of compound. The OB values control the fuel-rich and -poor conditions of bulk explosives. Fuel-lean conditions give positive OB values (R2.61), while fuel excess show negative OB values (R2.62).[282] Consequently, fuel-lean conditions drive more NO_x formation.[10] Later, NO is oxidised to NO_2 and N_2O_4 via the reactions[283-285] R2.63 and R2.64.

Detonation (Fuel excess): $2NH_4NO_3 + CH_2 \rightarrow 2N_2 + CO + 5H_2O$ R2.61

Detonation (Fuel lean): $5NH_4NO_3 + C \rightarrow 4N_2 + CO_2 + 11H_2O + NO$ R2.62

$2NO + O_2 \rightarrow 2NO_2$ R2.63

$2NO_2 \rightarrow N_2O_4$ R2.64

At an OB value of 15, the formation of NO and NO_2 peaks at a value of 9 L at STP/kg and 8 L at STP/kg, respectively. The low level of fuel oil, say 1 %, enhances the release of NO (10 L at STP/kg) and NO_2 (9 L at STP/kg). For a water content of 7 %, the generation of NO_x reaches a maxima (NO, 8 L at STP/kg and NO_2, 5 L at STP/kg) and minima (NO, 2 L at STP/kg and NO_2, 1.5 L at STP/kg) in the absence of moisture.[286]

Furthermore, the behaviour of nitrate ions plays a key role in the formation of NO_x under a limited fuel supply in ANFO. Under the condition of insufficient fuel, the deflagration reaction channels progress through R2.65-R2.67 when ammonium nitrate acts as the fuel as well as oxidiser. The two different valence states of nitrogen in ammonium nitrate allow one species to reduce and the other to oxidise. Thermodynamically, the deflagration and detonation reaction pathways acquired substantially negative free energy (-1,340 kJ/kg – -1,736 kJ/kg).[287]

Deflagration: $2NH_4NO_3 \rightarrow N_2 + 4H_2O + 2NO$ R2.65

Deflagration: $2NH_4NO_3 \rightarrow N_2O + 2H_2O$ R2.66

Deflagration: $4NH_4NO_3 \rightarrow 3N_2 + 8H_2O + 2NO_2$ R2.67

The literature proffered inclusive and varied analysis of the decomposition/cracking of NH_4NO_3 in condensed and gas-phase systems.[288-293] Most researchers agreed on the thermal decomposition of solid NH_4NO_3 from two pathways in the condensed phase: 1) ionic and 2) radical channels. In the course of the heating stage, NH_4NO_3 remains stable up to ~ 165 °C,

after which it starts decomposing through an ionic mechanism. In the condensed phase, the initial step towards NH_4NO_3 decomposition is the formation of H^+ along with NH_3 and nitric acid (HNO_3). The presence of ammonium ions (NH_4^+) proportionally speed up the decomposition of HNO_3.[291-292, 294-297]

$2NH_4NO_3 \rightarrow NH_3 + HNO_3$ R2.68

$HNO_3 + HA \rightarrow NO_2^+ + H_2O + A^-$ R2.69

where, HA = NH_4^+, HNO_3, H_3O^+

$NH_3 + NO_2^+ \rightarrow$ products (N_2O, H_2O) R2.70

$NH_3 + X^- \rightarrow$ products (NO, NO_2, H_2O) R2.71

The NH_4NO_3 ionic mechanism switches to radical gas phase reaction pathways as the temperature is increased and the species depart the condensed phase. Under fast heating and by utilising an instant probe (using rapid scan Fourier transform infrared (FTIR) spectroscopy), thermal products from decomposition of NH_4NO_3 includes HNO_3 (intermediate reaction product), N_2O, NO_2 and H_2O.[298-299]

At high temperatures and under radical pathways, the decomposition of HNO_3 proceeds as follows:

$2HNO_3 = NO_2 + H_2O + 1/2O_2$ R2.72

At a temperature interval of 342–387 °C, NO_2 oxidises NH_3 and further reactions proceed as follow:[299]

$NH_3 + NO_2^+ \rightarrow NH_2 + HNO_2$ 2.73

$NH_2 + NO_2 \rightarrow NH + HNO_2$ 2.74

$NH + NO_2 \rightarrow HNO + NO$ 2.75

$2HNO \rightarrow NO_2 + H_2O$ 2.76

$2HNO_2 \rightarrow NO_2 + NO + H_2O$ 2.77

The above reaction may proceed through the following elementary reaction scheme. Oxygen from reaction R2.72 (decomposition of HNO_3) reacts with NO and forms NO_2, which initiates chain reactions into nitrogen:[288, 299]

$3NO + 3/2O_2 \rightarrow NO_2$ R2.78

$2NO_2 + H_2O \rightarrow HNO_2 + HNO_3$ R2.79

$NH_3 + HNO_3 \rightarrow NH_4NO_3$ R2.80

$NH_3 + HNO_2 \rightarrow NH_4NO_2$ R2.81

$NH_4NO_2 \rightarrow N_2 + H_2O$ R2.82

Davies and Abraham[300] proposed the formation of a nitramide intermediate that decomposes into N_2O and H_2O. Brower et al.[289] suggested homolytic breaking of N–O bonds in HNO_3 at low temperatures, at which point H_2O and NH_3 inhibit the ionic reactions, while both species exhibit no influence at high temperatures. Anderson et al.[301] illustrate that surface decomposition (an endothermic reaction) is dominant at a high heating rate and produces NH_3 and HNO_3, while N_2O and H_2O are produced through bulk decomposition (exothermic reaction). In general, the rates of ionic and radical pathways depend on the operating temperature, heating rates, and pressure. Confinement plays a detrimental role in NO_x formation in the deflagration of AN.

2.7.2. Thermal decomposition of ammonium nitrate in the gas phase.

The initial step towards the decomposition of ammonium nitrate requires energy in a process that consumes NH_4NO_3 into NH_3 and HNO_3.[302] The subsequent reaction mechanisms are still unclear and are open to various speculations.[289] Moreover, the available modelled reaction scheme is limited to intermolecular H^+ transfer and hydrogen-bonded acid base adducts in NH_4NO_3.[303-304] Cagnina et al.[305] reported complex reaction mechanisms for the gas phase decomposition of NH_4NO_3 (Figure 2.16). They mapped out competing potential energy surfers for the homogenous fragmentation of NH_4NO_3, representing the major species reported in experimental studies.

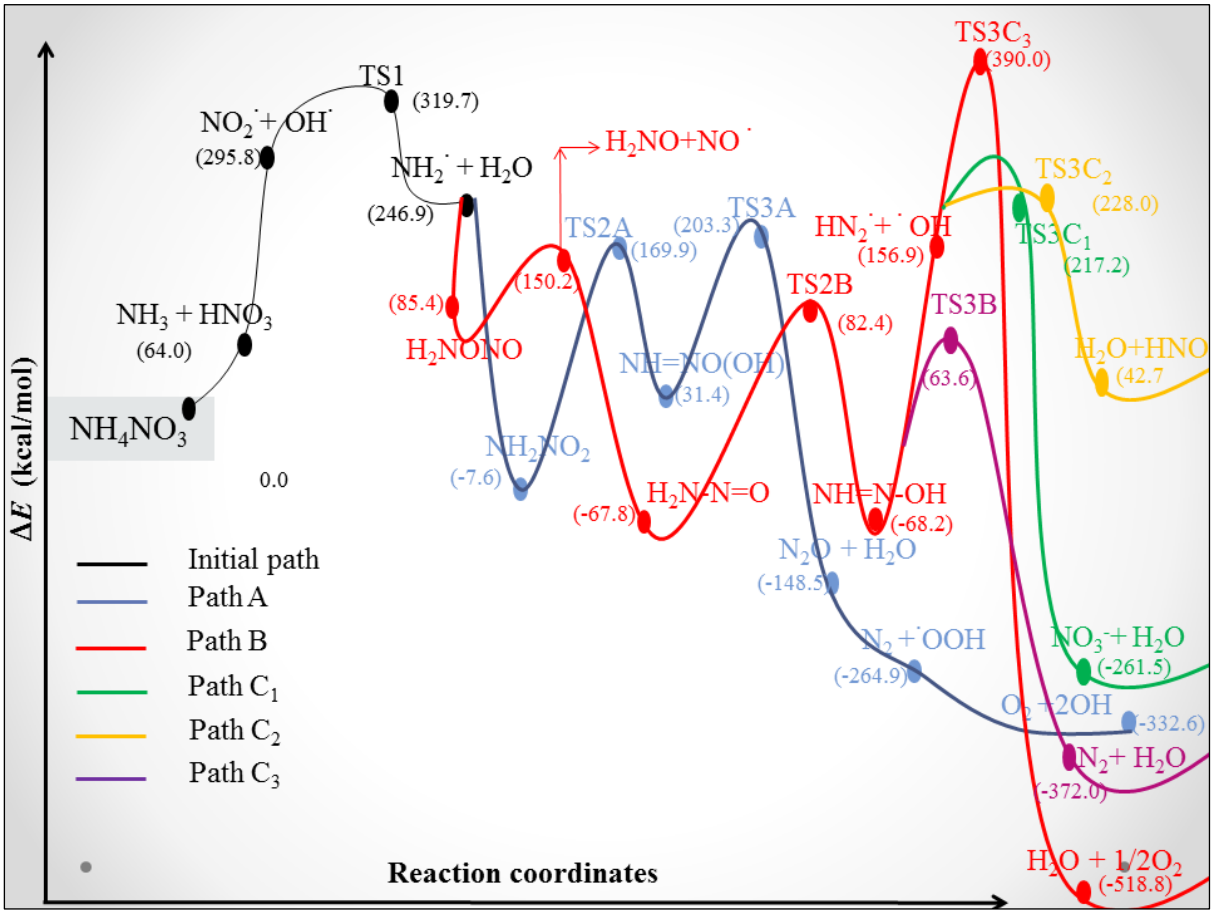

Figure 2.16. Potential energy surface for the decomposition of NH_4NO_3 in the gas phase.[305] All values are in kJ mol^{-1}.

2.7.3. High internal phase emulsion explosives

Emulsion explosives are high internal-phase water-in-oil emulsions that consist of a discontinuous phase of inorganic oxidiser salt mixture (mainly aqueous ammonium nitrate droplets), which is dispersed in a continuous organic fuel (diesel or other hydrocarbon) phase. Polyisobutylene succinic anhydride (PIBSA)-based emulsifier and the mixture of fuel oil makes the continuous phase of emulsion explosives. The emulsifier is added to the emulsions to increase the strength of the discontinuous phase and make it stable. Emulsion explosives are water resistant, cost effective, inherently safer and virtuous explosive properties.[290, 306-307]

The sensitisation of ammonium nitrate emulsion explosives through chemical gassing (addition of concentrated sodium nitrite with acetic acid) ends with nitrogen as the main gaseous product; however, in certain settings, a substantial amount of nitrogen oxide may form. The desired size of the bubbles and matrix density allow the introduction of a booster to generate a shock wave that initiates the explosion. Chemical gassing of the emulsion explosives occurs through a well-known nitrosation reaction. The initial step is the protonation of nitrite ions to produce nitrous acid (HNO_2).[308] Subsequently, HNO_2 reacts with the available nucleophilic species (A^-) to from nitrosating species.[309] In a mild acidic environment (pH 4–6), dinitrogen trioxide (N_2O_3) acts as an nitrosating species via R2.84 (low acidic media), while the nitrosyl ion (ON^+) forms in high acidic media via R2.85.[76, 308, 310]

$NO_2^- + H^+ \rightleftharpoons HNO_2$ R2.83

$HONO + NO_2^- + H^+ \rightleftharpoons N_2O_3 + H_2O$ R2.84

$HONO + H^+ \rightleftharpoons ON^+ + H_2O$ R2.85

Nitrosation of NH_3 is represented by reactions R2.86 and R2.87, and results in the formation of N_2 which induces the sensitisation in bulk emulsion explosives.

$N_2O_3 + NH_3 \rightarrow N_2 + NO_2^- + H^+ + H_2O$ R2.86

$ON+ + NH_3 \rightarrow N_2 + H^+ + H_2O$ R2.87

Also, under strong acidic media (pH < 2), HNO_2 decomposes as follows, producing NO and NO_2.

$2HNO_2 \rightleftharpoons NO + NO_2 + H_2O$ R2.77

In the presence of nucleophilic species A^- (Cl^-, Br^-, SCN^-, I^-, $SC(NH_2)_2$ and $(S_2O_2)^{-3}$, HNO_2 reacts through the following reactions[308, 311-312]

$HONO + A^- + H^+ \rightleftharpoons ONA+ H_2O$ R2.89

$ONA + NH_3 \rightarrow N_2 + A^-+ H^+ + H_2O$ R2.90

In the presence of added nucleophiles, the nitrosation pathway operates at increased reaction rates due to increases in nitrosating species concentrations within the system.[313]

Rayson et al.[314] demonstrated a nitrosyl thiocyanate (ONSCN) decomposition mechanism leading to the formation of NO_x during explosive sensitisation. The reaction of thiocyanate ion (SCN^-), as with HNO_2, produces ONSCN, which acts as a nitrosating species. At temperatures as low as 60 °C, ONSCN decomposes quickly to NO and SCN_2 via R2.92:

$$HONO + SCN^- + H+ \rightleftharpoons ONSCN + H_2O \quad \text{R2.91}$$

$$2ONSCN \rightarrow 2NO + (SCN)_2 \quad \text{R2.92}$$

Additionally, Rayson et al.[314] explored three reaction pathways for the decomposition of ONSCN, in particular during emulsion explosions. Two reaction pathways at high SCN^- concentrations are depicted in Figure 2.17.

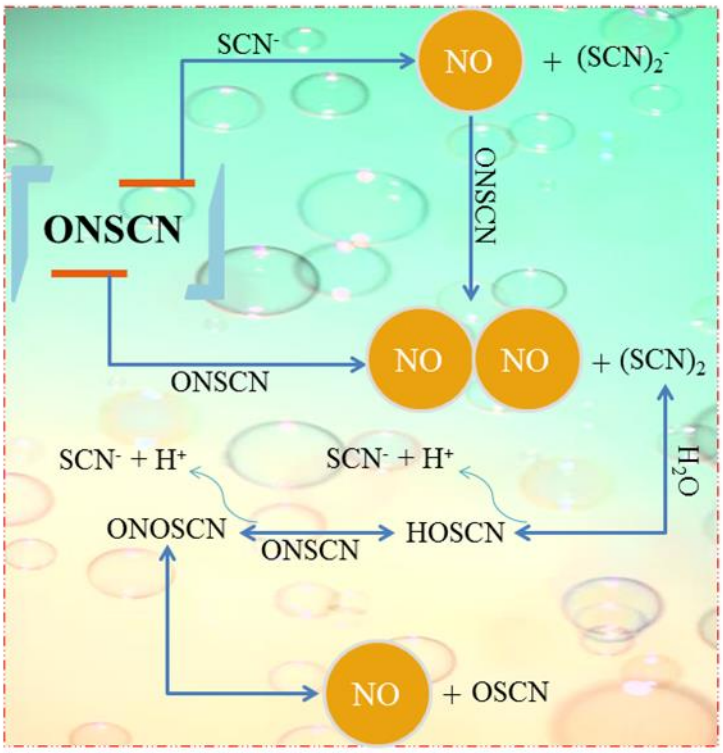

Figure 2.17. NO formation from decomposition of ONSCN during NH_4NO_3 emulsion explosions.

At low SCN^- concentrations, ONOSCN (formed from the reaction of ONSCN with HOSCN) released NO through the O–NO bond dissociation. At the end, OSCN dimerises and hydrolyses via reaction R2.96. N_2O can also be formed from the decomposition of ONH (product of ONSC hydrolysis).[314] The presence of HOSCN is confirmed in later studies.[209, 315]

$(SCN)_2 + H_2O \rightleftharpoons HOSCN + SCN^- + H^+$ R2.93

$ONSCN + HOSCN \rightleftharpoons ONOSCN + SCN^- + H^+$ R2.94

$ONOSCN \rightleftharpoons NO + OSCN$ R2.95

$2OSCN + H_2O \rightarrow HOSCN + HO_2SCN$ R2.96

2.7.4. NO_x mitigation in ammonium nitrate emulsions

The formation of NH_3 and NO_x often prevails during the early stages of decomposition of NH_4NO_3 blasting material.[316] Figure 2.18 demonstrates the path of NO_x reduction from NH_4NO_3 blasting. Ammonium nitrate based emulsion materials used for blasting on mine sites. These sites have reactive ground sulphide containing rocks (especially in Australia). Drilling of the blast hole produces pyrite powder which piles up at the bottom of the hole facilitating its reaction with energetic emulsions, resulting in a premature detonation.[317-318] Moreover, reactive ground pore water also contains solubilised iron (II) and (III) ions and sulphuric acid.[319-321] Through a series of reaction pathways, pyrite, iron ions and sulphuric acid react with NH_4NO_3 forming NO, NO_2, HNO_2 pollutants and Fe (III) ions.[320, 322-324] Ammonium nitrate reacts with sulphide through an autocatalysis reaction mechanism. The in situ undesired formation of Fe (III) ions and nitroso-species act as a catalyst to generate more pyrite and Fe (II) ions. At a certain level, when the formed in situ species concentration is high enough to produce a high level of NO_x and heat, this ultimately leads to thermal cracking of NH_4NO_3.[320]

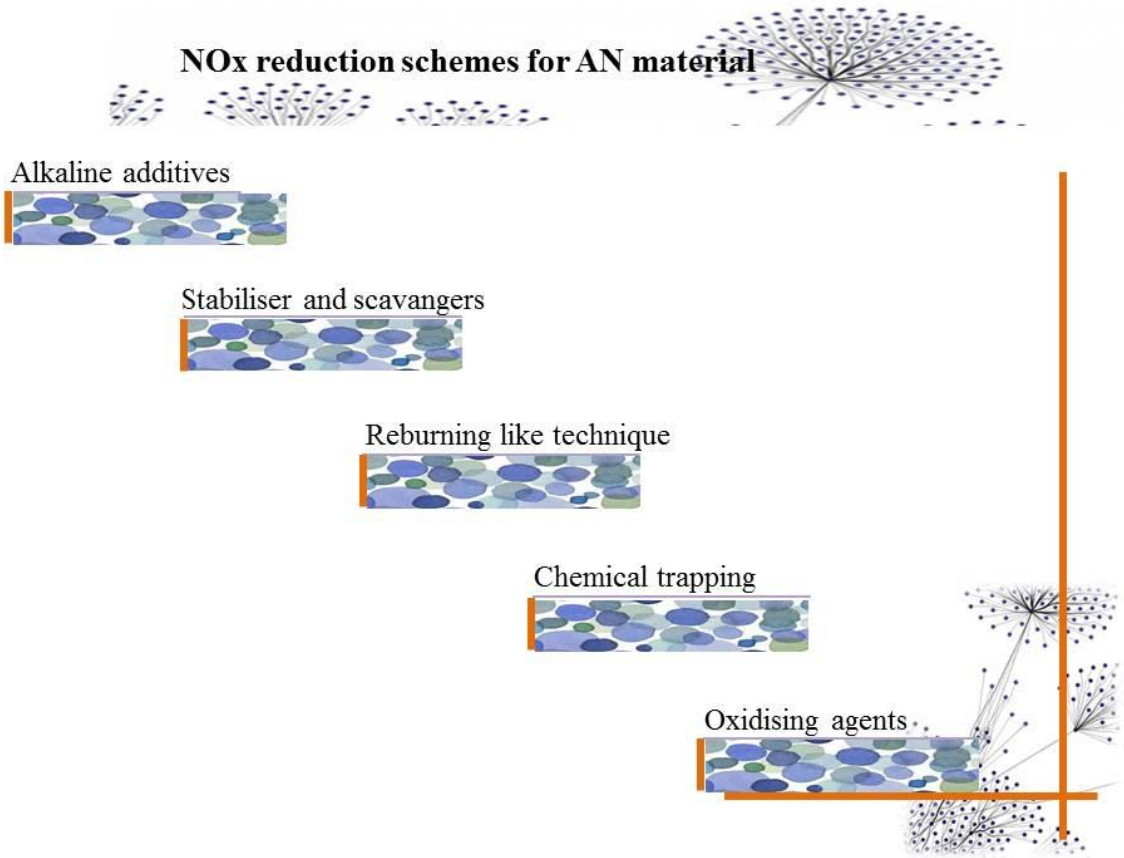

Figure 2.18. Possible NO_x mitigation strategies for AN blasting operations.

Azarkovich et al.[325] presented a pioneering study on the abatement of NO_x during blasting activities. They proposed alkaline neutralisation additives which exhibit a profound capacity to limit the NO_x generated from NH_4NO_3 materials. It is clear that additives like Na_2CO_3, $Ca(OH)_2$ and $CaCO_3$ capture NO_2 through reactions R2.97-R2.99 and 0.1–0.2 mass % of additives displayed an NO_2 reduction efficiency of 40–80 %.

$$Ca(OH)_2 + 2NO_2 + 1/2O_2 \rightleftharpoons Ca(NO_3)_2 + H_2O \quad \text{R2.97}$$

$$CaCO_3 + 2NO_2 + 1/2O_2 \rightleftharpoons Ca(NO_3)_2 + CO_2 \quad \text{R2.98}$$

$$Na_2CO_3 + 2NO_2 + 1/2O_2 \rightleftharpoons NaNO_3 + CO_2 \quad \text{R2.99}$$

Sapko et al.[281] suggested an amendment to the NH_4NO_3 configuration mitigating plausible NO_x formation in the reaction region that results from the detonation. They performed a real-time detonation in a mine chamber, enclosed by a sphere (3.7 m of diameter), and detonated the blasting material inside a galvanised steel pipe (10 cm). Through the stemming method, 48 % of the NO_2 reaction was achieved through mixing of acidic gases in Na_2CO_3. In addition to the stemming method, they estimated the performance of the selected additives (blended with NH_4NO_3 emulsion) such a urea, excess diesel fuel, aluminium and coal dust. For the excess diesel fuel (8 %) additive, the production of NO_2 was three times less than without the additive, but had no significant reduction for NO. Among urea, coal dust and aluminium additives, aluminium was the most effective at reducing NO_2 by a factor of 2.5. Oxley et al.[291] tested a wide array of NH_4NO_3 blends encompassing additives of pulverised potassium, calcium, sodium, ammonium, and several organic agents (formate, oxalate, urea) and guanidium salts.

Opoku et al.[326] prepared the mixed NH_4NO_3 salts to monitor the emission of NO_x from detonations pertinent to NH_4NO_3 blasting agents. They observed lower NO emission levels from thermal decomposition of NH_4NO_3 doped with the potassium additive. They reported 40 % reduction efficiency when using 5 mol % potassium co-recrystallised NH_4NO_3 salt.

For chemical gassing of emulsion blasting material, spin traps were tested as prominent NO diminution agents via the formation of stable NO-complexes. Venpin et al.[327] examined the effect of various molecular spin traps encompassing aromatic *ortho* substituted nitroso compounds, such as nitrosobenzene sulfonate, 3,5-dibromo-4-nitrosobenzene sulfonate, 3,5-dimethyl-4-nitrosobenzene sulfonate and 3,5- dichloro-4-nitrosobenzene sulfonate to capture NO during sensitisation (chemical gassing) of the NH_4NO_3 emulsion. The NO_x reduction efficiency measured reached 70 %.

2.8. Reactions of NH_2 radicals and hydrocarbons

The amidogen radical is an important intermediate species in most chemical transformations of ammonia and related compounds in the gas phase. It is generally produced by the hydrogen abstraction from ammonia, its thermal decomposition, photolysis or radiolysis. In this section, we report mechanistic and kinetic parameters dictating the reaction of NH_2 with hydrocarbons.

2.8.1. Experimental studies

Amidogen radicals (NH_2) react with alkane via hydrogen abstraction pathways according to a general reactions scheme of R-H + NH_2 → $R^{\cdot}$ + NH_3. Demissy and Lesclaux[328] investigated hydrogen abstraction reactions of NH_2 with a series of alkanes, namely methane, ethane, propane and butanes, as well as molecular hydrogen. Absolute rate constants for the abovementioned species were determined for the temperature window of 27–227 °C. The flash photolysis setup equipped with laser-based resonance absorption facilitated the recording of species time-histories. This highly sensitive method allows the estimation of very low reaction rates. The source of NH_2 radicals was photolysis of NH_3. They found a sluggish H abstraction reaction at low temperatures. Abstraction of H was more feasible from the thermodynamically weakest C-H site among these hydrocarbons; for example, abstraction of the tertiary C-H site in *iso*-butane (with bond dissociation energy, BDE of 381.0 kJ mol^{-1}) requires an activation energy (E_a) of 20.5 kJ mol^{-1}. Likewise, the removal of H from the secondary site of propane and *n*-butane (both with a BDE value of 395.5 kJ mol^{-1}) proceeds with 25.7 kJ mol^{-1} and 25.5 kJ mol^{-1} of E_a. The abstraction of primary H from methane (BDH, bond dissociation enthalpy = 438.5 kJ mol^{-1}) and propane (BDH = 418 kJ

mol^{-1}) demands higher activation energies of ~41.8 kJ mol^{-1} and 29.9 kJ mol^{-1}, respectively. Clearly, activation barriers show a linear relationship with BDE of the respective C–H sites in alkanes. The pre-exponential factors fitted between 27–227 °C based on two H abstractions of primary C–H in ethane is 6.14×10^{-13} cm^3 s^{-1} $molecule^{-1}$. Secondary C-H in propane incurs a value of 7.47×10^{-13} cm^3 s^{-1} $molecule^{-1}$. Tertiary C–H in *iso*-butane attains a value of 3.82×10^{-13} cm^3 s^{-1} $molecule^{-1}$. They performed a comparison of active radicals (OH and CH_3) in addition to NH_2 reactions with ethane, propane and *iso*-butane. They observed the reactivity of NH_2 in between these radicals. Due to the very slow rate of methane interaction with NH_2, Arrhenius parameters could not be determined accurately and only E_a was evaluated.

Earlier measurements of the H abstraction reaction of NH_2 from saturated hydrocarbons were recorded indirectly.[329-331,328] Hack et al.[332] performed the first direct measurement of the reaction $CH_4 + NH_2 \rightarrow CH_3 + NH_3$. The experiments were conducted in an isothermal discharge flow reactor linked directly to a laser-induced fluorescence cell at a temperature and pressure of 47–750 °C and 4.0 mbar. They reported a pre-exponential value of 9.61×10^{-12} cm^3 s^{-1} $molecule^{-1}$ and E_a value of 55.1 kJ mol^{-1}.

Henning and Wagner[333] studied the high temperature (1227–1827 °C) kinetics of NH_2 radicals with methane, ethane and propane in an aluminium shock tube. Highly sensitive measurements of NH_2 radicals using the laser (narrow line width) absorption method was reported. The kinetic rate constants for primary H removal in methane and ethane were reported as $k(T) = 1.99\times10^{-11}\exp(-63.6/(RT))$ cm^3 s^{-1} $molecule^{-1}$, $k(T) = 1.61\times10^{-11}\exp(-47.9/(RT))$ cm^3 s^{-1} $molecule^{-1}$, respectively, while rate expression for propane (combined primary and secondary H removal) was $k(T) = 2.82\times10^{-11}\exp(-44.6/(RT))$ cm^3 s^{-1} $molecule^{-1}$. Song et al.[334] investigated the removal of hydrogen from methane using a shock tube facility

over a temperature interval of 1318–1811 °C and 1.14 bar pressure, with NH_2 concentration measured using the frequency modulation absorption technique to report a reaction rate expression of $k(T) = 1.17\times10^{-10} \exp(-71.3/(RT))$ cm^3 s^{-1} $molecule^{-1}$

Ehbrecht et al.[335] explored the kinetics of H abstraction reactions from hydrocarbons (ethane, propane and cylcohexane) with NH_2 radicals in an isothermal flow reactor. Reaction rates were obtained in a temperature window of 325–700 °C and an applied pressure of 4.0 mbar. Time-dependent NH_2 profiles were monitored at *pseudo*-first-order conditions using the laser-induced fluorescence technique. For the removal of primary H from ethane, the calculated rate constant appeared as $k(T) = 1.61\times10^{-11} \exp(47.9/(RT))$ cm^3 s^{-1} $molecule^{-1}$. The combined rate of expression (primary and secondary H removal) from propane was fitted to $k(T) = 1.61\times10^{-11} \exp(-39.3/(RT))$ cm^3 s^{-1} $molecule^{-1}$. Finally, removal of H from cyclohexane showed a similar E_a (37.3 kJ mol^{-1}) and three times higher pre-exponential factor (4.48×10^{-11} cm^3 s^{-1} $molecule^{-1}$) compared to propane.

Hack et al.[336] investigated the NH_2 radical reaction with 1,3-butadiene in an isothermal discharge flow process at a temperature and pressure range of -43–87 °C and 2.0×10^{-3} – 1.0×10^{2} bar, respectively. The source of NH_2 radicals was NH_3, produced through the reaction of fluorine atoms with NH_3. Laser-induced fluorescence was employed to record the concentration of NH_2 radicals with a sensitivity of $\leq 2\times10^{-16}$ mol cm^{-3}. Kinetic rate parameters were determined at a *pseudo*-first-order decay of NH_2. The reaction showed dependency on temperature and an initial concentration of 1, 3-butadiene, but remained independent of pressure. They reported a pre-exponential factor of 6.31×10^{-13} cm^3 s^{-1} $molecule^{-1}$ and E_a value of 9.50 kJ mol^{-1}; however, it remains unclear if the reactions proceed via H abstraction or addition channels. There are two possible sites for the addition reaction

due to the presence of two π-bonds viable for attachment by NH_2 radicals. Owing to the relatively weak C–H bonds (366.2 kJ mol^{-1})[337], the H abstraction channel assumes more importance in reference to the addition channel.

Khe and Lesclaux[338] used the flash photolysis-laser resonance absorption technique and determined the absolute rate constants for the reaction system of olefins and NH_2 radicals. The NH_2 radicals were produced from photolysis of NH_3 in a quartz tube. The olefins studied were ethylene, propylene, *iso*-butene, 1-butene, *trans*-2-butene, *cis*-2-butene with temperature and pressure ranges of 27–227 °C and 1.33×10^{-2}–1.33×10^{-1} bar. The reactivity of NH_2 radicals with all the olefins was found to be very similar, with a pre-exponential value of $1.99–7.64\times10^{-2}$ and E_a values remaining within 16.5–20.3 kJ mol^{-1}. Due to the very strong C–H bonds (465.3–464.8 kJ mol^{-1}), the authors anticipated that an additional pathway is the main channel for ethylene and propylene. For all butenes, the reported results do not rule out the possibility of an H abstraction reaction based on similar Arrhenius parameters for both H addition and H abstraction reactions. Table 2.18 shows the work done for the reactions of hydrocarbons with NH_2.

Table 2.18. A summary of experimental studies that report activation energies (kJ mol^{-1}) and pre-exponential *A* factor (cm^3 s^{-1} $molecule^{-1}$) for the reactions of RH with NH_2.

Reaction Products	**Pressure kPa**	**Temperature °C**	***A***	E_a	**Excitation technique**	**Measured technique**
Methane + NH_2						
$CH_3^{\cdot}$ + NH_3[328]	66.7 kPa	27–247	8.3×10^{-13}	43.9	FP	Vis-UV absorption
$CH_3^{\cdot}$ + NH_3[332]	0.4 kPa	470–747	9.61×10^{-12}	55.1	ELB	Laser induced fluorescence
$CH_3^{\cdot}$ + NH_3[333]	7.4 kPa	1227–1827	1.99×10^{-11}	63.4	TH	Vis-UV absorption
$CH_3^{\cdot}$ + NH_3[334]	110-131 kPa	1381–1811	1.17×10^{-10}	71.3	TH	Frequency modulation absorption technique
Ethane + NH_2						
$C_2H_5^{\cdot}$ + NH_3[328]	66.7	27–247	6.14×10^{-13}	29.9	FP	Vis-UV absorption
$C_2H_5^{\cdot}$ + NH_3[339]	0.26–93.3	22–227	6.14×10^{-13}	29.9	FP	Vis-UV absorption
$C_2H_5^{\cdot}$ + NH_3[333]	7.4	1227–1827	1.61×10^{-11}	47.9	TH	Vis-UV absorption
$C_2H_5^{\cdot}$ + NH_3[335]	0.4	325–700	$1.61\text{x}10^{-11}$	44.4	ELB	Laser induced fluorescence

Propane + NH_2						
Product + NH_3[333]	7.4	1227–1827	2.82×10^{-11}	44.6	TH	Vis-UV absorption
Product + NH_3[335]	0.4	325–700	1.41×10^{-11}	39.3	ELB	Laser induced fluorescence
Product + NH_3[328]	0.05–60.0	27–227	7.47×10^{-13}	25.8	FP	Vis-UV absorption
***iso*-butane + NH_2**						
Product [340]	0.26–0.53	22–270	3.16×10^{-13}	19.8	ELB	Laser magnetic resonance
Product [328]	0.05–40.0	27–247	3.82×10^{-13}	20.5	FP	Vis-UV absorption
Product [339]	0.27–93.0	22–227	3.82×10^{-13}	20.5	FP	Vis-UV absorption
Product [338]	1.33–13.0	27–227	3.99×10^{-13}	21.0	FP	Vis-UV absorption
***n*-butane + NH_2**						
Product + NH_3[339]	0.27–93.3	22–227	1.16×10^{-12}	25.5	FP	Vis-UV absorption
Product + NH_3[328]	0.05–53.3		1.16×10^{-12}	25.5	FP	Vis-UV absorption
ethylene + NH_2						
Product [338]	1.33–13.3	27–227	1.99×10^{-13}	16.6	FP	Vis-UV

						absorption
Product [341]	0.13	22–232	2.16×10^{-15}	NA	ELB	Laser induced fluorescence
Product [342]	0.67–13.3	-23–192	3.42×10^{-14}	11.0	FP	Laser induced fluorescence
Product [333]	ambient	1367 – 1667	8.80×10^{-12}	42.9	TH	Vis-UV absorption
propylene + NH_2						
Product [343]	1.33–93.3	27–227	4.82×10^{-13}	18.0	FP	Vis-UV absorption
Product [341]	0.13	25	9.96×10^{-16}	NA	ELB	Laser induced fluorescence
Product [338]	1.33–13.3	27–227	4.65×10^{-13}	18.0	FP	Vis-UV absorption
Product [333]	ambient	1237–1507	1.25×10^{-11}	39.7	TH	Vis-UV absorption
***iso*-butene + NH_2**						
Product [338]	1.33–13.3	27–227	7.64×10^{-13}	18.8	FP	Vis-UV absorption
1-butene + NH_2						
Product [338]	1.33–13.3	27–227	4.65×10^{-13}	17.1	FP	Vis-UV absorption
***cis*-2-butene + NH_2**						

Product [338]	1.33–13.3	27–227	5.81×10^{-13}	17.8	FP	Vis-UV absorption
***trans*-2-butene + NH_2**						
Product [338]	1.33–13.3	27–227	5.48×10^{-13}	18.0	FP	Vis-UV absorption
Cyclohexane + NH_2						
$C_6H_{11}^{\cdot}$ + NH_3 [335]	0.4	325–700	$4.48\text{x}10^{-11}$	37.3	ELB	Laser induced fluorescence

Flash Photolysis = FP

Electron Beam = ELB

Thermal = TH

2.8.2. Theoretical studies

On the theoretical modelling side, a large number of studies have addressed abstraction reactions from hydrocarbons by NH_2. Leroy et al.[344] used the ab initio UHF/6-31G level to investigate H abstraction reactions of methane and NH_2 and computed energies with those obtained at the CI (Configuration Interactions) level. Transition state theory, with the inclusion of Eckart's tunnelling correction, determined the rate constants expressed as $k(T) = 3.8\times10^{-12}\exp(-59.8/(RT))$ cm^3 s^{-1} $molecule^{-1}$. Yu et al.[345] determined the abstraction kinetics of methane and NH_2 at UQCISD(T)/6-311 + G(2df, 2p)// UQCISD/6-311G level for the temperature interval of 27–1827 °C. The forward rate constant expression $k(T) = 1.8\times10^{-11}\exp(-70.0/(RT))$ cm^3 s^{-1} $molecule^{-1}$ was calculated based on the canonical variational transition state theory with small-curvature tunnelling correction. Mebel and Lin[346] executed

Gaussian-2 method (G2) computations to report rate constants for series alkanes with NH_2 radicals. The reaction rate expression for methane is $k(T) = 2.7\times10^{-11} \exp(-55.7/(RT))$ cm^3 s^{-1} $molecule^{-1}$; ethane : $k(T) = 1.54\times10^{-11} \exp(-40.8/(RT))$ cm^3 s^{-1} $molecule^{-1}$; primary H removal in propane: $k(T) = 1.72\times10^{-11} \exp(-43.9/(RT))$ cm^3 s^{-1} $molecule^{-1}$; secondary H removal in propane: $k(T) = 1.10\times10^{-11} \exp(-34.9/(RT))$ cm^3 s^{-1} $molecule^{-1}$; and, lastly, the rate expressions for primary and tertiary H abstraction from *iso*-butane are $k(T) = 1.07\times10^{-11} \exp(-45.8/(RT))$ cm^3 s^{-1} $molecule^{-1}$ and $k(T) = 1.11\times10^{-11} \exp(-31.8/(RT))$ cm^3 s^{-1} $molecule^{-1}$, respectively, at a temperature range of 27–1827 ^oC. At low temperatures, the computed rate constants – based on Wigner's tunnelling correction – underestimate experimental values, while a good agreement was attained when Eckart's tunnelling correction was applied. Mebel and Lin[346] computed that E_a values overestimate the shock tube experimental measurements for the temperature range 227–1827 °C. Clearly, future work is needed to reconcile this noticeable disagreement.

Song et al.[334] employed the KMLYP hybrid density functional method with the 6-311G(d,p) basis set to study H abstraction from methane with NH_2 over a temperature range of 27–1827 °C. The reported rate expression is $k(T) = 1.81\times10^{-11} \exp(-57.0/(RT))$ cm^3 s^{-1} $molecule^{-1}$ based on canonical transition state theory with WKB tunnelling's correction.

Valadbeigi and Farrokhpour[347] studied the reaction dynamics and kinetics of atmospheric reactions of NH_2 with C_1–C_3 alkanes. The reaction mechanism suggested the formation of amines, followed by hydrogen abstraction by H radicals from the produced amines at B3LYP and MP2 levels of theory, using 6–311++G(3df,3pd) and 6–311++G(d,p) basis sets, respectively.

Batiha et al.[348] conducted theoretical work on the reaction of benzene with NH_2 radicals using the hybrid meta-DFT functional of BB1 K. By comparing the addition and the abstraction pathways, they concluded that the rate constant (k = 6.47×10^{-11} exp(-68.8/(RT)) cm^3 s^{-1} $molecule^{-1}$) for the abstraction channel is faster than the addition channel ($k(T)$ = 4.71×10^{-13} exp(-64.5/(RT)) cm^3 s^{-1} $molecule^{-1}$) by about two orders of magnitude at all temperatures. Table 2.19 shows the theoretical work done for the reactions of hydrocarbons with NH_2.

Table 2.19. A summary of theoretical studies that reports activation energies (kJ mol^{-1}) and pre-exponential A factor (cm^3 s^{-1} $molecule^{-1}$) for the reactions of RH with NH_2.

Reaction Products	Temperature °C	A	E_a	Measured technique
$CH_3^{\cdot}$ + NH_3[344]	417–437	3.8×10^{-12}	59.78	UHF/6-31G level and CI/6-31G
$CH_3^{\cdot}$ + NH_3[345]	27–1827	1.78×10^{-11}	68.97	UQCISDT/6-311qG2df, 2p//UQCISD/6-311G
$CH_3^{\cdot}$ + NH_3[346]	27–1727	2.7×10^{-11}	55.7	G2
$CH_3^{\cdot}$ + NH_3[334]	27–1827	1.81×10^{-11}	57.0	KMLYP//6-311G(d,p)
$C_2H_5^{\cdot}$ + NH_3[346]	27–1727	1.54×10^{-11}	40.8	G2
p-$C_2H_5^{\cdot}$ + NH_3[346]	27–1727	1.72×10^{-11}	43.9	G2
s-$C_2H_5^{*}$ + NH_3[346]	27–1727	1.10×10^{-11}	34.9	G2
p-$C_4H_9^{\cdot *}$ + NH_3[346]	27–1727	1.07×10^{-11}	45.8	G2

t-$C_4H_9^{\cdot}$ + NH_3[346]	27–1727	1.11×10^{-11}	31.8	G2
$C_6H_5^{\cdot}$ + NH_3[348]	27–1727	6.47×10^{-11}	68.8	BB1 K

[*] *iso*-butane

There is a scarcity of accurate reaction kinetics of hydrogen abstraction from alkenes and alkynes; and to a lesser extent from alkanes. Likewise, the current literature does not report any experimental or theoretical kinetics values for the reaction of NH_2 with aromatic compounds, even for the simplest aromatic compounds (except benzene), either theoretically or experimentally. The discrepancies in literature and paucity of reaction kinetics drives our motivation in this thesis to report accurate kinetics parameters for H abstraction reactions of aliphatic hydrocarbons (alkanes, alkenes and alkynes) and alkylbenzenes (toluene, ethylbenzene and propylbenzene) by NH_2 radicals.

2.9. Reaction kinetics of NO_2 radicals and hydrocarbons

The NO_2 radicals owe high stability and the anticipated rate constants for the H abstraction generally assume low if compared with analogous values of NH_2. The hydrogen abstraction reaction of hydrocarbons by NO_2 radicals depends primarily on the isomeric form of the resultant HNO_2.

R–H + NO_2 → $R^{\cdot}$ + *trans*-HONO

R–H + NO_2 → $R^{\cdot}$ + *cis*-HONO

R–H + NO_2 → $R^{\cdot}$ + *iso*-HNO_2

Slack and Grillo[349] performed shock tube experiments for methane and NO_2 over temperatures and pressures of 1027–1627 °C and 200–400 kPa, respectively. Their reported rate constant assumed an expression of $k(T) = 1.16\times10^{-12}\exp(-126.0/(RT))$ cm^3 s^{-1} $molecule^{-1}$). In another study (P = 183–365 kPa and T = 1037–1790 °C), Slack[350] noted the rate constant of $k(T) = 1.99\times10^{-12}\exp(-126.0/(RT))$ cm^3 s^{-1} $molecule^{-1}$). Yamaguchi et al.[351] employed ab-initio calculations to study reactions between methane and NO_2, reporting a rate constant expression of $k(T) = 5.40\times10^{-20}\exp(-157.3/(RT))$ cm^3 s^{-1} $molecule^{-1}$ for *iso*-HNO_2 and $k(T) = 3.33\times10^{-22}\exp(-191.6/(RT))$ cm^3 s^{-1} $molecule^{-1}$ for HONO. The *iso*-HNO_2 adduct was found to be more thermodynamically stable than the *trans*-HONO conformer. Yamaguchi et al.[351] reported that rate constants for methane + NO_2 were a few orders of magnitude lower than the corresponding values reported by Slack and Grillo.[349]

Chan et al.[352] estimated the reaction rate constant for a variety of aliphatic alkanes, and only aromatic benzene. The alkanes considered were methane, ethane, propane and *iso*-butane. They executed ab initio DFT calculations at the BHandHLYP/6-311G** level of theory. For *trans*-HONO, Chen et al.[352] computed the reaction rate of the primary's H removal from methane and propane, represented as $k(T) = 3.49\times10^{-10}\exp(-170.0/(RT))$ cm^3 s^{-1} $molecule^{-1}$ and $k(T) = 9.47\times10^{-11}\exp(-154.0/(RT))$ cm^3 s^{-1} $molecule^{-1}$, correspondingly. For *cis*-HONO, the measured rate expression for primary H abstraction from ethane was $k(T) = 1.44\times10^{-10}\exp(-147.0/(RT))$ cm^3 s^{-1} $molecule^{-1}$. Furthermore, *iso*-HNO_2 isomer production from H abstraction of primary methane and ethane attains a reaction rate expressions of $k(T) = 1.58\times10^{-09}\exp(-141.2/(RT))$ cm^3 s^{-1} $molecule^{-1}$ and $k(T) = 2.66\times10^{-10}\exp(-113.3/(RT))$ cm^3 s^{-1} $molecule^{-1}$. The kinetic parameters of the remaining reactions (propane, *iso*-butane and benzene) are listed in Table 2.10. Overall, the aliphatic hydrocarbons showed comparable rates for *cis*-HONO and HNO over a temperature interval of 327–827 °C, whereas the

reaction of NO_2 with benzene proceeds with a faster rate into the *cis*-HONO channel rather than the *trans*-HONO and *iso*-HNO_2 isomers below about 1127 °C.

Table 2.10. Activation energies (kJ mol^{-1}) and pre-exponential factors (cm^3 s^{-1} $molecule^{-1}$) for the reactions of RH with NO_2.

Products	Temperature in °C (Pressure)	*A*	E_a	Computational methodology
Methane + NO_2				
Yamaguchi et al.[351]				
$CH_3^{\cdot}$ + HNO_2	527	5.40×10^{-20}	157.3	MP2/6-
$CH_3^{\cdot}$ + *trans*-HONO		3.33×10^{-22}	191.6	311++G(2d,p)
Chan et al.[352]				
$CH_3^{\cdot}$ + *trans*-HONO	327–827	3.49×10^{-10}	170.0	BHandHLYP/6-
$CH_3^{\cdot}$ + *cis*-HONO		1.44×10^{-10}	147.0	311G**
$CH_3^{\cdot}$ +*iso*-HNO_2		1.58×10^{-9}	161.0	
Ethane + NO_2				
Chan et al.[352]				
$C_2H_5^{\cdot}$ + *trans*-HONO	327–827	9.47×10^{-11}	154.0	BHandHLYP/6-
$C_2H_5^{\cdot}$ + *cis*-HONO		3.65×10^{-11}	130.0	311G**
$C_2H_5^{\cdot}$ +*iso*-HNO_2		2.66×10^{-10}	141.0	
Propane + NO_2				
Titarchuk et al.[353]				
iso-$C_3H_7^{\cdot}$ + HNO_2	150–225 (10.7 kPa)	3.99×10^{-13}	94.8	
Chan et al.[352]				
s-$C_3H_7^{\cdot}$ + *trans*-HONO	327–827	2.33×10^{-11}	141.0	BHandHLYP/6-
s-$C_3H_7^{\cdot}$ + *cis*-HONO		9.63×10^{-12}	118.0	311G**

s-$C_3H_7^{\cdot}$ +*iso*-HNO_2		4.98×10^{-11}	127.0	
iso-butane + NO_2				
Chan et al.[352]				
t-$C_3H_7^{\cdot}$ + *trans*-HONO	327–827	3.49×10^{-11}	134.0	BHandHLYP/6-
t-$C_3H_7^{\cdot}$ + *cis*-HONO		1.54×10^{-11}	108.0	311G**
t-$C_3H_7^{\cdot}$ +*iso*-HNO_2		4.65×10^{-11}	115.0	

For methane + NO_2, both the previous finding from Yamaguchi and Chan demonstrated that the reaction rate constant for *iso*-HNO_2 production is the fastest. Chan et al.[352] illustrated that the *cis*-HONO formation rate is nearly the same as *iso*-HNO_2. Conversely, the results of Yamaguchi et al.[351] indicate that the rate constant for the channel leading to *trans*-HONO is significantly slower than *iso*-HNO_2. Overall, there is a clear paucity in theoretical and experimental kinetics values for H abstraction by NO_2 from a large number of hydrocarbons. As elaborated, the relative importance of R-H + NO_2 → R + *trans*-HONO, *cis*-HONO and *iso*-HNO_2 is a subject of discrepancy among theoretical chemists.

2.10. Future directions

The literature review surveys kinetics, formation mechanisms and abatement technologies for various small N-containing gases; namely NO, NO_2, HCN, NH_3 and N_2O) and intermediates (e.g., NH_2) formed during the combustion of solid fuel and NH_4NO_3, as well as from NO_x mitigation methods. Despite a great deal of experimental results, the precise, underlying mechanistic steps are still largely speculative. Over the last decade or so, computational

chemistry methods have progressed enough to yield parameters that minimally deviate from analogous experimental measurements (for example, within 1.0 kcal/mol of an experimental BDH value). Furthermore, main-stream experimental techniques such as GC-MS are unable to detect highly transient species such as intermediate and transition states. For these reasons, mechanistic insight into the combustion chemistry of the title N-bearing species is best suited for purely theoretical investigation. Table 2.11 presents some of the gaps highlighted in this review that require addressing by means of theoretical modelling and experimental measurements.

Table 2.11. Selected gaps in knowledge on N-containing species present in combustion and high energy density materials.

Gap in knowledge	Addressed in Chapter
Accurate estimation of reaction kinetics for the abstraction of a hydrogen atom from hydrocarbons by NH_2 radicals. Considerable discrepancies exist in the kinetic parameters of R-H + NH_2 → R + NH_3 for a wide range of species, even the simplest C_1–C_3 hydrocarbons.	Chapter 4
Expanding the energy profiles and rate constants for H abstraction reactions of unreported aliphatic alkenes and alkynes with reactive NH_2 radicals that may have profound effects on the product distribution in	Chapter 4

combustion systems, yet to be determined.	
Thermochemistry and Arrhenius parameters pertinent to systems that consist of alkylbenzenes (i.e., major aromatic constituents in commercial transportation fuels) and NH_2 radicals are not precisely known. Analogous kinetic models often deploy values from corresponding species.	Chapter 5
The sensitising effect of NO_2 on the fuel oxidation characteristics in combustion chemistry and nitro-containing explosives demands reliable estimation of kinetics dictating H abstraction from small chain hydrocarbons.	Chapter 6
The deployed selective non-catalytic reduction efficiency of NO_x in combustion systems is overshadowed by the emission of N_2O gas. The inclusion of catechol, also a product of biomass combustion, may assist in reduction of N_2O. Reaction mechanism of N_2O with hydroxylated benzene isomers requires a through kinetic and mechanistic investigation as a crucial step in the pursuit of improving non-catalytic selective	Chapter 7

operations.	
Control of accident risks in mining sites requires complete understanding of NH_4NO_3 decomposition mechanisms, especially those related to the condensed phase occurring in emulsion explosives.	Chapter 8
Biomass is extensively being used for the reduction of NO_x. As such, it is vital to explore the essential mechanistic parameters underlying the thermal decomposition of catechol (a product of biomass combustion) in a reactive NO_x environment under oxidative condition. There is a need to assess the effectiveness of biomass surrogates to act as potent NO scavengers.	Chapter 9

2.11. References

1. Smoot, L. D.; Boardman, R. D.; Brewster, B. S.; Hill, S. C.; Foli, A. K., Development and Application of an Acid Rain Precursor Model for Practical Furnaces. *Energy Fuels* **1993**, *7*, 786-795.

2. Liu, D.; Mi, T.; Shen, B.; Feng, B.; Winter, F., Reducing N_2O Emission by Co-Combustion of Coal and Biomass. *Energy Fuels* **2002**, *16*, 525-526.

3. Wendt, J., Fundamental Coal Combustion Mechanisms and Pollutant Formation in Furnaces. *Prog. Energy Combust. Sci.* **1980**, *6*, 201-222.

4. Williams, A.; Jones, J.; Ma, L.; Pourkashanian, M., Pollutants from the Combustion of Solid Biomass Fuels. *Prog. Energy Combust. Sci.* **2012**, *38*, 113-137.

5. Chen, H.; Si, Y.; Chen, Y.; Yang, H.; Chen, D.; Chen, W., Nox Precursors from Biomass Pyrolysis: Distribution of Amino Acids in Biomass and Tar-N During Devolatilization Using Model Compounds. *Fuel* **2017**, *187*, 367-375.

6. Munroe, C. E.; Hall, C., *A Primer on Explosives for Coal Miners*; US Government Printing Office, 1911.

7. Meyers, S.; Shanley, E. S., Industrial Explosives-a Brief History of Their Development and Use. *J. Hazard. Mater.* **1990**, *23*, 183-201.

8. Streng, A., Evaluation of Toxic after-Detonation Gases Formed by Industrial Explosives. *Explosivstoffe* **1971**, *34*, 58-64.

9. Karmakar, N.; Banerjee, S., A Review of Laboratory and Field Test Methods for Studying Fume Characteristics of Explosives. *JMMF* **1984**, *32*, 398-402.

10. Mainiero, R.; Harris, M.; Rowland, J. In *Dangers of Toxic Fumes from Blasting*, Proceedings of the Annual Conference on Explosives and Blasting Technique, ISEE; 1999: 2007; p 73.

11. Harris, M. L.; Mainiero, R. J., Monitoring and Removal of Co in Blasting Operations. *Safety Sci.* **2008**, *46*, 1393-1405.

12. Vamvuka, D., *Overview of Solid Fuels Combustion Technologies*; Wiley Online Library: Weinheim, Germany, 2010.

13. Glarborg, P.; Jensen, A. D.; Johnsson, J. E., Fuel Nitrogen Conversion in Solid Fuel Fired Systems. *Prog. Energy Combust. Sci.* **2003**, *29*, 89-113.

14. Karavalakis, G.; Hajbabaei, M.; Durbin, T. D.; Johnson, K. C.; Zheng, Z.; Miller, W. J., The Effect of Natural Gas Composition on the Regulated Emissions, Gaseous Toxic

Pollutants, and Ultrafine Particle Number Emissions from a Refuse Hauler Vehicle. *Energy* **2013**, *50*, 280-291.

15. Hashemi, S. A.; Fattahi, A.; Sheikhzadeh, G. A.; Mehrabian, M. A., Investigation of the Effect of Air Turbulence Intensity on Nox Emission in Non-Premixed Hydrogen and Hydrogen-Hydrocarbon Composite Fuel Combustion. *Int. J. Hydrogen Energy* **2011**, *36*, 10159-10168.

16. Rutar, T.; Malte, P. C.; Kramlich, J. C., Investigation of NO_x and CO Formation in Lean-Premixed, Methane/Air, High-Intensity, Confined Flames at Elevated Pressures. *Proc. Comb. Inst.* **2000**, *28*, 2435-2441.

17. Naha, S.; Aggarwal, S. K., Fuel Effects on Nox Emissions in Partially Premixed Flames. *Combust. Flame* **2004**, *139*, 90-105.

18. Geddes, J.; Murphy, J., The Science of Smog: A Chemical Understanding of Ground Level Ozone and Fine Particulate Matter. In *Metropolitan Sustainability: Understanding and Improving the Urban Environment*, Elsevier: 2012; pp 205-230.

19. Cornell, S. E.; Jickells, T. D.; Cape, J. N.; Rowland, A. P.; Duce, R. A., Organic Nitrogen Deposition on Land and Coastal Environments: A Review of Methods and Data. *Atmos. Environ.* **2003**, *37*, 2173-2191.

20. Kramlich, J. C.; Linak, W. P., Nitrous Oxide Behavior in the Atmosphere, and in Combustion and Industrial Systems. *Prog. Energy Combust. Sci.* **1994**, *20*, 149-202.

21. Levine, J. In *The Global Atmospheric Budget of Nitrous Oxide*, Proc. of the 5th International Workshop on Nitrous Oxide Emissions, 1992, 1992.

22. LEVINE, J. S. In *Impacts of N20 and Other Trace Gases on Stratospheric Ozone*, EPA/IFP European Workshop on the Emission of Nitrous Oxide from Fossil Fuel Combustion, RueiI-Malmaison, France, June 1988, EPA-600/9-894)89 (NTIS PB90-126038)

(1989).

23. Pereira, C. J.; Amiridis, M. D., NO_x Control from Stationary Sources. In *Reduction of Nitrogen Oxide Emissions*, American Chemical Society: 1995; Vol. 587, pp 1-13.

24. Reis, S.; Pinder, R.; Zhang, M.; Lijie, G.; Sutton, M., Reactive Nitrogen in Atmospheric Emission Inventories. *Atmospheric Chem. Phys.* **2009**, *9*, 7657-7677.

25. Reis, S.; Pinder, R.; Zhang, M.; Lijie, G.; Sutton, M., Reactive Nitrogen in Atmospheric Emission Inventories-a Review. *Atmos Chem Phys Discuss* **2009**, *9*.

26. Olivier, J.; Bouwman, A.; Van der Hoek, K.; Berdowski, J., Global Air Emission Inventories for Anthropogenic Sources of No X, NH_3 and N_2O in 1990. *Environ. Pollut.* **1998**, *102*, 135-148.

27. Zhang, Y.; Wu, S.-Y.; Krishnan, S.; Wang, K.; Queen, A.; Aneja, V. P.; Arya, S. P., Modeling Agricultural Air Quality: Current Status, Major Challenges, and Outlook. *Atmos. Environ.* **2008**, *42*, 3218-3237.

28. Aneja, V. P.; Schlesinger, W. H.; Erisman, J. W.; Behera, S. N.; Sharma, M.; Battye, W., Reactive Nitrogen Emissions from Crop and Livestock Farming in India. *Atmos. Environ.* **2012**, *47*, 92-103.

29. Schlesinger, W. H.; Hartley, A. E., A Global Budget for Atmospheric NH_3. *Biogeochemistry* **1992**, *15*, 191-211.

30. Paerl, H. W., Coastal Eutrophication and Harmful Algal Blooms: Importance of Atmospheric Deposition and Groundwater as "New" Nitrogen and Other Nutrient Sources. *Limnol Oceanogr* **1997**, *42*, 1154-1165.

31. Krupa, S. V., Effects of Atmospheric Ammonia (Nh3) on Terrestrial Vegetation: A Review. *Environ. Pollut.* **2003**, *124*, 179-221.

32. Aneja, V. P.; Blunden, J.; Roelle, P. A.; Schlesinger, W. H.; Knighton, R.; Niyogi, D.; Gilliam, W.; Jennings, G.; Duke, C. S., Workshop on Agricultural Air Quality: State of the Science. *Atmos. Environ.* **2008**, *42*, 3195-3208.

33. Asman, W. A.; Sutton, M. A.; Schjørring, J. K., Ammonia: Emission, Atmospheric Transport and Deposition. *New Phytol.* **1998**, *139*, 27-48.

34. Sellegri, K.; Hanke, M.; Umann, B.; Arnold, F.; Kulmala, M., Measurements of Organic Gases During Aerosol Formation Events in the Boreal Forest Atmosphere During Quest. *Atmospheric Chem. Phys.* **2005**, *5*, 373-384.

35. Sorooshian, A.; Murphy, S.; Hersey, S.; Gates, H.; Padro, L.; Nenes, A.; Brechtel, F.; Jonsson, H.; Flagan, R.; Seinfeld, J., Comprehensive Airborne Characterization of Aerosol from a Major Bovine Source. *Atmospheric Chem. Phys.* **2008**, *8*, 5489-5520.

36. Hecht, S. S., Biochemistry, Biology, and Carcinogenicity of Tobacco-Specific N-Nitrosamines. *Chem. Res. Toxicol.* **1998**, *11*, 559-603.

37. Ge, X.; Wexler, A. S.; Clegg, S. L., Atmospheric Amines – Part I. A Review. *Atmospheric Environ.* **2011**, *45*, 524-546.

38. Lobert, J. M.; Scharffe, D. H.; Hao, W. M.; Crutzen, P. J., Importance of Biomass Burning in the Atmospheric Budgets of Nitrogen-Containing Gases. *Nature* **1990**, *346*, 552-554.

39. Yokelson, R. J.; Susott, R.; Ward, D. E.; Reardon, J.; Griffith, D. W., Emissions from Smoldering Combustion of Biomass Measured by Open-Path Fourier Transform Infrared Spectroscopy. *J. Geophys. Res.* **1997**, *102*, 18865-18877.

40. Simoneit, B. R. T.; Rushdi, A. I.; bin Abas, M. R.; Didyk, B. M., Alkyl Amides and Nitriles as Novel Tracers for Biomass Burning. *Environ. Sci. Technol.* **2003**, *37*, 16-21.

41. Qiu, C.; Zhang, R., Multiphase Chemistry of Atmospheric Amines. *Phys. Chem. Chem. Phys.* **2013**, *15*, 5738-5752.

42. Schade, G. W.; Crutzen, P. J., Emission of Aliphatic Amines from Animal Husbandry and Their Reactions: Potential Source of N_2O and Hcn. *J Atmos Chem.* **1995**, *22*, 319-346.

43. Mitchell, S., Iea Coal Research. *London, England* **1998**.

44. Tan, L. L.; Li, C.-Z., Formation of Nox and Sox Precursors During the Pyrolysis of Coal and Biomass. Part I. Effects of Reactor Configuration on the Determined Yields of HCN and NH_3 During Pyrolysis. *Fuel* **2000**, *79*, 1883-1889.

45. Leppälahti, J., Formation of NH_3 and HCN in Slow-Heating-Rate Inert Pyrolysis of Peat, Coal and Bark. *Fuel* **1995**, *74*, 1363-1368.

46. Ren, Q.; Zhao, C., Nox and N2o Precursors (NH_3 and HCN) from Biomass Pyrolysis: Interaction between Amino Acid and Mineral Matter. *Appl. Energy,* **2013**, *112*, 170-174.

47. Hansson, K.-M.; Samuelsson, J.; Tullin, C.; Åmand, L.-E., Formation of HNCO, HCN, and NH_3 from the Pyrolysis of Bark and Nitrogen-Containing Model Compounds. *Combust. Flame* **2004**, *137*, 265-277.

48. Ren, Q.; Zhao, C., Evolution of Fuel-N in Gas Phase During Biomass Pyrolysis. *Renew. Sustainable Energy Rev.* **2015**, *50*, 408-418.

49. Tian, F.-J.; Yu, J.-l.; McKenzie, L. J.; Hayashi, J.-i.; Chiba, T.; Li, C.-Z., Formation of NO_x Precursors During the Pyrolysis of Coal and Biomass. Part Vii. Pyrolysis and Gasification of Cane Trash with Steam. *Fuel* **2005**, *84*, 371-376.

50. Li, C.-Z.; Tan, L. L., Formation of NO_x and SO_x Precursors During the Pyrolysis of Coal and Biomass. Part iii. Further Discussion on the Formation of HCN and NH_3 During Pyrolysis. *Fuel* **2000**, *79*, 1899-1906.

51. Andreae, M. O.; Merlet, P., Emission of Trace Gases and Aerosols from Biomass Burning. *Global Biogeochem. Cycles* **2001**, *15*, 955-966.

52. Fiveland, W.; Wessel, R., Model for Predicting Formation and Reduction of NO_x in Three-Dimensional Furnaces Burning Pulverized Fuel. *J Energy Inst.* **1991**, *64*, 41-54.

53. Driscoll, J. F.; Chen, R.-H.; Yoon, Y., Nitric Oxide Levels of Turbulent Jet Diffusion Flames: Effects of Residence Time and Damkohler Number. *Combust. Flame* **1992**, *88*, 37-49.

54. Kramlich, J. C.; Malte, P. C., Modeling and Measurement of Sample Probe Effects on Pollutant Gases Drawn from Flame Zones. *Combust. Sci. Technol.* **1978**, *18*, 91-104.

55. Dean, J., *Properties of Atoms, Radicals, and Bonds*; McGRAWHILL Inc: University of Tennessee, Knoxville, 1999, p 36.

56. Zeldovich, J., The Oxidation of Nitrogen in Combustion and Explosions. *Acta Physiochimica U.R.S.S., XXI, Academy of Science of the USSR* **1946**.

57. Fenimore, C.; Jones, G., Nitrio Oxide Decomposition at 2200–2400 K. *J. Phys. Chem.* **1957**, *61*, 654-657.

58. Bowman, C. T. In *Kinetics of Nitric Oxide Formation Incombustion Processes*, Symposium (International) on Combustion, 1973; pp 729-738.

59. Thompson, D.; Brown, T.; Beer, J., NO_x Formation in Combustion. *Combust. Flame* **1972**, *19*, 69-79.

60. Bowman, C. T., Kinetics of Pollutant Formation and Destruction in Combustion. *Prog. Energy Combust. Sci.* **1975**, *1*, 33-45.

61. Glarborg, P.; Miller, J. A.; Kee, R. J., Kinetic Modeling and Sensitivity Analysis of Nitrogen Oxide Formation in Well-Stirred Reactors. *Combust. Flame* **1986**, *65*, 177-202.

62. Miller, J. A.; Bowman, C. T., Mechanism and Modeling of Nitrogen Chemistry in Combustion. *Prog. Energy Combust. Sci.* **1989**, *15*, 287-338.

63. Fenimore, C. In *Formation of Nitric Oxide in Premixed Hydrocarbon Flames*, Symposium (International) on Combustion, Elsevier: 1971; pp 373-380.

64. Bowman, C.; Seery, D., *Emissions from Continuous Combustion Systems*; plenum: New york, 1972, p 123.

65. Fenimore, C., Reactions of Fuel-Nitrogen in Rich Flame Gases. *Combust. Flame* **1976**, *26*, 249-256.

66. Bowman, C. T., Investigation of Nitric Oxide Formation Kinetics in Combustion Processes: The Hydrogen-Oxygen-Nitrogen Reaction. *Combust. Sci. Technol.* **1971**, *3*, 37-45.

67. Hayhurst, A. N.; Vince, I. M., Nitric Oxide Formation from N_2 in Flames: The Importance of "Prompt" No. *Prog. Energy Combust. Sci.* **1980**, *6*, 35-51.

68. Martin, G.; Berkau, E. In *An Investigation of the Conversion of Various Fuel Nitrogen Compounds to Nitrogen Oxides in Oil Combustion*, AICHE Symp. Sen, 1971; pp 45-54.

69. Turner, D. W.; Siegmund, C.; ANDREWS, R., Influence of Combustion Modification and Fuel Nitrogen Content on Nitrogen Oxides Emissions from Fuel Oil Combustion. *Combustion* **1972**, *44*, 21-&.

70. Palmer, H.; Seery, D., Chemistry of Pollutant Formation in Flames. *Annu. Rev. Phys. Chem.* **1973**, *24*, 235-262.

71. De Soete, G. G. In *Overall Reaction Rates of NO and N_2 Formation from Fuel Nitrogen*, Symposium (international) on combustion, Elsevier: 1975; pp 1093-1102.

72. Vandooren, J.; Sarkisov, O.; Balakhnin, V.; Van Tiggelen, P., Discussion on the Formation and Removal of NO_x in Ammonia Flames. *Chem. Phys. Lett.* **1991**, *184*, 294-300.

73. Fenimore, C.; Jones, G., Oxidation of Ammonia in Flames. *J. Phys. Chem.* **1961**, *65*, 298-303.

74. Bartok, W.; Engleman, V.; Goldstein, R.; del Valle, E. In *Basic Kinetic Studies and Modelling of Nitric Oxide Formation in Combustion Processes*, AICHE, Atlantic City, 1971.

75. Shaw, J. T.; Thomas, A. C. In *Oxides of Nitrogen in Relation to the Combustion of Coal*, Seventh internation conference on coal science, Prague, Czechoslovakia, June 1968.

76. Baxter, L. L.; Mitchell, R. E.; Fletcher, T. H.; Hurt, R. H., Nitrogen Release During Coal Combustion. *Energy Fuels* **1996**, *10*, 188-196.

77. Costa, M.; Godoy, S.; Lockwood, F.; Zhou, J., Initial Stages of the Devolatilization of Pulverized-Coal in a Turbulent Jet. *Combust. Flame* **1994**, *96*, 150-162.

78. Smoot, L. D.; Hedman, P. O.; Smith, P. J., Pulverized-Coal Combustion Research at Brigham Young University. *Prog. Energy Combust. Sci.* **1984**, *10*, 359-441.

79. Kelemen, S.; Gorbaty, M.; Kwiatek, P.; Fletcher, T.; Watt, M.; Solum, M.; Pugmire, R., Nitrogen Transformations in Coal During Pyrolysis. *Energy Fuels* **1998**, *12*, 159-173.

80. Yuan, S.; Zhou, Z.-j.; Li, J.; Chen, X.-l.; Wang, F.-c., HCN and NH_3 Released from Biomass and Soybean Cake under Rapid Pyrolysis. *Energy Fuels* **2010**, *24*, 6166-6171.

81. Leppälahti, J.; Koljonen, T., Nitrogen Evolution from Coal, Peat and Wood During Gasification: Literature Review. *Fuel Process. Technol.* **1995**, *43*, 1-45.

82. Zhou, J.; Masutani, S. M.; Ishimura, D. M.; Turn, S.; Kinoshita, C. In *Release of Fuel-Bound Nitrogen in Biomass During High Temperature Pyrolysis and Gasification*, Energy Conversion Engineering Conference, 1997. IECEC-97., Proceedings of the 32nd Intersociety, IEEE: 1997; pp 1785-1790.

83. Kambara, S.; Takarada, T.; Yamamoto, Y.; Kato, K., Relation between Functional Forms of Coal Nitrogen and Formation of Nitrogen Oxide (NO_x) Precursors During Rapid Pyrolysis. *Energy Fuels* **1993**, *7*, 1013-1020.

84. Slaughter, D. M.; Overmoe, B. J.; Pershing, D. W., Inert Pyrolysis of Stoker-Coal Fines. *Fuel* **1988**, *67*, 482-489.

85. Cai, H.-Y.; Güell, A.; Dugwell, D.; Kandiyoti, R., Heteroatom Distribution in Pyrolysis Products as a Function of Heating Rate and Pressure. *Fuel* **1993**, *72*, 321-327.

86. Choi, S.-S.; Ko, J.-E., Analysis of Cyclic Pyrolysis Products Formed from Amino Acid Monomer. *J. Chromatogr. A* **2011**, *1218*, 8443-8455.

87. Ren, Q.; Zhao, C.; Chen, X.; Duan, L.; Li, Y.; Ma, C., NO_x and N_2O Precursors (NH_3 and HCN) from Biomass Pyrolysis: Co-Pyrolysis of Amino Acids and Cellulose, Hemicellulose and Lignin. *Proc. Combust. Inst.* **2011**, *33*, 1715-1722.

88. Ren, Q.; Zhao, C., NO_x and N_2O Precursors from Biomass Pyrolysis: Role of Cellulose, Hemicellulose and Lignin. *Environ. Sci. Technol.* **2013**, *47*, 8955-8961.

89. Pohl, J. H.; Sarofim, A. F. In *Devolatilization and Oxidation of Coal Nitrogen*, Symposium (International) on Combustion, Elsevier: 1977; pp 491-501.

90. Song, Y. H.; Pohl, J. H.; Beér, J. M.; Sarofim, A. F., Nitric Oxide Formation During Pulverized Coal Combustion. *Combust. Sci. Technol.* **1982**, *28*, 31-40.

91. Johnsson, J. E., Formation and Reduction of Nitrogen Oxides in Fluidized-Bed Combustion. *Fuel* **1994**, *73*, 1398-1415.

92. Brown, B. W.; Smoot, L. D.; Hedman, P. O., Effect of Coal Type on Entrained Gasification. *Fuel* **1986**, *65*, 673-678.

93. Chen, S.; McCarthy, J.; Clark, W.; Heap, M.; Seeker, W.; Pershing, D. In *Bench and Pilot Scale Process Evaluation of Reburning for in-Furnace Nox Reduction*, Symposium (International) on Combustion, Elsevier: 1988; pp 1159-1169.

94. Chen, S.; Heap, M.; Pershing, D.; Nihart, R.; Rees, D. In *The Influence of Full Composition on the Formation and Control of NOx in Pulverized Coal Flames*, Western States Section Combustion Institute, Spring Meeting, Irvine, CA, 1980.

95. Takagi, T.; Tatsumi, T.; Ogasawara, M., Nitric Oxide Formation from Fuel Nitrogen in Staged Combustion: Roles of HCN and NH_i. *Combust. Flame* **1979**, *35*, 17-25.

96. Haynes, B., The Oxidation of Hydrogen Cyanide in Fuel-Rich Flames. *Combust. Flame* **1977**, *28*, 113-121.

97. Fenimore, C., Formation of Nitric Oxide from Fuel Nitrogen in Ethylene Flames. *Combust. Flame* **1972**, *19*, 289-296.

98. Song, Y.; Blair, D.; Siminski, V.; Bartok, W. In *Conversion of Fixed Nitrogen to N_2 in Rich Combustion*, Symposium (international) on Combustion, Elsevier: 1981; pp 53-63.

99. Corlett, R.; Monteith, L.; Halgren, C.; Malte, P., Molecular Nitrogen Yields from Fuel-Nitrogen in Backmixed Combustion. *Combust. Sci. Technol.* **1979**, *19*, 95-106.

100. Chae, J. O.; Chun, Y. N., Effect of Two-Stage Combustion on NO_x Emissions in Pulverized Coal Combustion. *Fuel* **1991**, *70*, 703-707.

101. Rees, D.; Smoot, L.; Hedman, P., 18th Symposium (International) on Combustion. *The Combustion Institute, Pittsburgh, PA* **1981**, 1305-1311.

102. Stubenberger, G.; Scharler, R.; Zahirović, S.; Obernberger, I., Experimental Investigation of Nitrogen Species Release from Different Solid Biomass Fuels as a Basis for Release Models. *Fuel* **2008**, *87*, 793-806.

103. Ren, Q.; Zhao, C.; Wu, X.; Liang, C.; Chen, X.; Shen, J.; Tang, G.; Wang, Z., Effect of Mineral Matter on the Formation of NO_x Precursors During Biomass Pyrolysis. *J. Anal. Appl. Pyrolysis* **2009**, *85*, 447-453.

104. Ren, Q.; Zhao, C.; Wu, X.; Liang, C.; Chen, X.; Shen, J.; Wang, Z., Formation of Nox Precursors During Wheat Straw Pyrolysis and Gasification with O_2 and CO_2. *Fuel* **2010**, *89*, 1064-1069.

105. Yu, Q. Z.; Brage, C.; Chen, G. X.; Sjöström, K., The Fate of Fuel-Nitrogen During Gasification of Biomass in a Pressurised Fluidised Bed Gasifier. *Fuel* **2007**, *86*, 611-618.

106. Ren, Q., NO_x and N_2O Precursors from Biomass Pyrolysis. *J. Therm. Anal. Calorim.* **2014**, *115*, 881-885.

107. Jones, J.; Pourkashanian, M.; Williams, A.; Hainsworth, D., A Comprehensive Biomass Combustion Model. *Renew. Energy* **2000**, *19*, 229-234.

108. Kær, S. K., Numerical Modelling of a Straw-Fired Grate Boiler. *Fuel* **2004**, *83*, 1183-1190.

109. Ren, Q.; Zhao, C.; Wu, X.; Liang, C.; Chen, X.; Shen, J.; Wang, Z., Catalytic Effects of Fe, Al and Si on the Formation of NO_x Precursors and Hcl During Straw Pyrolysis. *J. Therm. Anal. Calorim.* **2010**, *99*, 301-306.

110. Hill, S. C.; Douglas Smoot, L., Modeling of Nitrogen Oxides Formation and Destruction in Combustion Systems. *Prog. Energy Combust. Sci.* **2000**, *26*, 417-458.

111. Nelson, R.; Franklin, J.; Scherer, B., Power-Gen Americas' 94. *Livonia, MI* **1994**.

112. Smoot, L. D.; Hill, S. C.; Xu, H., NO_x Control through Reburning1this Mini-Review Paper Was Presented, Together with a Series of Other Review Papers, at the Tenth Annual Technical Conference of the Advanced Combustion Engineering Research Center, Held in Salt Lake City, Utah, in March 1997.1. *Prog. Energy Combust. Sci.* **1998**, *24*, 385-408.

113. Smith, P. J.; Hill, S. C.; Smoot, L. D. In *Theory for NO Formation in Turbulent Coal Flames*, Symposium (International) on Combustion, Elsevier: 1982; pp 1263-1270.

114. Wendt, J.; Sternling, C.; Matovich, M. In *Reduction of Sulfur Trioxide and Nitrogen Oxides by Secondary Fuel Injection*, Symposium (International) on Combustion, Elsevier: 1973; pp 897-904.

115. Dagaut, P.; Luche, J.; Cathonnet, M., Reduction of No by Propane in a JSR at 1atm: Experimental and Kinetic Modeling. *Fuel* **2001**, *80*, 979-986.

116. Dagaut, P.; Lecomte, F., Experiments and Kinetic Modeling Study of NO-Reburning by Gases from Biomass Pyrolysis in a JSR. *Energy Fuels* **2003**, *17*, 608-613.

117. Glarborg, P.; Kristensen, P. G.; Dam-Johansen, K.; Alzueta, M. U.; Millera, A.; Bilbao, R., Nitric Oxide Reduction by Non-Hydrocarbon Fuels. Implications for Reburning with Gasification Gases. *Energy Fuels* **2000**, *14*, 828-838.

118. Alzueta, M. U.; Bilbao, R.; Millera, A.; Glarborg, P.; Østberg, M.; Dam-Johansen, K., Modeling Low-Temperature Gas Reburning. NO_x Reduction Potential and Effects of Mixing. *Energy Fuels* **1998**, *12*, 329-338.

119. Kilpinen, P.; Glarborg, P.; Hupa, M., Reburning Chemistry: A Kinetic Modeling Study. *Ind. Eng. Chem. Res.* **1992**, *31*, 1477-1490.

120. Østberg, M.; Glarborg, P.; Jensen, A.; Johnsson, J. E.; Pedersen, L. S.; Dam-Johansen, K. In *A Model of the Coal Reburning Process*, Symposium (International) on Combustion, Elsevier: 1998; pp 3027-3035.

121. Wendt, J. O. L., Mechanisms Governing the Formation and Destruction of NO_x and Other Nitrogenous Species in Low NO_x Coal Combustion Systems1. *Combust. Sci. Technol.* **1995**, *108*, 323-344.

122. Dagaut, P.; Lecomte, F.; Chevailler, S.; Cathonnet, M., Experimental and Kinetic Modeling of Nitric Oxide Reduction by Acetylene in an Atmospheric Pressure Jet-Stirred Reactor. *Fuel* **1999**, *78*, 1245-1252.

123. Dagaut, P.; Luche, J.; Cathonnet, M., Experimental and Kinetic Modeling of the Reduction of NO by Propene at 1 Atm. *Combust. Flame* **2000**, *121*, 651-661.

124. Kristensen, P. G.; Glarborg, P.; Dam-Johansen, K., Nitrogen Chemistry During Burnout in Fuel-Staged Combustion. *Combust. Flame* **1996**, *107*, 211-222.

125. Ho, L.; Maly, P. M.; Seeker, W. R. In *Reburning Promoted by Nitrogen-and Sodium-Containing Compounds*, Symposium (International) on Combustion, Elsevier: 1996; pp 2075-2082.

126. Glarborg, P.; Karll, B.; Pratapas, J. In *Review of Natural Gas Reburning. Initial Full Scale Results, Report of Committee F. Industrial and Commercial Utilization of Gases*, Proceedings of the 19th World Gas Conference, Milan, 1994.

127. Lissianski, V. V.; Zamansky, V. M.; Maly, P. M., Effect of Metal-Containing Additives on NO_x Reduction in Combustion and Reburning. *Combust. Flame* **2001**, *125*, 1118-1127.

128. McCahey, S.; McMullan, J. T.; Williams, B. C., Techno-Economic Analysis of NO_x Reduction Technologies in P.F. Boilers. *Fuel* **1999**, *78*, 1771-1778.

129. Oluwoye, I.; Dlugogorski, B. Z.; Gore, J.; Vyazovkin, S.; Boyron, O.; Altarawneh, M., Thermal Reduction of NO_x with Recycled Plastics. *Environ. Sci. Technol.* **2017**, *51*, 7714-7722.

130. Hampartsoumian, E.; Folayan, O.; Nimmo, W.; Gibbs, B., Optimisation of NO_x Reduction in Advanced Coal Reburning Systems and the Effect of Coal Type☆. *Fuel* **2003**, *82*, 373-384.

131. Alzueta, M. U.; Røjel, H.; Kristensen, P. G.; Glarborg, P.; Dam-Johansen, K., Laboratory Study of the $CO/NH_3/NO/O_2$ System: Implications for Hybrid Reburn/Sncr Strategies. *Energy Fuels* **1997**, *11*, 716-723.

132. Wang, X. S.; Gibbs, B. M.; Rhodes, M. J., Impact of Air Staging on the Fate of NO and N_2O in a Circulating Fluidized-Bed Combustor. *Combust. Flame* **1994**, *99*, 508-515.

133. Lyngfelt, A.; Leckner, B., Combustion of Wood-Chips in Circulating Fluidized Bed Boilers — NO and CO Emissions as Functions of Temperature and Air-Staging. *Fuel* **1999**, *78*, 1065-1072.

134. Coda, B.; Kluger, F.; Förtsch, D.; Spliethoff, H.; Hein, K. R. G.; Tognotti, L., Coal-Nitrogen Release and NO_x Evolution in Air-Staged Combustion. *Energy Fuels* **1998**, *12*, 1322-1327.

135. Wendt, J. O. L.; Pershing, D. W.; Lee, J. W.; Glass, J. W., Pulverized Coal Combustion: NO_x Formation Mechanisms under Fuel Rich and Staged Combustion Conditions. *Symposium (International) on Combustion* **1979**, *17*, 77-87.

136. Spliethoff, H.; Greul, U.; Rüdiger, H.; Hein, K. R. G., Basic Effects on NO_x Emissions in Air Staging and Reburning at a Bench-Scale Test Facility. *Fuel* **1996**, *75*, 560-564.

137. Jodal, M.; Nielsen, C.; Hulgaard, T.; Dam-Johansen, K. In *A Comparative Study of Ammonia and Urea as Reductants in Selective Non-Catalytic Reduction of Nitric Oxide*, Achemasia, Beijing, 1989.

138. Caton, J.; Siebers, D., Comparison of Nitric Oxide Removal by Cyanuric Acid and by Ammonia. *Combust. Sci. Technol.* **1989**, *65*, 277-293.

139. Lyon, R. K., Thermal Denox Controlling Nitrogen Oxides Emissions by a Noncatalytic Process. *Combust. Sci. Technol.* **1987**, *21*, 231-236.

140. Lyon, R. K.; Hardy, J. E., Discovery and Development of the Thermal De NO_x Process. *Ind. Eng. Chem. Fundam.* **1986**, *25*, 19-24.

141. Muzio, L.; Arand, J.; Teixeira, D. In *Gas Phase Decomposition of Nitric Oxide in Combustion Products*, Symposium (International) on Combustion, Elsevier: 1977; pp 199-208.

142. Salimian, S.; Hanson, R., A Kinetic Study of NO Removal from Combustion Gases by Injection of NH_i-Containing Compounds. *Combust. Sci. Technol.* **1980**, *23*, 225-230.

143. Fenimore, C., Destruction of NO by NH_3 in Lean Burnt Gas. *Combust. Flame* **1980**, *37*, 245-250.

144. Miller, J. A.; Branch, M. C.; Kee, R. J., A Chemical Kinetic Model for the Selective Reduction of Nitric Oxide by Ammonia. *Combust. Flame* **1981**, *43*, 81-98.

145. Dean, A.; Hardy, J.; Lyon, R. In *Kinetics and Mechanism of NH_3 Oxidation*, Symposium (International) on Combustion, Elsevier: 1982; pp 97-105.

146. Silver, J. A.; Kolb, C. E., Kinetic Measurements for the Reaction of Amidogen + Nitric Oxide over the Temperature Range 294-1215 K. *J. Phys. Chem.* **1982**, *86*, 3240-3246.

147. Lyon, R. K., The NH_3-NO-O_2 Reaction. *Int. J. Chem. Kinet.* **1976**, *8*, 315-318.

148. Robin, M.; Price, H.; Squires, R. In *Tailoring NH_3 Based Sncr for Installation on Power Plants Boilers*, Joint EPA/EPRI Symposium on Stationary Combustion NO_x Control, Springfield: VA: 1991.

149. Caton, J.; Narney, J.; Cariappa, H.; Laster, W., The Selective Non-Catalytic Reduction of Nitric Oxide Using Ammonia at up to 15% Oxygen. *Can. J. Chem. Eng.* **1995**, *73*, 345-350.

150. Lyon, R. K.; Benn, D. In *Kinetics of the $NO-NH_3-O_2$ Reaction*, Symposium (International) on Combustion, Elsevier: 1979; pp 601-610.

151. Lodder, P.; Lefers, J. B., Effect of Natural Gas, C_2H_6 and O on the Homogeneous Gas Phase Reduction of NO_x by NH_3. *Chem. Eng. J.* **1985**, *30*, 161-167.

152. Wenli, D.; Dam-Johansen, K.; Østergaard, K. In *Widening the Temperature Range of the Thermal De* NO_x *Process. An Experimental Investigation*, Symposium (International) on Combustion, Elsevier: 1991; pp 297-303.

153. Silver, J. A., The Effect of Sulfur on the Thermal Denox Process. *Combust. Flame* **1983**, *53*, 17-21.

154. Azuhata, S.; Akimoto, H.; Hishinuma, Y., Effect of H_2O_2 on Homogeneous Gas Phase No Reduction Reaction with NH_3. *AICHE J.* **1982**, *28*, 7-11.

155. Wenli, D.; Dam-Johansen, K.; Ostergaard, K. In *The Influence of Additives on Selective Non-Catalytic Reduction of Nitric Oxide with* NH_3, Achemasia, Beijing, 1989.

156. Muris, S.; Hemberger, R.; Wolfrum, P. In *An Experimental and Modelling Study of Selective Non-Catalytic Reduction of NO by Ammonia in Presence of Hydrocarbon*, 25th Symposium (International) on Combustion, The Combustion Institute, Pitsburgh, 1994.

157. Tayyeb Javed, M.; Irfan, N.; Gibbs, B. M., Control of Combustion-Generated Nitrogen Oxides by Selective Non-Catalytic Reduction. *J. Environ. Econ. Manag.* **2007**, *83*, 251-289.

158. Lyon, R.; Longwell, J. In *Selective Non-Catalytic Reduction of* NO_x *by* NH_3, EPRI NO_x Control Technology Seminar, San Francisco, California, 1976.

159. Teixeira, D.; Muzio, L.; Montgomery, T.; Quartucy, G.; Martz, T. In *Widening the Urea Temperature Window*, Proceedings of 1991 Joint Symposium on Stationary Combustion NO_x Control. NTIS, 1991.

160. Chen, S. L.; Cole, J. A.; Heap, M. P.; Kramlich, J. C.; McCarthy, J. M.; Pershing, D. W., Advanced Nox Reduction Processes Using-Nh and -Cn Compounds in Conjunction with Staged Air Addition. *Symposium (International) on Combustion* **1989**, *22*, 1135-1145.

161. Arand, J. K.; Muzio, L. J.; Sotter, J. G., Urea Reduction of NO_x in Combustion Effluents. Google Patents: 1980.

162. Mansour, M.; Nahas, S.; Quartucy, G.; Nylander, J.; Kerry, H.; Radak, L.; Eskinazi, D.; Behrens, T. In *Full Scale Evaluation of Urea Injection for No Removal*, Proceedings of the Joint EPA/EPRI Symposium on Stationary Combustion NO_x Control. New Orleans, Louisiana, 1987; pp 1-23.

163. In *Jones, D.G., Muzio, L.J., Stocker, E., Nuesch, P.C., Negrea, S., Ofenbau, K.K., Lautenschlager, G., Wachter, E., Rose, G., 1989. Two-Stage De* NO_x *Process Test Data for 300 Tpd Msw Inceniration Plant. In: 82nd APCA Meeting and Exhibition, Anaheim, Ca, pp. 21–27.*

164. Lin, M.; Knenlein, M. In *Cement Kiln* NO_x *Reduction Experience Using the* NO_x*OUT Process*, 2000 International Joint Power Generation Conference., Miami Beach, Florida, 2000.

165. Higgins, S.T., Douglas, R.E., 1990. Injection of NH_3 and NH_3-Based Compounds for the Control of Nitrous Oxides at Homer City. In: Sixth International Pitsburgh Coal Conference, Pitsburgh, Pa, pp. 827–836.

166. Lee, J. B.; Kim, S. D., Kinetics of NO_x Reduction by Urea Solution in a Pilot Scale Reactor. *J. Chem. Eng. Jpn.* **1996**, *29*, 620-626.

167. Negrea, S., Jones, D.G., Rose, G., Smith, R.A., Shiomoto, G.H., 1990. Urea Injection NO_x Removal on a 325 MW Brown Coal-Fired Electric Utility Boiler in West Germany. Oell-KRC and Fossil Energy Research Corporation, Private Communication.

168. Muzio, L.J., Teague, M.E., Montgomery, T.A., Samuelsen, G.S., Kramlich, J.C., Lyon, R.K., 1989. Measurement of N_2O from Combustion Sources, Symposium on Stationary Combustion Nitrogen Oxide Control, Epri Proceeding Gs-6423, 1, pp. 55–72.

169. Irfan, N.; Gibbs, B., Flue Gas Nitrogen Oxides (NO_x) Control Using Selective Non Catalytic Reduction Process. In *Environ. Pollut.*, 1997.

170. Hossain, K. A.; Mohd-Jaafar, M. N.; Appalanidu, K. B.; Mustafa, A.; Ani, F. N., Application of Urea Based Sncr System in the Combustion Effluent Containing Low Level of Baseline Nitric Oxide. *Environ. Technol.* **2005**, *26*, 251-260.

171. Abele, A.R., Kwan, Y. Mansour, M.N., 1991. Performance of Urea NO_x Reduction Systems on Utility Boilers, Joint EPA/EPRI Symposium on Stationary Combustion NO_x Control, NTIS, Springfield, Va, Section. 6a, pp. 1–19.

172. In *Nylander, J.H., Mansour, M.N., Douglas, R.B., 1989. Demonstration of an Automated Urea Injection System at Encina Unit 2, EPA/EPRI Joint Symposium on Stationary Combustion* NO_x *Control, San Francisco, 35–56.*

173. Irfan, N. Control of Gaseous Emissions by Flue Gas Treatment. Ph.D. Thesis. The University of Leads, 1995. .

174. Koebel, M.; Elsener, M., Nitrogen Removal from Waste Gases after the SNCR Process-Ammonia or Urea as Reductant. *Chem. Eng. Technol.* **1992**, *64*, 934-937.

175. Rota, R.; Antos, D.; Zanoelo, É. F.; Morbidelli, M., Experimental and Modeling Analysis of the NO_xOUT Process. *Chem. Eng. Sci.* **2002**, *57*, 27-38.

176. Miller, J. A.; Glarborg, P., Modelling the Formation of N_2O and NO_2 in the Thermal De-NO_x Process. In *Gas Phase Chemical Reaction Systems*, Springer: 1996; pp 318-333.

177. Rota, R.; Zanoelo, É. F.; Antos, D.; Morbidelli, M.; Carra, S., Analysis of the Thermal DeNO_x Process at High Partial Pressure of Reactants. *Chem. Eng. Sci.* **2000**, *55*, 1041-1051.

178. Glarborg, P.; Kristensen, P. G.; Jensen, S. H.; Dam-Johansen, K., A Flow Reactor Study of HNCO Oxidation Chemistry. *Combust. Flame* **1994**, *98*, 241-258.

179. Demirbas, A., Combustion Characteristics of Different Biomass Fuels. *Prog. Energy Combust. Sci.* **2004**, *30*, 219-230.

180. Han, K.; Niu, S.; Lu, C., Experimental Study on Biomass Advanced Reburning for Nitrogen Oxides Reduction. *Process Saf. Environ. Prot.* **2010**, *88*, 425-430.

181. Li, G.; Chi, Z.; Si, D., Test and Study on Reburning of Biological Wastes to Reduce NO_x Emission. *Power Gene* **2004**, *33*, 41-44.

182. Adams, B. R.; Harding, N. S., Reburning Using Biomass for NO_x Control. *Fuel Process. Technol.* **1998**, *54*, 249-263.

183. Harding, N. S.; Adams, B. R., Biomass as a Reburning Fuel: A Specialized Cofiring Application. *Biomass Bioenergy* **2000**, *19*, 429-445.

184. Zhuang, H.; Niu, Y.; Gong, Y.; Zhang, Y.; Zhang, Y.; Hui, S., Influence of Biomass Reburning on Nox Reductions During Pulverized Coal Combustion. *Energy Fuels* **2017**, *31*, 5597-5602.

185. Shu, Y.; Zhang, F.; Wang, H.; Zhu, J.; Tian, G.; Zhang, C.; Cui, Y.; Huang, J., An Experimental Study of NO Reduction by Biomass Reburning and the Characterization of Its Pyrolysis Gases. *Fuel* **2015**, *139*, 321-327.

186. Casaca, C.; Costa, M., Nox Control through Reburning Using Biomass in a Laboratory Furnace: Effect of Particle Size. *Proc. Comb. Inst.* **2009**, *32*, 2641-2648.

187. Wang, X.; Zhao, Q.; Tan, H.; Xu, T.; Hui, S., Kinetic Analysis of Nitric Oxide Reduction Using Biogas as Reburning Fuel. *Afr J Biotechnol* **2009**, *8*.

188. Vilas, E.; Skifter, U.; Jensen, A. D.; López, C.; Maier, J.; Glarborg, P., Experimental and Modeling Study of Biomass Reburning. *Energy Fuels* **2004**, *18*, 1442-1450.

189. Luan, J.; Sun, R.; Wu, S.; Lu, J.; Yao, N., Experimental Studies on Reburning of Biomasses for Reducing NO_x in a Drop Tube Furnace. *Energy Fuels* **2009**, *23*, 1412-1421.

190. Casaca, C.; Costa, M., The Effectiveness of Reburning Using Rice Husk as Secondary Fuel for NO_x Reduction in a Furnace. *Combust. Sci. Technol.* **2005**, *177*, 539-557.

191. Ballester, J.; Ichaso, R.; Pina, A.; González, M. A.; Jiménez, S., Experimental Evaluation and Detailed Characterisation of Biomass Reburning. *Biomass Bioenergy* **2008**, *32*, 959-970.

192. Lu, P.; Wang, Y.; Huang, Z.; Lu, F.; Liu, Y., Study on NO Reduction and Its Heterogeneous Mechanism through Biomass Reburning in an Entrained Flow Reactor. *Energy Fuels* **2011**, *25*, 2956-2962.

193. Baulch, D.; Cobos, C.; Cox, R.; Esser, C.; Frank, P.; Just, T.; Kerr, J.; Pilling, M.; Troe, J.; Walker, R., Evaluated Kinetic Data for Combustion Modeling. *J. Phys. Chem. Ref. Data* **1992**, *21*, 411-734.

194. Thorne, L. R.; Branch, M. C.; Chandler, D. W.; Kee, R. J.; Miller, J. A., Hydrocarbon/Nitric Oxide Interactions in Low-Pressure Flames. *Symposium (International) on Combustion* **1988**, *21*, 965-977.

195. Li, B. W.; Wu, K.; Moyeda, D. K.; Payne, R., Use of Computer Models for Reburning/Cofiring Boiler Performance Evaluations. *ASME Fact* **1993**, *17*, 87-94.

196. Hura, H. S.; Breen, B. P. In *Chemical Kinetic Simulation of Nitric Oxide Reduction During Natural Gas Reburning in Pulverized Coal Fired Boilers*, the 1993 International Joint Power Generation Conference, Kansas City, MO, USA, 10/17-22/93, 1993; pp 51-69.

197. Burch, T. E.; Tillman, F. R.; Chen, W. Y.; Lester, T. W.; Conway, R. B.; Sterling, A. M., Partitioning of Nitrogenous Species in the Fuel-Rich State of Reburning. *Energy Fuels* **1991**, *5*, 231-237.

198. Chen, W.-Y.; Lester, T.; Babcock, L. *Formation and Destruction of Nitrogen Oxides in Coal Combustion.[Reburning]*; Louisiana State Univ., Baton Rouge, LA (United States): 1988.

199. Chen, W.; Smoot, L. D.; Fletcher, T. H.; Boardman, R. D., A Computational Method for Determining Global Fuel-NO Rate Expressions. Part 1. *Energy Fuels* **1996**, *10*, 1036-1045.

200. Chen, W.; Smoot, L. D.; Hill, S. C.; Fletcher, T. H., Global Rate Expression for Nitric Oxide Reburning. Part 2. *Energy Fuels* **1996**, *10*, 1046-1052.

201. Kee, R. J.; Rupley, F. M.; Miller, J. A. *Chemkin-Ii: A Fortran Chemical Kinetics Package for the Analysis of Gas-Phase Chemical Kinetics*; Sandia National Labs., Livermore, CA (USA): 1989.

202. Oluwoye, I.; Altarawneh, M.; Gore, J.; Bockhorn, H.; Dlugogorski, B. Z., Oxidation of Polyethylene under Corrosive NO_x Atmosphere. *J. Phys. Chem. C* **2016**, *120*, 3766-3775.

203. Koebel, M.; Elsener, M., Selective Catalytic Reduction of NO over Commercial De NO_x -Catalysts: Experimental Determination of Kinetic and Thermodynamic Parameters. *Chem. Eng. Sci.* **1998**, *53*, 657-669.

204. Kang, M.; Kim, D. J.; Park, E. D.; Kim, J. M.; Yie, J. E.; Kim, S. H.; Hope-Weeks, L.; Eyring, E. M., Two-Stage Catalyst System for Selective Catalytic Reduction of NO_x by NH_3 at Low Temperatures. *Appl. Catal., B* **2006**, *68*, 21-27.

205. Liu, C.; Shi, J.-W.; Gao, C.; Niu, C., Manganese Oxide-Based Catalysts for Low-Temperature Selective Catalytic Reduction of NO_x with NH_3: A Review. *Appl. Catal., A* **2016**, *522*, 54-69.

206. Fu, M.; Li, C.; Lu, P.; Qu, L.; Zhang, M.; Zhou, Y.; Yu, M.; Fang, Y., A Review on Selective Catalytic Reduction of NO_x by Supported Catalysts at 100 – 300 °C—Catalysts, Mechanism, Kinetics. *Catal. Sci. Technol.* **2014**, *4*, 14-25.

207. Kang, M.; Park, E. D.; Kim, J. M.; Yie, J. E., Manganese Oxide Catalysts for NO_x Reduction with NH_3 at Low Temperatures. *Appl. Catal., A* **2007**, *327*, 261-269.

208. Chen, Z.; Yang, Q.; Li, H.; Li, X.; Wang, L.; Chi Tsang, S., Cr–MnO_x Mixed-Oxide Catalysts for Selective Catalytic Reduction of NO_x with NH_3 at Low Temperature. *J. Catal.* **2010**, *276*, 56-65.

209. Kalmár, J. z.; Woldegiorgis, K. L.; Biri, B.; Ashby, M. T., Mechanism of Decomposition of the Human Defense Factor Hypothiocyanite near Physiological Ph. *J. Am. Chem. Soc.* **2011**, *133*, 19911-19921.

210. Shan, W.; Song, H., Catalysts for the Selective Catalytic Reduction of NO_x with NH_3 at Low Temperature. *Catal. Sci. Technol.* **2015**, *5*, 4280-4288.

211. Busca, G.; Lietti, L.; Ramis, G.; Berti, F., Chemical and Mechanistic Aspects of the Selective Catalytic Reduction of NO_x by Ammonia over Oxide Catalysts: A Review. *Appl. Catal., B* **1998**, *18*, 1-36.

212. Liang, Z.; Ma, X.; Lin, H.; Tang, Y., The Energy Consumption and Environmental Impacts of SCR Technology in China. *Appl. Energy* **2011**, *88*, 1120-1129.

213. Zhang, T.; Qiu, F.; Chang, H.; Peng, Y.; Li, J., Novel W-Modified $SnMnCeO_x$ Catalyst for the Selective Catalytic Reduction of NO_x with NH_3. *Catal Commun.* **2017**, *100*, 117-120.

214. Devadas, M.; Kröcher, O.; Elsener, M.; Wokaun, A.; Söger, N.; Pfeifer, M.; Demel, Y.; Mussmann, L., Influence of NO_2 on the Selective Catalytic Reduction of NO with Ammonia over Fe-ZSM5. *Appl. Catal., B* **2006**, *67*, 187-196.

215. Väliheikki, A.; Petallidou, K. C.; Kalamaras, C. M.; Kolli, T.; Huuhtanen, M.; Maunula, T.; Keiski, R. L.; Efstathiou, A. M., Selective Catalytic Reduction of NO_x by Hydrogen (H_2-SCR) on WO_x-Promoted $Ce_zZr_{1-z}O_2$ Solids. *Appl. Catal., B* **2014**, *156*, 72-83.

216. Li, J.; Wang, S.; Zhou, L.; Luo, G.; Wei, F., No Reduction by Co over a Fe-Based Catalyst in FCC Regenerator Conditions. *Chem. Eng. J.* **2014**, *255*, 126-133.

217. Barreau, M.; Tarot, M. L.; Duprez, D.; Courtois, X.; Can, F., Remarkable Enhancement of the Selective Catalytic Reduction of NO at Low Temperature by Collaborative Effect of Ethanol and NH_3 over Silver Supported Catalyst. *Appl. Catal., B* **2017**.

218. Wang, X.; Chen, H.-Y.; Sachtler, W. M. H., Mechanism of the Selective Reduction of NO_x over Co/MFI: Comparison with Fe/MFI. *J. Catal.* **2001**, *197*, 281-291.

219. Qi, G.; Yang, R. T.; Chang, R., MnO_x-CeO_2 Mixed Oxides Prepared by Co-Precipitation for Selective Catalytic Reduction of NO with NH_3 at Low Temperatures. *Appl. Catal., B* **2004**, *51*, 93-106.

220. Tang, X.; Li, J.; Wei, L.; Hao, J., MnO_x-SnO_2 Catalysts Synthesized by a Redox Coprecipitation Method for Selective Catalytic Reduction of NO by NH_3. *Chinese J Catal.* **2008**, *29*, 531-536.

221. Liu, F.; He, H.; Ding, Y.; Zhang, C., Effect of Manganese Substitution on the Structure and Activity of Iron Titanate Catalyst for the Selective Catalytic Reduction of NO with NH_3. *Appl. Catal., B* **2009**, *93*, 194-204.

222. Singoredjo, L.; Korver, R.; Kapteijn, F.; Moulijn, J., Alumina supported Manganese Oxides for the Low-Temperature Selective Catalytic Reduction of Nitric Oxide with Ammonia. *Appl. Catal., B* **1992**, *1*, 297-316.

223. Smirniotis, P. G.; Sreekanth, P. M.; Peña, D. A.; Jenkins, R. G., Manganese Oxide Catalysts Supported on TiO_2, Al_2O_3, and SiO_2: A Comparison for Low-Temperature SCR of NO with NH_3. *Ind. Eng. Chem. Res.* **2006**, *45*, 6436-6443.

224. Dzwigaj, S.; Janas, J.; Gurgul, J.; Socha, R. P.; Shishido, T.; Che, M., Do Cu(II) Ions need Al Atoms in Their Environment to Make CuSiBEA Active in the SCR of NO by Ethanol or Propane? A Spectroscopy and Catalysis Study. *Appl. Catal., B* **2009**, *85*, 131-138.

225. Boutros, M.; Gálvez, M. E.; Onfroy, T.; Da Costa, P., Influence of Synthesis Parameters of SBA-15 Supported Palladium Catalysts for Methane Combustion and Simultaneous NO_x Reduction. *Microporous Mesoporous Mater.* **2014**, *183*, 1-8.

226. Boutros, M.; Trichard, J.-M.; Da Costa, P., Silver Supported Mesoporous SBA-15 as Potential Catalysts for SCR NO_x by Ethanol. *Appl. Catal., B* **2009**, *91*, 640-648.

227. Komatsu, T.; Tomokuni, K.; Yamada, I., Outstanding Low Temperature HC-SCR of NO_x over Platinum-Group Catalysts Supported on Mesoporous Materials Expecting Diesel-Auto Emission Regulation. *Catal. Today* **2006**, *116*, 244-249.

228. Pieterse, J. A. Z.; van den Brink, R. W.; Booneveld, S.; de Bruijn, F. A., Influence of Zeolite Structure on the Activity and Durability of Co-Pd-Zeolite Catalysts in the Reduction of NO_x with Methane. *Appl. Catal., B* **2003**, *46*, 239-250.

229. Stakheev, A. Y.; Lee, C. W.; Park, S. J.; Chong, P. J., Selective Catalytic Reduction of NO with Propane over CoZSM-5 Containing Alkaline Earth Cations. *Appl. Catal., B* **1996**, *9*, 65-76.

230. Altarawneh, M.; Jaf, Z.; Oskierski, H.; Jiang, Z.-T.; Gore, J.; Dlugogorski, B. Z., Conversion of NO into N_2 over Γ-Mo_2N. *J. Phys. Chem. C* **2016**, *120*, 22270-22280.

231. He, H.; Dai, H. X.; Ngan, K. Y.; Au, C. T., Molybdenum Nitride for the Direct Decomposition of NO. *Catal. Lett.* **2001**, *71*, 147-153.

232. Change, I. P. O. C., Climate Change 2007: The Physical Science Basis. *Agenda* **2007**, *6*, 333.

233. Mereb, J. B.; Wendt, J. O., Air Staging and Reburning Mechanisms for NO_x Abatement in a Laboratory Coal Combustor. *Fuel* **1994**, *73*, 1020-1026.

234. Linak, W. P.; McSorley, J. A.; Hall, R. E.; Ryan, J. V.; Srivastava, R. K.; Wendt, J. O.; Mereb, J. B., Nitrous Oxide Emissions from Fossil Fuel Combustion. *J. Geophys. Res.* **1990**, *95*, 7533-7541.

235. Smith, K.; Crutzen, P.; Mosier, A.; Winiwarter, W., The Global Nitrous Oxide Budget: A Reassessment. *Nitrous Oxide and Climate Change* **2010**, 63-84.

236. Banin, A., Global Budget of N_2O: The Role of Soils and Their Change. *Sci. Total Environ.* **1986**, *55*, 27-38.

237. Li, M.; Shimizu, M.; Hatano, R., Evaluation of N_2O and CO_2 Hot Moments in Managed Grassland and Cornfield, Southern Hokkaido, Japan. *CATENA* **2015**, *133*, 1-13.

238. Prather, M. J.; Holmes, C. D.; Hsu, J., Reactive Greenhouse Gas Scenarios: Systematic Exploration of Uncertainties and the Role of Atmospheric Chemistry. *Geophys. Res. Lett.* **2012**, *39*.

239. Edenhofer, O., R. Pichs-Madruga, Y. Sokona, E. Farahani, S. Kadner, K. Seyboth, A. Adler, I. Baum, S. Brunner, P. Eickemeier, B. Kriemann, J. Savolainen, S. Schlömer, C. von Stechow, T. Zwickel and J.C. Minx (eds.), Climate Change 2014: Mitigation of Climate Change; International Panel on Climate Change (Ippc)S, Cambridge University Press Cambridge, Uk, and New York, 2014.

240. Inventory of U.S. Greenhouse Gas Emissions and Sinks: 1990-2015. https://www.epa.gov/ghgemissions/inventory-us-greenhouse-gas-emissions-and-sinks-1990-2015 (accessed 17 July).

241. Global Green House Gas Emission Data. https://www.epa.gov/ghgemissions/global-greenhouse-gas-emissions-data (accessed (accessed 17 July).

242. Armesto, L.; Boerrigter, H.; Bahillo, A.; Otero, J., N_2O Emissions from Fluidised Bed Combustion. The Effect of Fuel Characteristics and Operating Conditions☆. *Fuel* **2003**, *82*, 1845-1850.

243. Muzio, L.; Montgomery, T.; Samuelsen, G.; Kramlich, J. C.; Lyon, R.; Kokkinos, A. In *Formation and Measurement of N_2O in Combustion Systems*, Symposium (International) on Combustion, Elsevier: 1991; pp 245-250.

244. Colorado, A.; McDonell, V.; Samuelsen, S., Direct Emissions of Nitrous Oxide from Combustion of Gaseous Fuels. *Int. J. Hydrogen Energy* **2017**, *42*, 711-719.

245. Kramlich, J. C.; Cole, J. A.; McCarthy, J. M.; Lanier, W. S.; McSorley, J. A., Mechanisms of Nitrous Oxide Formation in Coal Flames. *Combust. Flame* **1989**, *77*, 375-384.

246. Koornneef, J.; Junginger, M.; Faaij, A., Development of Fluidized Bed Combustion—an Overview of Trends, Performance and Cost. *Prog. Energy Combust. Sci.* **2007**, *33*, 19-55.

247. Abbas, T.; Costa, M.; Costen, P.; Lockwood, F., Nitrous Oxide Emissions from an Industry-type Pulverized-Coal Burner. *Combust. flame* **1991**, *87*, 104-108.

248. Russo, N.; Fino, D.; Saracco, G.; Specchia, V., N_2O Catalytic Decomposition over Various Spinel-Type Oxides. *Catal. Today* **2007**, *119*, 228-232.

249. Leckner, B., Fluidized Bed Combustion: Mixing and Pollutant Limitation. *Prog. Energy Combust. Sci.* **1998**, *24*, 31-61.

250. Svoboda, K.; Pohořelý, M., Influence of Operating Conditions and Coal Properties on NO_x and N_2O Emissions in Pressurized Fluidized Bed Combustion of Subbituminous Coals. *Fuel* **2004**, *83*, 1095-1103.

251. Collings, M. E.; Mann, M. D.; Young, B. C., Effect of Coal Rank and Circulating Fluidized-Bed Operating Parameters on Nitrous Oxide Emissions. *Energy Fuels* **1993**, *7*, 554-558.

252. Luis, F.; Londono, C. A.; Wang, X. S.; Gibbs, B. M., Influence of Operating Parameters on NO_x and N_2O Axial Profiles in a Circulating Fluidized Bed Combustor. *Fuel* **1996**, *75*, 971-978.

253. Valentim, B.; Lemos de Sousa, M. J.; Abelha, P.; Boavida, D.; Gulyurtlu, I., Combustion Studies in a Fluidised Bed—the Link between Temperature, NO_x and N_2O Formation, Char Morphology and Coal Type. *Int J Coal Geol.* **2006**, *67*, 191-201.

254. Lyngfelt, A.; Åmand, L.-E.; Leckner, B., Reversed Air Staging — a Method for Reduction of N_2O Emissions from Fluidized Bed Combustion of Coal. *Fuel* **1998**, *77*, 953-959.

255. Johnsson, J. E.; Åmand, L.-E.; Dam-Johansen, K.; Leckner, B., Modeling N_2O Reduction and Decomposition in a Circulating Fluidized Bed Boiler. *Energy Fuels* **1996**, *10*, 970-979.

256. Gustavsson, L.; Glarborg, P.; Leckner, B., Modeling of Chemical Reactions in Afterburning for the Reduction of N_2O. *Combust. Flame* **1996**, *106*, 345-358.

257. Shen, B.; Mi, T.; Liu, D.; Feng, B.; Yao, Q.; Winter, F., N_2O Emission under Fluidized Bed Combustion Condition. *Fuel Process. Technol.* **2003**, *84*, 13-21.

258. Xiangsong, H.; Hai, Z.; Shi, Y.; Junfu, L.; Guangxi, Y., N_2O Decomposition over the Circulating Ashes from Coal-Fired CFB Boilers. *Chem. Eng. J.* **2008**, *140*, 43-51.

259. Murakami, T.; Suzuki, Y.; Durrani, A. K., New Approach to Understanding NO Emission During Bubbling Fluidized Bed Coal Combustion: Separation of NO Formation and Reduction Processes in the Bed. *Energy Fuels* **2009**, *23*, 1950-1955.

260. Liu, H.; Feng, B.; Lu, J.; Zheng, C., Coal Property Effects on N_2O and NO_x Formation from Circulating Fluidized Bed Combustion of Coal. *Chem. Eng. Commun.* **2005**, *192*, 1482-1489.

261. Hulgaard, T.; Dam-Johansen, K., Homogeneous Nitrous Oxide Formation and Destruction under Combustion Conditions. *AICHE J.* **1993**, *39*, 1342-1354.

262. Zhou, H.; Li, Y.; Li, N.; Qiu, R.; Cen, K., NO and N_2O Emissions During Devolatilization and Char Combustion of a Single Biomass Particle under Oxy-Fuel Conditions at Fluidized Bed Temperature. *Energy Fuels* **2017**.

263. Hansson, K.-M.; Åmand, L.-E.; Habermann, A.; Winter, F., Pyrolysis of Poly-*L*-Leucine under Combustion-Like Conditions. *Fuel* **2003**, *82*, 653-660.

264. Zhou, H.; Huang, Y.; Mo, G.; Liao, Z.; Cen, K., Experimental Investigations of the Conversion of Fuel-N, Volatile-N and Char-N to NO_x and N_2O During Single Coal Particle Fluidized Bed Combustion. *J Energy Inst.* **2017**, *90*, 62-72.

265. Hayhurst, A. N.; Lawrence, A. D., Emissions of Nitrous Oxide from Combustion Sources. *Prog. Energy Combust. Sci.* **1992**, *18*, 529-552.

266. Jiang, X.; Huang, X.; Liu, J.; Han, X., Nox Emission of Fine-and Superfine-Pulverized Coal Combustion in O_2/CO_2 Atmosphere. *Energy Fuels* **2010**, *24*, 6307-6313.

267. Goel, S. K.; Morihara, A.; Tullin, C. J.; Sarofim, A. F., Effect of NO and O_2 Concentration on N_2O Formation During Coal Combustion in a Fluidized-Bed Combustor: Modeling Results. *Symposium (International) on Combustion* **1994**, *25*, 1051-1059.

268. Miller, J. A.; Glarborg, P., Modelling the Formation of N_2O and NO_2 in the Thermal De-NO_x Process. In *Gas Phase Chemical Reaction Systems: Experiments and Models 100 Years after Max Bodenstein Proceedings of an International Symposion, Held at the "Internationales Wissenschaftsforum Heidelberg", Heidelberg, Germany, July 25 – 28, 1995*, Wolfrum, J.; Volpp, H. R.; Rannacher, R.; Warnatz, J., Eds. Springer Berlin Heidelberg: Berlin, Heidelberg, 1996; pp 318-333.

269. Araos, M.; Onederra, I., Development of a Novel Mining Explosive Formulation to Eliminate Nitrogen Oxide Fumes. *Min. Technol.* **2015**, *124*, 16-23.

270. Onederra, I.; Araos, M., Preliminary Quantification of the in Situ Performance of a Novel Hydrogen Peroxide Based Explosive. *Min. Technol.* **2017**, *126*, 113-122.

271. Callinan, R. *Locals Fuming as Mine Blasts Release Toxic Clouds into Neighbourhood, the Australian, 5 October*; 2001.

272. EETM, N., National Pollutant Inventory, Emission Estimation Technique Manual for Explosives Detonation and Firing Ranges. Version: 2008.

273. Oluwoye, I.; Dlugogorski, B. Z.; Gore, J.; Oskierski, H. C.; Altarawneh, M., Atmospheric Emission of NO_x from Mining Explosives: A Critical Review. *Atmos. Environ* **2017**, *167*, 81-96.

274. Cook, M. A.; Talbot, E. L., Explosive Sensitivity of Ammonium Nitrate-Hydrocarbon Mixtures. *Ind. Eng. Chem.* **1951**, *43*, 1098-1102.

275. Nazarian, A.; Presser, C., Thermal Signature Measurements for Ammonium Nitrate/Fuel Mixtures by Laser Heating. *Thermochim Acta* **2016**, *623*, 120-135.

276. Resende, S. A.; Lima, H. M. d., Study of Non-Conventional Fuels for Explosives Mixes. *Rem Rev. Esc. Minas*, **2014**, *67*, 297-302.

277. Hurley, C.; Petr, V.; Liu, S.; Banker, J. In *Properties of Alternatively Fueled Ammonium Nitrate Explosives*, Proceedings of the 9th International Symposium on Rock Fragmentation by Blasting-FRAGBLAST9, Granada, Spain, 2009.

278. Abdollahisharif, J.; Bakhtavar, E.; Nourizadeh, H., Monitoring and Assessment of Pollutants Resulting from Bench-Blasting Operations. *INT. J. MIN.* **2016**, *7*, 109-118.

279. Bhattacharyya, M.; Singh, P.; Ram, P.; Paul, R., Some Factors Influencing Toxic Fume Generation by NG-Based Semigel Explosives in Laboratory Studies. *PEP* **2001**, *26*, 69-74.

280. De Souza, E. M.; Katsabanis, P. D., On the Prediction of Blasting Toxic Fumes and Dilution Ventilation. *Min. Sci. Technol.* **1991**, *13*, 223-235.

281. Sapko, M.; Rowland, J.; Mainiero, R.; Zlochower, I. In *Chemical and Physical Factors That Influence Nox Production During Blasting-Exploratory Study*, Proceedings of the Annual Conference on Explosives and Blasting Technique, ISEE; 1999: 2002; pp 317-330.

282. Cooper, P., *Explosives Engineering, Publisher Wiley-Vch*; Wiley-VCH, 1996.

283. Mainiero, R.; Rowland, J.; Harris, M.; Sapko, M. In *Behavior of Nitrogen Oxides in the Product Gases from Explosive Detonations*, Proceedings of the Annual Conference on Explosives and Blasting Technique, ISEE; 1999: 2006; p 93.

284. Baulch, D. L., *Evaluated Kinetic Data for High Temperature Reactions*; CRC Press, 1972.

285. Hall Jr, T.; Blacet, F., Separation of the Absorption Spectra of NO_2 and N_2O_4 in the Range of 2400–5000A. *J. Chem. Phys.* **1952**, *20*, 1745-1749.

286. Ermolin, N., Modeling of Pyrolysis of Ammonium Dinitramide Sublimation Products under Low-Pressure Conditions. *Combust. Explos. Shock Waves* **2004**, *40*, 92-109.

287. Onederra, I.; Bailey, V.; Cavanough, G.; Torrance, A., Understanding Main Causes of Nitrogen Oxide Fumes in Surface Blasting. *Min. Technol.* **2012**, *121*, 151-159.

288. Chaturvedi, S.; Dave, P. N., Review on Thermal Decomposition of Ammonium Nitrate. *J Energ Mater.* **2013**, *31*, 1-26.

289. Brower, K.; Oxley, J. C.; Tewari, M., Evidence for Homolytic Decomposition of Ammonium Nitrate at High Temperature. *J. Phys. Chem.* **1989**, *93*, 4029-4033.

290. Xu, Z.-X.; Wang, Q.; Fu, X.-Q., Thermal Stability and Mechanism of Decomposition of Emulsion Explosives in the Presence of Pyrite. *J. Hazard. Mater.* **2015**, *300*, 702-710.

291. Oxley, J. C.; Smith, J. L.; Rogers, E.; Yu, M., Ammonium Nitrate: Thermal Stability and Explosivity Modifiers. *Thermochim. Acta* **2002**, *384*, 23-45.

292. Rosser, W. A.; Inami, S. H.; Wise, H., The Kinetics of Decomposition of Liquid Ammonium Nitrate. *J. Phys. Chem.* **1963**, *67*, 1753-1757.

293. Vyazovkin, S.; Clawson, J. S.; Wight, C. A., Thermal Dissociation Kinetics of Solid and Liquid Ammonium Nitrate. *Chem. Mater.* **2001**, *13*, 960-966.

294. Sinditskii, V. P.; Egorshev, V. Y.; Levshenkov, A. I.; Serushkin, V. V., Ammonium Nitrate: Combustion Mechanism and the Role of Additives. *PEP* **2005**, *30*, 269-280.

295. Izato, Y.-i.; Miyake, A., Thermal Decomposition Mechanism of Ammonium Nitrate and Potassium Chloride Mixtures. *J. Therm. Anal. Calorim.* **2015**, *121*, 287-294.

296. Skarlis, S. A.; Nicolle, A.; Berthout, D.; Dujardin, C.; Granger, P., Combined Experimental and Kinetic Modeling Approaches of Ammonium Nitrate Thermal Decomposition. *Thermochim. Acta* **2014**, *584*, 58-66.

297. Oxley, J. C.; Kaushik, S. M.; Gilson, N. S., Thermal Decomposition of Ammonium Nitrate-Based Composites. *Thermochim. Acta* **1989**, *153*, 269-286.

298. Russell, T. P.; Brill, T. B., Thermal Decomposition of Energetic Materials 31—Fast Thermolysis of Ammonium Nitrate, Ethylenediammonium Dinitrate and Hydrazinium Nitrate and the Relationship to the Burning Rate. *Combust. Flame* **1989**, *76*, 393-401.

299. Patil, D. G.; Jain, S. R.; Brill, T. B., Thermal Decomposition of Energetic Materials 56. On the Fast Thermolysis Mechanism of Ammonium Nitrate and Its Mixtures with Mangnesium and Carbon. *PEP* **1992**, *17*, 99-105.

300. Davis, T. L.; Abrams, A. J., The Dehydration of Ammonium Nitrate. *J. Amer. Chem. Soc.* **1925**, *47*, 1043-1045.

301. Andersen, W.; Bills, K.; Mishuck, E.; Moe, G.; Schultz, R., A Model Describing Combustion of Solid Composite Propellants Containing Ammonium Nitrate. *Combust. Flame* **1959**, *3*, 301-317.

302. Lurie, B. A.; Lianshen, C., Kinetics and Mechanism of Thermal Decomposition of Ammonium Nitrate Powder under the Action of Carbon Black. *Combust. Explos. Shock Waves* **2000**, *36*, 607-617.

303. Nguyen, M.-T.; Jamka, A. J.; Cazar, R. A.; Tao, F.-M., Structure and Stability of the Nitric Acid–Ammonia Complex in the Gas Phase and in Water. *J. Chem. Phys.* **1997**, *106*, 8710-8717.

304. Kumarasiri, M.; Swalina, C.; Hammes-Schiffer, S., Anharmonic Effects in Ammonium Nitrate and Hydroxylammonium Nitrate Clusters. *J. Phys. Chem. B* **2007**, *111*, 4653-4658.

305. Cagnina, S.; Rotureau, P.; Fayet, G.; Adamo, C., The Ammonium Nitrate and Its Mechanism of Decomposition in the Gas Phase: A Theoretical Study and a Dft Benchmark. *Phys. Chem. Chem. Phys.* **2013**, *15*, 10849-10858.

306. Alymova, Y. V.; Annikova, V.; Vlasova, N. Y.; Kondrikov, B., Detonation Characteristics of Emulsion Explosives. *Combust. Explos. Shock Waves* **1994**, *30*, 340-345.

307. Xu, S.; Tan, L.; Liu, J.-p.; Chen, X.; Jiang, W.; Chen, Y.; Liu, D.-b., Cause Analysis of Spontaneous Combustion in an Ammonium Nitrate Emulsion Explosive. *J. Loss Prev. Process Ind* **2016**, *43*, 181-188.

308. Silva, G. D.; Dlugogorski, B. Z.; Kennedy, E. M., Elementary Reaction Step Model of the N-Nitrosation of Ammonia. *Int. J. Chem. Kinet.* **2007**, *39*, 645-656.

309. Ridd, J., Nitrosation, Diazotisation, and Deamination. *Chem. Soc. Rev.* **1961**, *15*, 418-441.

310. Markovits, G.; Schwartz, S.; Newman, L., Hydrolysis Equilibrium of Dinitrogen Trioxide in Dilute Acid Solution. *Inorg. Chem.* **1981**, *20*, 445-450.

311. Al-Mallah, K.; Collings, P.; Stedman, G., Electrophilic Nitrosation at Sulphur and Nitrogen in Thiourea. *J. Chem. Soc.* **1974**, 2469-2472.

312. da Silva, G.; Dlugogorski, B. Z.; Kennedy, E. M., An Experimental and Theoretical Study of the Nitrosation of Ammonia and Thiourea. *Chem. Eng. Sci.* **2006**, *61*, 3186-3197.

313. Williams, D. L. H., *Nitrosation Reactions and the Chemistry of Nitric Oxide*; Elsevier: Amsterdam, 2004.

314. Rayson, M. S.; Mackie, J. C.; Kennedy, E. M.; Dlugogorski, B. Z., Experimental Study of Decomposition of Aqueous Nitrosyl Thiocyanate. *Inorg. Chem.* **2011**, *50*, 7440-7452.

315. Wu, Z.; Xu, J.; Liu, Q.; Dong, X.; Li, D.; Holzmann, N.; Frenking, G.; Trabelsi, T.; Francisco, J. S.; Zeng, X., The Hypothiocyanite Radical Oscn and Its Isomers. *Phys. Chem. Chem. Phys.* **2017**, *19*, 16713-16720.

316. Gunawan, R.; Freij, S.; Zhang, D.-k.; Beach, F.; Littlefair, M., A Mechanistic Study into the Reactions of Ammonium Nitrate with Pyrite. *Chem. Eng. Sci.* **2006**, *61*, 5781-5790.

317. Proulx, R.; Scovira, S., Feature Articles-Drilling and Blasting in Hot, Reactive Ground at Meikle. *Mining Engineering* **2001**, *53*, 31-37.

318. Priyananda, P.; Djerdjev, A. M.; Gore, J.; Neto, C.; Beattie, J. K.; Hawkett, B. S., Premature Detonation of an NH_4NO_3 Emulsion in Reactive Ground. *J. Hazard. Mater.* **2015**, *283*, 314-320.

319. *Aeisg Code of Practice, Prevention and Management of Blast Generated NO_x Gases in Surface Blasting* New South Wales 2011.

320. Rumball, J. A. The Interaction of Partially Weathered Sulphides in the Mt Mcrae Shale Formation with Ammonium Nitrate. Murdoch University, Murdoch University, Perth, Australia, 1991.

321. BRIGGS, T. J.; KELSO, I. J., Ammonium Nitrate-Sulfide Reactivity at the Century Zn-Pb-Ag Mine, Northwest Queensland, Australia. *Explor. Min. Geol.* **2001**, *10*, 177-190.

322. Aeisg. 2011. [Cited 2014 April]. Available From: Http://

www.Aeisg.Org/Images/Stories/Aeisg_Cop_NO_x_Edition_02aug2011.Pdf.

323. Epstein, I. R.; Kustin, K.; Warshaw, L. J., A Kinetics Study of the Oxidation of Iron (II) by Nitric Acid. *J. Am. Chem. Soc.* **1980**, *102*, 3751-3758.

324. Gok, O., Catalytic Oxidation Mechanism of Oxy-Nitrogen Species (NO_x) in $FeSO_4$ Electrolyte. *Nitric Oxide* **2011**, *25*, 47-53.

325. Azarkovich, A.; Bolkhovitinov, L.; Pernik, L., Possibility of Minimizing Generation of Nitrogen Oxides in Blasting of Ammonium Nitrate Explosives. *J. Min. Sci* **1995**, *31*, 147-151.

326. Opoku, M. K.; Dlugogorski, B. Z.; Kennedy, E. M.; Mackie, J. C., The Effect of Additive on Nox Emission During Thermal Decomposition of Nano-Recrystallised Nitrate Salts. *Advances in Materials Science for Environmental and Energy Technologies III, Volume 250* **2014**, 307-319.

327. Venpin, W. K. P. F.; Kennedy, E. M.; Mackie, J. C.; Dlugogorski, B. Z., Trapping of Nitric Oxide, Generated During Sensitization of Ammonium Nitrate Emulsion Explosive, by Aromatic Nitroso Sulfonates. *Ind. Eng. Chem. Res.* **2013**, *52*, 10561-10568.

328. Demissy, M.; Lesclaux, R., Kinetics of Hydrogen Abstraction by Amino Radicals from Alkanes in the Gas Phase. A Flash Photolysis-Laser Resonance Absorption Study. *J. Amer. Chem. Soc.* **1980**, *102*, 2897-2902.

329. Trotman-Dickenson, A. F.; Steacie, E. W. R., The Reactions of Methyl Radicals. Iv. The Abstraction of Hydrogen Atoms from Cyclic Hydrocarbons, Butynes, Amines, Alcohols, Ethers, and Ammonia. *J. Chem. Phys.* **1951**, *19*, 329-336.

330. Gray, P.; Thynne, J. C. J., Kinetics of Hydrogen Abstraction from Hydrazine, Ammonia and Trideuteroammonia. *Trans. Farday Soc.* **1964**, *60*, 1047-1052.

331. Edwards, D. A.; Kerr, J. A.; Lloyd, A. C.; Trotman-Dickenson, A. F., Hydrogen-Abstraction Reactions by Methyl Radicals from Nitrogen-Containing Compounds. *J. Chem. Soc.* **1966**, 621-622.

332. Hack, W.; Kurzke, H.; Rouveirolles, P.; Wagner, H. G., Direct Measurements of the Reaction $NH_2+CH_4 \rightarrow NH_3+CH_3$ in Temperature Range $743 \leq T/K \leq 1023$. *Symposium (International) on Combustion* **1988**, *21*, 905-911.

333. Hennig, G.; Wagner, H. G. G., A Kinetic Study About the Reactions of $NH_2(\bar{X}_2B_1)$ Radicals with Saturated Hydrocarbons in the Gas Phase. *Ber. Bunsenges. Phys. Chem.* **1995**, *99*, 863-869.

334. Song, S.; Golden, D. M.; Hanson, R. K.; Bowman, C. T.; Senosiain, J. P.; Musgrave, C. B.; Friedrichs, G., A Shock Tube Study of the Reaction $NH_2+CH_4 \rightarrow NH_3+CH_3$ and Comparison with Transition State Theory. *Int. J. Chem. Kinet.* **2003**, *35*, 304-309.

335. Ehbrecht, J.; Hack, W.; Rouveirolles, P.; Gg. Wagner, H., Hydrogen Abstraction Reactions by $NH_2(\bar{X}_2B_1)$-Radicals from Hydrocarbons in the Gas Phase. *Ber. Bunsenges. Phys. Chem.* **1987**, *91*, 700-708.

336. Hack, W.; Schröter, M. R.; Gg. Wagner, H., Kinetics of the Reaction NH_2 + 1,3-Butadiene. *Ber. Bunsenges. Phys. Chem.* **1982**, *86*, 326-330.

337. Gribov, L. A.; Novakov, I. A.; Pavlyuchko, A. I.; Kuchurov, I. V., Spectroscopic Calculation of CH Bond Dissociation Energy for Aliphatic Derivatives from the Ethylene Series. *J. Struct. Chem.* **2006**, *47*, 629-634.

338. Pham, V. K.; Lesclaux, R., Kinetics of the Reaction of Amino Radicals with Olefins. *J. Phys. Chem.* **1979**, *83*, 1119-1122.

339. Lesclaux, R.; Demissy, M., The Kinetics of the Gas Phase Reactions of NH_2 Radicals with Alkane and Alkyl Radicals. *J. Photochem.* **1978**, *9*, 110-112.

340. Dransfeld, P.; Hack, W.; Kurzke, H.; Temps, F.; Wagner, H. G., Direct Studies of Elementary Reactions of NH_2-Radicals in the Gas Phase. *Symposium (International) on Combustion* **1985**, *20*, 655-663.

341. Hack, W.; Schacke, H.; Schröter, M.; Wagner, H. G., Reaction Rates of Nh2-Radicals with NO, NO_2, C_2H_2, C_2H_4 and Other Hydrocarbons. *Symposium (International) on Combustion* **1979**, *17*, 505-513.

342. Bosco, S. R.; Nava, D. F.; Brobst, W. D.; Stief, L. J., Temperature and Pressure Dependence of the Absolute Rate Constant for the Reactions of NH_2 Radicals with Acetylene and Ethylene. *J. Chem. Phys.* **1984**, *81*, 3505-3511.

343. Lesclaux, R.; Soulignac, J. C.; Van Khě, P., The Kinetics of the Reaction between NH_2 and Propylene Studied by Laser Resonance Absorption. *Chem. Phys. Lett.* **1976**, *43*, 520-523.

344. Leroy, G.; Sana, M.; Tinant, A., Theoretical study of hydrogen abstraction reactions RH + X .dblharw. R + HX, with R, X=H, CH_3, NH_2,OH and F. *Can. J. Chem.* **1985**, *63*, 1447-1456.

345. Yu, Y.-X.; Li, S.-M.; Xu, Z.-F.; Li, Z.-S.; Sun, C.-C., An Ab Initio Study on the Reaction $NH_2+CH_4 \rightarrow NH_3+CH_3$. *Chem. Phys. Lett.* **1998**, *296*, 131-136.

346. Mebel, A. M.; Lin, M. C., Prediction of Absolute Rate Constants for the Reactions of NH_2 with Alkanes from Ab Initio G2M/TST Calculations. *J. Phys. Chem. A.* **1999**, *103*, 2088-2096.

347. Valadbeigi, Y.; Farrokhpour, H., Theoretical Study on the Mechanism and Kinetics of Atmospheric Reactions C_nH_{2n+2} +NH_2 (n = 1–3). *Struct Chem* **2015**, *26*, 383-391.

348. Batiha, M.; Altarawneh, M.; Alsofi, A.; Al-Harahsheh, M.; Altarawneh, I.; Alrawadieh, S., Theoretical Study on the Reaction of Hydrogen Atoms with Aniline. *Theor. Chem. Acc.* **2011**, *129*, 823-832.

349. Slack, M.; Grillo, A. In *Kinetics of Hydrogen-Oxygen and Methane-Oxygen Ignition Sensitized by NO or NO_2*, Proceedings of the Eleventh International Symposium, Seattle, Wash., July 11-14, 1977, Seattle, Wash, University of Washington Press: Seattle, Wash, 1978; pp p. 408-415.

350. Slack, M.; Grillo, A., Shock Tube Investigation of Methane-Oxygen Ignition Sensitized by NO_2. *Combust. Flame* **1981**, *40*, 155-172.

351. Yamaguchi, Y.; Teng, Y.; Shimomura, S.; Tabata, K.; Suzuki, E., Ab Initio Study for Selective Oxidation of Methane with NO_x (x= 1, 2). *J. Phys. Chem. A* **1999**, *103*, 8272-8278.

352. Chan, W.-T.; Heck, S. M.; Pritchard, H. O., Reaction of Nitrogen Dioxide with Hydrocarbons and Its Influence on Spontaneous Ignition. A Computational Study. *Phys. Chem. Chem. Phys.* **2001**, *3*, 56-62.

353. Titarchck, T.; Ballod, A.; Shtern, V. Y., Rate Constants for the Generation of Isopropyl Radicals During Thermal Nitration of Propane by Nitrogen Dioxide. *Kinet. Catal* **1976**, *17*, 1070.

Chapter 3

Research and Methodology

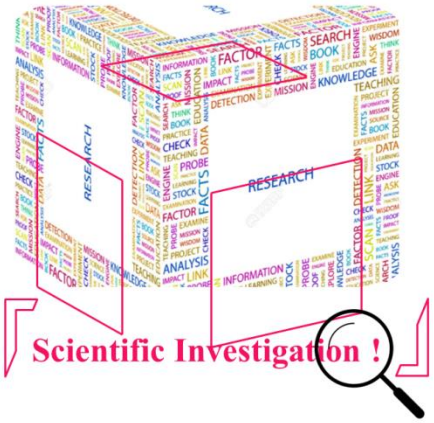

This chapter collates a systematic research plan of the quantum chemical calculations, background theories, modelling tools and the experimental approach that includes chemicals, experimental rig and analytical techniques employed in this research under controlled conditions.

3.1. Computational methodology

In this thesis, we outline the theoretical tools we utilised herein to investigate the thermodynamics and kinetic parameters, and the mechanistic pathways involving selected N-containing chemical species (NH_2, NO_2, NO_x and N_2O) related to combustion and high energy density materials. In this chapter, we describe the mathematical formulations behind quantum chemical methods. We devote a section to describing the electronic structure package of Gaussian09, which we used to carry out all computations reported in the thesis. The software utilises ab initio, density functional theory (DFT), semi empirical, and chemistry models. Figure 3.1 illustrates an overview of the computation algorithm, retrieval of information and validation of the particular applied methods.

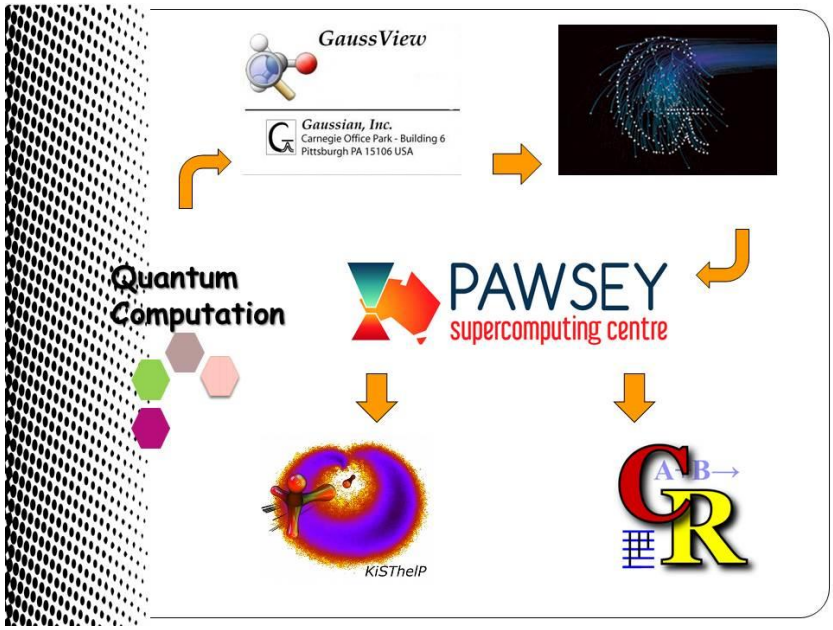

Figure 3.1. Flow representation of the applied computational plan.

3.1.1. Ab initio methods

The ab initio quantum chemistry method is solely based on principles of quantum mechanics. These methods are currently widely utilised to predict structure, energetics, chemical reactions and electronic descriptors. For accurate computations, a number of approximations and mathematical transformations are applied to obtain solutions of the fundamental equations. Quantum mechanics play a vital role and describes the dual nature of entities such as electrons that hold both wave-like and particle-like properties. The domain of quantum mechanics relies on describing electron behaviour in molecular systems through the solution of the time-independent Schrödinger equation that is considered as the theoretical foundation of modern computational chemistry. Equation 3.1 defines the stationary states of a quantum system for the Schrödinger equation:

$$\hat{\mathrm{H}}\Psi = E\Psi \qquad \text{E3.1}$$

Where $\hat{H}$ is the Hamiltonian operator that is associated with the observable energy; Ψ is the wave function, which defines the function of the particles position (electrons and nuclei) in the molecular system; E is the total energy of the system. $\hat{\mathrm{H}}$ is defined as:

$$\hat{\mathrm{H}} = -\sum_{i}^{particles}\left(\frac{\nabla^2}{2m_i}\right) + \sum_{i<j}^{particles}\sum\frac{q_i q_j}{r_{ij}} \qquad \text{E3.2}$$

In equation 3.2, ∇ is the Laplacian operator acting on particle *i* represent the probability of finding an electron is given by:

$$\nabla_i^2 = \left(\frac{\partial^2}{\partial x_i^2} + \frac{\partial^2}{\partial y_i^2} + \frac{\partial^2}{\partial z_i^2}\right) \qquad \text{E3.3}$$

In equation 3.3, *i* (particle) presents both electrons and nuclei; the symbol m is mass; q_i is a charge of particle *I*; and r_{ij} is the distance between particles. The first term in equation 3.2 is the kinetic energy of the particle within a wave formulation and the second term represents energy owing to the Coulombic attraction or repulsion of particles.

The solution of the Schrödinger equation provides the energy and many other properties of the system by applying several approximations.

3.1.2. Hartree-Fock method

The Hartree-Fock (HF) method is the primary and simplest method that solves the Schrödinger equation for polyelectronic systems based on the central approximations and serves as a basis for molecular orbital theory.[1-2] It includes the Columbic repulsion term to describe electron-electron repulsion.[3] The Hartree-Fock method assumes that electron motion does not depend on the instantaneous motion of other electrons in the vicinity; therefore, each electron senses the presence of another electron implicitly through an effective potential. In HF theory, the movement of electrons' (atomic or molecular wave function) total electronic wave function is depicted by the total electronic wave function known as the Hartree product, stated in the form of the following equation:

$$\Psi_{HP}(r_1, r_2, r_3, \ldots\ldots, r_N) = \varphi_1(r_1)\varphi_2(r_2)\varphi_3(r_3)\ldots\ldots\varphi_N \qquad \text{E3.4}$$

where φ are one-electron orbitals. The equation 3.4 has proved fairly convenient; however, it poses one serious shortcoming, as it is unable to assure the wave function to follow antisymmetric principles for interchange space-spin coordinates. Therefore, the HF product is modified to incorporate the spin orbital instead of the spatial orbital. Spin orbital is the product of spatial orbital and spin function as $\chi(x) = \varphi(r)\alpha$.

$$\Psi_{HP}(r_1, r_2, r_3, \dots\dots, r_N) = \chi_1(r_1)\chi_2(r_2)\chi_3(r_3)\dots\dots\chi_N \qquad \text{E3.5}$$

The modified Spin orbital wave function is presented in equation 3.6.

$$\Psi_{HP}(r_1, r_2, r_3, \dots\dots, r_N) = -\Psi_1(r_1, r_2, r_3 \dots\dots r_N) \qquad \text{E3.6}$$

The HF energy is defined in the form:

$$E^{HF} = E_T + E_v + E_J + E_K \qquad \text{E3.7}$$

In equation 3.7, the term E_T is the electronic kinetic energy; E_V is the electron-nuclear potential energy; E_J is columbic energy; and E_K is the HF exchange energy.

3.1.3. Electron correlation: Møller Plesset methods

The Hartree-Fock method considers exchange and Columb interactions but ignores the electron correlations. Møller Plesset theory improves the HF method by introducing electron correlation effects. Therefore, it reduces the value of calculated energy compared to the true ground state energy. The energy term is modified in the form of equation 3.8 as:

$$E_{MP} = E_{HF} + E_{corr} \quad \text{E3.8}$$

E_{corr} is the electron correlation contribution that included as a perturbation from HF wave function that is first order perturbation in perturbation theory formulation.

Among the non-perturbative methods are configuration interaction, the couple-cluster method and the quadratic configuration interaction.

3.1.4. Quadratic configuration interaction

Configuration interaction (CI) method states the correlation of electrons of ground state Slater determinants with excited state slater determinants.[4-5]

The true wave function does not include the contributions from ground state configurations; therefore, it is articulated as a linear combination of configuration functions for other states, written as:

$$\Psi = \Sigma_i(C_i\Phi_i) \quad \text{E3.9}$$

Theoretical model chemistry CI methods should be well defined, size consistent and exact to provide the unique value of energy; a continuous potential surface and can be applied to a two electron system. However, these CI methods were not size consistent, affording inaccurate results and excluding the triple substitution effect, although CI methods were variational, so computed energies corresponding to wave function is an upper bound to the true energy. To satisfy the remaining requirements of size consistency and accuracy, the Quadratic Configuration Interaction (QCI) method was developed.[4]

The CI equation was treated in a simple way by adding quadratic terms in a general substitution operator that restored the size consistency property by losing its variational character. These substitutions become very useful as they provide a highly accurate estimation for organic molecules with low computational cost. In the case of single and double substitutions, the QCI method adopts the space configuration as single and double substituent (QCISD). It also incorporates a limited account of triple substitution, though QCISD(T) accounts for triple perturbative. The incorporation of a (T) correction in QCISD brings significant improvement in computed energy values that become more considerable for stretch bonds.[6]

3.1.5. Couple cluster method-CCSD(T)

The couple cluster theory based on the exponential configuration of the wave operation and extended into cluster excitation operators. Moreover, it is improved due to inclusion of higher excitation operator. Triple (T) excitation is key factor for covalent and non-covalent interaction with more reliable CCSD(T) method. This method featured by iterative inclusion of single and double excitations coupled with perturbative addition of triple excitation. The CCSD(T) is prominent CC method and promised gold standard for its accuracy for the computational cost ratio.[7-8]

3.1.6. Density functional theory

Ab initio and HF methods are both used to calculate the electronic properties of atoms and molecules based on the electronic wave function. These methods are confined due to the non-measureable electronic wave functions that are based on 3N (N is total number of electrons) spatial and one spin variables.[9] Conversely, density functional theory (DFT) evaluates the properties based on a measurable quantity; i.e., electron density.[10] Electron density can be estimated experimentally using electron diffraction or X-ray diffraction techniques. Hence, DFT computes all electronic properties of atoms and molecule by calculating its electron density. Therefore, DFT becomes one of the most commonly used computational methodology today that calculates accurate results as advanced ab initio methods such as the MP method, but with much reduced computational time that relies on three spatial coordinates (x,y,z). The theoretical background of DFT depends on a number of theorems as discussed below:

3.1.6.1. The Thomas-Fermi model

The Thomas-Fermi (TF) model, was the first theoretical approach using electron density to calculate atomic and molecular properties in 1927[11] and became the precursor to modern DFT. The Thomas-Fermi model first postulates the idea of homogeneous electron gas (HEG); a function of electron density alone. Electron density expressed a total number of electrons per unit volume. Thomas-Fermi introduced the first TF kinetic energy functional equation articulated as a function of local electron density that is considered as a good first approximation of everything.

$$T_{HF}[\rho] = C_F \int e^{\frac{5}{8}}(r) d^3r \qquad \text{E3.10}$$

In equation 3.10 ρ is a 3-dimensional electron density, C_F is the total energy of HEG, and is equal to the value of $3/10(3\pi^2)^{2/3}$. The TF model is very good at describing atomic properties; however, it works poorly for complex systems or the system incorporating chemical interactions due to its inadequacy to include certain orbital configurations of electrons.

3.1.6.2. The Hohenberg-Kohn theorems

In the 1920s, Fermi and Dirac attempted to model the atoms as a system of positively charged bodies found in a uniform electron-gas. Current DFT relies mainly on Kohn-Sham theorem.[12] Hohenberg and Kohn proposed the preliminary theorems to Kohn-Sham theorem.[13] The first Hohenberg theorem proposed in 1964 states that the electron density in the ground state is estimated by the electron wave-function and obtains molecular electronic properties at ground level. Kohn theory further adds the information describing that electron

distribution energy is a function of electron density. The first Kohn theorem includes the same ground state density for two different systems that were not possible in reality. To fulfil this drawback, Hohenberg-Kohn proposed a second theorem, suggesting a ground state electron density that minimises the total energy as a function of electron density, also corresponding to the solution of Schrödinger's equation. Thus, the Hohenberg-Kohn energy is presented as:

$$E[\rho] = T[\rho] + V_{ee}[\rho] + V_{ext}[\rho] \qquad \text{E3.11}$$

Where $T[\rho]$ is the kinetic energy function; V_{ee} is the electron-electron energy repulsion function, written as:

$$V_{ee}[\rho] = \frac{1}{2}\iint \frac{(\rho(\vec{r}_1)\rho(\vec{r}_2)}{r_{12}} d\vec{r}_1 d\vec{r}_2 + E_{ncl}(\rho) \qquad \text{E3.12}$$

And V_{ext} represents the external potential energy operating on the N-electron density, presented as:

$$V_{ext}[\rho] = \int \rho(\vec{r}) v_{ext}(\vec{r}) d\vec{r} \qquad \text{E3.13}$$

E_{ncl} entails the effects of self-interaction corrections, Coulomb and exchange correlations and depicts the counterpart of electron-electron interactions.

3.1.6.3. Kohn-sham DFT

Density functional theory computational methods are employed in the fields of chemistry, physics and material sciences to calculate atomic and molecular electronic structures.[14] Current DFT methods use the Kohn-sham (KS) equation to depict all electronic properties.[12] The KS methods explain many particle interacting systems in the form of non-interacting particle systems[15] that utilise the electron density of the interacting systems to show the effective potential of non-interacting particle systems called the density functional. Thus, the KS equation computes the energy of molecules in terms of the energy (becomes the ideal energy) of fictitious non-interacting systems (set as a reference system). The ideal energy is usually obtained in the form of an exact value. The deviation of energy (actual from the ideal system) is taken in the form of an unknown functional. Therefore, the total energy in DFT is represented as the sum of (i) electronic kinetic energy (E^T); (ii) the potential energy (E^V) of electron-nuclear repulsion and interaction; (iii) energy of the electron-electron repulsion in addition to the electron density coulomb self-interaction (E^J); and (iv) exchange-correlation energy (E^{XC}).

$$E = E^T + E^V + E^J + E^{XC} \qquad \text{E3.14}$$

E^{XC} term in the above equation includes the deviation correction factors of kinetic and potential energies from their ideal corresponding values in the non-interacting systems. All energy terms in equation 3.14 are the functions of electron density, except the one that is nuclear-nuclear repulsion. E^J and E^{XC} functionals are presented as:

$$E^J(\rho) = {}^1/_2 \iint \frac{(\rho(r_1)\rho(r_2)}{\overrightarrow{r_{12}}} dr_1 dr_2 \qquad \text{E3.15}$$

$$E^{XC}(\rho) = \int \varepsilon_{XC}^{KS}(r)\rho(r)\mathrm{d}r \qquad \text{E3.16}$$

The KS differential equation takes the form of:

$$\left(-\frac{1}{2}\nabla^2 + v_{ext}(r) + v_H(r) + v_{xc}(r)\right)\phi_i(r) = \epsilon_i\phi_i(r) \qquad \text{E3.17}$$

In the above equation, r depict the position of ϕ_i; ϵ_i is the orbital energy of the corresponding KS orbital, ϕ_i; and v_{XC} is the exchange-correlation potential, articulated as:

$$v_{XC}(r) = \frac{\delta E^{XC}[\rho(r)]}{\delta[\rho(r)]} \qquad \text{E3.18}$$

3.1.6.4. The exchange-correlation functional

The correlation energy functional is known for the KS DFT depending on the function ρ(r). The exact exchange-correlation functional is not known in DFT and, therefore, it is difficult to obtain good values for the exchange function. Therefore, a number of approximations were introduced since the development of DFT in order to obtain their accurate values. Initially, E^{XC} was computed as a function of electron spin density ρ and its gradient $\nabla\rho$. Perdew[16] first attempted to obtain the exchange functional approximation by developing a method called "Jacob's ladder". The functionals are arranged on the rungs of a ladder based on their level of complexity, leaving HF approximation at the bottom and exact exchange functional correlation at the top within the framework of local density approximation (LDA)[17]. The LDA method is applied to the homogeneous electron gas where ρ(r) changes very slowly with respect to r. The LDA approach provides larger values of cohesive and dissociation energies in comparison to experiments[18-20] owing to the fact that electron density

in the gas phase varies considerably with respect to position. Thus, LDA is considered as a non-feasible option for rapidly changing density systems.

To overcome this shortcoming, generalised gradient approximations (GGAs) known as "semi-local" functionals have been proposed that deploy electron density along with its gradient. GGA method proved to be more accurate than LDAs in computing various properties of solids and molecules such as geometries and ground state energies.[21] These approximations are suitable for the system accompanied by weak covalent bonds. The Becke-88 exchange functional (B88)[22], the Lee-Yang-Parr (LYP),[23] and Perdew-Wang exchange functional (PW91)[24] are the most employed GGA functionals. One of the most employed GGA functional is meta-GGA ,[25-26] which lies in the rung above GGAs on the Jacob's ladder and utilises kinetic-energy density as an additional functional ingredient. Meta GGA functionals are orbital dependent. Most famous GGA functionals includes meta-GGA functionals TPSSLYP1W[27], M06-L,[28] M11-L[29], etc. M05 and M06-2X,[28] functionals are applied essentially for the electronic excitation energies and noncovalent interactions as well as thermochemistry and reaction kinetics. The M05 and M06 series functionals are entirely reported for "medium-range" electron correlation since these series are parametrised for the dispersion interactions of various systems.[30]

3.1.7. One-Electron basissets

The linear arrangements of atomic orbitals (AOs) , linear combination of one electron function, produce molecular orbitals (MO).[31]

3.1.7.1. Pople basis sets

People and co-workers developed the Pople basis sets or a split-valence basis set which is an extended basis sets and splits the MO into core and valence shell orbitals.[32] Core and valence shell orbitals are described by three or more Gaussian primitives and two or more primitives, respectively. The basis set functions are defined as L-M1M2M3G notations and L represents the primitive's numbers of core basis function, and M depicts the each valence shell number orbital basis functions. To elaborate the discussion, for example, the 6-311G basis set for carbon uses six primitives to elucidate the core 1s orbital and three basis functions to explain each of the 2s and 2p orbitals that accumulate a total of 13 basis functions. The three valance shell basis function consists of one 3 primitives and other 2 has 1 primitives only. For the accurate distribution of the above basis function, polarisation (*d*, *p* or *f* orbitals) and diffuse function may be included in the basis set. The addition of the polarisation function represented as * and diffuse function denoted by + can be used for the polarisation of AO charge distribution and to improve the status of the loosely attached electrons in *s* and *p* orbitals, respectively.[10, 24, 33]

3.1.7.2. Correlation consistent basis sets

Dunning developed the correlation-consistent basis sets to extract the maximum electron correlation energy for each atom.[34-36] The correlation-consistent basis sets is abbreviated as "cc-pVNZ", which is shorthand for correlation (cc) polarised split-valence (pV) N-zeta (NZ), where N shows the degree to which the valence space is split. For carbon, the cc-pVDZ basis sets relate to DZ in the valence region and contain a single set of d function. For cc-pVTZ

basis set is TZ in the valence region and contain two sets of the *d* functions and single set of *f* function.

3.1.8. Quantum chemical methods for studying reaction pathways

3.1.8.1. The Born-Oppenheimer approximation

The Born-Oppenheimer Approximation[37] method is used to simplify the Schrödinger equation for a molecule with the assumption of non-existence of the nuclear velocity. The time independent Schrödinger equation based on the Born-Oppenheimer Approximation is as below;

$$\left[-\frac{1}{2}\sum_{i=1}^{N}\nabla_i^2 - \sum_{i=1}^{N}V(\boldsymbol{r}_i) + \sum_{i=1}^{N}\sum_{j<1}U(\boldsymbol{r}_i,\boldsymbol{r}_j)\right]\Psi = E\Psi \qquad \text{E3.19}$$

The first, second and the third terms are kinetic energy of electrons, attraction of electrons to nuclei and the repulsion between electrons, respectively. The Born-Oppenheimer approximation describes the change in the electronic energy of molecules with molecular nuclear geometry and developed potential energy surface. Thermodynamic properties of the reactants, products and transition states offer measurement of the thermodynamics and chemical kinetics based on the transition state theory (TST). TST is basically determined the way of chemical reaction take place via the accurate properties of the PES such as harmonic vibrational frequencies, rotational constants and energies.[38-39]. The determination of minima

on PES is more reliable using gradient based methods as compared to the energy only methods and first derivative methods.[40]

The intrinsic reaction coordinate (IRC) provides useful information along the path of PES connecting the reactants, transition states and products. Not only it determines the barrier height but also gives necessary information for the thermodynamic characteristics.[41]

3.1.9. Applied methods

M05 and M05-2X functionals relate to the fourth rung of Jacob's ladder. They include electron spin density, kinetic energy density, density gradient (semi local) and HF exchange (nonlocal) and are known as hybrid meta-GGAs.[30] The energetics computed from the M05 functionals are dependent on the chosen quadrature grid and considered in, for example, Wheeler and Houk,[42] who performed a detailed sensitivity analysis for M05-2X functional to increase the factor of the kinetic energy density. Specifically, M05-2X is a hybrid meta-exchange correlation functional that is generally is suitable for the thermo-kinetic parameters for general applications in organic chemistry. Meta-hybrid methods afford, in general, relatively accurate structures and energies for open and closed shell species alike, in reference to the more computationally expensive chemistry models such as CBS-QB3 and Gn methods. Energies acquired at the M05-2X functional provide minimum grid error due to the convergence of the functional regarding the integration grid.[42-43] For the noncovalent interactions, Hohenstein et al. [44] have demonstrated that M05−2X offer substantial enhancement over conventional density functionals and justified via the JSCH-2005 test set. Moreover, researchers describe the model functional M05-2X/6-31+G(d,p) as an accurate (the highest correlation (R = 0.9958)) optimising and computational method presented when

compared with the experimental findings. This result indicated that M05-2X is suitable for studies based on the estimation of neutral structure phenolic chemical species.[45] Herein, we deployed M05-2X method to investigate the reduction of N_2O using catechol and decomposition of ammonium nitrate molecules in the gas phase and under an aqueous medium.

Advancement in quantum mechanical configuration and structural theory introduced an updated version of methodologies pertinent to molecular energies calculations. These methods include G2,[46] G2(MP2),[47] BAC-MP4,[48] PCI-X[49] and the complete basis set (CBS).[50] For small and low sized molecules, the accuracy associated with these methods generally lies within 1-2 kcal mol^{-1} from analogous experimental measurements.

The complete basis set models include the chemistry models of CBS-4, CBS-q, CBS-Q, CBS-APNO, and CBS-QB3. The mean absolute deviation (MAD) of CBS-4, CBS-q, and CBS-Q is 2.0, 1.7 and 1.0 kcal mol^{-1}, respectively. CBS-APNO displays a much better accuracy of electronic energies calculation with 0.5 kcal mol^{-1} of MAD;[51-55] however, CBS-QB3 provides improved results as compared to CBS-Q due to consistency in geometry optimisation and frequency calculations.[56]

CBS-QB3 utilises low level of self-consistency field (SCF) and zero point energy estimations that involve small, large and mid-sized basis sets for high-level correlation and second order correlation corrections, respectively. The CCSD(T) level energy extrapolation is included in this approach[51-52, 56-59] that corrects Møller-Polleset second order energies.[28] Overall, the CBS-QB3 method involves the use of the B3LYP method for geometry and frequency calculations with 0.99 ZPE correction factor, and uses the CCSD/6-31+G* and MP4(SDQ)/6-

31+G(d(f),p) single point energy estimation. CBS-QB3 is corrected for the error of truncation of the basis set. The N^{-1} MP2 asymptotic convergence is used to extrapolate energies to the CBS limit.[52-53, 56, 60] the accuracy of the CBS-QB3 from previous literature[60-63], especially for H transfer reactions,[64] set grounds for its use in the theoretical calculations reported in this thesis.

A comprehensive variety of computational methods are available for the modelling of the chemical reactions. As such, it is vital to explore and confirm the suitability of the chosen method for the specific type of reaction systems. This is achieved by running benchmarking calculations on similar reactions, for which experimental data are available that offer reliability of un-probed chemical species thermochemistry and reaction kinetics. Furthermore, the selected computational methodology, such as CBS-QB3 for the hydrogen abstraction/transfer reactions, is confirmed from the recent research conducted. In most parts of the thesis, we deploy CBS-QB3 calculations to investigate H abstraction reactions from low carbon range aliphatic and modelled alkylbenzene using NH_2 and NO_2 radicals.

3.1.10. Solvation method

The theoretical methods explained thus far relate to the estimation of gas phase molecular energies that include isolated and non-interacting molecular species; however, when studying the decomposition of Ammonium nitrate in liquid phase, we must account for the interaction of reactants and the solvent. These calculations are performed using solvation methods[65] and explicitly added water molecules at CBS-QB3 and M05-2X/6-311+G(d,p) level of theories. Solvation methods resemble self-consistent reaction field (SCRF) and polarisable continuum models (PCM). These models offer an alternative for the generally more expensive

calculations involving explicit water molecules via representing a homogenous continuum of the even dielectric constant. These models execute an iterative process and measure electrostatic solute-solvent interactions for the solute placed inside ta cavity and surrounded by continuum. Numerous models have been developed to illustrate the solvent cavity[66] and measurement of non-electrostatic elements of solvation free energy.[67]

The general accuracy of PCM is within ± 4 kJ mol^{-1} for neutral species while an average of ±2-60 kJ mol^{-1} is computed for larger ionic chemical moieties. Advancements in PCM methods focusing on a short range interaction of the solvent area displays an accuracy of ± 2 kJ mol^{-1} and ± 17 kJ mol^{-1} for neutral and charged species, correspondingly.[67] The underlying research adopted a continuum solvation model density-polarizable continuum model (SMD-PCM) to simulate the effect of bulk water on the enthalpic trends during decomposition of AN in the condensed phase.

3.2. Computational tools

3.2.1. Gaussian09

Guassain09[68] performs optimisation of molecular structures and computations of energies, vibrational frequencies, and molecular properties through a wide array DFT, chemistry model methods and ab initio methods; Gaussian computational chemistry software is used for both simple and complex systems and applied for the short-lived species appearing in experimental measurements, such as intermediates and transition structures for both gaseous and aqueous phases. The software predicts the kinetics and thermodynamics of chemical reactions by computing the difference in thermodynamic parameters for optimised structures. Gaussian09[68] efficiently locates transition structures (intermediate adduct; state between reactant and product) and verifies their minimum values to investigate the reaction pathways. Guassian09 used intrinsic reaction coordinates (IRC) to link the respective reactants, products and transition geometries.[69] The features of IRC calculations enable one to verify the nature of the located transition structure. Obtained reaction barriers, along with vibrational frequencies for reactants and transition states, are then used to estimate reaction rate parameters through the application of conventional transition state theory or variational transition state theory. [70]

3.2.2. ChemRate

ChemRate[71] program serves to compute reaction rate coefficients and Arrhenius parameters, along with the molecular thermodynamic properties at different temperatures and pressures under steady and non-steady conditions. The software estimates temperature-dependent

thermodynamic properties of both reactions and chemical species. It works by using the database of unimolecular reactions and database of experimental results in relation to transition states and molecular structures.[72] In ChemRate, a master equation solver is designed based on Rice–Ramsperger–Kassel–Marcus theory (RRKM)[73-74] (for unimolecular reactions). It also deployed the transition state theory (TST)[75] along with treatment for hindered rotors and tunnelling to estimate reaction rate parameters for bimolecular reactions and unimolecular reactions (at the high- pressure limit for the latter).

3.2.3. KiSThelP

KiSThelP, a kinetic and statistical thermodynamic package programme, was developed to compute molecular and reaction properties by using electronic structure data[76] extracted from (Gaussian, GAMESS, and NWChem) output files. Kisthelp executes statistical mechanics calculations based on ab initio quantum chemistry data. This data is treated based on the set algorithm and converted into the desired molecular thermodynamic properties, thermal equilibria and reaction rate parameters[77-78]. This is achieved by preparing input files that contain molecular mass, potential energy, electronic degeneracy, rotational symmetry number, vibrational frequencies and inertial moment data. The kinetic parameters of gaseous reactions are obtained via conventional TST, variational transition state theory (VTST)[79] and RRKM theory. One-dimensional tunnelling treatment (Wigner correction or the Eckart potential energy barrier) increased the accuracy of the reaction parameters.[80]

3.3. Experimental methods

3.3.1. Chemicals

We studied the decomposition of NO in the presence of a biomass surrogate (Catechol) compound, a solid white to faintly beige powder, purchased from Sigma Aldrich (Australia) in a purity of purity > 99.0 %. A high purity (99.999 %) helium carrier gas was acquired from BOC Australia. Helium gas serves three purposes: 1) as a carrier gas for the reaction system; 2) in a triple quadruple mass spectrometer (QQQ-MS); and 3) for quantification of N_2. The reaction gas nitrogen oxide, total NO_x 1036 ppm balance with helium, was purchased from core gas with the certified relative uncertainty of 5 %.

3.3.2. Experimental procedure

3.3.2.1. Apparatus

A laboratory scale bench type apparatus was constructed to investigate the gas phase interaction of NO_x and Catechol. The experimental setup divided into one of three main streams: (i) a solid vaporiser; (ii) isothermal horizontal tubular reactor; and (iii) a product collection system for capturing chemical species. Figure 3.2 depicts a schematic diagram of the experimental assembly. Solid fuel (catechol) loaded into vaporiser tube of 10 mm diameter (i.d.) at ambient temperature. The vaporiser tube is fixed in high temperature, forced convection with vertical draught (manufactured by S.E.M Pty Ltd) oven equipped with inlet and outlet gas flow lines and accurate temperature controller (digital PID control). The oven is set at 80ºC to evaporate reactant and a gas stream of helium passed through the

vaporiser tube carrying the catechol vapours and entering into the reactor. The concentration of NO maintained at 600 ppm and catechol loading of 0.1 mole % ± 5 % into the reactor, delivering a fuel-oxygen equivalence ratio of ϕ =1.25.

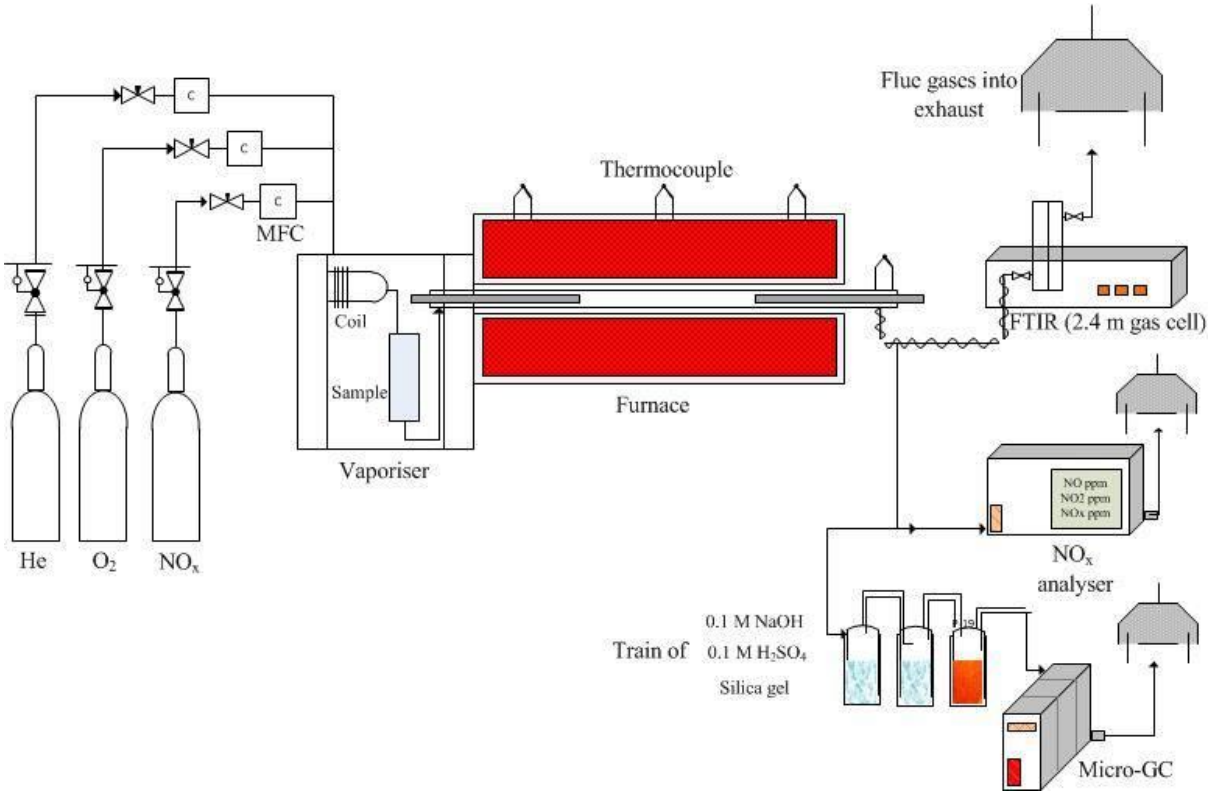

Figure 3.2. Schematic diagram of the experimental setup.

The reaction unit included a superior purity (>99.995 %) quartz reactor (H. Baumbach & Co Ltd, USA) with dimensions of 12.7 mm O.D., 10 mm I.D., and 960 mm length, 235 mm^3 volume. The reactor tube is placed along the center line of a 3-zone horizontal furnace (Labec HTFS40/300-3). The furnace is fitted with accurate temperature controllers (UDAIN 708, the accuracy of 0.2 %, Australia) for each zone independently. Furnace calibration is performed to verify the region of the isothermal zone (specifically the central region) by using an external thermocouple positioned and moved horizontally along the center line; it found accuracy within ± 5 ^oC along the distance of 12 cm to 40 cm, as shown in figure 3.3.

To keep the inlet flow of gases and residence time (2 s) constant and to run the experiments at different operating temperatures, we placed two high-purity, hollow at one end, closed rods (9.5 mm O.D.) on opposite sides of the reactor tube. The one end of the reactor is connected with the feed preparation section (vaporiser) and a second end is attached to the product collection system.

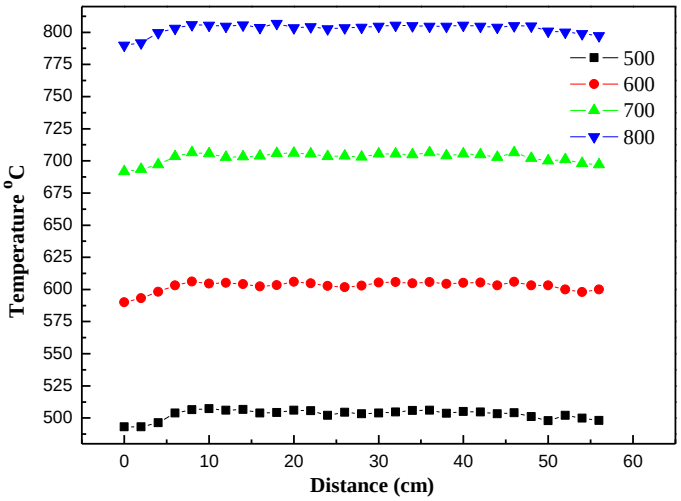

Figure 3.3. Temperature profile of horizontal tubular furnace.

3.3.3. Experimental procedure

The gas phase analysis consists of ***in-situ*** experiments measurements.

3.3.3.1. Gas-phase analysis

The exit line of the reactor is designed to capture nitrogen (N_2), nitric oxide (NO), nitrogen dioxide (NO_2), ammonia (NH_3), small hydrocarbons, hydrogen cyanide (HCN), carbon

monoxide (CO) and carbon dioxide (CO_2). We performed two runs for each experimental condition due to different product analysis techniques. In the first run, the gaseous products from the exit of the reactor tube directed to a Perkin Elmer Fourier transform infrared spectroscopy (FTIR) via heater (140^oC) transfer line for the online analysis. In the second run, the outlet of the reactor is connected simultaneously to the NO_x analyser and micro gas chromatogram (GC). The outer stream of product gases distribute into two parts. The first part enters into the Thermo Scientific model 42i-HL NO_x analyser to determine the concentrations of nitrogenous oxygenated compounds like NO and NO_2. A second fraction of gases after passing through successive trays of 1M NaOH, 0.1M H_2SO_4 and bed of silica gel to remove acidic, basic and moisture content of product gases, correspondingly, and then pass through Agilent 490 micro-gas chromatography (μ-GC) for the measurement of molecular N_2. Prior to each experiment, the reactor tube is cleaned with solvent and purged with a stream of nitrogen, first followed by helium gas in order to remove all contaminants from the preceding runs.

3.3.3.2. Fourier transform infrared spectroscopy

A Fourier transform infrared (FTIR) spectroscopy (Perkin Elmer) facilitated the in-situ analysis of reactants and products pertinent to experimental work. The experimental rig is facilitated with a heated Teflon transfer line (at 140 ^oC) downstream of the reactor that prevents condensation of volatile products and further directs to the gas cell of the FTIR instrument. The identification of different species is ensured through the gas cells with path-length at 2.4 m (online analysis, volume at 100.0 ml). The Linear response between the species concentration and absorption value (usually < 0.7) will ensure the better quantitation of the identified chemical species. The spectrometer averaged 32 accumulated scans per

spectrum at 1 cm^{-1} resolution. The gas cell of FTIR compartment was flushed with high purity of helium three times prior to obtaining a background spectrum. The in-situ recording of the spectrum displayed with the background automatically subtracted from the sample spectrum. The desired product gases were quantified using QASoft program based on a standard spectrum available from the QASoft library.

3.3.3.3. Micro Gas chromatography

Agilent 490 micro-gas quad chromatography, 20 m MolSieve-5A column, heated injection assisted N_2 quantitation using thermal conductivity detector. Helium gas is used as a mobile phase for the instrument. Calibration and analysis of the N_2 are conducted at the injector and column temperatures of 70 ^oC with injection and run times of 40 ms and 300 s, respectively.

3.3.3.4. Chemiluminescence NO_x analysis

Chemiluminescence NO_x analysis provides the in-situ quantification of the NO and NO_2 to probe the reduction of the NO_x, majorly NO, from biomass fragments. NO_x chemiluminescence principle operation is based on the specific luminescence that results from the decay of excited NO_2 to lower energy states. The air sample is routed to ozonator via solenoid valves to get the necessary ozone for the chemiluminescence reaction. The ozone reacts with the NO from the product gases and generates NO_2 that was subsequently converted into NO by molybdenum convertor operated at 350 ^oC, or at 625 ^oC in a stainless steel chamber. Automatic mode operation of the NO_x analyser allows a minimum average time of 10 s.

3.3.3.5. Gas chromatography mass spectrometry

We use advanced Shimadzu GC-QQQMS instrument for the identification and quantification of catechol. This instrument consist of a gas chromatograph (GC) unit for the separation of components (GC-2010 plus) and a triple quadrupole mass analyser (QQQMS) for quantitation of components masses (QQQMS-TQ8040 series, Shimadzu Japan). In GC unit, a temperature-controlled capillary column separates the products into its individual components. The volatile components travel faster and elute (retention time) before as compared to the components with high boiling points and enter into MS through a transfer line.

In GC-QQQMS, a constant flow rate of helium (a carrier gas) was maintained at 1.5 ml min^{-1}. The GC oven temperature programmed at 30 °C for initial 3 min, and then the temperature was raised to 100 °C at the rate of 4 °C min^{-1}. Finally staying for 2 min at 100 °C, it was increased at 6 °C min^{-1} to final temperature of 250 °C. The temperature of injectors and ion sources was kept at 250 °C and 200 °C, respectively. The ionisation electron impact voltages were set at 70 eV. The eluted catechol specie is identified by comparing its mass spectra with information from the NIST library. Later, we validated the identified specie by the injection of genuine standards. Analysis mode used is Q3scan with ions transmission mode.

3.4. References

1. Lewars, E. G., *Computational Chemistry: Introduction to the Theory and Applications of Molecular and Quantum Mechanics*; Springer: New York, 2016.

2. Ramachandran, K.; Deepa, G.; Namboori, K., *Computational Chemistry and Molecular Modeling: Principles and Applications*; Springer-Verlag: Heidelberg, 2008.

3. Hartree, D. R. In *The Wave Mechanics of an Atom with a Non-Coulomb Central Field. Part I. Theory and Methods*, MPCPS, Cambridge University Press: 1928; pp 89-110.

4. Čížek, J., On the Correlation Problem in Atomic and Molecular Systems. Calculation of Wavefunction Components in Ursell-Type Expansion Using Quantum-Field Theoretical Methods. *J. Chem. Phys.* **1966**, *45*, 4256-4266.

5. Levine, I. N., *Quantum Chemistry 5th Ed*; Prentice-Hall Inc: Brooklyn, New Jersey, 1991.

6. Pople, J. A.; Head-Gordon, M.; Raghavachari, K., Quadratic Configuration Interaction. A General Technique for Determining Electron Correlation Energies. *J. Chem. Phys.* **1987**, *87*, 5968-5975.

7. Bartlett, R. J.; Musiał, M., Coupled-Cluster Theory in Quantum Chemistry. *RvMP* **2007**, *79*, 291-352.

8. Řezáč, J.; Šimová, L.; Hobza, P., CCSD[T] Describes Noncovalent Interactions Better Than the CCSD(T), CCSD(TQ), and CCSDT Methods. *J. Chem. Theory Comput.* **2013**, *9*, 364-369.

9. Sholl, D.; Steckel, J. A., *Density Functional Theory: A Practical Introduction*; John Wiley & Sons: Hoboken, New Jersey, 2011.

10. Becke, A. D., Density Functional Calculations of Molecular Bond Energies. *J. Chem. Phys.* **1986**, *84*, 4524-4529.

11. Koch, W.; Holthausen, M. C., *A Chemist's Guide to Density Functional Theory*; John Wiley & Sons: Weinheim, Germany, 2015.

12. Kohn, W.; Sham, L. J., Self-Consistent Equations Including Exchange and Correlation Effects. *Phys. Rev.* **1965**, *140*, A1133.

13. Hohenberg, P.; Kohn, W., Inhomogeneous Electron Gas. *Phys. Rev.* **1964**, *136*, B864.

14. Capelle, K., A Bird's-Eye View of Density-Functional Theory. *Braz. J. Phys.* **2006**, *36*, 1318-1343.

15. Van Leeuwen, R. Kohn-Sham Potentials in Density Functional Theory. Vrije Universiteit Amsterdam, The Netherlands, 1994.

16. Perdew, J. P.; Schmidt, K., Jacob's Ladder of Density Functional Approximations for the Exchange-Correlation Energy. *AIP Conf. Proc.* **2001**, *577*, 1-20 DOI: 10.1063/1.1390175.

17. Andriotis, A. N., Lda Exchange-Energy Functional. *Phys. Rev. B* **1998**, *58*, 15300.

18. Staroverov, V. N.; Scuseria, G. E.; Tao, J.; Perdew, J. P., Tests of a Ladder of Density Functionals for Bulk Solids and Surfaces. *Phys. Rev. B* **2004**, *69*, 075102.

19. Csonka, G. I.; Perdew, J. P.; Ruzsinszky, A.; Philipsen, P. H.; Lebègue, S.; Paier, J.; Vydrov, O. A.; Ángyán, J. G., Assessing the Performance of Recent Density Functionals for Bulk Solids. *Phys. Rev. B* **2009**, *79*, 155107.

20. Harl, J.; Schimka, L.; Kresse, G., Assessing the Quality of the Random Phase Approximation for Lattice Constants and Atomization Energies of Solids. *Phys. Rev. B* **2010**, *81*, 115126.

21. Gupta, V., *Principles and Applications of Quantum Chemistry*; Academic Press, 2015.

22. Becke, A. D., Density-Functional Exchange-Energy Approximation with Correct Asymptotic Behavior. *Phys. Rev. A* **1988**, *38*, 3098.

23. Lee, C.; Yang, W.; Parr, R. G., Development of the Colle-Salvetti Correlation-Energy Formula into a Functional of the Electron Density. *Phys. Rev. B* **1988**, *37*, 785.

24. Perdew, J. P.; Burke, K.; Ernzerhof, M., Generalized Gradient Approximation Made Simple. *Phys. Rev. Lett.* **1996**, *77*, 3865.

25. Ul-Haq, Z.; Madura, J. D., *Frontiers in Computational Chemistry: Volume 2: Computer Applications for Drug Design and Biomolecular Systems*; Elsevier, 2015.

26. Kohanoff, J., *Electronic Structure Calculations for Solids and Molecules: Theory and Computational Methods*; Cambridge University Press: London, 2006.

27. Tao, J.; Perdew, J. P.; Staroverov, V. N.; Scuseria, G. E., Climbing the Density Functional Ladder: Nonempirical Meta–Generalized Gradient Approximation Designed for Molecules and Solids. *Phys. Rev. Lett.* **2003**, *91*, 146401.

28. Zhao, Y.; Truhlar, D. G., The M06 Suite of Density Functionals for Main Group Thermochemistry, Thermochemical Kinetics, Noncovalent Interactions, Excited States, and Transition Elements: Two New Functionals and Systematic Testing of Four M06-Class Functionals and 12 Other Functionals. *Theo.r Chem. Acc.* **2008**, *120*, 215-241.

29. Peverati, R.; Truhlar, D. G., M11-L: A Local Density Functional That Provides Improved Accuracy for Electronic Structure Calculations in Chemistry and Physics. *J. Phys. Chem. Lett.* **2011**, *3*, 117-124.

30. Zhao, Y.; Schultz, N. E.; Truhlar, D. G., Design of Density Functionals by Combining the Method of Constraint Satisfaction with Parametrization for Thermochemistry, Thermochemical Kinetics, and Noncovalent Interactions. *J. Chem. Theory Comput.* **2006**, *2*, 364-382.

31. Lu, Q.; Peterson, K. A., Correlation Consistent Basis Sets for Lanthanides: The Atoms La–Lu. *J. Chem. Phys.* **2016**, *145*, 054111.

32. Hehre, W. J., Ab Initio Molecular Orbital Theory. *Acc. Chem. Res.* **1976**, *9*, 399-406.

33. Cramer, C. J., *Essentials of Computational Chemistry: Theories and Models*; Wiley, 2013.

34. Kendall, R. A.; Jr., T. H. D.; Harrison, R. J., Electron Affinities of the First-Row Atoms Revisited. Systematic Basis Sets and Wave Functions. *J. Chem. Phys.* **1992**, *96*, 6796-6806.

35. Jr., T. H. D., Gaussian Basis Sets for Use in Correlated Molecular Calculations. I. The Atoms Boron through Neon and Hydrogen. *J. Chem. Phys.* **1989**, *90*, 1007-1023.

36. Woon, D. E.; Jr., T. H. D., Gaussian Basis Sets for Use in Correlated Molecular Calculations. III. The Atoms Aluminum through Argon. *J. Chem. Phys.* **1993**, *98*, 1358-1371.

37. Born, M.; Oppenheimer, R., Zur Quantentheorie Der Molekeln. *ANP* **1927**, *389*, 457-484.

38. Kassel, L. S., Studies in Homogeneous Gas Reactions. I. *The Journal of Physical Chemistry* **1927**, *32*, 225-242.

39. Rice, O. K.; Ramsperger, H. C., Theories of Unimolecular Gas Reactions at Low Pressures. *J. Am. Chem. Soc.* **1927**, *49*, 1617-1629.

40. Hratchian, H. P.; Schlegel, H. B., Chapter 10 - Finding Minima, Transition States, and Following Reaction Pathways on Ab Initio Potential Energy Surfaces A2 - Dykstra, Clifford E. In *Theory and Applications of Computational Chemistry*, Frenking, G.; Kim, K. S.; Scuseria, G. E., Eds. Elsevier: Amsterdam, 2005; pp 195-249.

41. Heidrich, D., *The Reaction Path in Chemistry: Current Approaches and Perspectives*; Springer Netherlands, 2013.

42. Wheeler, S. E.; Houk, K. N., Integration Grid Errors for Meta-Gga-Predicted Reaction Energies: Origin of Grid Errors for the M06 Suite of Functionals. *J. Chem. Theory Comput.* **2010**, *6*, 395-404.

43. Altarawneh, M.; Dlugogorski, B. Z., A Mechanistic and Kinetic Study on the Formation of Pbdd/Fs from Pbdes. *Environ. Sci. Technol.* **2013**, *47*, 5118-5127.

44. Hohenstein, E. G.; Chill, S. T.; Sherrill, C. D., Assessment of the Performance of the M05− 2x and M06− 2x Exchange-Correlation Functionals for Noncovalent Interactions in Biomolecules. *J. Chem. Theory Comput.* **2008**, *4*, 1996-2000.

45. Zhao, Y.; Truhlar, D. G., A Density Functional That Accounts for Medium-Range Correlation Energies in Organic Chemistry. *Org. Lett.* **2006**, *8*, 5753-5755.

46. Curtiss, L. A.; Raghavachari, K.; Trucks, G. W.; Pople, J. A., Gaussian-2 Theory for Molecular Energies of First-and Second-Row Compounds. *J. Chem. Phys.* **1991**, *94*, 7221-7230.

47. Curtiss, L. A.; Raghavachari, K.; Pople, J. A., Gaussian-2 Theory Using Reduced Mo/Ller–Plesset Orders. *J. Phys. Chem.* **1993**, *98*, 1293-1298.

48. Ho, P.; Melius, C. F., Theoretical Study of the Thermochemistry of Fluorosilanes (Sifn and Sihnfm) Compounds and Hexafluorodisilane. *J. Phys. Chem.* **1990**, *94*, 5120-5127.

49. Siegbahn, P. E.; Blomberg, M. R.; Svensson, M., Pci-X, a Parametrized Correlation Method Containing a Single Adjustable Parameter X. *Chem. Phys. Lett.* **1994**, *223*, 35-45.

50. Montgomery Jr, J.; Ochterski, J.; Petersson, G., A Complete Basis Set Model Chemistry. Iv. An Improved Atomic Pair Natural Orbital Method. *J. Chem. Phys.* **1994**, *101*, 5900-5909.

51. Ochterski, J. W.; Petersson, G. A.; Montgomery Jr, J. A., A Complete Basis Set Model Chemistry. V. Extensions to Six or More Heavy Atoms. *J. Chem. Phys.* **1996**, *104*, 2598-2619.

52. Nyden, M. R.; Petersson, G., Complete Basis Set Correlation Energies. I. The Asymptotic Convergence of Pair Natural Orbital Expansions. *J. Chem. Phys.* **1981**, *75*, 1843-1862.

53. Petersson, G.; Al-Laham, M. A., A Complete Basis Set Model Chemistry. Ii. Open-Shell Systems and the Total Energies of the First-Row Atoms. *J. Chem. Phys.* **1991**, *94*, 6081-6090.

54. Petersson, G.; Yee, A. K.; Bennett, A., Complete Basis Set Correlation Energies. Iii. The Total Correlation Energy of the Neon Atom. *J. Chem. Phys.* **1985**, *83*, 5105-5128.

55. Montgomery Jr, J.; Frisch, M.; Ochterski, J.; Petersson, G.; Raghavachari, K.; Zakrzewski, V., Comment on "Assessment of Complete Basis Set Methods for Calculation of Enthalpies of Formation"[J. Chem. Phys. 108, 692 (1998)]. *J. Chem. Phys.* **1998**, *109*, 6505-6506.

56. Montgomery Jr, J. A.; Frisch, M. J.; Ochterski, J. W.; Petersson, G. A., A Complete Basis Set Model Chemistry. Vi. Use of Density Functional Geometries and Frequencies. *J. Chem. Phys.* **1999**, *110*, 2822-2827.

57. Casasnovas, R.; Frau, J.; Ortega-Castro, J.; Salvà, A.; Donoso, J.; Muñoz, F., Simplification of the Cbs-Qb3 Method for Predicting Gas-Phase Deprotonation Free Energies. *Int. J. Quantum Chem.* **2010**, *110*, 323-330.

58. Bartlett, R. J.; Watts, J.; Kucharski, S.; Noga, J., Non-Iterative Fifth-Order Triple and Quadruple Excitation Energy Corrections in Correlated Methods. *Chem. Phys. Lett.* **1990**, *165*, 513-522.

59. Stanton, J. F., Why Ccsd (T) Works: A Different Perspective. *Chem. Phys. Lett.* **1997**, *281*, 130-134.

60. Montgomery Jr, J. A.; Frisch, M. J.; Ochterski, J. W.; Petersson, G. A., A Complete Basis Set Model Chemistry. Vii. Use of the Minimum Population Localization Method. *J. Chem. Phys.* **2000**, *112*, 6532-6542.

61. Ess, D. H. Quantum Mechanical Theory of Reactivity and Selectivity in Organic and Organometallic Reactions. Ph.D. Dissertation, University of California, Los Angeles, 2007.

62. Stanton, J. F., On the Extent of Spin Contamination in Open-Shell Coupled-Cluster Wave Functions. *J. Chem. Phys.* **1994**, *101*, 371-374.

63. Shiroudi, A.; Deleuze, M. S., Theoretical Study of the Oxidation Mechanisms of Thiophene Initiated by Hydroxyl Radicals. *J. Mol. Model.* **2015**, *21*, 301.

64. Vandeputte, A. G.; Sabbe, M. K.; Reyniers, M.-F.; Van Speybroeck, V.; Waroquier, M.; Marin, G. B., Theoretical Study of the Thermodynamics and Kinetics of Hydrogen Abstractions from Hydrocarbons. *J. Phys. Chem. A.* **2007**, *111*, 11771-11786.

65. Liptak, M. D.; Shields, G. C., Experimentation with Different Thermodynamic Cycles Used for Pka Calculations on Carboxylic Acids Using Complete Basis Set and Gaussian-N Models Combined with Cpcm Continuum Solvation Methods. *Int. J. Quantum Chem.* **2001**, *85*, 727-741.

66. Tomasi, J.; Mennucci, B.; Cancès, E., The Ief Version of the PCM Solvation Method: An Overview of a New Method Addressed to Study Molecular Solutes at the QM Ab Initio Level. *J. Mol. Struc. Theochem* **1999**, *464*, 211-226.

67. Marenich, A. V.; Cramer, C. J.; Truhlar, D. G., Universal Solvation Model Based on Solute Electron Density and on a Continuum Model of the Solvent Defined by the Bulk Dielectric Constant and Atomic Surface Tensions. *J. Phys. Chem. B.* **2009**, *113*, 6378-6396.

68. M. J. Frisch, G. W. T., H. B. Schlegel, G. E. Scuseria, M. A. Robb, J. R. Cheeseman, G. Scalmani, V. Barone, B. Mennucci, G. A. Petersson, et al. , Gaussian 09, Revision A.1., Gaussian, Inc.:. Wallingford, CT, 2009.

69. Fukui, K., The Path of Chemical Reactions-the Irc Approach. *Acc. Chem. Res.* **1981**, *14*, 363-368.

70. Truhlar, D., *In the Reaction Path in Chemistry: Current Approaches and Perspectives; Heidrich*; Kluwer: Dordrecht, The Netherlands, 1995.

71. Mokrushin, V.; Bedanov, V.; Tsang, W.; Zachariah, M.; Knyazev, V.; McGivern, W. S. Chemrate, Version 1.5.10. NIST: Gaithersburg, MD, 2011.

72. Di Giacomo, F., A Short Account of Rrkm Theory of Unimolecular Reactions and of Marcus Theory of Electron Transfer in a Historical Perspective. *J. Chem. Educ.* **2014**, *92*, 476-481.

73. Lindemann, F.; Arrhenius, S.; Langmuir, I.; Dhar, N.; Perrin, J.; Lewis, W. M., Discussion on "the Radiation Theory of Chemical Action". *J. Chem. Soc. Faraday* **1922**, *17*, 598-606.

74. Laidler, K. J.; King, M. C., Development of Transition-State Theory. *J. Phys. Chem.* **1983**, *87*, 2657-2664.

75. Canneaux, S.; Bohr, F.; Henon, E., Kisthelp: A Program to Predict Thermodynamic Properties and Rate Constants from Quantum Chemistry Results. *J. Comput. Chem.* **2014**, *35*, 82-93.

76. Fernández-Ramos, A.; Ellingson, B. A.; Meana-Pañeda, R.; Marques, J. M.; Truhlar, D. G., Symmetry Numbers and Chemical Reaction Rates. *Theor. Chem. Acc.* **2007**, *118*, 813-826.

77. Truhlar, D. G.; Garrett, B. C.; Klippenstein, S. J., Current Status of Transition-State Theory. *J. Phys. Chem.* **1996**, *100*, 12771-12800.

78. Eckart, C., The Penetration of a Potential Barrier by Electrons. *Phys. Rev.* **1930**, *35*, 1303.

79. Truhlar, D. G.; Garrett, B. C.; Klippenstein, S. J., Current Status of Transition-State Theory. *J. Phys. Chem.* **1996**, *100*, 12771-12800.

80. Johnston, H. S.; Heicklen, J., Tunnelling Corrections for Unsymmetrical Eckart Potential Energy Barriers. *J. Phys. Chem.* **1962**, *66*, 532-533.

Chapter 4

Hydrogen Abstraction from Hydrocarbons by NH_2

Siddique, K.; Altarawneh, M.; Gore, J.; Westmoreland, P. R.; Dlugogorski, B. Z., Hydrogen Abstraction from Hydrocarbons by NH_2. *The Journal of Physical Chemistry A* **2017**, *121*, 2221-2231. **DOI:**10.1021/acs.jpca.6b12890

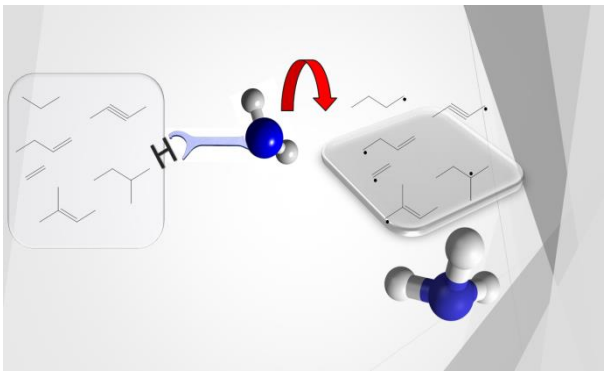

This chapter develops the comprehensive data of H abstraction reactions from wide range hydrocarbons by NH_2 radical. Further, this contribution compares the computed reaction kinetic with the analogous experimental data in gas phase medium and set out the accuracy for the first ever reported kinetics of the R-H + NH_2 systems.

4.1. Abstract

This chapter investigates thermokinetic parameters of bimolecular gas-phase reactions involving the amidogen (NH_2) radical and a large number of saturated and unsaturated hydrocarbons. These reactions play an important role in combustion and pyrolysis of nitrogen-rich fuels, most notably biomass. Computations performed at the CBS-QB3 level and based on the conventional TST yield potential-energy surfaces and reaction rate constants, accounting for tunnelling effects and the presence of hindered rotors. In an analogy to other H abstraction systems, we demonstrate only a small influence of variational effects on the rate constants for selected reaction. The studied reactions cover the abstraction of hydrogen atoms by the NH_2 radical from the C–H bonds in C_1–C_4 species, and four C_5 hydrocarbons of 2-methylbutane, 2-methyl-1-butene, 3-methyl-1-butene, 3-methyl-2-butene, and 3-methyl-1-butyne. For the abstraction of H from methane, in the temperature window of 300–500 K and 1600–2000 K, the calculated reaction rate constants concur with the available experimental measurements i.e., $k_{calculated}/k_{experimetal}$ = 0.3–2.5 and 1.1–1.4 and the previous theoretical estimates. Abstraction of H atom from ethane attains the ratio of $k_{calculated}/k_{experimetal}$ equal to 0.10–1.2 and 1.3–1.5 over the temperature windows of available experimental measurements; i.e., 300–900 K and 1500–2000 K, respectively. For the remaining alkanes (propane and *n*-butane), the average $k_{experimental}/k_{calculated}$ ratio remains 2.6 and 1.3 over the temperature range of experimental data. Also comparing the calculated standard enthalpy of reaction ($\Delta_r H^o_{298}$) with the available experimental measurements for alkanes, we found the mean unsigned error of computations as 3.7 kJ mol^{-1}. This agreement provides an accuracy benchmark of our methodology, affording the estimation of the unreported kinetic parameters for H abstractions from alkenes and alkynes. Based on the Evans-Polanyi plots, calculated bond dissociation enthalpies (BDHs) correlate linearly with

the standard enthalpy of activation ($\Delta^{\ddagger}H^{o}_{298}$), allowing estimation of the enthalpy barrier for reaction of NH_2 with other hydrocarbons in future work. Finally, we develop six sets of the generalised Arrhenius rate parameters for H abstractions from different C–H bond types. These parameters extend the application of the present results to any non-cyclic hydrocarbon interacting with the NH_2 radical.

4.2. Introduction

Reactions of NH_2 govern the behaviour of various combustion systems such as pyrolysis and oxidation of ammonia,[1-2] oxy-steam combustion,[3] coal nitrogen gasification[4] and oxidation of volatile nitrogen-bearing compounds in biomass.[5] Reactions involving NH_2 assume central importance in NO_x abatement technologies, including the thermal DeNO_x and NO_xOUT processes.[6-8] In the aforementioned combustion systems, NH_2 originates mainly from two pathways, oxidation of NH_3[9] and decomposition of HCN.[10] Hydrogen cyanide (HCN) appears as a primary product when nitrogen atom forms part of an aromatic ring.[11] Ammonia evolves when a fuel contains NH_2 groups.[12] In general, thermal decomposition of nitrogen-rich fuels produces ammonia, HCN and isocyanic acid (HNCO).[13] Formation of NH_2 from the decomposition of HCN proceeds via a complex reaction mechanism summarised as follow:

$$HCN + NCO \rightleftharpoons CN + HNCO$$

$$HNCO + H \rightleftharpoons NH_2 + CO$$

The direct abstraction of hydrogen atoms from alkanes by NH_2 produces ammonia and alkyl radicals. Literature reports numerous experimental measurements of the kinetic parameters for these reactions, over a wide range of operational *T-P* conditions (300–3000 K, 0.4–93.0 kPa). For example, Ehbrecht et al.[14] and Hack et al.[15] operated an isothermal flow reactor equipped with a laser-induced fluorescence to measure histories of NH_2 consumption in a temperature range of 400 to 1080 K, for reactions of NH_2 with CH_4, C_2H_6, C_3H_8, *i*-C_4H_{10}, and cyclohexane. In another study, Hennig and Wagner[16] deployed a shock tube to measure

the reaction rate constant of NH_2 with methane, ethane, and propane at temperatures between 1500 and 2100 K. Demissy and Lesclaux[17] implemented flash photolysis employing laser-resonance absorption for detection of NH_2 and measured reaction kinetics of H abstraction reactions for a series of alkanes at temperatures between 300 and 520 K.

In contrast to experimental work, available theoretical data are rather scarce and limited to reactions of NH_2 with few saturated hydrocarbons. Leory et al.[18] investigated reaction of methane with NH_2 at the CI/6-31G//UHF/6-31G level of theory. Another computational study employed UMP2, CCSD(T)//UMP2 and B3LYP approaches to examine the same reaction.[19] Mebel and Lin[20] performed Gaussian-2 method (G2M) computations to construct potential energy surfaces and to report rate constants for reactions of alkanes (CH_4, C_2H_6, C_3H_8, and *i*-C_4H_{10}) with NH_2. Valadbeigi and Farrokhpour[21] studied the dynamics and kinetics of atmospheric reactions of NH_2 with C_1–C_3 alkanes that form amines and then the subsequent H atom abstraction by hydrogen from the produced amines, at B3LYP and MP2 levels of theory. Song et al.[22] elucidated the H abstraction from CH_4 with NH_2, both experimentally and computationally. Their experiments involved shock tube studies to measure the rate constant in a temperature window of 1591–2084 K, whereas their computations employed KMLYP hybrid density functional method with the 6-311G(d,p) basis set over temperature range of 300–2100 K.

The current contribution reports the results of accurate CBS-QB3 investigations into reactions of NH_2 with the complete series of C_1–C_4 hydrocarbons, and 2-methylbutane, 2-methyl-1-butene, 3-methyl-1-butene, 3-methyl-2-butene, and 3-methyl-1-butyne. Literature provides no kinetic data of reactions of NH_2 with alkenes and alkynes. Thus, in addition to the reactions of NH_2 with C_1–C_4 alkanes considered by Mebel and Lin[20], we also explore

reaction with *n*-butane, short-chained alkenes and alkynes and selected C_5 species. To aid in discussion and presentation of the results, prefixes *p*, *s*, and *t* precede the formed radicals to denote removal of a hydrogen atom from primary, secondary and tertiary C–H bonds, respectively. Prefix *a* refers to an allylic hydrogen attached to the carbon adjacent to the sp^2 carbon and *v* signifies a vinylic hydrogen connected to the sp^2 carbon.

This chapter aims to: (i) present potential energy profiles for reactions of NH_2 with C_1-C_5 hydrocarbons listed in Table 4.1 as R1–R16, (ii) compute the reaction rate constants and fit them to an Arrhenius equation over a temperature range of 300–2000 K, and (iii) develop a relationship between the standard enthalpy of activation ($\Delta^{\ddagger}H^{o}_{298}$) and the bond dissociation enthalpy (BDH) for the title reactions. Guided by our computed BDHs values as well as the experimental BDHs compiled by Luo,[23] we generally limit the kinetic analysis for H abstraction from the weakest C–H site. However, for some molecules, we also present reaction rate parameters for competing channels; for example, primary versus secondary sites in linear alkanes, secondary versus tertiary sites in branched alkanes and allylic versus vinylic sites in alkenes. For alkanes, the current analysis yields estimates of kinetic parameters in close agreement with the experimental values reported in literature. For alkenes and alkynes reacting with NH_2, we provide first ever estimates of the kinetic parameters, unavailable from other sources. Grouping the kinetic parameters by bond types allows us to propose average values of the Arrhenius constants, for H abstraction by the NH_2 radical, for a wide range of non-cyclic hydrocarbons.

Table 4.1. H abstraction reactions from C_1–C_5 via NH_2 radical in gas phase system.

Hydrocarbons	Reactions	
methane	$CH_4 + NH_2 \rightarrow NH_3 + p\text{-}CH_3$	R1
ethane	$C_2H_6 + NH_2 \rightarrow NH_3 + p\text{-}C_2H_5$	R2
propane	$C_3H_8 + NH_2 \rightarrow NH_3 + p\text{-}C_3H_7$	R3a
	$C_3H_8 + NH_2 \rightarrow NH_3 + s\text{-}C_3H_7$	R3b
n-butane	$n\text{-}C_4H_{10} + NH_2 \rightarrow p\text{-}C_4H_9 + NH_3$	R4a
	$n\text{-}C_4H_{10} + NH_2 \rightarrow s\text{-}C_4H_9 + NH_3$	R4b
i-butane	$i\text{-}C_4H_{10} + NH_2 \rightarrow p\text{-}C_4H_9 + NH_3$	R5a
	$i\text{-}C_4H_{10} + NH_2 \rightarrow t\text{-}C_4H_9 + NH_3$	R5b
2-methylbutane	$C_5H_{12} + NH_2 \rightarrow t\text{-}C_5H_{11} + NH_3$	R6
propene	$C_3H_6 + NH_2 \rightarrow v\text{-}C_3H_5 + NH_3$	R7a
	$C_3H_6 + NH_2 \rightarrow a\text{-}C_3H_5 + NH_3$	R7b
1-butene	$1\text{-}C_4H_8 + NH_2 \rightarrow p\text{-}C_4H_7 + NH_3$	R8
2-butene	$2\text{-}C_4H_8 + NH_2 \rightarrow a\text{-}C_4H_7 + NH_3$	R9
2-methyl-1-butene	$C_5H_{10} + NH_2 \rightarrow a\text{-}C_5H_9 + NH_3$	R10
3-methyl-1-butene	$C_5H_{10} + NH_2 \rightarrow p\text{-}C_5H_9 + NH_3$	R11a
	$C_5H_{10} + NH_2 \rightarrow a\text{-}C_5H_9 + NH_3$	R11b
ethylene	$C_2H_4 + NH_2 \rightarrow v\text{-}C_2H_3 + NH_3$	R12

3-methyl-2-butene	$C_5H_{10} + NH_2 \rightarrow a\text{-}C_5H_9 + NH_3$	R13
1-butyne	$C_4H_6 + NH_2 \rightarrow s\text{-}C_4H_5 + NH_3$	R14
2-butyne	$C_4H_6 + NH_2 \rightarrow p\text{-}C_4H_5 + NH_3$	R15
3-methyl-1-butyne	$C_5H_8 + NH_2 \rightarrow t\text{-}C_5H_7 + NH_3$	R16

4.3. Computational methodology

We perform geometry optimisations, vibrational frequency calculations and total energy computations at the composite method of CBS-QB3 as implemented in the Gaussian 09[24] suite of programs. The absence of imaginary frequencies verifies the true minima of reactants and products while a transition structure retains one, and only one, imaginary frequency along the specified reaction coordinate. CBS-QB3 approach optimises geometries at the B3LYP/CBSB7 level of theory and employs the Møller–Plesset second-order energies, empirical and spin orbit[25-27]. CBS-QB3 methodology corrects for spin contamination in open-shell species through the energy factor $\Delta E_{\text{spin}} = -0.00954(< S^2 > - < S^2_{th} >)$ in which $<S^2>$ stands for the actual eigenvalue for the S^2 operator and S^2_{th} signifies the corresponding theoretical value (i.e., 0.75 for a doublet).

Literature has established the satisfactory performance of the CBS-QB3 method in predicting thermochemical and kinetic parameters for H abstraction/transfer reactions.[28] To further demonstrate the satisfactory performance of the CBS-QB3 method, Table S4.1 in the supporting information contrasts reaction and activation enthalpies for three selected reactions (R1–R3) with analogous values obtained by the CBS-APNO and G4 composite

methods. The CBS-QB3 and CBS-APNO values reside within 2.0 kJ mol^{-1}. Mean unsigned errors for the difference in reaction and activation enthalpies between CBS-QB3 and G4 values attain values of 1.48 and 2.94 kJ mol^{-1}; respectively. Clearly, this indicates the comparable performance of the CBS-QB3 with the more computational intensive chemistry models.

The close agreement between these methods concurs with a detailed analysis carried out by Simmie et al[29]. compared the two methods on enthalpies of formation and bond dissociation energies of selected alkyl hydroperoxides. While reaction enthalpies by the G4 method are closer to corresponding values of the CBS-QB3; the former method overshoots activation enthalpies by the latter by up to 5.0 kJ mol^{-1}. Nonetheless, the CBS-QB3 computations are typically executed at a fraction of the time required in G4 calculations; rendering the latter to be not feasible for relatively large systems. A recent study by Somers and Simmie[30] has demonstrated that the G4 method systematically outperforms the CBS-QB3 method in predicting enthalpies of formation for closed- and open-shell C_xH_yO species, however, literature provides no corresponding kinetic benchmarking. The CBS-QB3 remains the most widely deployed accurate and cost-effective" method in routine kinetics and thermodynamics computations pertinent to combustion reactions.

Calculations of the intrinsic reaction coordinates (IRC) connect all transition structures with their analogous reactants and products. We quote all calculated standard activation and reaction enthalpies at 298.15 K. All computed values of C–H BDHs for hydrogen attached to primary, secondary, tertiary, vinylic and allylic carbons display a mean unsigned error of below 7.1 kJ mol^{-1}, in comparison with the analogous experimental measurements summarised in Table S4.2 of Appendix I.

KiSThelP[31], a kinetic and statistical thermodynamic package, estimates reaction rate constants based on the formalism of the TST.[32-33] We account for the effect of quantum tunnelling on computed rate constants by using a one-dimensional asymmetrical Eckart barrier.[34] In estimation of the correct reaction degeneracy, we follow the approach of Fernández-Ramos et al.[33] In this formalism, the total reaction degeneracies are calculated by multiplying a symmetry number of each reaction (i.e., symmetry number of separated reactants/symmetry number of the transition state) by the number of equivalent abstractable hydrogen atoms. We have found that, the calculated barrier heights for H abstraction from equivalent sites are the same (i.e., within the 0.5 kJ mol^{-1} error bound of the adopted methodology), allowing to treat them as identical transition structures. The KiSThelP code employs the approach of McClurg et al.[35] in treating hindered rotors. As the effect of internal rotations about C–C bonds in hydrocarbons largely cancels out between reactants and transition states, we have treated these rotations as harmonic oscillators. However, this approach does not suffice for the internal rotation of the NH_2 group, as this group appears only in transition states, necessitating its rigorous treatment as a hindered rotor. In a like-manner to the study on NH_2 + ethylamine,[36] the rotor potential of the NH_2 is two-fold symmetric with an overall barrier in the range of 5.0 to 7.0 kJ mol^{-1}. In the case of H abstraction from primary sites in alkanes, it is important to account for the internal rotations about methyl groups in reactants as they freeze in transition states. Nonetheless, treating the hindered C–CH_3 rotors in alkanes as harmonic oscillators should not change the dominance of H abstraction from secondary site derived by the noticeable difference in the C–H strength among the two sites. Furthermore, to ensure that reactants correspond to lowest energy conformers, we have carried out partial optimisations with respect to selected dihedral angles.

H abstraction reactions are often associated with minimal variational effects.[36-37] Herein, we assess the variational effects by comparing the reaction rate constants derived from the TST treatment with the analogous values computed by the methodology of the variational transition state theory (VTST),[33] for Reaction R3b (abstraction from a secondary site) using KiSThelP software. We estimate VTST reaction rate constants by considering the minimum energy points (MEPs) along the reaction coordinate of -0.25 – 0.25 bohr. Table S4.3 (Supplementary Material) provide zero-point corrected energies (ZPE) at 0 K obtained at the CBS-QB3 level of theory, together with the vibrational frequencies and the relevant moments of inertia, for MEPs along the reaction coordinates of R3b. Figure S4.1 plots the energy profiles for the reaction. Table S4.4 contrasts the reaction rate constants calculated by the TST and VTST treatments and Figure S4.2, draws the Arrhenius plots. For Reaction R3b, values of k^{TST}/k^{VTST} decreases from 1.2 to 1.1 within the considered temperature interval of 300–2000 K. These results concur with those of a previous study on estimating the thermochemical and kinetic parameters for bimolecular reactions of ethylamine with three radicals; namely, H, CH_3 and NH_2.[31] Table S4.5 (Appendix I) provides the comparison of the experimental[38] and calculated standard enthalpy change of reaction ($\Delta_r H^o_{298}$) of alkanes indicating 3.7 kJ mol^{-1} as a mean unsigned error.

4.4. Results and discussion

4.4.1. Reaction dynamics of saturated hydrocarbons

Figure 4.1 portrays the optimised transition structures for H abstractions by NH_2 from alkanes. Labels of the transition structures reflect reaction numbers as given in Table 4.1.

Figure 4.2 represents a schematic diagram of the potential energy profiles of the considered alkanes. Table 4.2 illustrates the thermochemistry parameters of C_1–C_4 alkanes at 0 K and 298.15 K. The activation barriers ($\Delta^{\#}E_0$, i.e. at 0 K) for Reactions R1 and R2, calculated by the G2M method amount to 62.3 kJ mol^{-1} and 51.1 kJ mol^{-1},[20] respectively . Our CBS-QB3 calculated $\Delta^{\#}E_0$ for Reaction R1 corresponds to 55.1 kJ mol^{-1}, and Reaction R2 displays $\Delta^{\#}E_0$ of 40.8 kJ mol^{-1}. Clearly, the values obtained at the G2M (0 K) level of theory overestimate those derived by application of the more accurate CBS-QB3 (0 K) formalism. Mebel and Lin[20] reported energy barriers ($\Delta^{\#}E_0$) for Reactions R3a and R3b as 46.4 kJ mol^{-1} and 35.1 kJ mol^{-1}, respectively. These values overestimate the analogous values of 38.7 kJ mol^{-1} and 29.9 kJ mol^{-1} (CBS-QB3) computed herein. The trend continues for Reactions R5a and R5b with the G2M-based $\Delta^{\#}E_0$ values of 51.8 kJ mol^{-1}and 34.7 kJ mol^{-1} [20], overestimating the more accurate CBS-QB3 computations of 38.3 kJ mol^{-1}and 21.2 kJ mol^{-1}. Consequently, we observed the overall $\Delta^{\#}E_0$ mean unsigned error of 9.5 kJ mol^{-1} for the selected alkanes itemised in Table 2. In all subsequent discussion, we report standard enthalpies of activation at 298.15 K ($\Delta^{\ddagger}H^{o}_{298}$).

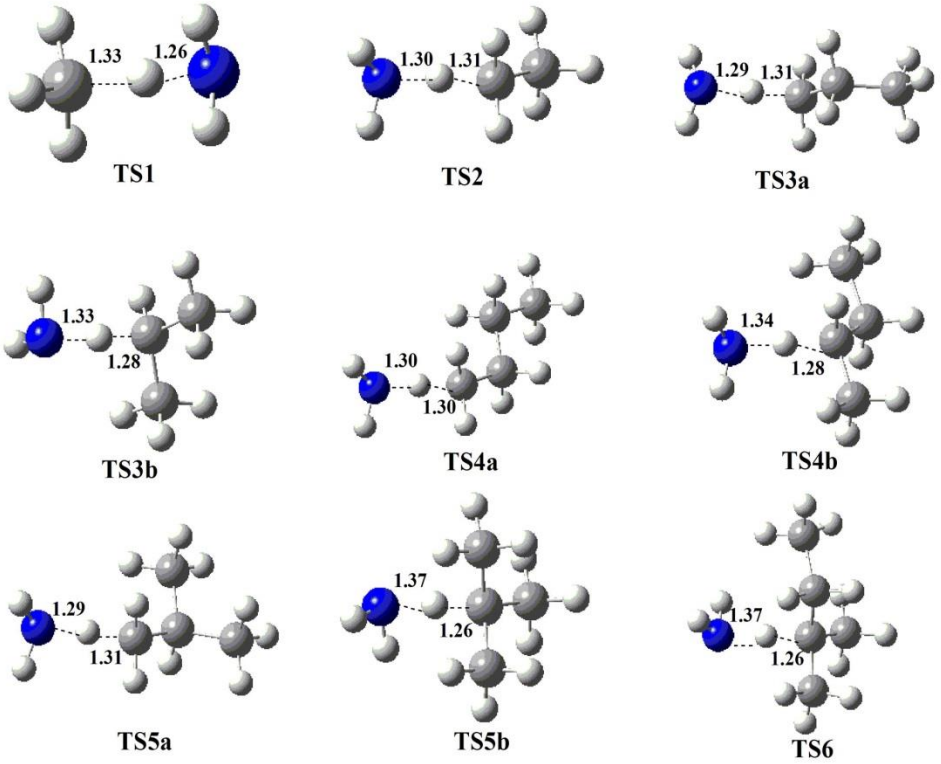

Figure 4.1. Optimised geometries of the transition states for the reactions of the NH_2 radical with alkanes. Distances are in Å. Blue colour = N, white = H and grey = C.

Reactions R1 and R2 present the highest enthalpy of activation ($\Delta^{\ddagger}H^{o}_{298}$) among all alkanes of 50.1 kJ mol^{-1} and 37.5 kJ mol^{-1} (Figure 2), evidently showing a significant difference between methane and ethane. This is because; the BDH of methyl C–H bond in methane of 440.9 kJ mol^{-1} exceeds that for ethane of 425.4 kJ mol^{-1}. This trend concurs with a higher exothermicity of Reaction R2 with respect to Reaction R1, as illustrated in Figure 4.2. Also, the $\Delta_r H^{o}_{298}$ values of Reactions R1 and R2 agree well with the corresponding literature values, with a minor difference of 1.5–2.0 kJ mol^{-1}, as listed in Table 2.

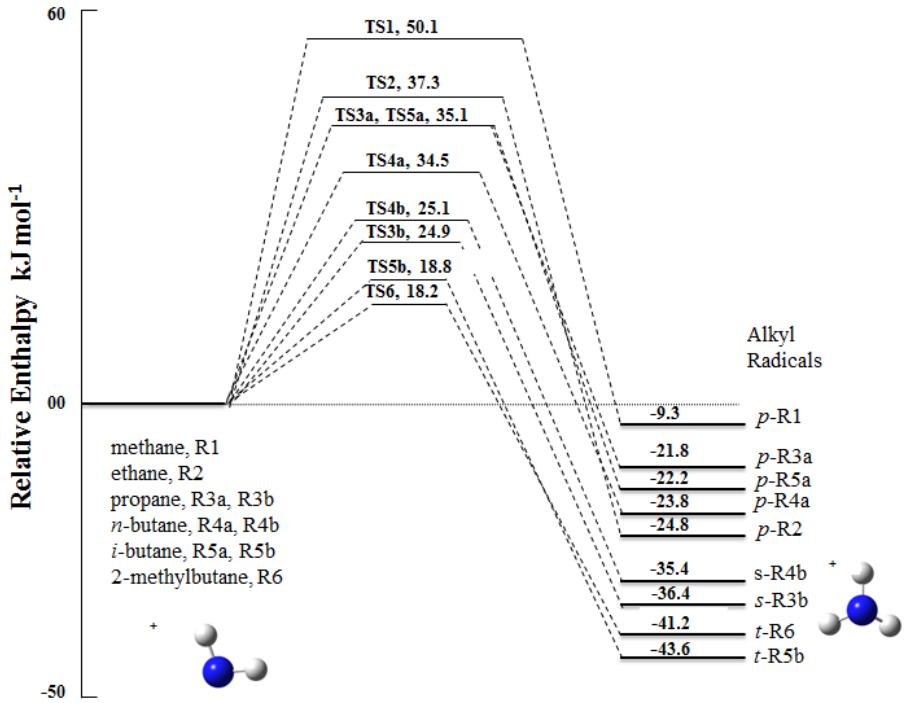

Figure 4.2. Schematic diagram of the relative enthalpies for the systems of NH_2 + alkanes at 298.15 K.

Table 4.2. Comparison of experimental and calculated (at CBS-QB3 level) standard enthalpy of reaction ($\Delta_r H^o_{298}$). The table presents the values of heat of reaction at 0 K ($\Delta_r E_0$), activation barrier at 0 K ($\Delta^{\ddagger} E_0$) and standard activation enthalpy ($\Delta^{\ddagger} H^{\circ}_{298}$). All values are in kJ mol^{-1}.

Reaction	$\Delta_r H^o_{298}$ [a]	$\Delta_r H^o_{298}$ [b]	$\Delta_r E_0$ [c]	$\Delta^{\ddagger} E_0$ [d]	$\Delta^{\ddagger} E_0$ [e]	$\Delta^{\ddagger} H^o_{298}$ [f]
R1	-10.9	-9.4	-9.6	62.3	55.2	50.1
R2	-26.8	-24.8	-23.8	51.1	40.8	37.3
R3a	-29.2	-21.8	-20.9	46.4	38.7	35.1
R3b	-36.8	-36.4	-34.3	35.1	29.9	26.9
R5a	-30.9	-22.2	-20.9	51.8	38.3	35.1
R5b	-45.9	-43.7	-40.9	34.7	21.2	18.8

[a] Experimental standard enthalpy change of reaction at 298.15 K from reference 37.

[b] Calculated standard enthalpy change of reaction using CBS-QB3 method at 298.15 K (present work).

[c] Heat of reaction calculated at the G2M level at 0 K, from reference 20.

[d] Activation barrier ($\Delta^{\ddagger} E_0$) computed at the G2M level from reference 20.

[e] Calculated activation barrier using CBS-QB3 method at 0 K (present work).

[f] Standard enthalpy of activation calculated at CBS-QB3 level at 298.15 K.

In principle, H abstraction from propane by NH_2 involves primary and secondary C–H sites. Fission of a secondary C–H bond incurs a lower BDH (413.9 kJ mol^{-1}) contrasted with the separation of the primary C–H bond (428.4 kJ mol^{-1}). Reaction R3b that produces *s*-C_3H_7

displays elevated exothermicity in comparison to Reaction R3a that generates *p*-C_3H_7, suggesting differences in their corresponding enthalpy barriers. The $\Delta^{\ddagger}H^{o}_{298}$ of Reaction R3b attains a value of 26.9 kJ mol^{-1}, i.e., lower by 8.3 kJ mol^{-1} than that of Reaction R3a. We noted a small deviation of 0.4 kJ mol^{-1} in $\Delta_r H^{o}_{298}$ for Reaction R3b as compared to 7.4 kJ mol^{-1} in $\Delta_r H^{o}_{298}$ of Reaction R3b from the analogous values reported by Kee et al.[35]

Similarly to propane, reactions of *n*-C_4H_{10} with NH_2 proceed via H abstraction from primary and secondary sites. The BDH value of primary C–H bond in *n*-C_4H_{10} surpasses that of a secondary C–H bond by 11.6 kJ mol^{-1}. The $\Delta^{\ddagger}H^{o}_{298}$ associated with Reaction R4a surpasses that of Reaction R4b by 9.4 kJ mol^{-1}. Reactions of NH_2 with *i*-C_4H_{10} ensue by two exit channels, the H abstraction from primary and tertiary C−H bonds. The BDH of the tertiary C-H bond in *i*-C_4H_{10} is weaker than that of the primary C-H bond, resulting in the higher exothermicity of the Reaction R5b channel as compared to the Reaction R5a corridor. Our BDH for tertiary C−H bond in *i*-C_4H_{10} (406.6 kJ mol^{-1}) compares well with the analogous experimental values of 400.4 kJ mol^{-1} reported in the table S4.2 (Appendix I). The $\Delta_r H^{o}_{298}$ attains -22.2 kJ mol^{-1} and -43.7 kJ mol^{-1} at 298.15 K for Reactions R5a and R5b, respectively. The corresponding experimental $\Delta_r H^{o}_{298}$, reported in literature, amounts to -30.9 kJ mol^{-1} and -45.9 kJ mol^{-1}, respectively. Table S4.5 (Appendix I) presents the unsigned errors of calculated $\Delta_r H^{o}_{298}$ compared to the experimental $\Delta_r H^{o}_{298}$ of H abstraction from C_1–C_4 alkanes. The mean unsigned error for $\Delta_r H^{o}_{298}$ for selected alkanes corresponds to 3.7 kJ mol^{-1} (Table S4.5), in reference to the experimental values.

The H abstraction from the tertiary carbon (BDH = 409.3 kJ mol^{-1}) in 2-methylbutane (R6) requires $\Delta^{\#}H^{o}_{298}$ similar to that of R5b (Table 3). Reactions R5b and R6 reveal the more reactant-like transition states characters among all transition states of Figure 1. These

transition states exhibit the shortest length of the disappearing C−H bond (1.26 Å) and the longest length of the emerging N−H bond (1.37 Å). Reactions R3b and R4b demonstrate similar C–H and N–H bond lengths for the abstraction of a secondary H atom by NH_2. Overall, the geometries of transition structures remain insensitive to the size of the carbon chain in alkanes. Having established the benchmarks for $\Delta^{\ddagger}E_0$ and $\Delta_r H^o_{298}$, based on Reactions R1, R2, R3a, R3b, R5a and R5b, our next objective is to elaborate the reaction dynamics of H abstraction from alkenes and alkynes by the NH_2 radical.

4.4.2. Reaction dynamics of unsaturated hydrocarbon

Figure 4.3 displays the optimised transition structures for reactions involving selected alkenes and alkynes with NH_2. Figure 4.4 elucidates the energy profiles of these reactions. For propene, abstraction of an H atom may involve a vinylic (R7a) or an allylic (R7b) site. In Reaction R7a, the vinylic C–H bond (466.6 kJ mol^{-1}) is noticeably stronger than the allylic C–H bond in R7b (359.3 kJ mol^{-1}). Accordingly, the $\Delta^{\ddagger}H^o_{298}$ of R7a exceeds significantly that of R7b; i.e., 44.3 kJ mol^{-1} versus 19.7 kJ mol^{-1}. According to the BDH compilation in Table S4.2, the primary C–H bonds are stronger in 1-butene (410.5 kJ mol^{-1}) than allylic C–H bonds in 2-butene (355.8 kJ mol^{-1}). Because of the strength of the vinylic C–H bonds, we only consider H abstractions from the primary site in 1-butene and from the allylic carbon in 2-butene. TS8 (1-butene, R8) and TS9 (2-butene, R9) reside 31.0 kJ mol^{-1} and 23.2 kJ mol^{-1} above their corresponding reactants. For the transition states, the emerging N–H bond in R9 is longer by 0.11 Å than a similar bond in R8, and the breaking C–H bond in TS9 is shorter by 0.06 Å in comparison to that in TS8. Based on the calculated BDHs, the most plausible corridor for the abstraction of H in 2-methyl-1-butene (R10) involves the allylic site. The

computed BDH for this site amounts to 358.8 kJ mol^{-1} with a calculated $\Delta^{\ddagger}H^{o}_{298}$ of 13.8 kJ mol^{-1}.

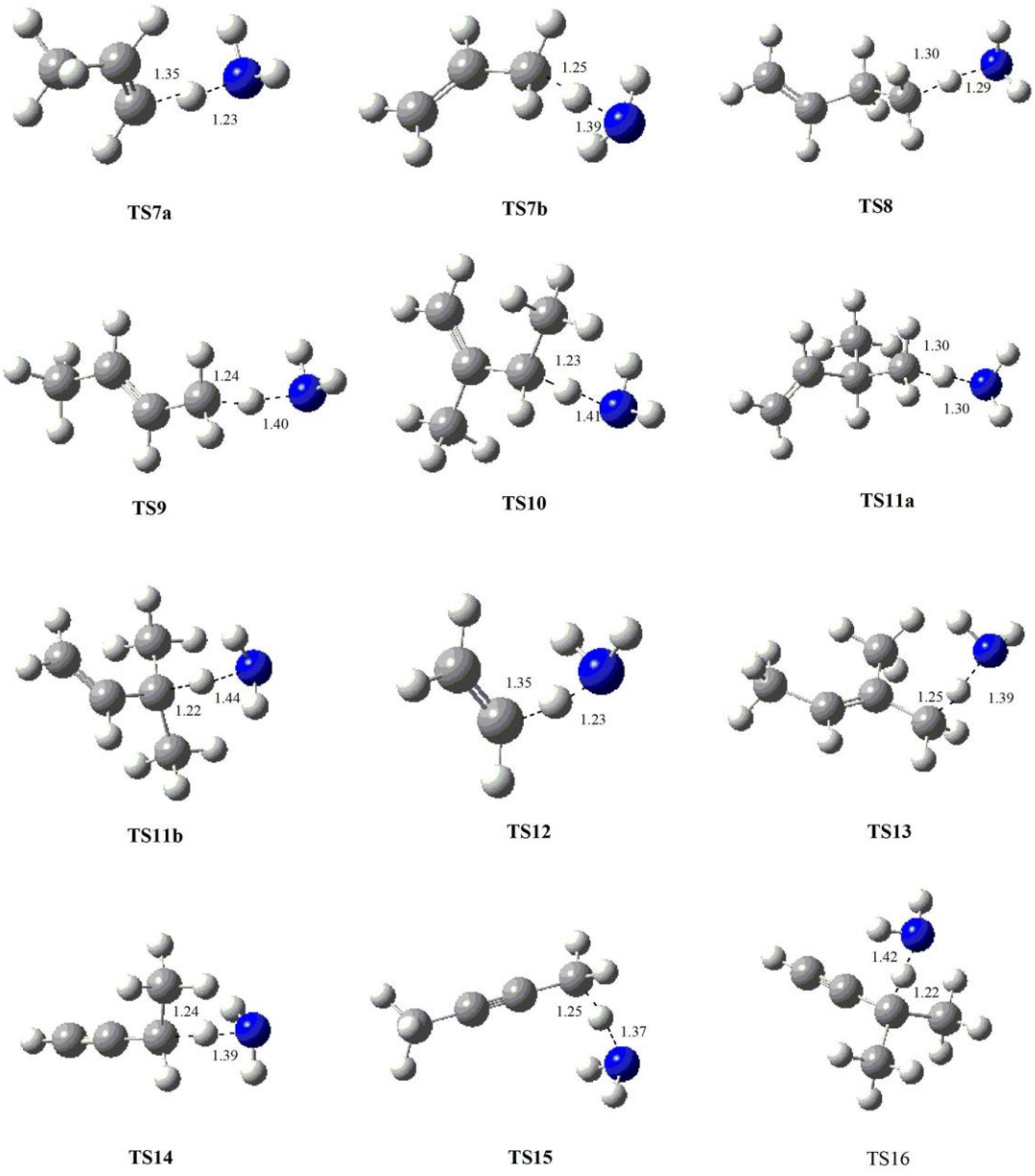

Figure 4.3. Optimised geometries of the transition states for the reactions of the NH_2 radical with alkenes and alkynes. Distances are in Å.

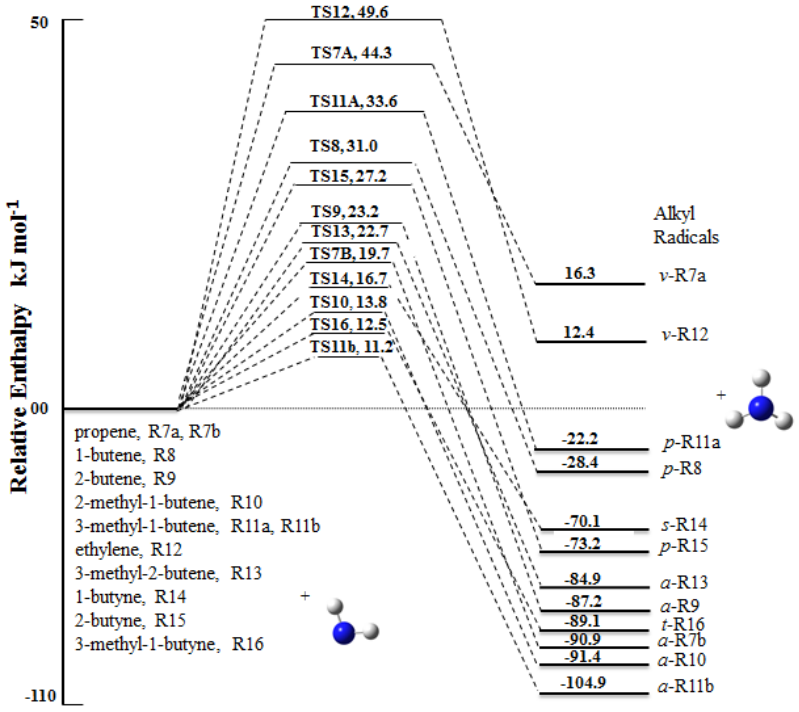

Figure 4.4. Schematic diagram of the relative enthalpies for the systems of NH_2 + alkenes and alkynes at 298.15 K.

We consider two possibilities for H abstraction from 3-methyl-1-butene (R11): (i) from the primary C−H bond (R11a) and (ii) from the allylic (i.e., tertiary) C−H bond (R11b). The allylic C-H bond in 3-methyl-1-butene is weaker than that associated with the primary C-H bond, resulting in the higher exothermicity of the R11b channel as compared to the R11a corridor. Our calculated BDH for the allylic C−H bond in 3-methyl-1-butene (345.3 kJ mol^{-1}) correlates with the analogous experimental values of 332.6 kJ mol^{-1} reported in Table S4.2 Reactions R11a and R11b display $\Delta^{\ddagger}H^{o}_{298}$ values of 33.6 kJ mol^{-1} and 11.2 kJ mol^{-1}, respectively. Interestingly, the calculated $\Delta^{\ddagger}H^{o}_{298}$ in Reactions R11a and R11b fall within 1.5–7.2 kJ mol^{-1} off the analogous barriers for Reactions R5a and R5b. In Reaction R12, ethylene undergoes H abstraction that exhibits a sizable barrier of 49.6 kJ mol^{-1} and thus occupies the highest position in Figure 4.4, i.e., 5.3 kJ mol^{-1} higher than that of TS7a. The lengths of C–H (1.35 Å) and N–H (1.23 Å) bonds in TS12 and TS7a are similar and both

Reactions R7 and R12 exhibit modest endothermicity. H abstraction from the allylic carbon in 3-methyl-2-butene (R13) requires $\Delta^{\#}H^{o}_{298}$ similar to that of R7b (22.7 kJ mol^{-1} versus 19.7 kJ mol^{-1}). Transition structures for both reactions share similar geometrical features, as shown in Figure 4.3.

In the alkyne family, H abstraction from 1-butyne (R14) and 3-methyl-1-butyne (R16) proceeds from the secondary and tertiary-like sites, respectively. Scission of C–H bond in the CH_2 group of R14 requires higher BDH of 365.2 kJ mol^{-1} if contrasted with the BDH of 356.9 kJ mol^{-1} of the tertiary-like site in R16. The $\Delta^{\ddagger}H^{o}_{298}$ of Reaction R14 amounts to 16.7 kJ mol^{-1}; i.e., higher by only 2.9 kJ mol^{-1} than that of Reaction R16. The removal of an H atom from the methyl group in 2-butyne (R15) requires $\Delta^{\ddagger}H^{o}_{298}$ of 27.2 kJ mol^{-1} and results in reaction exothermicity of 73.2 kJ mol^{-1}. The higher activation barrier[39] ($\Delta^{\ddagger}E_0$) of 109.9 kJ mol^{-1} associated with an elevated BDH of 556.6 kJ mol^{-1} [40] justifies the trend in $\Delta^{\ddagger}H^{o}_{298}$ for Reactions R14, R15 and R16 as function of BDH.

4.4.3. Reaction kinetics

Table 4.3 assembles the Arrhenius parameters for the title reactions and Table 4.4 presents the generalised rate constant for H abstraction reactions from different C–H bond types via NH_2 per one abstractable H atom, with Figures S4.3a-S4.3f (Appendix I) comparing the generalised constants with those of relevant reactions.

Table 4.3. Rate parameters for H abstraction reactions by NH_2, fitted between 300 and 2000 K. Values of the Arrhenius parameters (A and E_a) are in units of $cm^3\ s^{-1}$ molecule^{-1} and kJ mol^{-1}, respectively.

Reaction	Transition state	A	E_a
R1	TS1	5.75×10^{-11}	57.8
R2	TS2	1.75×10^{-11}	44.0
R3a	TS3a	2.27×10^{-11}	42.0
R3b	TS3b	2.45×10^{-11}	35.7
R4a	TS4a	3.51×10^{-11}	41.3
R4b	TS4b	2.86×10^{-11}	32.5
R5a	TS5a	3.06×10^{-11}	42.1
R5b	TS5b	2.24×10^{-11}	27.0
R6	TS6	4.59×10^{-12}	27.0
R7a	TS7a	2.35×10^{-11}	49.6
R7b	TS7b	2.49×10^{-11}	27.9
R8	TS8	7.19×10^{-11}	36.4
R9	TS9	2.28×10^{-11}	33.5
R10	TS10	1.02×10^{-11}	24.3
R11a	TS11a	2.56×10^{-11}	40.8
R11b	TS11b	8.09×10^{-12}	22.6
R12	TS12	2.59×10^{-11}	56.1
R13	TS13	1.88×10^{-11}	32.2
R14	TS14	2.69×10^{-11}	25.0
R15	TS15	1.65×10^{-10}	35.6
R16	TS16	4.43×10^{-10}	13.7

Table 4.4. Generalised rate parameters for H abstraction reactions by NH_2 for different C–H bond types, fitted between 300 and 2000 K per one abstractable H atom. Values of the Arrhenius parameters (A and E_a) are in units of $cm^3\ s^{-1}\ molecule^{-1}$ and $kJ\ mol^{-1}$, respectively.

	A	E_a		A	E_a
Primary C–H (alkane)	2.19×10^{-11}	42.4	Primary C–H (alkene)	2.44×10^{-11}	38.6
Secondary C–H (alkane)	1.33×10^{-11}	34.1	Vinylic C–H (alkene)	1.24×10^{-11}	52.8
Tertiary C–H (alkane)	1.35×10^{-11}	27 .0	Allylic C–H (alkene)	2.22×10^{-11}	28.1

Overall, our calculated rate constants reasonably match the relevant values reported in literature. For instance, Fig 5.5a shows comparison of Arrhenius plots between the calculated and the previous available experimental and theoretical data. For Reaction R1, our rate expression appears as $k(T) = 5.75\times10^{-11} \exp(-57.8/(RT))\ cm^3\ s^{-1}\ molecule^{-1}$, i.e., in close agreement with the theoretically-fitted rate constant of Mebel and Lin[20] that reads as $k(T) = 2.77\times10^{-11} \exp(-55.7/(RT))\ cm^3\ s^{-1}\ molecule^{-1}$ in a temperature range of 300–2000 K. Hennig and Wagner[16] obtained $k(T) = 1.99\times10^{-11} \exp(-63.4/(RT))\ cm^3\ s^{-1}\ molecule^{-1}$ from a shock tube experiments for Reaction R1, for temperatures between 1500 and 2100 K. The estimated ratio of $k_{calculated}/k_{experimental}$ of around 1.8 display veritable values for 1500–2000 K. Demissy and Lesclaux[17] estimated a rate constant of $k(T) = 8.30\times10^{-13} \exp(-43.9/(RT))\ cm^3\ s^{-1}\ molecule^{-1}$ for the low temperature range of 300 to 520 K. The ratio of $k_{caclculated}/k_{experimental}$ equals 0.26–1.1, between 400–500 K. Our calculated rate constant overestimates the experimental rate constant by a factor of 2.4 at 300 K. We observed a good agreement with

the latest experimental study[22] for Reaction R1 in a temperature window of 1600–2000 K, corresponding to the ratio of $k_{calculated}/k_{experimental}$ of 1.1–1.4. The average ratio of $k_{calculated}/k_{experimental}$ for Reaction R1 amounts to 1.5.

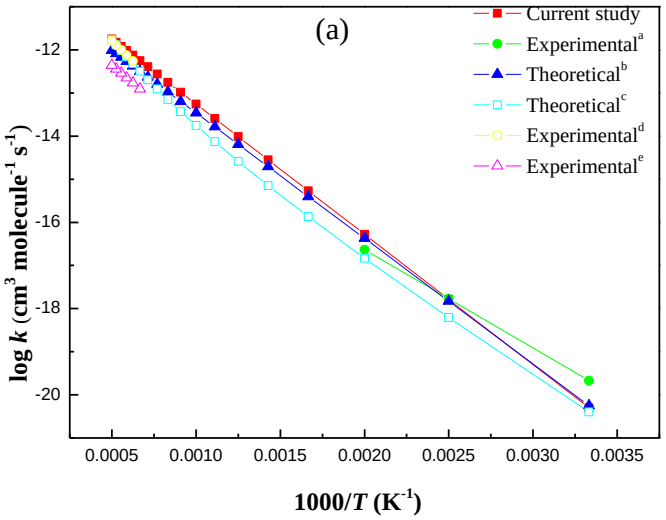

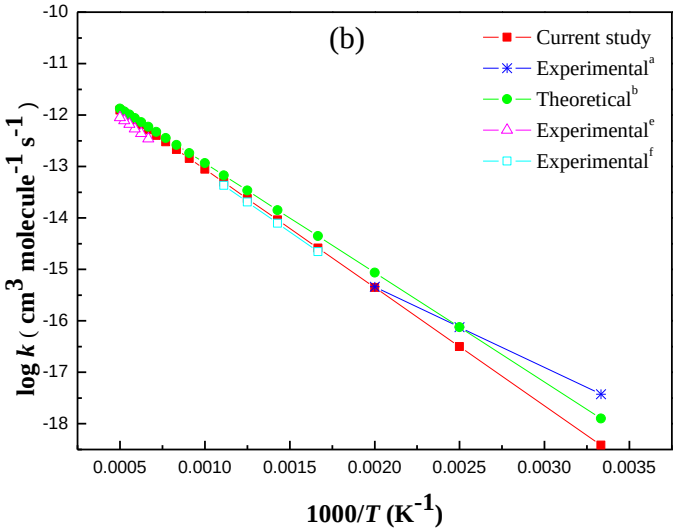

Figure 4.5. (a) Arrhenius plot of the rate constant for Reaction R1; [a]Ref 17, [b]Ref 20, [c,d]Ref 22, [e]Ref16. (b) Arrhenius plot of the rate constant for Reaction R2; [a]Ref 17, [b]Ref 20, [e]Ref16, [f]Ref 14.

Figure 4.5b depicts Arrhenius plots of the calculated and the previously available experimental and theoretical rate constants. For Reaction R2, the theoretically estimated[20] rate constant $k = 1.54\times10^{-11}$ exp(-40.7/(*RT*)) cm^3 s^{-1} $molecule^{-1}$ concurs well with our expression of $k(T) = 1.75\times10^{-11}$ exp(-44.0/(*RT*)) cm^3 s^{-1} $molecule^{-1}$. Hennig and Wagner,[16] using the same experimental setup for Reaction R2 as for Reaction R1, for temperatures between 1500 K and 2100 K, reported $k(T) = 1.61\times10^{-11}$ exp(-47.9/(*RT*)) cm^3 s^{-1} $molecule^{-1}$ with the $k_{calculated}/k_{experimental}$ ratio of 1.4–1.5 for 1500-2000 K. Finally, Demissy and Lesclaux[17] obtained a rate constant of $k(T) = 6.14\times10^{-13}$ exp(-29.9/(*RT*)) cm^3 s^{-1} $molecule^{-1}$ from experiments for the low temperature range of 300 K to 520 K. These measurements together with our calculations yield the $k_{calculated}/k_{experimental}$ ratio of 0.10–0.97. Furthermore, the calculated rate constant agree well with the rate recommended by Ehbrecht et al.[14] based on the experiments performed by these investigators in the temperature window of 600–900 K, with the relevant $k_{calculated}/k_{experimental}$ ratio of around 1.2. Overall, for Reactions R1 and R2, the estimated activation energies derived from experiments[14,15,16,17], fitted in the range 600–2000 K, concur closely with the values of the present computations reported in Table 4.3.

Figure 4.6a shows the Arrhenius plots for the overall rate constant of Reaction R3 (primary and secondary) in comparison with the available experimental and theoretical values. Within the temperature range of 300–500 K, our calculated rate constant coincide relatively well with the values reported by Demissy and Lesclaux[17], with the $k_{calculated}/k_{experimental}$ ratios of 0.17–0.69. The current theoretical finding overestimates the experimental results of Ehbrecht et al.[14] (i.e., $k_{calculated}/k_{experimental}$ ratios of 3.8–4.4 in the temperature interval of 500–1000 K). Hennig and Wagner[16] experimentally-determined rate constant match well with our theoretically-derived constant between 1500–2000 K with $k_{calculated}/k_{experimental}$ ratios placed in

the narrow range of 2.4–2.7. Figure 4.6b provides Arrhenius plot for the rate constant for combined reaction R4 ($k_{R4} = k_{R4a} + k_{R4b}$). The analogous experimental values display a relatively fair agreement with previous experimental measurements[17] (at 300 K) with ratio $k_{calculated}/k_{experimental}$ 1.5 but overestimate (between 400–500 K) with ratios $k_{calculated}/k_{experimental}$. stretch between 3.2–5.2. Nonetheless, the previous theoretical study[41]. underestimates our calculated rate constants by a factor of 0.05 as shown in Figure 4.6b The average ratios of $k_{calculated}/k_{experimental}$ for Reaction R3 and R4 correspond to 2.8 and 3.3, respectively.

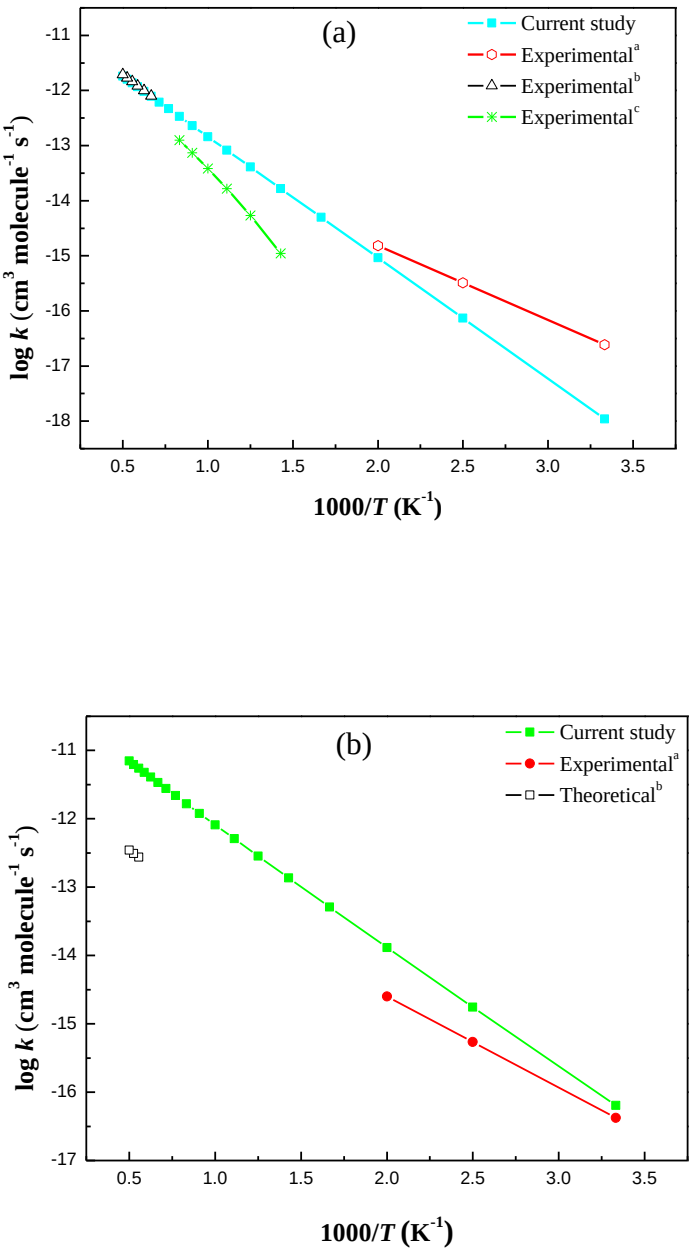

Figure 6. (a) Arrhenius plot of the rate constant for Reaction R3; [a]Ref 17, [b]Ref 16, [c]Ref 14. (b) Arrhenius plot of the rate constant for Reaction R4; [a]Ref 17, [b]Ref 40.

For a more insightful comparison, Table 4.5 contrasts our fitted Arrhenius parameters with analogous experimental evaluations for Reactions R1 and R2 between 300–500 K. Our estimated A and E_a values match very well their experimental counterparts. For Reaction R1,

the ratio of experimental rate constant to calculated rate constant, $k_{calculated}/k_{experimental}$, resides between 1.2–1.3. Similarly for Reaction R2, the $k_{calculated}/k_{experimental}$ ratio remains virtually constant at 1.1–1.4 between 300-500 K.

Table 4.5. Rate parameters for H abstraction reactions by NH_2, fitted between 300 and 500 K. Values of the Arrhenius parameters (A and E_a) are in units of $cm^3\ s^{-1}\ molecule^{-1}$ and kJ mol^{-1}, respectively**.**

Reaction	Transition state	A	E_a	$k_{caculatedl}/k_{experimental}$	Reference
R1	TS1	8.65×10^{-13} 8.30×10^{-13}	43.3 43.9	1.2–1.3	Current study Demissy and Lesclaux[17]
R2	TS2	1.19×10^{-12} 6.14×10^{-13}	31.5 29.9	1.1–1.4	Current study Demissy and Lesclaux[17]

Having established an accuracy benchmark for kinetic parameters of NH_2 reactions with alkanes, we now turn our attention to present computed rate constants for H abstraction of alkene and alkyne. Literature provides no experimental and theoretical calculations of kinetic parameters for NH_2 reactions with any alkene and alkyne. Figure 4.7 portrays calculated rate constants for H abstraction by NH_2 from six alkenes namely ethylene, propene, 1-butene, 2-butene, 2-methyl-1-butene, 3-methyl-1-butene and 3-methyl-2-butene. Owing to higher activation enthalpies, Reactions R12 and R7a hold the slowest reaction rate constants in this series. In the case of alkyne, the computed rate constant for Reaction R16 exceeds those for Reactions R15 and R14 as illustrated in Figure. 4.8.

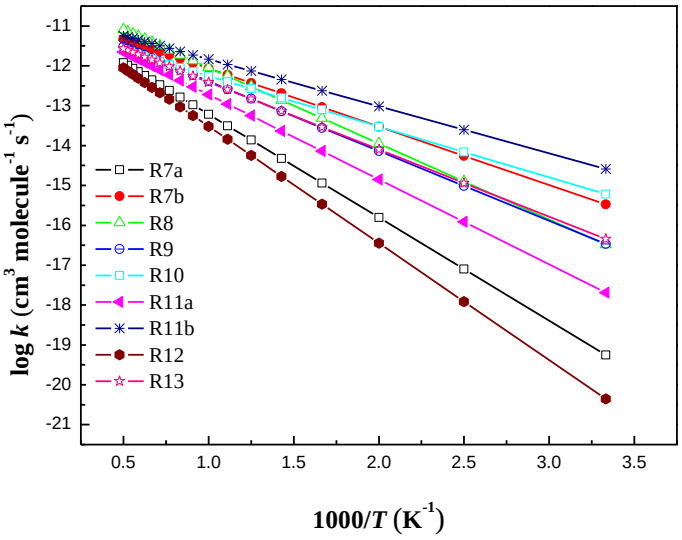

Figure 4.7. Arrhenius plot for the rate constant of reactions of alkenes with NH_2, obtained from the TST formalism corrected for the Eckart tunnelling at the CBS-QB3 level of theory.

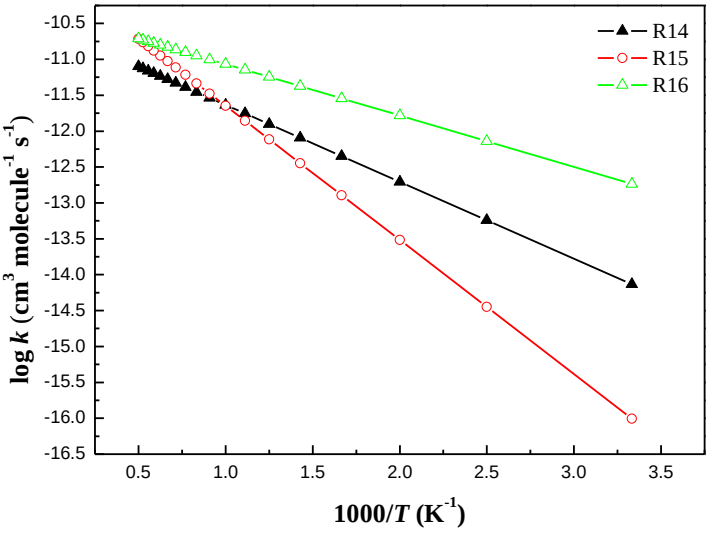

Figure 4.8. Arrhenius plot for the rate constant of reactions of alkyne + NH_2 using the TST approach and corrected for the Eckart tunnelling at the CBS-QB3 level of theory.

4.5. Evans-Polanyi correlation

Figure 4.9 elucidates a correlation between BDHs and $\Delta^{\ddagger}H^{o}_{298}$ for the three hydrocarbon series. The rate of H abstraction generally depends on bond strengths (as reflected by BDH) undergoing the fission process. We have found a linear correlation between $\Delta^{\ddagger}H^{o}_{298}$ and BDHs. For a certain attacking radical X, the same X–H bond forms in all reactions. Therefore, the Evans-Polanyi assumes a linear energy relationship in the form of

$$\Delta^{\ddagger}H^{o}_{298} = \alpha\,[\mathrm{BDH}_{298}\,(\mathrm{C–H}) + C]$$

where α and C denote constants.[17]

For Alkanes, $\Delta^{\ddagger}H^{o}_{298} = 0.90\,[\mathrm{BDH}_{298}\,(\mathrm{C–H}) + (-352.01)]$

For alkenes, $\Delta^{\ddagger}H^{o}_{298} = 0.26\,[\mathrm{BDH}_{298}\,(\mathrm{C–H}) + (-76.02)]$

For alkynes, $\Delta^{\ddagger}H^{o}_{298} = 0.45\,[\mathrm{BDH}_{298}\,(\mathrm{C–H}) + (-144.52)]$

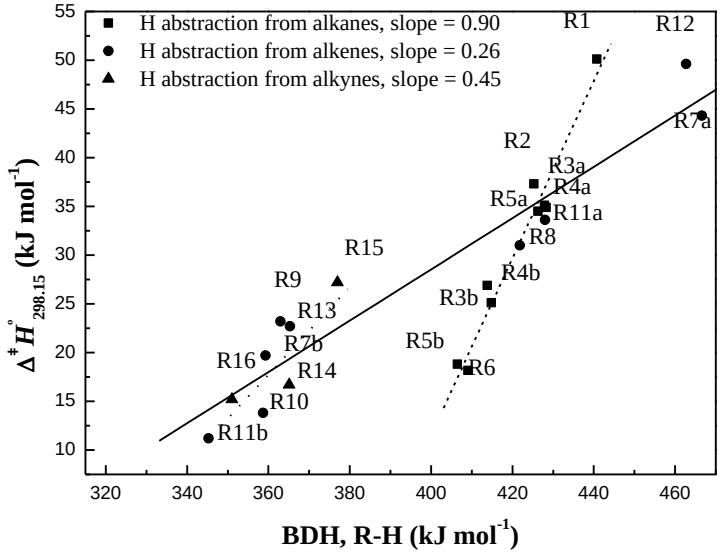

Figure 4.9. Evans-Polanyi plot for the H abstraction reaction $NH_2 + R–H \rightarrow NH_3 + R$.

The three dissimilar linear fits stem from the noticeable difference in BDH values of the dissociating C–H bonds. The least square slope coefficients lie within the expected range for the Evans-Polanyi plots (0.0–1.0). The $\Delta^{\ddagger}H^{o}_{298}$ of H abstractions from alkanes, alkenes, and alkynes by NH_2 correlate linearly with the relevant BDHs. The same behaviour was previously observed for H abstractions from hydrocarbons, by HO_2 radicals.[41,42] According to Hammond's postulates, the closer the transition states toward the reactant like geometry, the higher will be the exothermicity of the reactions for that transition states Intuitively, reactions for transition states in alkanes (TS3b, TS4b, TS5b and TS6) approaching towards reactant side and encompasses higher exothermicity than transition states (TS1, TS2, TS3a, TS4a and TS5a) that acquired lower reaction exothermicity. We also observed the similar trend for the H abstraction reactions in alkenes and alkynes. The present Evans-Polanyi plot affords estimation of the $\Delta^{\ddagger}H^{o}_{298}$ for the reaction of NH_2 with other hydrocarbons, not reported herein.

4.6. Conclusions

We reported herein a comprehensive thermochemical and kinetic account into the reactions of NH_2 radicals with the complete series of C_1–C_4 species in addition to selected C_5 compounds. The mean unsigned error of the bond dissociation enthalpies (BDH) of the titled hydrocarbons corresponds to 7.1 kJ mol^{-1}. The calculated standard enthalpy of activation ($\Delta^{\ddagger}H^{o}_{298}$) for $CH_4 + NH_2$ amounts to 50.1 kJ mol^{-1}, significantly exceeding the barriers for the removal of primary H atoms from other alkanes, such as C_2H_6, C_3H_8, *n*-C_4H_{10} and *i*-C_4H_{10}. The $\Delta^{\#}H^{o}_{298}$ decreases to 25.1 kJ mol^{-1} and 26.9 kJ mol^{-1} for H abstraction from secondary C-H bonds in *n*-C_4H_{10} and C_3H_8, respectively. For a hydrogen placed on a tertiary carbon in

C_5H_{12} (2-methylbutane) and *i*-C_4H_{10} molecules, $\Delta^{\neq}H^{o}_{298}$ declines to 18.2 kJ $mol^{-1}$and 18.8 kJ mol^{-1}, correspondingly, in line with the decreasing strength of the relevant C–H bonds. The length of the hydrocarbon chain displays a minimal influence on the computed standard activation and reaction enthalpies. By averaging the Arrhenius rate values, we developed the generalised parameters for H abstraction reactions by NH_2 form different C-H bond types, per one abstractable H atom. The average ratio of $k_{calculated}$ /$k_{experimental}$ for methane, ethane and *n*-butane remains within 1.1–1.5, rising to 2.6 for propane, for temperature ranges of experimental measurements. The kinetic rate parameters presented in this study will assist in constructing kinetic models for combustion and pyrolysis of nitrogen-rich fuels.

Appendix I: Supplementary Information

Bond dissociation enthalpies, CBS-QB3 0 K energies, vibrational frequencies and moment of inertia for MEPs along the reaction coordinates, comparison of standard enthalpies of activation, standard enthalpy changes of reactions, constructed energy profiles, reaction rate constants calculated by TST and VTST, Arrhenius plots, and the ratio k^{TST}/k^{VTST}.

4.7. References

1. Rahinov, I.; Ditzian, N.; Goldman, A.; Cheskis, S., NH_2 Radical Formation by Ammonia Pyrolysis in a Temperature Range of 800–1000 K. *Appl. Phys. B.* **2003**, *77*, 541-546.

2. Miller, J. A.; Smooke, M. D.; Green, R. M.; Kee, R. J., Kinetic Modeling of the Oxidation of Ammonia in Flames. *Combust. Sci. Technol.* **1983**, *34*, 149-176.

3. Zou, C.; He, Y.; Song, Y.; Han, Q.; Liu, Y.; Guo, F.; Zheng, C., The Characteristics and Mechanism of the NO Formation during Oxy-Steam Combustion. *Fuel* **2015**, *158*, 874-883.

4. Mckenzie, L. J.; Tian, F.-J.; Li, C.-Z., NH_3 Formation and Destruction during the Gasification of Coal in Oxygen and Steam. *Environ. Sci. Technol.* **2007**, *41*, 5505-5509.

5. Mendiara, T.; Glarborg, P., Ammonia Chemistry in Oxy-Fuel Combustion of Methane. *Combust. Flame* **2009**, *156*, 1937-1949.

6. Tayyeb Javed, M.; Irfan, N.; Gibbs, B. M., Control of Combustion-Generated Nitrogen Oxides by Selective Non-Catalytic Reduction. *J. Environ. Manage.* **2007**, *83*, 251-289.

7. Bae, S. W.; Roh, S. A.; Kim, S. D., NO Removal by Reducing Agents and Additives in the Selective Non-Catalytic Reduction (SNCR) Process. *Chemosphere* **2006**, *65*, 170-175.

8. Glarborg, P.; Dam-Johansen, K.; Miller, J. A.; Kee, R. J.; Coltrin, M. E., Modeling the Thermal $DeNO_x$ Process in Flow Reactors. Surface Effects and Nitrous Oxide Formation. *Int. J. Chem. Kinet.* **1994**, *26*, 421-436.

9. Davidson, D. F.; Kohse-Höinghaus, K.; Chang, A. Y.; Hanson, R. K., A Pyrolysis Mechanism for Ammonia. *Int. J. Chem. Kinet.* **1990**, *22*, 513-535.

10. Miller, J. A.; Bowman, C. T., Mechanism and Modeling of Nitrogen Chemistry in Combustion. *Prog. Energy Combust. Sci.* **1989**, *15*, 287-338.

11. Solomon, P. R.; Fletcher, T. H., Impact of Coal Pyrolysis on Combustion. *Proc. Combust. Inst.* **1994**, *25*, 463-474.

12. Hill, S.; Smoot, L. D., Modeling of Nitrogen Oxides Formation and Destruction in Combustion Systems. *Prog. Energy Combust. Sci.* **2000**, *26*, 417-458.

13. Glarborg, P.; Jensen, A.; Johnsson, J. E., Fuel Nitrogen Conversion in Solid Fuel Fired Systems. *Prog. Energy Combust Sci.* **2003**, *29*, 89-113.

14. Ehbrecht, J.; Hack, W.; Rouveirolles, P.; Wagner, H. G., Hydrogen Abstraction Reactions by $NH_2(\tilde{X}^2B_1)$-Radicals from Hydrocarbons in the Gas Phase. *Ber. Bunsenges. Phys. Chem.* **1987**, *91*, 700-708.

15. Hack, W.; Kurzke, H.; Rouveirolles, P.; Wagner, H. G., Hydrogen Abstraction Reactions by $NH_2(\tilde{X}^2B_1)$-Radicals from Hydrocarbons in the Gas Phase. *Ber. Bunsenges. Phys. Chem.* **1986**, *90*, 1210-1219.

16. Hennig, G.; Wagner, H. G., A Kinetic Study about the Reactions of $NH_2(\tilde{X}^2B_1)$ Radicals with Saturated Hydrocarbons in the Gas Phase. *Ber. Bunsenges. Phys. Chem.* **1995**, *99*, 863-869.

17. Demissy, M.; Lesclaux, R., Kinetics of Hydrogen Abstraction by Amino Radicals from Alkanes in the Gas Phase. A Flash Photolysis-Laser Resonance Absorption Study. *J. Am. Chem. Soc.* **1980**, *102*, 2897-2902.

18. Leroy, G.; Sana, M.; Tinant, A., Étude Théorique des Réactions d'Abstraction d'Hydrogène RH + X ⇌ R , Avec R, X≡H, CH_3, NH_2,OH et F. *Can. J. Chem.* **1985**, *63*, 1447-1456.

19. Basch, H.; Hoz, S., Ab Initio Study of Hydrogen Abstraction Reactions. *J. Phys. Chem. A.* **1997**, *101*, 4416-4431.

20. Mebel, A. M.; Lin, M. C., Prediction of Absolute Rate Constants for the Reactions of NH_2 with Alkanes from Ab Initio G2M/TST Calculations. *J. Phys. Chem. A.* **1999**, *103*, 2088-2096.

21. Valadbeigi, Y.; Farrokhpour, H., Theoretical Study on the Mechanism and Kinetics of Atmospheric Reactions C_nH_{2n+2} + NH_2 (n=1–3). *Struct. Chem.* **2015**, *26*, 383-391.

22. Song, S.; Golden, D. M.; Hanson, R. K.; Bowman, C. T.; Senosiain, J. P.; Musgrave, C. B.; Friedrichs, G., A Shock Tube Study of the Reaction $NH_2 + CH_4 \rightarrow NH_3 + CH_3$ and Comparison with Transition State Theory. *Int. J. Chem. Kinet.* **2003**, *35*, 304-309.

23. Luo, Y.-R., *Handbook of Bond Dissociation Energies in Organic Compounds*; CRC Press: Boca Raton, FL, 2003.

24. Frisch, M. J.; Trucks, G. W.; Schlegel, H. B.; Scuseria, G. E.; Robb, M. A.; Cheeseman, J. R.; Scalmani, G.; Barone, V.; Mennucci, B.; Petersson, G. A. et al. *Gaussian 09*, revision A.1.; Gaussian, Inc.: Wallingford, CT, 2009.

25. Vandeputte, A. G.; Sabbe, M. K.; Reyniers, M.-F.; Van Speybroeck, V.; Waroquier, M.; Marin, G. B., Theoretical Study of the Thermodynamics and Kinetics of Hydrogen Abstractions from Hydrocarbons. *J. Phys. Chem. A.* **2007**, *111*, 11771-11786.

26. Casasnovas, R.; Frau, J.; Ortega-Castro, J.; Salvà, A.; Donoso, J.; Muñoz, F., Simplification of the CBS-QB3 Method for Predicting Gas-Phase Deprotonation Free Energies. *Int. J. Quant. Chem.* **2010**, *110*, 323-330.

27. Montgomery, J. A.; Frisch, M. J.; Ochterski, J. W.; Petersson, G. A., A Complete Basis Set Model Chemistry. Vi. Use of Density Functional Geometries and Frequencies. *J.Chem. Phys.* **1999**, *110*, 2822-2827.

28. Ahubelem, N.; Altarawneh, M.; Dlugogorski, B. Z., Dehydrohalogenation of Ethyl Halides. *Tetrahedron Lett.* **2014**, *55*, 4860-4868.

29. Simmie, J. M.; Black, G.; Curran, H. J.; Hinde, J. P., Enthalpies of Formation and Bond Dissociation Energies of Lower Alkyl Hydroperoxides and Related Hydroperoxy and Alkoxy Radicals. *J. Phys. Chem. A.* **2008**, *112*, 5010-5016.

30. Somers, K. P.; Simmie, J. M., Benchmarking Compound Methods (CBS-QB3, CBS-APNO, G3, G4, W1BD) against the Active Thermochemical Tables: Formation Enthalpies of Radicals. *J. Phys. Chem. A.* **2015**, *119*, 8922-8933.

31. Canneaux, S.; Bohr, F.; Henon, E., KiSThelP: A Program to Predict Thermodynamic Properties and Rate Constants from Quantum Chemistry Results. *J. Comput. Chem.* **2014**, *35*, 82-93.

32. Truhlar, D. G.; Garrett, B. C.; Klippenstein, S. J., Current Status of Transition-State Theory. *J. Phys. Chem.* **1996**, *100*, 12771-12800.

33. Fernández-Ramos, A.; Ellingson, B. A.; Meana-Pañeda, R.; Marques, J. M.; Truhlar, D. G., Symmetry Numbers and Chemical Reaction Rates. *Theor. Chem. Acc.* **2007**, *118*, 813-826.

34. Eckart, C., The Penetration of a Potential Barrier by Electrons. *Phys. Rev.* **1930**, *35*, 1303.

35. McClurg, R. B.; Flagan, R. C.; Goddard III, W. A., The Hindered Rotor Density-of-States Interpolation Function. *J. Chem. Phys.* **1997**, *106*, 6675-6680.

36. Altarawneh, M.; Almatarneh, M. H.; Marashdeh, A.; Dlugogorski, B. Z., Decomposition of Ethylamine through Bimolecular Reactions. *Combust. Flame* **2016**, *163*, 532-539.

37. Robinson, R.; Lindstedt, R., A Comparative Ab Initio Study of Hydrogen Abstraction from *n*-Propyl Benzene. *Combust. Flame* **2013**, *160*, 2642-2653.

38. Kee, R. J.; Rupley, F. M.; Miller, J. A. Sandia Report Sand 89-8009B; Sandia National Laboratories; Livermore, CA, **1993**.

39. Moskaleva, L. V.; Lin, M. C., Theoretical Study of the NH_2 + C_2H_2 Reaction. *J. Chem. Phys.* **1998**, *102*, 4687-4693.

40. Berkowitz, J.; Ellison, G. B.; Gutman, D., Three Methods to Measure RH Bond Energies. *J. Chem. Phys.* **1994**, *98*, 2744-2765.

41. Manion, J. A.; Huie, R. E.; Levin, R. D.; Burgess Jr, D. R.; Orkin, V. L.; Tsang, W.; McGivern, W. S.; Hudgens, J. W.; Knyazev, V. D.; Atkinson, D. B. et al. NIST Chemical Kinetics Database, NIST Standard Reference Database 17, Version 7.0 (Web Version), Release 1.6.8, Data version 2016.10, National Institute of Standards and Technology, Gaithersburg, Maryland, 20899-8320. Web address: http://kinetics.nist.gov/, (retrieved October 26, 2016).

42. Aguilera-Iparraguirre, J.; Curran, H. J.; Klopper, W.; Simmie, J. M., Accurate Benchmark Calculation of the Reaction Barrier Height for Hydrogen Abstraction by the Hydroperoxyl Radical from Methane. Implications for C_nH_{2n+2} where $n = 2 \rightarrow 4$. *J. Phys. Chem. A.* **2008**, *112*, 7047-7054.

43. Carstensen, H.-H.; Dean, A. M.; Deutschmann, O., Rate Constants for the H Abstraction from Alkanes (R–H) by Radicals: A Systematic Study on the Impact of R and R′. *Proc. Combust. Inst.* **2007**, *31*, 149-157.

Chapter 5

Interaction of NH_2 radical with Alkylbenzenes

Siddique, K.; Altarawneh, M.; Gore, J.; Dlugogorski, B. Z., Interaction of NH_2 radical with Alkylbenzenes. *Combustion and Flame*. Submitted (in modified form) for publication 2017.

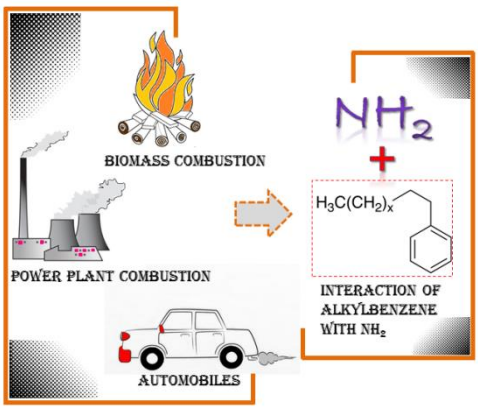

The current chapter lay out the interaction of amidogen radical (NH_2) with alkylbenzenes with the aim of finding thermochemistry and reaction kinetics of abstraction and addition reactions. It also reveals the feasible reaction pathways in regard to H abstraction from alkylbenzene by NH_2 radical or addition of NH_2 radical to the aromatic ring of alkylbenzenes.

5.1. Abstract

Abstraction of a H atom from the alkyl side chain, attached to a benzene ring, by the amidogen (NH_2) plays, critical importance in thermal processes that involve the presence of alkylbenzene species and NH_2-containing species, as in the pyrolysis of biomass. Yet, the literature provides no thermo-kinetic account of this important category of reactions. In this contribution, we compute standard reaction ($\Delta_r H^o_{298}$) and activation ($\Delta^{\neq} H^o_{298}$) enthalpies for H removal from the alkyl side chains in toluene, ethylbenzene and *n*-propylbenzene, as well as addition of NH_2 at the four possible sites of the phenyl ring in toluene and ethylbenzene. Abstraction of the benzylic H atom in toluene constitutes the sole feasible channel at all temperatures. The same finding applies to ethylbenzene, albeit with the gradual increase of the contribution from the channel of abstraction of primary H with increasing temperatures. In the all temperature regime, the rate constant of the abstraction of benzylic H in *n*-propylbenzene dominates that of the primary and secondary H atoms. The branching ratios confirm the dominance of H abstraction corridors over the addition channels, even at low temperatures. For primary H abstraction reactions, comparing reaction rate constants of alkylbenzenes with those of the analogous sites in alkanes indicates minor influence of the aromatic ring. The results of the present calculations apply to any branched aromatic hydrocarbon interacting with the NH_2 radical.

5.2. Introduction

A great deal of combustion research has focused on gaining an improved understanding of chemical events contributing to the emission of NO_x from nitrogen-rich fuels, most notably biomass. In complex reaction networks, hydrogen cyanide and ammonia serve as important gaseous precursors for the synthesis of NO_x from pyrolysis and combustion of coal and biomass.[1-9] Decomposition of hydrogen cyanide,[10] thermal degradation of alkyl amines[11] and oxidation of ammonia[12] produce the active amidogen intermediate (NH_2 radicals) in the course of chemical transformations of nitrogenous compounds. NH_2 radicals play a vital role in the combustion chemistry underlying co-gasification of coal with biomass,[11] oxidation of volatile nitrogen-linking compounds in biomass,[13] and oxidation and pyrolysis of ammonia.[12,14-16] In flames, CH and CH_2 intermediates react with molecular nitrogen, forming HCN, NH and H_2CN[17] that subsequently transform to NH_2 radical.

Aromatic compounds represent major constituents of petroleum-based fuels (~30 % in gasoline and ~20 % in diesel fuel).[18-22] In particular, alkylbenzenes account for a ~10 % mass fraction of diesel fuel.[23] The combustion of aliphatic hydrocarbons generates aromatic hydrocarbons that plays a key role in particulate emission, formation of polyaromatic hydrocarbons[24-25] and soot nucleation.[22] Branched aromatic hydrocarbons serve as anti-knocking agents in transportation fuels.[26] Reactions of NO_x species represent an important atmospheric sink for alkylbenzenes, especially in urban areas.[27] Generation of ammonia in petrol and diesel engines confirms the appearance of reactions that involve the amidogen radical.[28] Thus, it is evident that, aromatic alkylbenzenes[29-33] and NH_2 radicals [34-35] may co-exist in the combustion processes.[36-38]

In fact, literature has reported the presence of alkylbenzenes and ammonia in several combustion systems. For example, Nowakowska et al.[39] studied the pyrolysis and oxidation of anisole (a primary tar from pyrolysis of lignin) in a jet stirred reactor, under temperature and pressure conditions of 673 to 1173 K and 106.7 kPa, respectively. They observed the formation of aromatic compounds that included benzene, toluene and ethylbenzene in addition to polyaromatic and non-aromatic compounds. Hernandez et al.[40] characterised the tar formed in gasification of biomass, in a small-scale drop-tube pilot plant, reporting the detection of benzene, toluene, and ethylbenzene. Likewise, Wang et al.[41] analysed the emission characteristics of volatile organic compounds (VOCs) from biomass combustion to identify benzene, toluene, ethylbenzenes, propylbenzene and other aromatic compounds using gas chromatography-mass spectrometry (GC-MS) and gas chromatography coupled to flame ionisation and electron capture detectors (GC-FID/ECD). Similarly, ammonia appears as a product from industrial pyrolysis, gasification and combustion processes of coal and biomass.[42-43] Pyrolysis of fuel-bound nitrogen present in biomass yields NH_3 and HCN.[44-46] Along the same line of enquiry, Hansson et al.[38] reported the release of several nitrogen-containing species such as NH_3, HCN and HNCO from the pyrolysis of biomass in a fluidised bed reactor between 973 and 1273 K. Hansson et al.[44] also conducted the pyrolysis of biomass surrogates, poly-L-leucine and poly-L-proline, in a fluidised bed reactor between 973 and 1073 K, and identified NH_3, HCN and HNCO using an infrared spectrometer. Decomposition of alkylamines present in biofuels represents a direct corridor for the formation of NH_2 radical.[47] Thus, it stands to reason to investigate the interactions of NH_2 radical with alkylbenzenes and the underlying kinetics of the interactions, for these species occur together in combustion systems and in fuel-processing operations.

Literature provides accounts of reactions between NH_2 and several highly reactive (radical) species (e.g., NO_2, OH, NO, etc..[48-50] For example, over a wide range of temperatures and pressures, several experimental and theoretical studies reported kinetics of NH_2 reacting with aliphatic hydrocarbons.[51-55] In particular, Mebel and Lin performed theoretical thermo-kinetic computations, based on Gaussian-2 method (GM), on plausible H abstraction from distinct sites in alkanes (primary, secondary and tertiary sites) with NH_2 in the temperature window of 300–2000 K.[55] Nonetheless, there is clear scarcity of kinetic data for H abstraction from alkylbenzenes by NH_2 when compared with the analogous reactions involving OH, HO_2 and CH_3 radicals.[56-59]

This contribution reports the results from a theoretical investigation into reactions of NH_2 with toluene, ethylbenzene and *n*-propylbenzene. These three molecules represent model compounds of alkylbenzenes. More specifically, we study abstraction (primary, secondary and benzylic) and addition (*ipso*, *ortho*, *meta* and *para*) channels for the title alkylbenzene molecules. To the best of my knowledge, literature provides no kinetic data on reactions of NH_2 with the above-mentioned species. The current study expands on-going efforts to provide a comprehensive kinetic database for the reactions of NH_2 with RH species.[60-61] It has a threefold aim, to: (i) provide reaction rate parameters for H abstractions by NH_2 from the side chain in alkylbenzene; (ii) compare the contribution of the addition channel with the generally more feasible abstraction route from the alkyl chain; and, (iii) assess the influence of the aromatic ring on the kinetics and thermodynamics of the reactions between alkanes and NH_2 radicals. The thermo-kinetic parameters developed in this contribution will underpin further development of robust kinetic models for the pyrolysis of nitrogen-rich fuels.

5.3. Reaction systems and computational methods

Herein, the current study entails H abstraction reactions from the alkyl side chain in toluene, ethylbenzene, and *n*-propylbenzene by NH_2. Prefixes *p*, *s* and *b* are used to denote removal of a hydrogen atom from primary, secondary and benzylic C–H sites, respectively, of the alkylbenzene side chain. Addition reactions comprise attachment of the NH_2 at *ipso*, *ortho*, *meta*, and *para* sites in toluene and ethylbenzene. The two sequences of reactions can thus be written as:

Abstraction

Toluene	$C_6H_5CH_3 + NH_2 \rightarrow NH_3 + b\text{-}C_7H_7$	(R1)
Ethylbenzene	$C_6H_5C_2H_5 + NH_2 \rightarrow NH_3 + p\text{-}C_8H_9$	(R2)
	$C_6H_5C_2H_5 + NH_2 \rightarrow NH_3 + b\text{-}C_8H_9$	(R3)
n-Propylbenzene	$C_6H_5C_3H_7 + NH_2 \rightarrow NH_3 + p\text{-}C_9H_{11}$	(R4)
	$C_6H_5C_3H_7 + NH_2 \rightarrow NH_3 + s\text{-}C_9H_{11}$	(R5)
	$C_6H_5C_3H_7 + NH_2 \rightarrow NH_3 + b\text{-}C_9H_{11}$	(R6)
Propane	$C_3H_8 + NH_2 \rightarrow NH_3 + p\text{-}C_3H_7$	(R7)
	$C_3H_8 + NH_2 \rightarrow NH_3 + s\text{-}C_3H_7$	(R8)
n-Butane	$n\text{-}C_4H_{10} + NH_2 \rightarrow NH_3 + p\text{-}C_4H_9$	(R9)
	$n\text{-}C_4H_{10} + NH_2 \rightarrow NH_3 + s\text{-}C_4H_9$	(R10)

Addition

Toluene	$C_6H_5CH_3 + NH_2 \rightarrow ipso\text{-}(C_7H_8)NH_2$	(R11)
	$C_6H_5CH_3 + NH_2 \rightarrow ortho\text{-}(C_7H_8)NH_2$	(R12)
	$C_6H_5CH_3 + NH_2 \rightarrow meta\text{-}(C_7H_8)NH_2$	(R13)

$C_6H_5CH_3 + NH_2 \rightarrow$ *para*-$(C_7H_8)NH_2$ (R14)

Ethylbenzene

$C_6H_5C_2H_5 + NH_2 \rightarrow$ *ipso*-$(C_8H_{10})\ NH_2$ (R15)

$C_6H_5C_2H_5 + NH_2 \rightarrow$ *ortho*-$(C_8H_{10})\ NH_2$ (R16)

$C_6H_5C_2H_5 + NH_2 \rightarrow$ *meta*-$(C_8H_{10})\ NH_2$ (R17)

$C_6H_5C_2H_5 + NH_2 \rightarrow$ *para*-$(C_8H_{10})\ NH_2$ (R18)

The Gaussian09[62] suite of programs executes structural optimisations, vibrational-frequency calculations and total-energy computations at the accurate composite model of CBS-QB3. The CBS-QB3 approach comprises a complete-basis-set model with initial geometry optimisation and frequency calculations performed at the B3LYP/6-311G(2d,d,p) level of theory, followed by successive estimation of single point energies at higher ab initio levels.[63-66] Thermochemical properties across a wide range of temperatures (300 – 2000 K) calculated using ChemRate[67] software and reported as Tables S5.1 in Appendix II of Supporting Information (SI). All values of standard activation ($\Delta^{\ddagger}H^{o}_{298}$) and standard reaction ($\Delta_r H^{o}_{298}$) enthalpies are calculated at 298.15 K.

KiSThelP[68] code provides estimates of the kinetic parameters with the inclusion of the one-dimensional Eckart barrier to account for the possible contribution from the quantum tunnelling effect.[69] The conventional transition state theory (TST) affords the computation of kinetic parameters.[70-71] Total reaction degeneracy, which accounts for multiple conformers and reaction sites, is simply evaluated by multiplying a symmetry number of each reaction by the quantity of equivalent abstractable hydrogen atoms employing the methodology of Fernández-Ramos et al.[71]

We performed hindered-rotor calculations to account for the internal rotations in reactants and transition structures. In this formalism, we carry out partial optimisations along the corresponding angles for the rotation of methyl, ethyl and propyl groups. The two internal rotations of the methyl and the groups in ethylbenzene correspond to vibrational frequencies of 220.8 cm^{-1} (barrier of 14.1 kJ mol^{-1}) and 50.9 cm^{-1} (barrier of 4.9 kJ mol^{-1}), respectively. Similarly, the three rotational barriers in *n*-propylbenzene (methyl, ethyl and propyl groups) amount to torsional barriers of 5.3 kJ mol^{-1}, 12.4 kJ mol^{-1} and 22.6 kJ mol^{-1}, correspondingly. The internal rotation in the methyl group in toluene displays a very low barrier of 0.07 kJ mol^{-1}, permitting its treatment as a free rotor. In the previous studies, the unique coupling of internal rotations of the methyl and ethyl groups in alkylbenzenes and their effects on reaction kinetics are addressed in detail. [59,72] The barriers were obtained for internal rotations in transition states by performing single point energy calculations at B3LYP/6-31G(d) while varying the corresponding dihedral angles. Overall, rotational barriers for methyl, ethyl and propyl groups in transition states exhibit values similar to those displayed by the ground-state molecules.

Several literature studies have provided accuracy benchmarks for the CBS-QB3 method[73] in estimating thermochemical and kinetic parameters for H atom abstraction and transfer reactions in hydrocarbons.[47,59,74-76] The literature studies on H abstraction reactions from ethylbenzene and *n*-propylbenzene by HO_2 set a benchmark for the accuracy of the adopted computational methodology. These studies employed the isodesmic reactions to calculate the standard enthalpy of formation of ethylbenzene, *n*-propylbenzene and their derived radicals, to obtain enthalpies of formation to 4.5 kJ mol^{-1} mean absolute deviation from experimental values.[59,77] Also, our calculated bond dissociation enthalpy (BDH) for the benzylic C–H amounts to 379.1 kJ mol^{-1}; a value that concurs closely with the analogous experimental

measurement of 375±4 kJ mol^{-1}.[78] The overall mean absolute deviation of BDH (C–H bond) for the titled reactions amounts to 4.5 kJ mol^{-1}. Lastly, as an estimate of the expected accuracy of the present results, we note that, our previously reported combined rate constants of primary and secondary H abstraction from ethylbenzene by HO_2 display difference of 1.50 times from the analogous experimental measurements.[77] Table 5.1 compares the experimental enthalpy change of reactions ($\Delta_r H^o_{298}$) with the analogous CBS-QB3 values for Reactions R1–R6, with the mean unsigned error estimated as 7.0 kJ mol^{-1}. The $\Delta_r H^o_{298}$ values are derived from the measured standard heat of formation of individual species in each reaction and their values are provided as Supplementary Information (SI) in Appendix II as Table S5.2. This good agreement should serve as a benchmark for the accuracy underpinning the thermochemical values reported herein.

Table 5.1. Comparison of computed (CBS-QB3) and literature (derived from experimental heat of formation of reactants and products) standard enthalpies of reactions ($\Delta_r H^o_{298}$) for reactions R1–R6. All values are in kJ mol^{-1}. Supporting Information provides sources for the literature data as table S5.2.

Reactions	Literature[a] $\Delta_r H^o_{298}$	CBS-QB3 $\Delta_r H^o_{298}$	Absolute deviation
R1	-75.3	-71.2	4.1
R2	-27.1	-20.6	6.5
R3	-88.0	-79.6	8.4
R4	-29.9	-22.4	7.5
R5	-34.5	-33.7	0.8
R6	-92.0	-77.6	14.5
		Mean unsigned error	7.0

5.4. Results and discussion

5.4.1. H Abstraction reactions

Because of the significant difference in the BDH values of aromatic C–H bonds (~460.0 kJ mol^{-1})[59] in comparison with those of the C–H bonds on the alkyl side chain (~360.0–422.0 kJ mol^{-1}),[59,72,78] the analysis of the abstraction channels to the side chains is considered for the analysis. The study on HO_2 + ethylbenzene indicated a negligible contribution from benzene-

ring hydrogens to the overall H abstraction.[72] Ethylbenzene comprises three different types of C–H bonds, namely, the aromatic C–H bonds on the phenyl ring, benzylic ethyl bonds (–CH_2–) and primary methyl bonds (–CH_3–). An additional type of secondary C–H bond exists in the *n*-propylbenzene molecule. Figure 5.1 illustrates the optimised structure of the three considered alkylbenzenes and their derived radicals. Figure 5.2 portrays optimised structures of the transition states in the abstraction channels while labels of the transition structures reflect reaction numbers. Transition states TS1, TS3, TS5 and TS6 exhibit truly reactant-like characters. C–H bond distances are shorter than the N–H bond distances, indicating that the transition states occur at the beginning of the reactions, when the NH_2 radical remains somewhat far from the reactant. The transition states TS2 and TS4 acquire the same C–H and N–H bond length, that is 1.30 Å. This result agrees with Hammond's[79] postulate that transition states of exothermic reactions typically exhibit a more reactants-like character rather than a product-like character.

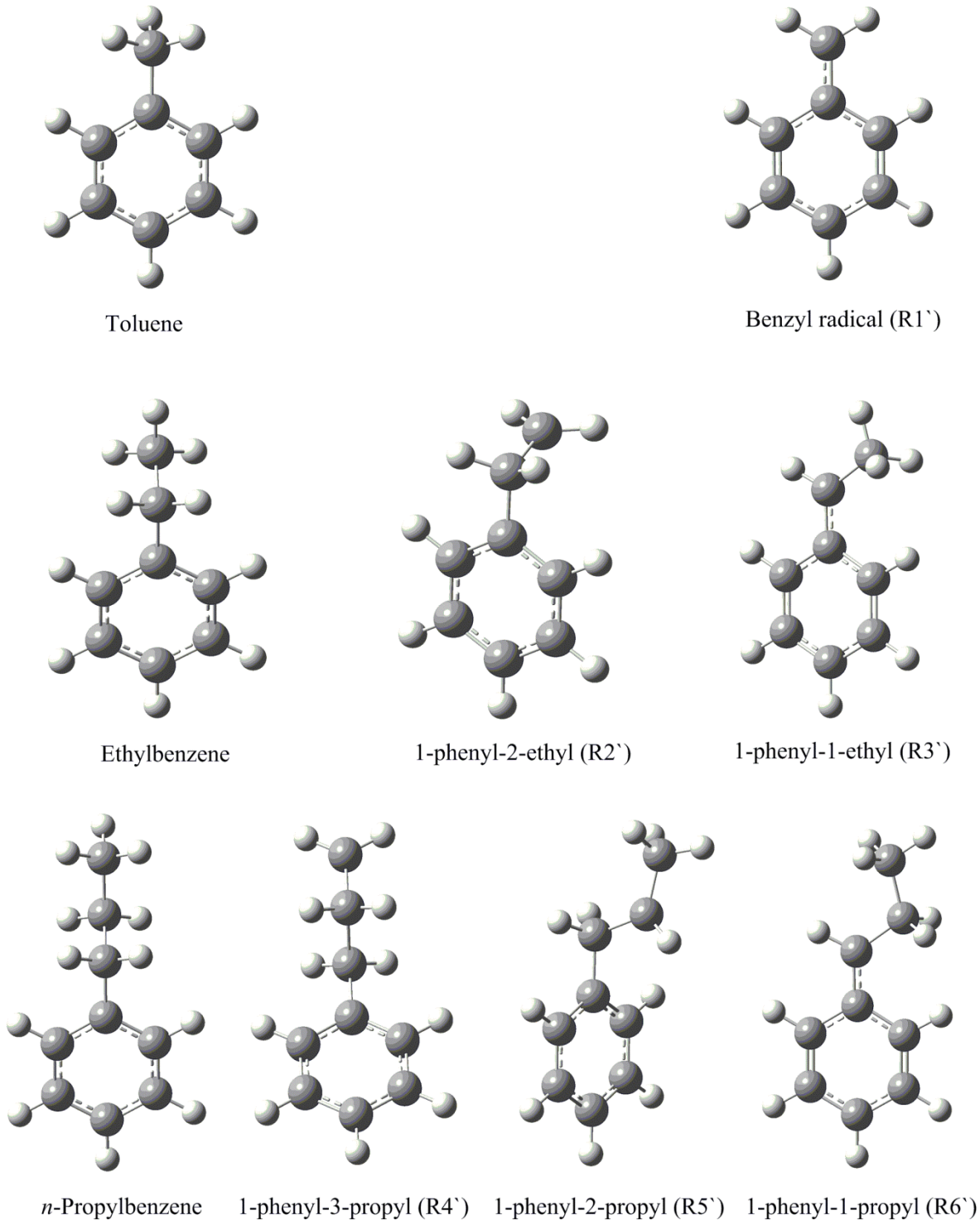

Figure 5.1. Optimised geometries of toluene, ethylbenzene, *n*-propylbenzene and their derived radicals. Distances are in Å.

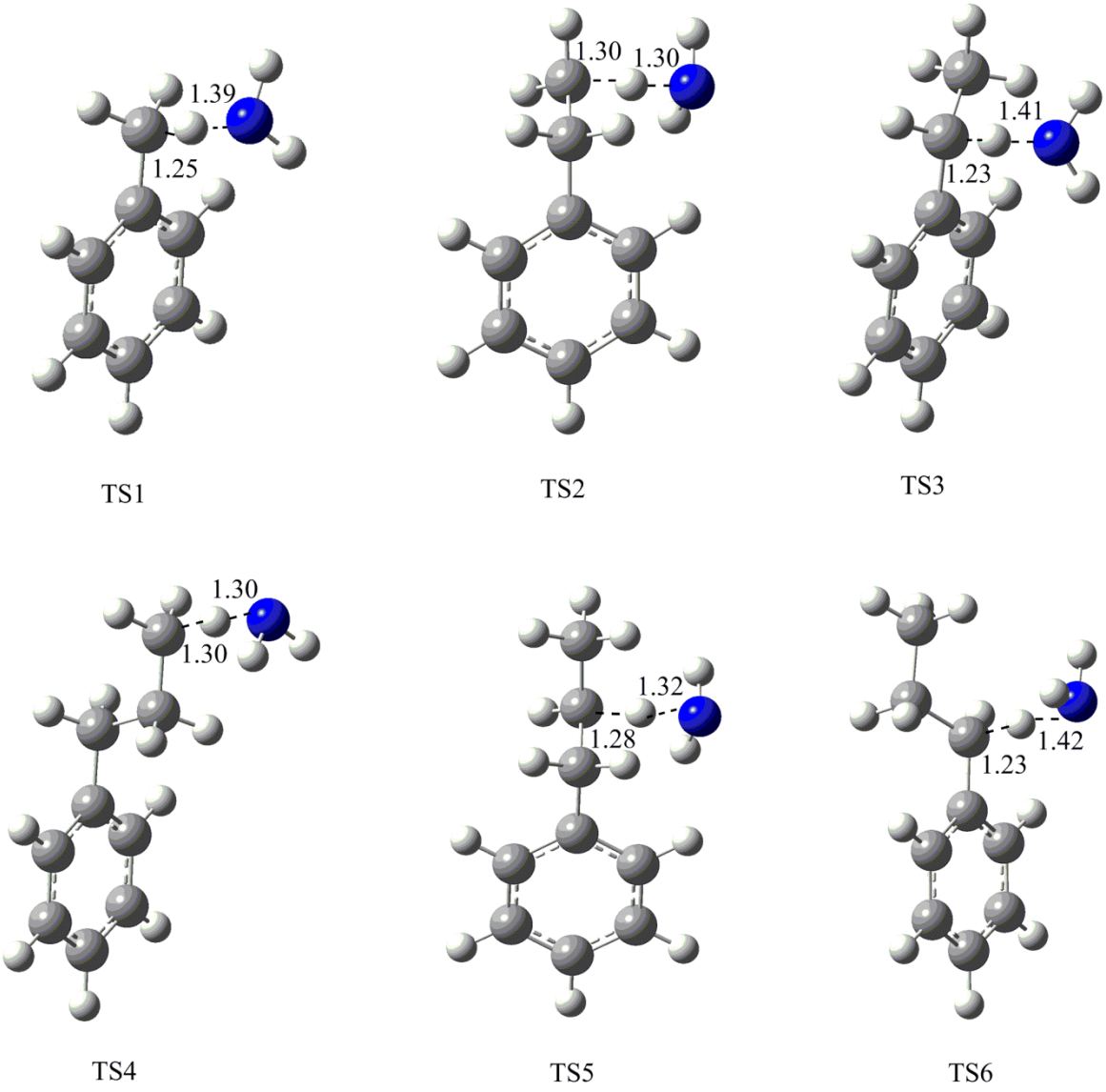

Figure 5.2. Optimised geometries of the transition states for the H abstraction by the NH_2 radical from alkylbenzenes. Distances are in Å.

The BDH value of the benzylic H in toluene is significantly weaker than the aromatic C–H bonds (459.8 kJ mol^{-1}).[80-81] The calculated BDH for the benzylic C–H bond in toluene amounts to 379.1 kJ mol^{-1} and concurs well with the analogous experimental value of 375±4 kJ mol^{-1}.[78] Tully et al.[82] investigated the abstraction of H atom from toluene and benzene by

OH radicals in the temperature and pressure ranges of 213–1150 K and 0.02–0.26 bar, respectively. Experimental results revealed that, at temperatures above 500 K, the H abstraction channel in both molecules, benzene (aromatic C–H) and toluene (side chain H), predominates the addition route. The authors attributed this trend to profound instability of OH–ring adducts, the initial intermediate encountered in the addition channel. Likewise, Seta et al. also corroborated the dominant importance of the H abstraction channel over the addition mechanism during interaction of OH radicals with benzene (at 908–1736 K) and toluene (at 919–1481 K).[22] Similarly, the previous study of ethylbenzene + HO_2,[72] the contribution of the H the corresponding relative importance of the abstraction and addition channels for the studied NH_2 + alkylbenzene systems is discussed.

Table 5.2 lists $\Delta_r H^o_{298}$ and $\Delta^{\ddagger} H^{\circ}_{298}$ values for Reactions R1–R18. For Reaction R1 (toluene), $\Delta^{\ddagger} H^o_{298}$ of H abstraction from the benzylic site by NH_2 amounts to 29.5 kJ mol^{-1} with a corresponding $\Delta_r H^o_{298}$ of -71.2kJ mol^{-1}. Since literature provides no $\Delta^{\ddagger} H^o_{298}$ values for any of the investigated reactions, the benchmark on the accuracy of $\Delta^{\ddagger} H^o_{298}$ is studied by contrasting them with those of other hydrocarbons with similar C–H BDHs. This comparison also allows us to remark on the effect of the aromatic ring on the thermodynamics and kinetics of H abstraction from alkanes. For example, the BDH value of the weakest C–H bond in 2-butyne corresponds to 379.5 kJ mol^{-1},[61] which corroborates the current calculated BDH of the benzylic C–H bond in toluene of 379.1 kJ mol^{-1}. Likewise, estimates of $\Delta^{\ddagger} H^o_{298}$ for the toluene + NH_2 and 2-butyne + NH_2 reactions reveal disparity of only 2.2 kJ mol^{-1}. In view of the difference in BDHs between the two distinct C–H bonds in the ethyl group in ethylbenzene (421.3 kJ mol^{-1} versus 359.9 kJ mol^{-1}),[72] H abstraction in Reaction R2 (primary) is associated with a higher $\Delta^{\ddagger} H^o_{298}$ value of 32.4 kJ mol^{-1} when contrasted with $\Delta^{\ddagger} H^o_{298}$ of 23.9 kJ mol^{-1} (benzylic) of Reaction R3.

Table 5.2. Standard activation ($\Delta^{\ddagger}H^{o}_{298}$) and standard reaction ($\Delta_r H^{o}_{298}$) enthalpies of abstraction and addition channels for toluene, ethylbenzene and *n*-propylbenzene. All values are in kJ mol^{-1}.

Reactants	Products	Reactions	Activation enthalpy $\Delta^{\ddagger}H^{o}_{298}$	Reaction enthalpy $\Delta_r H^{o}_{298}$
$C_6H_5CH_3 + NH_2$	NH_3 + *b*-$C_6H_5CH_2$	R1	29.5	-71.2
	ipso-$(C_6H_5CH_3)NH_2$	R11	27.2	-46.7
	ortho-$(C_6H_5CH_3)NH_2$	R12	22.9	-69.7
	meta-$(C_6H_5CH_3)NH_2$	R13	30.6	-31.7
	para-$(C_6H_5CH_3)NH_2$	R14	30.9	-42.0
$C_6H_5C_2H_5 + NH_2$	NH_3 + *p*-$C_6H_5C_2H_4$	R2	32.4	-20.7
	NH_3 + *b*-$C_6H_5C_2H_4$	R3	23.9	-79.6
	ipso-$(C_6H_5C_2H_5)NH_2$	R15	25.2	-48.9
	ortho-$(C_6H_5C_2H_5)NH_2$	R16	24.5	-43.6
	meta-$(C_6H_5C_2H_5)NH_2$	R17	33.8	-38.3
	para-$(C_6H_5C_2H_5)NH_2$	R18	34.1	-37.7
$C_6H_5C_3H_7 + NH_2$	NH_3 + *p*-$C_6H_5C_3H_6$	R4	37.5	-22.4
	NH_3 + *s*-$C_6H_5C_3H_6$	R5	35.6	-33.7
	NH_3 + *b*-$C_6H_5C_3H_6$	R6	26.4	-77.5

In order to reveal the effect of the aromatic ring on the energetics of studied title reactions, Table 5.3 compares $\Delta_r H^{o}_{298}$ and $\Delta^{\ddagger}H^{o}_{298}$ for H abstraction by NH_2 from alkanes and their

corresponding alkylbenzenes at 298.15 K. For abstraction of primary H, $\Delta^{\ddagger}H^{o}_{298}$ of Reaction R2 (32.4 kJ mol^{-1}) concurs well with that of Reaction R7 (34.9 kJ mol^{-1}). This indicates a nominal influence of the electron delocalised aromatic system on the kinetics of H abstraction by NH_2. The BDH value of primary C–H bond in ethylbenzene (421.3 kJ mol^{-1})[72] closely matches the corresponding value in propane (428.4 kJ mol^{-1}),[61] which justifies a marginal difference in $\Delta^{\ddagger}H^{o}_{298}$ for H abstraction from the primary C–H bond in the two molecules; i.e., 32.4 kJ mol^{-1} versus 34.9 kJ mol^{-1}.

Table 5.3. Standard activation ($\Delta^{\ddagger}H^{o}_{298}$) and standard reaction ($\Delta_r H^{o}_{298}$) enthalpies for H abstraction by NH_2 from selected alkylbenzenes and alkanes. All values are in kJ mol^{-1}.

	Reactions	Reactants	Products	Reaction enthalpy $\Delta_r H^{o}_{298}$	Activation enthalpy $\Delta^{\ddagger}H^{o}_{298}$
Primary-H	R2	$C_6H_5C_2H_5 + NH_2$	$NH_3 + p\text{-}C_6H_5C_2H_4$	-20.6	32.4
	R4	$n\text{-}C_6H_5C_3H_7 + NH_2$	$NH_3 + p\text{-}C_6H_5C_3H_6$	-22.4	37.5
	R7	$C_3H_8 + NH_2$	$NH_3 + p\text{-}C_3H_7$	-21.8	34.9[a]
	R9	$n\text{-}C_4H_{10} + NH_2$	$NH_3 + p\text{-}C_4H_9$	-23.8	34.5[b]
Secondary-H	R5	$n\text{-}C_6H_5C_3H_7 + NH_2$	$NH_3 + s\text{-}C_6H_5C_3H_6$	-33.7	35.6
	R8	$C_3H_8 + NH_2$	$NH_3 + s\text{-}C_3H_7$	-36.4	26.8[c]
	R10	$n\text{-}C_4H_{10} + NH_2$	$NH_3 + s\text{-}C_4H_9$	-35.5	25.0[d]
Benzylic-H	R1	$C_6H_5CH_3 + NH_2$	$NH_3 + b\text{-}C_6H_5CH_2$	-71.2	29.4
	R3	$C_6H_5C_2H_5 + NH_2$	$NH_3 + b\text{-}C_6H_5C_2H_4$	-79.3	23.8
	R6	$n\text{-}C_6H_5C_3H_7 + NH_2$	$NH_3 + b\text{-}C_6H_5C_3H_6$	-77.5	26.4

[a,b,c,d]Ref. 61

The alkyl chain in *n*-propylbenzene displays three distinct C–H bonds, namely, benzylic propyl bonds (–CH_2–), secondary ethyl bonds (–CH_2–) and primary methyl bonds (CH_3–). The resonance stabilised benzylic radical of Reaction R6 displays a noticeable difference in BDH in comparison with the genuine secondary and primary radicals. Scission of a secondary C–H bond requires a higher BDH (410.4 kJ mol^{-1}) than that of the separation of the benzylic C–H bond (372.4 kJ mol^{-1}), but lower than that of the primary C–H (420.5 kJ mol^{-1}).[59]

The standard enthalpy of activation of H abstraction of the primary C–H bond in Reaction R4, the secondary C–H bond in Reaction R5 and the benzylic C–H site in Reaction R6 attain values of 37.5 kJ mol^{-1}, 35.6 kJ mol^{-1} and 26.4 kJ mol^{-1} with corresponding $\Delta_r H^o_{298}$ -22.4 kJ mol^{-1}, -33.7 kJ mol^{-1} and -77.5 kJ mol^{-1}, respectively Thus, $\Delta_r H^o_{298}$ and $\Delta^{\ddagger} H^o_{298}$ for *n*-propylbenzene display a proportional correlation. This trend is in line with the decreasing strength of the C–H bond in *n*-propylbenzene (primary > secondary > benzylic). For example, NH_2 prefers to attack the weakest C–H site (benzylic) in the *n*-propylbenzene that shows the most favorable reaction pathways with $\Delta^{\ddagger} H^o_{298}$ of 26.4 kJ mol^{-1} and $\Delta_r H^o_{298}$ of -77.5 kJ mol^{-1}. We previously noticed a similar trend of decreasing $\Delta^{\ddagger} H^o_{298}$ for abstraction of primary to benzylic H for the reaction of *n*-propylbenzene + HO_2.[59] The value of $\Delta^{\ddagger} H^o_{298}$ calculated for H abstraction from the primary C–H bond in *n*-butane (R9, 34.5 kJ mol^{-1}) reasonably matches with the $\Delta^{\ddagger} H^o_{298}$ for the analogous quantity in *n*-propylbenzene (R4, 37.5 kJ mol^{-1}). Conversely, $\Delta^{\ddagger} H^o_{298}$ for abstraction of the secondary C–H atom in *n*-propylbenzene (R5, 35.6 kJ mol^{-1}) overestimates the analogous abstraction from the secondary C–H site in *n*-butane (R10, 25.0 kJ mol^{-1}). Notably, both reactions share very similar $\Delta_r H^o_{298}$ values at -33.7 kJ mol^{-1} and -35.5 kJ mol^{-1}. Finally, inspection of $\Delta^{\ddagger} H^o_{298}$ values for H abstraction from the benzylic C–H in the three considered alkylbenzenes

indicates a noticeable effect for the alkyl chain, with $\Delta^{\ddagger}H^{o}_{298}$ for abstraction from the benzylic C–H in toluene exceeding those for ethylbenzene and *n*-propylbenzene by 5.6 kJ mol^{-1} and 3.0 kJ mol^{-1}, respectively. This indicates the necessity of some carefully tailored adjustments when attempting to generalise kinetics of H abstraction from toluene to higher alkylbenzenes.

5.4.2. NH_2 addition channels

As the phenyl ring in alkylbenzene is aromatic, we anticipate that, the length of alkyl chain exerts minimal influence on the kinetics of the NH_2 addition to the phenyl ring. For this reason, we have only studied the addition channels for toluene and ethylbenzene. Figure 5.3 reveals the transition structures of the addition channel of NH_2 to the phenyl ring of toluene. Table 5.2 lists the $\Delta^{\ddagger}H^{o}_{298}$ and $\Delta_r H^{o}_{298}$ values for the four addition channels. Addition of NH_2 radical results in slightly displaced (from planarity) methyl group (for addition at *ipso* position) and H atoms (for additions at *ortho, meta* and *para* sites). Addition at an *ortho* site in toluene (R12) displays the lowest $\Delta^{\ddagger}H^{o}_{298}$ value (22.9 kJ mol^{-1}) and the highest reaction exothermicity ($\Delta_r H^{o}_{298}$ at -69.7 kJ mol^{-1}) among the all four addition corridors in toluene. The formation of *meta* NH_2-toluene in Reaction R13 and *para* adduct via Reaction R14 adducts leads to similar values of $\Delta^{\ddagger}H^{o}_{298}$ values of 30.6 and 30.9 kJ mol^{-1} with the corresponding estimates of $\Delta_r H^{o}_{298}$ as -31.7 and -42.0 kJ mol^{-1}, respectively. The standard activation enthalpy for addition of NH_2 at an *ipso* site of toluene in Reaction R11 amounts to 27.2 kJ mol^{-1} with $\Delta_r H^{o}_{298}$ of -46.7 kJ mol^{-1}.

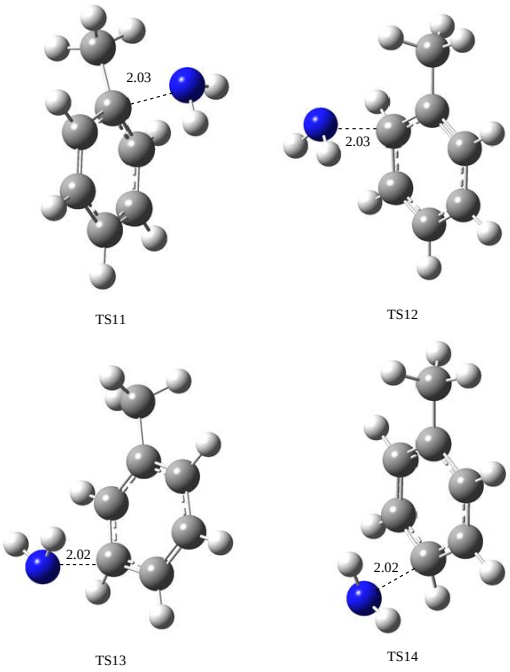

Figure 5.3. Optimised geometries of the transition states for the addition of the NH_2 radical to toluene. Distances are in Å.

Figure 5.4 depicts the transition-state geometries of the addition channel of NH_2 to the phenyl ring of ethylbenzene, with the related values of $\Delta^{\ddagger}H^{o}_{298}$ and $\Delta_r H^{o}_{298}$ assembled in Table 5.2. Similarly to Reaction R12, addition of NH_2 at an *ortho* site (R16) of the phenyl ring in ethylbenzene exhibits the smallest $\Delta^{\ddagger}H^{o}_{298}$ (24.5 kJ mol^{-1}) with the largest reaction exothermicity $\Delta_r H^{o}_{298}$ (-43.6 kJ mol^{-1}) next to Reaction R15. The production of the *meta* moiety in Reaction R17 and the *para* adduct in Reaction R18 demands $\Delta^{\ddagger}H^{o}_{298}$ of 33.8 and 34.1 kJ mol^{-1} with corresponding $\Delta_r H^{o}_{298}$ of -38.3 and -37.7 kJ mol^{-1}, respectively. The standard activation enthalpy for addition of NH_2 at an *ipso* site in Reaction R15 requires a modest activation enthalpy of 25.2 kJ mol^{-1} with $\Delta_r H^{o}_{298}$ of -48.9 kJ mol^{-1}.

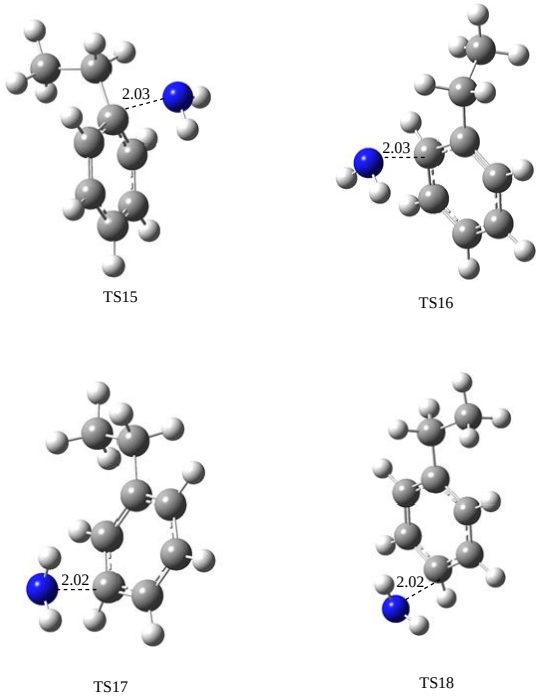

Figure 5.4. Optimised geometries of the transition states for the addition reactions of the NH_2 radical to ethylbenzene. Distances are in Å.

Based on the energetics reported in Table 5.2, addition channels at the *para* and *meta* sites in toluene and ethylbenzene require higher $\Delta^{\ddagger}H^{o}_{298}$ than the plausible abstraction corridors. For example, addition of NH_2 at the *meta* and *para* sites of the phenyl ring in toluene necessitates $\Delta^{\ddagger}H^{o}_{298}$ of 30.6 kJ mol^{-1} and 30.9 kJ mol^{-1}, respectively, while attachments of NH_2 to the *ortho* and *ipso* sites proceed through barriers of 22.9 kJ mol^{-1} and 27.2 kJ mol^{-1}, respectively. These values contrast with that for the abstraction of H from the methyl group in toluene of $\Delta^{\ddagger}H^{o}_{298}$ of 29.5 kJ mol^{-1}. In the ethylbenzene + NH_2 system, abstraction of the benzylic H requires the lowest $\Delta^{\ddagger}H^{o}_{298}$ (23.9 kJ mol^{-1}) followed by addition of NH_2 at an *ortho* site (24.5 kJ mol^{-1}) and at an *ipso* position (25.2 kJ mol^{-1}). Addition of NH_2 at the *meta* (33.8 kJ mol^{-1}) and *para* (34.1 kJ mol^{-1}) sites of the aromatic ring of ethylbenzene incur higher $\Delta^{\ddagger}H^{o}_{298}$, while the abstraction channel via the primary site exhibits a barrier of 32.4 kJ mol^{-1}. The previous study demonstrated that, the abstraction of H from benzene by NH_2 (barrier of 58.6

kJ mol^{-1}) dominates the addition of NH_2 to the benzene ring (barrier of 62.8 kJ mol^{-1}).[60] Below, we address the effect of entropy of activation on the reaction rates that make the abstraction of hydrogen atoms from side chains as the preferred initiation route.

5.4.3. Reaction kinetics

As conveyed earlier, the recent work on reactions of HO_2 radicals with ethylbenzene[72,83] and *n*-propylbenzene[59] revealed that, the abstraction of an aromatic H is of negligible significance, if compared with the dominant channels that remove hydrogen atoms from ethyl and propyl chains. Therefore, in this study, the kinetic analysis is limit to the most important benzylic, secondary and primary H abstraction channels and addition of NH_2 at four possible sites on the aromatic ring in toluene and ethylbenzene.

Table 5.4 assembles the Arrhenius parameters, and Figure S5.1 (in Appendix II- SI) draws the Arrhenius plots of the rates for abstraction Reactions R1–R6. Likewise, Figure S5.2 portrays Arrhenius plots while Table 5.5 lists the kinetic parameters for the addition of NH_2 radical at *ipso*, *ortho*, *meta* and *para* sites of toluene. Formation of *ortho*-$(C_6H_5CH_3)NH_2$ in Reaction R12 represents the dominant addition channel in the low temperature window of 300–600 K over the three other addition corridors with the rate expression of $k(T) = 1.45\times10^{-13}$ $\exp(-47\,800/(RT))$ cm^3 s^{-1} $molecule^{-1}$, whereas the formation of the *meta*-$(C_6H_5CH_3)NH_2$ adduct in Reaction R13 governs the NH_2 addition between 600–2000 K with the reaction rate of $k(T) = 7.55\times10^{-14}$ $\exp(-52\,700/(RT))$ cm^3 s^{-1} $molecule^{-1}$. Formation of *para*-$(C_6H_5CH_3)NH_2$ in Reaction R14 constitutes the slowest reaction pathway among the addition routes. Figure S5.3 (Appendix II-SI) draws the Arrhenius plots for ethylbenzene + NH_2 addition reactions in which the *ipso* and *ortho* sites exhibit comparable importance.

Table 5.4. Kinetic parameters for abstraction of H atom by NH_2 radicals from selected alkylbenzenes. Reaction rate constants are fitted in the temperature range of 300-2000 K. Values of the Arrhenius parameters (A and E_a) are in units of $cm^3\ s^{-1}$ molecule^{-1} and kJ mol^{-1}, respectively.

	Reactant	Products	A	E_a
R1	$C_6H_5CH_3 + NH_2$	$NH_3 + b\text{-}C_6H_5CH_2$	1.65×10^{-10}	42.5
R2	$C_6H_5C_2H_5 + NH_2$	$NH_3 + p\text{-}C_6H_5C_2H_4$	4.53×10^{-11}	41.0
R3	$C_6H_5C_2H_5 + NH_2$	$NH_3 + b\text{-}C_6H_5C_2H_4$	8.65×10^{-11}	36.2
R4	$n\text{-}C_6H_5C_3H_7 + NH_2$	$NH_3 + p\text{-}C_6H_5C_3H_6$	7.19×10^{-11}	44.9
R5	$n\text{-}C_6H_5C_3H_7 + NH_2$	$NH_3 + s\text{-}C_6H_5C_3H_6$	8.83×10^{-12}	44.7
R6	$n\text{-}C_6H_5C_3H_7 + NH_2$	$NH_3 + b\text{-}C_6H_5C_3H_6$	1.04×10^{-10}	37.5

Table 5.5. Kinetic parameters for addition of NH_2 radical at four possible sites of selected alkylbenzenes. Reaction rate constants are fitted in the temperature range of 300–2000 K. Values of the Arrhenius parameters (A and E_a) are in units of $cm^3\ s^{-1}\ molecule^{-1}$ and $kJ\ mol^{-1}$, respectively.

	Reactant	Products	A	E_a
R11	$C_6H_5CH_3 + NH_2$	*ipso*-$(C_6H_5CH_3)NH_2$	7.55×10^{-14}	52.7
R12	$C_6H_5CH_3 + NH_2$	*ortho*-$(C_6H_5CH_3)NH_2$	1.45×10^{-13}	47.8
R13	$C_6H_5CH_3 + NH_2$	*meta*-$(C_6H_5CH_3)NH_2$	4.87×10^{-13}	54.7
R14	$C_6H_5CH_3 + NH_2$	*para*-$(C_6H_5CH_3)NH_2$	1.56×10^{-13}	70.3
R15	$C_6H_5C_2H_5 + NH_2$	*ipso*-$(C_6H_5C_2H_5)NH_2$	5.26×10^{-13}	52.9
R16	$C_6H_5C_2H_5 + NH_2$	*ortho*-$(C_6H_5C_2H_5)NH_2$	1.20×10^{-12}	52.5
R17	$C_6H_5C_2H_5 + NH_2$	*meta*-$(C_6H_5C_2H_5)NH_2$	1.31×10^{-12}	61.7
R18	$C_6H_5C_2H_5 + NH_2$	*para*-$(C_6H_5C_2H_5)NH_2$	2.30×10^{-12}	61.9

Based on the reaction rate constants given in Tables 5.4 and 5.5 for toluene, one can readily note the dominance of H abstraction from a benzylic H site. Addition at the phenyl ring assumes negligible importance at all temperatures. While the addition channels in toluene incur slightly higher activation energies than the abstraction of benzylic H, the higher A factor for the latter defines its dominant character. Lower A factors for the addition channels stem from the lower entropy changes between transition states and separated reactants, in comparison to the abstraction channels, as depicted in Figure S5.4 (Appendix II- SI). The sum of the contribution from the four addition pathways in toluene, within temperature range of 300–2000 K, peaks at 2.4 %, and conveys minimal importance of the addition channel even at low temperatures.

Figure 5.5 illustrates the branching ratios for all addition and abstraction channels in ethylbenzene. The benzylic H abstraction channel (R2) dominates over the entire temperature interval of between 300–2000 K. The maximum contribution from primary H abstraction in Reaction R1 reaches 28.3 % at the far end of the temperature region (2000 K) and only 7.1 % towards the lower temperature window (300 K). Similarly to the insignificance of NH_2 addition to toluene, the formation of the NH_2-phenyl ring adduct for ethylbenzene displays negligible importance. The overall contribution from the addition of NH_2 at *ipso*, *ortho*, *meta* and *para* sites of the aromatic ring in ethylbenzene sums up to a maximum of 9.3 %. The dominance of the abstraction channel (mainly benzylic) in the case of NH_2 matches the analogous behaviour that we found for reactions of HO_2 with ethylbenenze.[72]

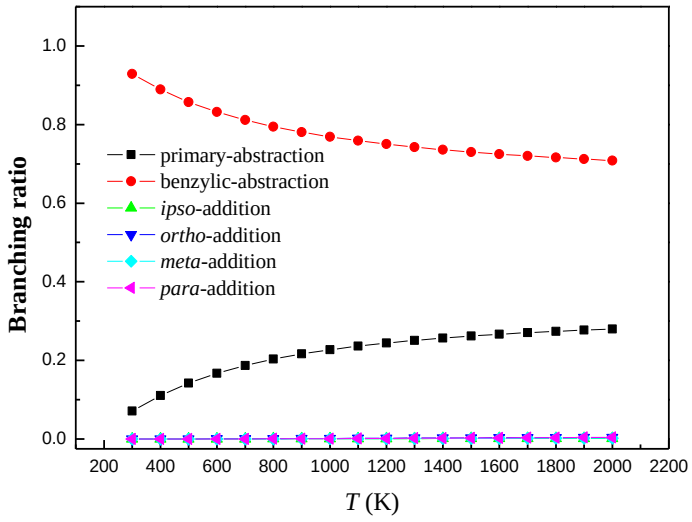

Figure 5.5. Branching ratios for NH_2 interaction with ethylbenzene.

Figure 5.6 portrays the branching ratios for the three plausible H abstraction corridors in *n*-propylbenzene by NH_2. The formation of 1-phenyl-1-propyl (via H abstraction from the

benzylic site) remains the leading pathway at all temperature ranges (300–2000 K). The formation of 1-phenyl-3-propyl through H abstraction from the primary site becomes the second dominant channel. The generation of the 1-phenyl-2-propyl radical (through H abstraction from the secondary site) contributes minimally in the overall reaction rate of *n*-propylbenzene with NH_2. The contribution of H abstraction from the secondary site in *n*-propylbenzene remains within 0.4–3.6 % throughout the considered temperature range. This due to the lower entropy factor of TS5 in H removal from secondary site as compared to the entropy value of H abstraction form primary site in TS4. The present findings somehow contradict the results from our previous investigation of the system of HO_2 + *n*-propylbenzene.[59] For example, abstraction of the secondary H atom from *n*-propylbenzene by HO_2 plays the role of the leading channel below 600 K, while removal of benzylic H dominates above 600 K.

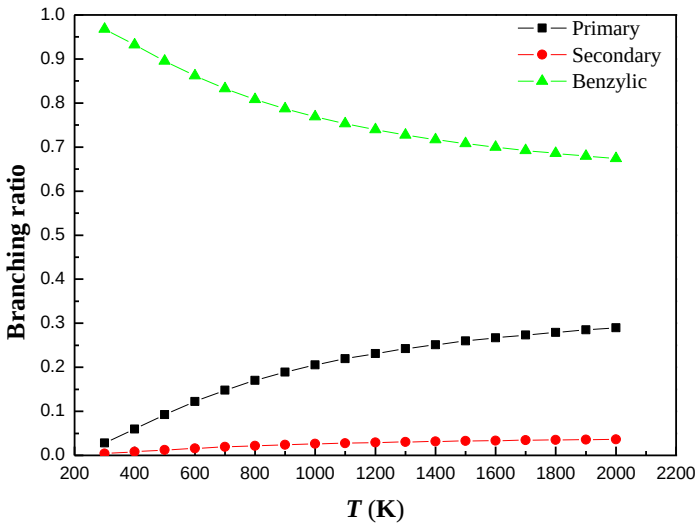

Figure 5.6. Branching ratios for H abstraction by NH_2 from primary, secondary and benzylic sites in *n*-propylbenzene.

5.4.3.1. Trend of benzylic, primary and secondary H removal in alkylbenzenes

Abstraction of the benzylic H atom from toluene by NH_2 incurs similar activation energy when compared with an analogous system of benzylic H + NH_2 in other alkylbenzenes. Activation energy (E_a) for H abstraction from the benzylic position in toluene (42.5 kJ mol^{-1}) matches corresponding values for the benzylic C–H bond in ethylbenzene (36.2 kJ mol^{-1}) and *n*-propylbenzene (37.5 kJ mol^{-1}). The *A* factor for H abstraction from the benzylic position in ethylbenzene and *n*-propylbenzene falls below that of toluene by 0.52 and 0.63 times. A plausible explanation stems from the noticeable difference in the standard entropy of activation ($\Delta^{\ddagger}S_{298}$). The previous studies on HO_2 + alkylbenzenes established that, $\Delta^{\ddagger}S^{o}_{298}$ values for H abstraction from the benzylic site in toluene fall below the analogous quantity for abstraction of benzylic H from *n*-propylbenzene.[59] Figure S5.5 (Appendix II-SI) displays a similar behaviour of $\Delta^{\ddagger}S^{o}_{298}$ for abstraction of benzylic H from toluene versus ethylbenzene over the temperature interval of 600–1400 K.

Table 5.6 reports the calculated Arrhenius parameters fitted in the temperature range of 300–2000 K for H abstractions from primary and secondary positions in C_3–C_5 alkanes and C_2–C_3 alkylbenzenes and from benzylic positions in C_1–C_3 alkylbenzene.

Table 5.6. Kinetic parameters for abstraction of H atom by NH_2 radicals from the selected alkylbenzenes and alkanes. Reaction rate constants are fitted in the temperature range of 300-2000 K. Values of the Arrhenius parameters (A and E_a) are in units of $cm^3\ s^{-1}\ molecule^{-1}$ and kJ mol^{-1}, respectively. Values of $k(T)$ are reported at 600 K, 800 K and 1200 K. Reaction degeneracy is incorporated in fitted reaction rate constants.

Reactions	A	E_a	k (600 K)	k (800 K)	k (1200 K)
R1	1.65×10^{-10}	42.5	3.39×10^{-14}	2.85×10^{-13}	2.40×10^{-13}
R2	4.53×10^{-11}	41.0	1.23×10^{-14}	9.64×10^{-14}	7.52×10^{-13}
R3	8.65×10^{-11}	36.2	6.14×10^{-14}	3.77×10^{-13}	2.31×10^{-12}
R4	7.19×10^{-11}	44.9	8.91×10^{-15}	8.47×10^{-14}	8.05×10^{-13}
R5	8.83×10^{-12}	44.7	1.14×10^{-15}	1.08×10^{-14}	1.02×10^{-13}
R6	2.31×10^{-11}	37.5	6.29×10^{-14}	4.02×10^{-13}	2.57×10^{-12}
R7	2.27×10^{-11}	42.0	4.98×10^{-15}	4.10×10^{-14}	3.37×10^{-13}
R8	2.45×10^{-11}	35.7	1.89×10^{-14}	1.13×10^{-13}	6.83×10^{-13}
R9	3.51×10^{-11}	41.3	8.81×10^{-15}	7.01×10^{-14}	5.57×10^{-13}
R10	2.86×10^{-11}	32.5	4.20×10^{-14}	2.15×10^{-13}	1.09×10^{-12}

To the best of our knowledge, literature provides no theoretical or experimental estimation of rate constants for any alkylbenzene + NH_2 reaction. Thus, the calculated values for the current system are compared with the results of my previous computations for interacting systems of propane and butane with NH_2.[61] Such comparison is intuitively appealing in view of the very similar BDHs of the abstractable H atoms; our computed (CBS-QB3) BDH values of primary H in propane and *n*-butane[61] vs ethylbenzene[72] and *n*-propylbenzene[59] correspond to 428.4 kJ mol^{-1} and 426.4 kJ mol^{-1} versus 421.3 kJ mol^{-1} and 420.5 kJ mol^{-1}, respectively. Figures 5.7a and 5.7b compare reaction rate constants of H abstraction from the primary C–H

bond from ethylbenzene versus propane and *n*-propylbenzene versus *n*-butane (per one abstractable H atom). The activation energy for H abstraction from the primary position in ethylbenzene (42.5 kJ mol^{-1}) reasonably matches the equivalent value from *n*-propylbenzene (44.5 kJ mol^{-1}). Similar trends appear for the activation energies of removal of primary hydrogen atoms from propane and butane versus ethylbenzene and *n*-propylbenzene by HO_2 radical.[59] The *A* factor for H abstraction from the primary position in *n*-propylbenzene is 1.59 times higher as compared to ethyl benzene. Activation energies for the abstraction of the primary H from these four molecules clusters within 5.0 kJ mol^{-1}.

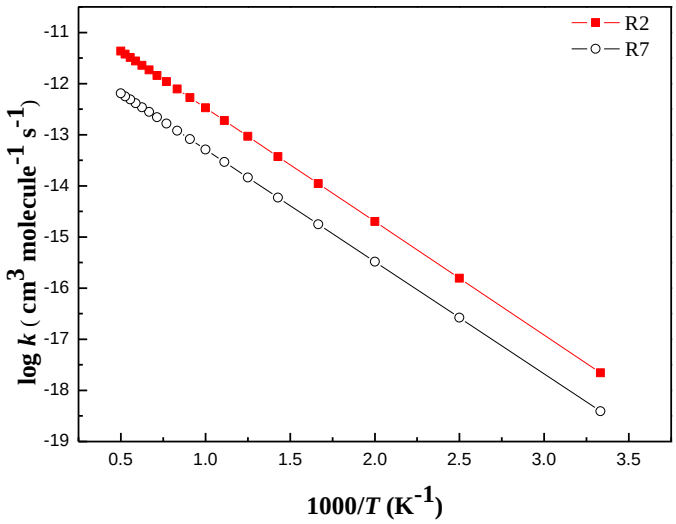

(a)

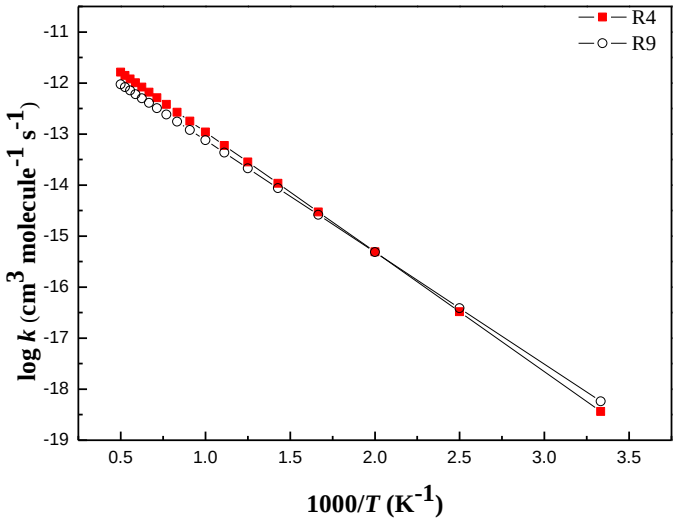

(b)

Figure 5.7. Comparison of primary H abstraction reaction for (a) propane (R7) vs ethylbenzene (R2) and (b) *n*-butane (R9) vs *n*-propylbenzene (R4) by NH_2 radical, per one abstractable H atom.

Figure 5.8 compares rates for a similar (BDH, 410.4–411.1 kJ mol^{-1}) secondary H abstractions reactions of propane and *n*-butane with NH_2 obtained in our previous computations[61] and the current study of *n*-propylbenzene. The reaction rate constant for H abstraction from the primary site in ethylbenzene (R2) produce a difference of 0.42 and 0.45 in reference to the analogous rates for H removal from the primary site in propane[61] (R7) at 800 K and 1200 K, respectively. Likewise, the rate constant for the removal of primary H in *n*-propylbenzene (R4) is comparable with the corresponding site in *n*-butane[61] (R7); i.e., these rates differ by 0.82 and 0.69 at 800 K and 1200 K, respectively.

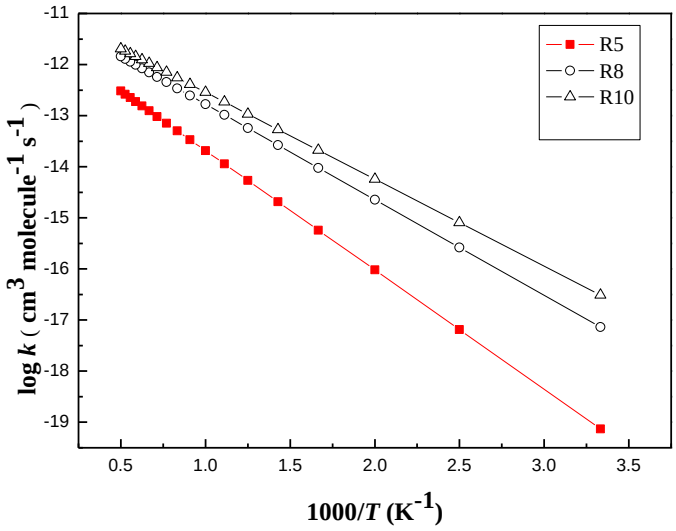

Figure 5.8. Comparison of secondary H abstraction reaction in propane (R8), *n*-butane (R10), and *n*-propylbenzene (R5) by NH_2 radical, per one abstractable H atom.

Figure 5.9 compares the removal of benzylic H atom from toluene, ethylbenzene and *n*-propylbenzene by NH_2 radical (per one abstractable H atom). At temperatures below 600 K, H abstraction from the benzylic site in ethylbenzene exceeds (2.3–9.8 and 8.3–14.0 times) that

of toluene and *n*-propylbenzene, respectively. Between 600–2000 K, the rate of removal of benzylic H from toluene (R1) and ethylbenzene (R3) become very similar.

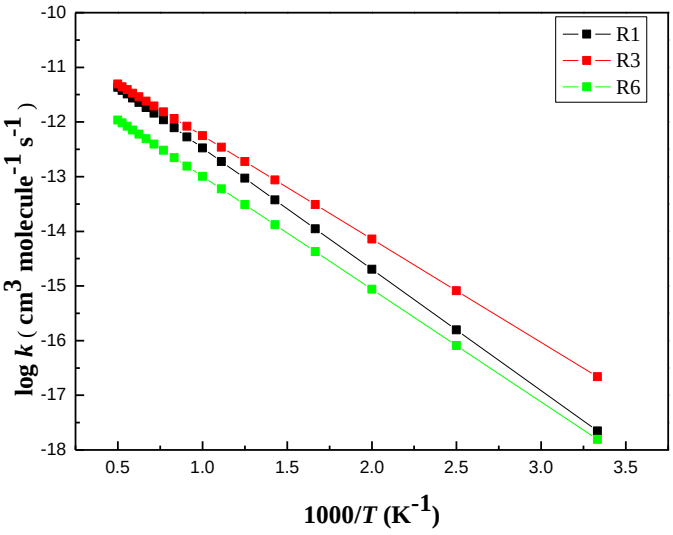

Figure 5.9. Comparison of of the rates of abstraction reaction of benzylic H in toluene (R1), ethylbenzene (R3) and *n*-propylbenzene (R6) by NH_2 radical, per one abstractable H.

5.5. Conclusion

The current study carried out a comprehensive thermochemical and kinetic investigation into the reactions of NH_2 radical with a series of C_1–C_3 alkyl chains attached to a benzene ring. Hydrogen abstraction by NH_2 radical from primary and secondary sites in alkanes and alkylbenzenes incurs similar activation ($\Delta^{\ddagger}H^{o}_{298}$) and reaction ($\Delta_r H^{o}_{298}$) enthalpies. Abstraction of the benzylic H atom in toluene (R1) and ethylbenzene (R3) dominates the rates of hydrogen removal from other positions, at all temperatures. The importance of abstraction of primary H in ethylbenzene increases gradually with increasing temperature. In

the case of *n*-propylbenzene, the rate constant of abstraction of the benzylic H atoms in *n*-propylbenzene dominates that of the secondary and primary H atoms towards at the entire temperature window. The length of the hydrocarbon chain exerts minimal influence on the computed activation and reaction enthalpies. Hydrogen abstraction reactions incur higher $\Delta_r H^o_{298}$ than those of the addition of NH_2 radical to the aromatic ring of toluene and ethylbenzene. The maximum overall contribution of addition reactions reached only 2.4 % for toluene and 9.3 % for ethylbenzene. The current kinetic data of H abstraction reactions of ethylbenzene and *n*-propylbenzene is compared with the results of our previous study of abstraction of H atoms by the NH_2 radical from propane and *n*-butane at selected temperatures. Abstraction of the benzylic H atom from toluene and ethylbenzene molecules entails higher rate constants when compared with that of *n*-propylbenzene. The kinetic data presented in this study will assist in constructing kinetic models for combustion and pyrolysis of nitrogen-rich fuels.

Appendix II: Supporting Information

Figure S5.1. Arrhenius plots for the rate constant for H abstraction reactions from the alkylside chain in alkylbenzenes by NH_2

Figure S5.2. Arrhenius plots for the rate constant for addition reactions of NH_2 to toluene.

Figure S5.3. Arrhenius plots for the rate constant for addition reactions of NH_2 to ethylbenzene.

Figure S5.4. $\Delta^{\ddagger}S_{298}$ values for abstraction and addition reactions of NH_2 with toluene (R1, R11, R12, R13 and R14) over temperature interval of 600–1400 K.

Figure S5.5. $\Delta^{\ddagger}S_{298}$ values for benzylic H abstraction reactions from toluene (R1) and ethylbenzene (R3) by NH_2 over temperature interval of 600–1400 K.

Cartesian coordinates for all the transition states.

Table S5.1. Thermodynamic data for each species appearing in this study.

Table S5.2. Calculated standard reaction enthalpies of Reaction R1-R6. All values in italic are experimental standard heat of formation of individual species from the cited literature and in unit of kJ mol^{-1}.

5.6. References

1. Li, C.-Z.; Tan, L. L., Formation of NO_x and SO_x Precursors during the Pyrolysis of Coal and Biomass. Part III. Further Discussion on the Formation of HCN and NH_3 during Pyrolysis. *Fuel* **2000**, *79*, 1899-1906.

2. Bae, S. W.; Roh, S. A.; Kim, S. D., NO Removal by Reducing Agents and Additives in the Selective Non-Catalytic Reduction (SNCR) Process. *Chemosphere* **2006**, *65*, 170-175.

3. Rota, R.; Antos, D.; Zanoelo, E. F.; Morbidelli, M., Experimental and Modeling Analysis of the NO_xOut Process. *Chem. Eng. Sci.* **2002**, *57*, 27-38.

4. Javed, M. T.; Irfan, N.; Gibbs, B., Control of Combustion-Generated Nitrogen Oxides by Selective Non-Catalytic Reduction. *J. Environ. Econ. Manage.* **2007**, *83*, 251-289.

5. Haynes, B., Reactions of Ammonia and Nitric Oxide in the Burnt Gases of Fuel-Rich Hydrocarbon-Air Flames. *Combust. Flame* **1977**, *28*, 81-91.

6. Mahmoudi, S.; Baeyens, J.; Seville, J. P., NO_x Formation and Selective Non-Catalytic Reduction (SNCR) in a Fluidized Bed Combustor of Biomass. *Biomass Bioenerg.* **2010**, *34*, 1393-1409.

7. Gentemann, A. M.; Caton, J. A., Flow Reactor Experiments on the Selective Non-Catalytic Removal (SNCR) of Nitric Oxide Using a Urea-Water Solution. *VDI Berichte* **2003**, *1750*, 497-502.

8. Glarborg, P.; Dam-Johansen, K.; Miller, J. A.; Kee, R. J.; Coltrin, M. E., Modeling the Thermal DeNO_x Process in Flow Reactors. Surface Effects and Nitrous Oxide Formation. *Int. J. Chem. Kinet.* **1994**, *26*, 421-436.

9. Mendoza-Covarrubias, C.; Romero, C. E.; Hernandez-Rosales, F.; Agarwal, H., N_2O Formation in Selective Non-Catalytic NO_x Reduction Processes. *J. Environ. Prot.* **2011**, *2*, 1095.

10. Miller, J. A.; Bowman, C. T., Mechanism and Modeling of Nitrogen Chemistry in Combustion. *Prog. Energy Combust. Sci.* **1989**, *15*, 287-338.

11. Lucassen, A.; Zhang, K.; Warkentin, J.; Moshammer, K.; Glarborg, P.; Marshall, P.; Kohse-Höinghaus, K., Fuel-Nitrogen Conversion in the Combustion of Small Amines using Dimethylamine and Ethylamine as Biomass-Related Model Fuels. *Combust. Flame* **2012**, *159*, 2254-2279.

12. Davidson, D. F.; Kohse-Höinghaus, K.; Chang, A. Y.; Hanson, R. K., A Pyrolysis Mechanism for Ammonia. *Int. J. Chem. Kinet.* **1990**, *22*, 513-535.

13. Mendiara, T.; Glarborg, P., Ammonia Chemistry in Oxy-Fuel Combustion of Methane. *Combust. Flame* **2009**, *156*, 1937-1949.

14. Rahinov, I.; Ditzian, N.; Goldman, A.; Cheskis, S., NH_2 Radical Formation by Ammonia Pyrolysis in a Temperature Range of 800–1000 K. *Appl. Phys. B.* **2003**, *77*, 541-546.

15. Miller, J. A.; Smooke, M. D.; Green, R. M.; Kee, R. J., Kinetic Modeling of the Oxidation of Ammonia in Flames. *Combust. Sci. Technol.* **1983**, *34*, 149-176.

16. Rayson, M. S.; Altarawneh, M.; Mackie, J. C.; Kennedy, E. M.; Dlugogorski, B. Z., Theoretical Study of the Ammonia−Hypochlorous Acid Reaction Mechanism. *J. Phys. Chem. A.* **2010**, *114*, 2597-2606.

17. Hess, M. A.; Haas, M. J.; Foglia, T. A.; Marmer, W. N., Effect of Antioxidant Addition on NO_x Emissions from Biodiesel. *Energy Fuels* **2005**, *19*, 1749-1754.

18. Dooley, S.; Won, S.H.; Chaos, M.; Heyne, J.; Ju, Y.; Dryer, F.L.; Kumar, K.; Sung, C.J.; Wang, H.; Oehlschlaeger, M.A.; et al. A jet fuel surrogate formulated by real fuel properties. *Combust. Flame* **2010**, *157, 2333-2339.*

19. Nakamura, H.; Darcy, D.; Mehl, M.; Tobin, C. J.; Metcalfe, W. K.; Pitz, W. J.; Westbrook, C. K.; Curran, H. J., An Experimental and Modeling Study of Shock Tube and Rapid Compression Machine Ignition of *n*-Butylbenzene/Air Mixtures. *Combust. Flame* **2014**, *161*, 49-64.

20. Darcy, D.; Nakamura, H.; Tobin, C. J.; Mehl, M.; Metcalfe, W. K.; Pitz, W. J.; Westbrook, C. K.; Curran, H. J., A High-Pressure Rapid Compression Machine Study of *n*-Propylbenzene Ignition. *Combust. Flame* **2014**, *161*, 65-74.

21. Darcy, D.; Nakamura, H.; Tobin, C. J.; Mehl, M.; Metcalfe, W. K.; Pitz, W. J.; Westbrook, C. K.; Curran, H. J., An Experimental and Modeling Study of Surrogate Mixtures of *n*-Propyl- and *n*-Butylbenzene in *n*-Heptane to Simulate *n*-Decylbenzene Ignition. *Combust. Flame* **2014**, *161*, 1460-1473.

22. Seta, T.; Nakajima, M.; Miyoshi, A., High-Temperature Reactions of OH Radicals with Benzene and Toluene. *J. Phys. Chem. A.* **2006**, *110*, 5081-5090.

23. Battin-Leclerc, F., Detailed Chemical Kinetic Models for the Low-Temperature Combustion of Hydrocarbons with Application to Gasoline and Diesel Fuel Surrogates. *Prog. Energy Combust. Sci.* **2008**, *34*, 440-498.

24. Atkinson, R., Kinetics and Mechanisms of the Gas-Phase Reactions of the Hydroxyl Radical with Organic Compounds under Atmospheric Conditions. *Chem. Rev.* **1986**, *86*, 69-201.

25. Perry, R. A.; Atkinson, R.; Pitts, J. N., Kinetics and Mechanism of the Gas Phase Reaction of Hydroxyl Radicals with Aromatic Hydrocarbons over the Temperature Range 296-473 K. *J. Phys. Chem.* **1977**, *81*, 296-304.

26. Roubaud, A.; Minetti, R.; Sochet, L. R., Oxidation and Combustion of Low Alkylbenzenes at High Pressure: Comparative Reactivity and Auto-Ignition. *Combust. Flame* **2000**, *121*, 535-541.

27. Atkinson, R.; Arey, J., Atmospheric Degradation of Volatile Organic Compounds. *Chem. Rev.* **2003**, *103*, 4605-4638.

28. Sutton, M. A.; Dragosits, U.; Tang, Y. S.; Fowler, D., Ammonia Emissions from Non-Agricultural Sources in the Uk. *Atmos. Environ.* **2000**, *34*, 855-869.

29. Yuan, B.; Liu, Y.; Shao, M.; Lu, S.; Streets, D. G., Biomass Burning Contributions to Ambient VOCs Species at a Receptor Site in the Pearl River Delta (Prd), China. *Environ. Sci. Technol.* **2010**, *44*, 4577-4582.

30. Ohmukai, Y.; Hasegawa, I.; Mae, K., Pyrolysis of the Mixture of Biomass and Plastics in Countercurrent Flow Reactor Part I: Experimental Analysis and Modeling of Kinetics. *Fuel* **2008**, *87*, 3105-3111.

31. Williams, P. T.; Horne, P. A., Analysis of Aromatic Hydrocarbons in Pyrolytic Oil Derived from Biomass. *J. Anal. Appl. Pyrol.* **1995**, *31*, 15-37.

32. Lappas, A. A.; Kalogiannis, K. G.; Iliopoulou, E. F.; Triantafyllidis, K. S.; Stefanidis, S. D., Catalytic Pyrolysis of Biomass for Transportation Fuels. *Wiley Interdisciplinary Reviews: Energy and Environment* **2012**, *1*, 285-297.

33. Cheng, Y. T.; Jae, J.; Shi, J.; Fan, W.; Huber, G. W., Production of Renewable Aromatic Compounds by Catalytic Fast Pyrolysis of Lignocellulosic Biomass with Bifunctional Ga/ZSM-5 Catalysts. *Angew. Chem., Int. Ed.* **2012**, *124*, 1416-1419.

34. Becidan, M.; Skreiberg, Ø.; Hustad, J. E., NO_x and N_2O Precursors (NH_3 and HCN) in Pyrolysis of Biomass Residues. *Energy Fuels* **2007**, *21*, 1173-1180.

35. Mullins, O. C.; Mitra-Kirtley, S.; Van Elp, J.; Cramer, S. P., Molecular Structure of Nitrogen in Coal from Xanes Spectroscopy. *Appl. Spectrosc.* **1993**, *47*, 1268-1275.

36. Andreae, M. O.; Merlet, P., Emission of Trace Gases and Aerosols from Biomass Burning. *Glob. Biogeochem. Cycles* **2001**, *15*, 955-966.

37. Li, C.; Suzuki, K., Tar Property, Analysis, Reforming Mechanism and Model for Biomass Gasification—an Overview. *Renew. Sustainable Energy Rev.* **2009**, *13*, 594-604.

38. Hansson, K.-M.; Samuelsson, J.; Tullin, C.; Åmand, L.-E., Formation of HNCO, HCN, and NH_3 from the Pyrolysis of Bark and Nitrogen-Containing Model Compounds. *Combust. Flame* **2004**, *137*, 265-277.

39. Nowakowska, M.; Herbinet, O.; Dufour, A.; Glaude, P.-A., Detailed Kinetic Study of Anisole Pyrolysis and Oxidation to Understand Tar Formation During Biomass Combustion and Gasification. *Combust. Flame* **2014**, *161*, 1474-1488.

40. Hernández, J. J.; Ballesteros, R.; Aranda, G., Characterisation of Tars from Biomass Gasification: Effect of the Operating Conditions. *Energy* **2013**, *50*, 333-342.

41. Wang, S.; Wei, W.; Du, L.; Li, G.; Hao, J., Characteristics of Gaseous Pollutants from Biofuel-Stoves in Rural China. *Atmos. Environ* **2009**, *43*, 4148-4154.

42. Miller, J. A.; Kee, R. J.; Westbrook, C. K., Chemical Kinetics and Combustion Modeling. *Annu. Rev. Phys. Chem.* **1990**, *41*, 345-387.

43. Tian, F.-J.; Yu, J.; McKenzie, L. J.; Hayashi, J.-i.; Li, C.-Z., Conversion of Fuel-N into HCN and NH_3 During the Pyrolysis and Gasification in Steam: A Comparative Study of Coal and Biomass. *Energy Fuels* **2007**, *21*, 517-521.

44. Hansson, K.-M.; Åmand, L.-E.; Habermann, A.; Winter, F., Pyrolysis of Poly-L-Leucine under Combustion-Like Conditions. *Fuel* **2003**, *82*, 653-660.

45. Ren, Q.; Zhao, C.; Wu, X.; Liang, C.; Chen, X.; Shen, J.; Wang, Z., Formation of NO_x Precursors During Wheat Straw Pyrolysis and Gasification with O_2 and CO_2. *Fuel* **2010**, *89*, 1064-1069.

46. Ren, Q.; Zhao, C., NO_x and N_2O Precursors from Biomass Pyrolysis: Nitrogen Transformation from Amino Acid. *Environ. Sci. Technol.* **2012**, *46*, 4236-4240.

47. Altarawneh, M.; Almatarneh, M. H.; Marashdeh, A.; Dlugogorski, B. Z., Decomposition of Ethylamine through Bimolecular Reactions. *Combust. Flame* **2016**, *163*, 532-539.

48. Klippenstein, S. J.; Harding, L. B.; Glarborg, P.; Gao, Y.; Hu, H.; Marshall, P., Rate Constant and Branching Fraction for the NH_2+ NO_2 Reaction. *J. Phys. Chem. A.* **2013**, *117*, 9011-9022.

49. Sun, F.; DeSain, J.; Scott, G.; Hung, P.; Thompson, R.; Glass, G.; Curl, R., Reactions of NH_2 with NO_2 and of OH with NH_2O. *J. Phys. Chem. A.* **2001**, *105*, 6121-6128.

50. Wolf, M.; Yang, D.; Durant, J., A Comprehensive Study of the Reaction NH_2 + NO → Products: Reaction Rate Coefficients, Product Branching Fractions, and Ab Initio Calculations. *J. Phys. Chem. A.* **1997**, *101*, 6243-6251.

51. Ehbrecht, J.; Hack, W.; Rouveirolles, P., Hydrogen Abstraction Reactions by NH_2 ($\bar{X}^2B_1$)-Radicals from Hydrocarbons in the Gas Phase. *Ber. Bunsen-Ges. Phys. Chem.* **1987**, *91*, 700-708.

52. Hack, W.; Kurzke, H.; Rouveirolles, P.; Wagner, H. G., Hydrogen Abstraction Reactions by NH_2($\tilde{X}^2B_1$)-Radicals from Hydrocarbons in the Gas Phase. *Ber. Bunsen-Ges. Phys. Chem.* **1986**, *90*, 1210-1219.

53. Hennig, G.; Wagner, H., A Kinetic Study About the Reactions of NH_2($\bar{X}^2B_1$) Radicals with Saturated Hydrocarbons in the Gas Phase. *Ber. Bunsen-Ges. Phys. Chem.* **1995**, *99*, 863-869.

54. Demissy, M.; Lesclaux, R., Kinetics of Hydrogen Abstraction by Amino Radicals from Alkanes in the Gas Phase. A Flash Photolysis-Laser Resonance Absorption Study. *J. Am. Chem. Soc.* **1980**, *102*, 2897-2902.

55. Mebel, A.; Lin, M., Prediction of Absolute Rate Constants for the Reactions of NH_2 with Alkanes from Ab Initio G2M/TST Calculations. *J. Phys. Chem. A.* **1999**, *103*, 2088-2096.

56. Wang, Z.; Li, Y.; Zhang, F.; Zhang, L.; Yuan, W.; Wang, Y.; Qi, F., An Experimental and Kinetic Modeling Investigation on a Rich Premixed *n*-Propylbenzene Flame at Low Pressure. *Proc. Combust. Inst.* **2013**, *34*, 1785-1793.

57. Dagaut, P.; Ristori, A.; El Bakali, A.; Cathonnet, M., Experimental and Kinetic Modeling Study of the Oxidation of *n*-Propylbenzene. *Fuel* **2002**, *81*, 173-184.

58. Husson, B.; Ferrari, M.; Herbinet, O.; Ahmed, S. S.; Glaude, P.-A.; Battin-Leclerc, F., New Experimental Evidence and Modeling Study of the Ethylbenzene Oxidation. *Proc. Combust. Inst.* **2013**, *34*, 325-333.

59. Altarawneh, M.; Dlugogorski, B. Z., Reactions of HO_2 with *n*-Propylbenzene and its Phenylpropyl Radicals. *Combust. Flame* **2015**, *162*, 1406-1416.

60. Batiha, M.; Altarawneh, M.; Alsofi, A.; Al-Harahsheh, M.; Altarawneh, I.; Alrawadieh, S., Theoretical Study on the Reaction of Hydrogen Atoms with Aniline. *Theor. Chem. Acc.* **2011**, *129*, 823-832.

61. Siddique, K.; Altarawneh, M.; Gore, J.; Westmoreland, P. R.; Dlugogorski, B. Z., Hydrogen Abstraction from Hydrocarbons by NH_2. *The Journal of Physical Chemistry A* **2017**, *121*, 2221-2231.

62. Frisch, M. J.; Trucks,G. W.; Schlegel, H. B.; Scuseria, G. E.; Robb, M. A.; Cheeseman, J. R.; Scalmani,G.; Barone,V.; Mennucci, B.; Petersson, G. A.; et al. , Gaussian 09, revision A.1; Gaussian, Inc.: Wallingford, CT, 2009.

63. Wang, H.; Bozzelli, J. W., Thermochemical Properties ($\Delta_f H°_{(298\ K)}$, $S°_{(298\ K)}$, $C_p(T)$) and Bond Dissociation Energies for C_1–C_4 Normal Hydroperoxides and Peroxy Radicals. *J. Chem. Eng. Data* **2016**, *61*, 1836-1849.

64. Montgomery, J. A.; Frisch, M. J.; Ochterski, J. W.; Petersson, G. A., A Complete Basis Set Model Chemistry. VII. Use of the Minimum Population Localization Method. *J. Chem. Phys.* **2000**, *112*, 6532-6542.

65. Vandeputte, A. G.; Sabbe, M. K.; Reyniers, M.-F.; Van Speybroeck, V.; Waroquier, M.; Marin, G. B., Theoretical Study of the Thermodynamics and Kinetics of Hydrogen Abstractions from Hydrocarbons. *J. Phys. Chem. A.* **2007**, *111*, 11771-11786.

66. Casasnovas, R.; Frau, J.; Ortega-Castro, J.; Salvà, A.; Donoso, J.; Muñoz, F., Simplification of the CBS-QB3 Method for Predicting Gas-Phase Deprotonation Free Energies. *Int. J. Quantum Chem.* **2010**, *110*, 323-330.

67. Mokrushin, V.; Bedanov, V.; Tsang, W.; Zachariah, M.; Knyazev, V., Chemrate, Version 1.19. *NIST: Gaithersburg, MD* **2002**.

68. Canneaux, S.; Bohr, F.; Henon, E., Kisthelp: A Program to Predict Thermodynamic Properties and Rate Constants from Quantum Chemistry Results†. *J. Comput. Chem.* **2014**, *35*, 82-93.

69. Eckart, C., The Penetration of a Potential Barrier by Electrons. *Phys. Rev.* **1930**, *35*, 1303-1309.

70. Truhlar, D. G.; Garrett, B. C.; Klippenstein, S. J., Current Status of Transition-State Theory. *J. Phys. Chem. A.* **1996**, *100*, 12771-12800.

71. Fernández-Ramos, A.; Ellingson, B. A.; Meana-Pañeda, R.; Marques, J. M.; Truhlar, D. G., Symmetry Numbers and Chemical Reaction Rates. *Theor. Chem. Acc.* **2007**, *118*, 813-826.

72. Altarawneh, M. K.; Dlugogorski, B. Z.; Kennedy, E. M.; Mackie, J. C., Rate Constants for Reactions of Ethylbenzene with Hydroperoxyl Radical. *Combust. Flame* **2013**, *160*, 9-16.

73. Desmet, G. B.; D'hooge, D. R.; Sabbe, M. K.; Marin, G. B.; Du Prez, F. E.; Espeel, P.; Reyniers, M.-F., Computational Study and Kinetic Aanalysis of the Aminolysis of Thiolactones. *J. Org. Chem* **2015**, *80*, 8520-8529.

74. Ess, D. H.; Hayden, A. E.; Klärner, F.-G.; Houk, K. N., Transition States for the Dimerization of 1,3-Cyclohexadiene: A DFT, CASPT2, and CBS-QB3 Quantum Mechanical Investigation. *J. Org. Chem* **2008**, *73*, 7586-7592.

75. Ahubelem, N.; Altarawneh, M.; Dlugogorski, B. Z., Dehydrohalogenation of Ethyl Halides. *Tetrahedron Lett.* **2014**, *55*, 4860-4868.

76. Zavala-Oseguera, C.; Galano, A., CBS-QB3 + VTST Study of Methyl *n*-Methylcarbamate + OH Gas-Phase Reaction: Mechamism, Kinetics, and Branching Ratios. *J. Chem. Theory Comput.* **2009**, *5*, 1295-1303.

77. Altarawneh, M. K.; Dlugogorski, B. Z.; Kennedy, E. M.; Mackie, J. C., Rate Constants for Reactions of Ethylbenzene with Hydroperoxyl Radical. *Combust. Flame* **2013**, *160*, 9-16.

78. Luo, Y. R., *Handbook of Bond Dissociation Energies in Organic Compounds*; CRC Press, 2002.

79. Arteca, G. A.; Mezey, P. G., Validity of the Hammond Postulate and Constraints on General One-Dimensional Reaction Barriers. *J. Comput. Chem.* **1988**, *9*, 728-744.

80. Uc, V. H.; Alvarez-Idaboy, J. R.; Galano, A.; García-Cruz, I.; Vivier-Bunge, A., Theoretical Determination of the Rate Constant for OH Hydrogen Abstraction from Toluene. *J. Phys. Chem. A.* **2006**, *110*, 10155-10162.

81. Altarawneh, M.; Al-Muhtaseb, A. A. H.; Dlugogorski, B. Z.; Kennedy, E. M.; Mackie, J. C., Rate Constants for Hydrogen Abstraction Reactions by the Hydroperoxyl Radical from Methanol, Ethenol, Acetaldehyde, Toluene, and Phenol. *J. Comput. Chem.* **2011**, *32*, 1725-1733.

82. Tully, F.; Ravishankara, A.; Thompson, R.; Nicovich, J.; Shah, R.; Kreutter, N.; Wine, P., Kinetics of the Reactions of Hydroxyl Radical with Benzene and Toluene. *J. Phys. Chem. A.* **1981**, *85*, 2262-2269.

83. Altarawneh, M.; Dlugogorski, B. Z.; Kennedy, E. M.; Mackie, J. C., Theoretical Investigation into the Low-Temperature Oxidation of Ethylbenzene. *Proc. Combust. Inst.* **2013**, *34*, 315-323

Chapter 6

Reaction Kinetics of Hydrocarbons + NO_2

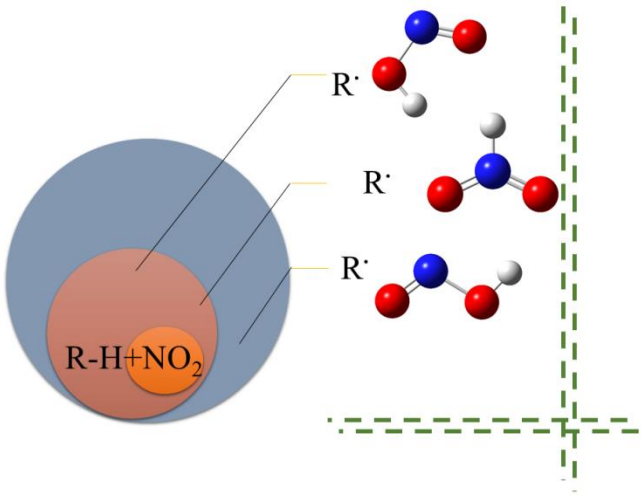

This chapter elaborates on the thermochemistry and reaction kinetics for the formation of three different isomers of nitrous acid that evolve from the hydrogen abstraction of alkanes, alkenes and ethylbenzene by NO_2 radical that are relevant to the processes where small aliphatic and alkylbenzene exit in an NO_x environment.

6.0. Abstract

Nitrogen dioxide (NO_2) exhibits a certain affinity for H atom abstraction from hydrocarbons and assumes a vital role in low-temperature combustion processes. The high accuracy computational method (CBS-QB3) is deployed herein to predict the thermodynamic and kinetic parameters of H abstraction from C_1-C_4 aliphatic saturated and unsaturated hydrocarbons and aromatic hydrocarbon (ethylbenzene) by the NO_2 radical. These abstraction reactions lead to the formation of three distinct nitrous acid isomers, namely *trans*-HONO, *cis*-HONO and *iso*-HNO_2. The reaction rate calculations were performed based on the conventional transition state theory at the high-pressure limit. Tunnelling of the migrating H atom through the reaction barrier is included based on the Eckart method. Formation of *cis*-HONO is more favourable over *iso*-HNO_2 and *trans*-HONO owing to the lower standard activation enthalpies ($\Delta^{\ddagger}H^{o}_{298}$) corresponding to the *cis* conformer compared to the *iso* and *trans* isomers. For the abstraction of H from methane via NO_2 producing *trans*-HONO (R1A) and *cis*-HONO (R1B), in the temperature window of 800–1100 K, the calculated reaction rate constants (sum of R1A and R1B) concur with the available experimental measurements, i.e. $k_{calculated}/k_{experimental}$ ratio of around 0.47–0.73. This sanctifies the accuracy conformity of our methodology, underpinning the calculation of the unreported kinetic parameters for H abstractions from aliphatic and aromatic hydrocarbons. Among all the reactions reported here, the dominant product is *cis*-HONO + R resulting from H abstraction of *iso*-butane (tertiary C–H) followed by propene (allylic C–H) and ethylbenzene (benzylic C–H).

6.1. Introduction

Nitrogen oxides (NO_x) have found a wide range of applications in organic synthesis, both in industry and research laboratories.[1-2] The reaction of nitrogen dioxide (NO_2) with hydrocarbons plays an important role in the nitrogen cycle during combustion/pyrolysis of nitrogen-rich fuels, i.e. biomass[3]. NO_2, a ubiquitous and toxic containment of urban air, reacts with alkanes and alkenes at 298 K via a free radical mechanism.[4-7] Organic nitro-compounds promote the ignition of hydrocarbon fuels. It has been established that the enhancement of ignition in the presence of NO_x is mainly derived by facile abstraction of hydrogen atoms by NO_2 that arises from the direct decomposition of organic nitro-compounds[8]. NO_2 is also formed by the oxidation of NO and HNO_2[9], and by the decomposition of organic nitrates in diesel engines.[10-11]. Several studies have reported rates for NO_x formation from nitrogen bearing compounds in shock-induced combustion under lean hydrogen-oxygen mixtures in the presence of diluted concentrations of ammonia.[12] Likewise, oxidation of hydrocarbons (methane, ethane, propane, ethylene and propene) leads to HO_2 production and thereby increases the conversion of NO to NO_2 along the reaction NO + HO_2 ⇌ NO_2 + OH. The capacity of hydrocarbons to undergo conversion of NO to NO_2 varies with temperature. For example, at 700 K, propane converts approximately 90–95 % of NO to NO_2 while methane, ethane, propane and ethylene convert less than 5 % of NO into NO_2 at residence time of 0.5–1.5 s. At 1000 K, the conversion of NO to NO_2 lies between 68 and 72 % by all the above-mentioned hydrocarbons except methane.[13-14]

In view of the aforementioned importance underlying the reaction of hydrocarbons with NO_2, this has been the subject of numerous experimental studies covering a broad range of operational conditions (e.g., temperature, pressure). The majority of these studies have aimed

to reveal the pronounced ignition-promoting effect of NO_2 on hydrocarbon.[9, 15-23] For example, Oluwoye et al.[24] conducted an experimental work on NO_x + a biomass surrogate (morpholine) in a tubular reactor at pressure of 1.01 bar and residence time of 1.0 s. It was established that under fuel-rich conditions, NO_x (620 ppm) lowered the ignition temperature of morpholine from 773 K to 623 K.[24] Other literature[4-5, 25-27] has reported that the reaction of alkenes with NO_2 proceeded by the addition to the double bond at ambient temperature. On the contrary, NO_2 reacts with toluene via the benzylic H abstraction with toluene[28]. In olefins, abstraction of the allylic H atom appeared to compete with the addition at double bonds. Pryor et al.[6] demonstrated that the mechanism of NO_2-alkene reactions changed mainly from addition to abstraction as the NO_2 concentration decreased from high volume percentage (50 %) to low parts per million levels (1 %). Depending on the concentration of NO_2, initiation of methane oxidation by NO_2 predominates the CH_4 + O_2 channel due to a lower activation barrier associated with the former reaction.[29]

Yamaguchi et al.[30] performed a computational ab initio MP2 level of theory investigation into the H abstraction reaction from CH_4 by NO_x at 800 K and 1 bar. They reported two isomeric channels of nitrous acid leading to the generation of (1) methyl radical and *trans*-HONO and (2) methyl radical and *iso*-HNO_2. Later, Chan et al.[31] conducted a similar theoretical H abstraction study focusing on the role of organic nitrate in improving the ignition behaviour of diesel engines. They derived kinetic parameters for the H abstraction reaction of NO_2 with aliphatic hydrocarbon (C_1–C_4) at 600–1100 K and also considered *cis*-HONO conformer in addition to *trans*-HONO and *iso*-HNO_2 isomers previously reported by Yamaguchi and co-workers.[30] Chen at al.[31] discovered that the transition state linked to *cis*-HONO incurred the lowest energy barrier compared to *trans*-HONO and *iso*-HNO_2. Recently, Gaun and Yang[8]

employed high-level computational methods (M06-2X/MG3S, B3LYP/6-311G(2d,d,p) and MP2/6-311+G(2df,p)) to develop the thermochemistry for the reaction of NO_2 and methane.

The current contribution reports the thermochemical and kinetics of high accuracy computational method (CBS-QB3) investigations into abstraction reactions of NO_2 with the complete series of aliphatic C_1–C_4 hydrocarbons and ethylbenzene leading to three different isomers of nitrous acid (*trans*, *cis* and *iso*). Previous literature provides rather limited kinetic data pertinent to H abstraction by NO_2 from alkenes and branched alkyl benzenes. In addition to C_1–C_4 alkanes, we also explore H atom abstraction from short-chained alkenes and a model compound for alkyl benzenes, i.e. ethylbenzene. Findings from the present study shall assist in attaining an atomic-base insight into the combustion chemistry underlying the coexistence of NO_2 + hydrocarbons (aliphatic and alkyl benzenes); a scenario that prevails in a practical system such as nitro-containing explosives.

6.2. Computational methodology

The Gaussian 09[32] software program was applied to optimise geometries of reactant, transition states and products for the composite chemistry model of CBS-QB3. The CBS-QB3 method calculates geometries and frequencies at the B3LYP/6-311G(2d,d,p) level of theory with inclusion of 2d and d-polarisation functions on the second and first row elements.[33] A series of successive single point energies are then performed at MP4(SDQ)/6-311G(2d(f),p) and CCSD(T)/6-31+G(d`) levels of theory.[34] The CCSD(T) is believed to be more accurate than QCISD(T) for spin-contaminated radicals.[35] Several studies have

demonstrated a satisfactory performance of the CBS-QB3 method in determining thermo-kinetic parameters for H abstraction/transfer reactions.[36-38]

We computed reaction kinetic parameters using the KiSThelP[39] code based on the conventional transition state theory[40]. Inclusion of one dimensional asymmetrical Eckart tunnelling accounts for the quantum tunnelling effect on the reaction rate constants.[41] We applied the methodology of Fernández-Ramos et al.[42] to account for total reaction degeneracy. Treating internal rotations as harmonic oscillators often leads to substantial inaccuracies in thermodynamic partition functions.[37, 43] We mapped out rotors for the internal rotations (mainly $–CH_3$, $–CH_2CH_3$) in C_2–C_4 species (ethane, propane and butane) and transition structures by performing partial optimisations along the dihedral angle at an interval of 30°. Internal rotations of methyl and ethyl groups in ethylbenzene correspond to vibrational frequencies of 220.8 cm^{-1} and 50.9 cm^{-1}, respectively, and energy barriers of 14.1 kJ mol^{-1} and 4.9 kJ mol^{-1}, respectively.

To underpin the influence of the internal rotations on the estimated reaction rate constants, Table 6.1 itemises Arrhenius parameters for selected reactions based on the harmonic oscillator and hindered rotor treatments. Only minimal differences in the pre-exponential factor *A* (0.97–1.12 cm^3 $molecule^{-1}$ s^{-1}) were observed among the two treatments. This is expected since the effect of most hindered rotors cancels out as they exist in reactants and transition structures alike. Consequently, we computed all reaction rate constants based on the harmonic oscillator approach for the internal rotation.

Table 6.1. Comparison of computed Arrhenius parameters with and without the hindered rotors treatment for reactions R2–R4 at 300–2000 K temperature range. Arrhenius parameters (A and E_a) are in units of $cm^3\ s^{-1}\ molecule^{-1}$ and $kJ\ mol^{-1}$, respectively.

Reaction		Internal rotations are treated as harmonic oscillators		Internal rotations are treated as hindered rotors	
		A	E_a	A	E_a
R2A	$C_2H_6 + NO_2 \rightarrow C_2H_5 +$ *trans*-HONO	1.01×10^{-10}	142.8	1.00×10^{-11}	142.8
R3Aa	$C_3H_8 + NO_2 \rightarrow$ *p*-C_3H_7 + *trans*-HONO	5.99×10^{-11}	142.0	5.36×10^{-11}	142.8
R3Ab	$C_3H_8 + NO_2 \rightarrow$ *p*-C_3H_7 + *trans*-HONO	1.82×10^{-11}	132.3	1.47×10^{-11}	132.3
R4Aa	*n*-$C_4H_{10} + NO_2 \rightarrow$ *p*-C_4H_9 + *trans*-HONO	3.25×10^{-10}	142.8	2.60×10^{-10}	142.3
R4Ab	*n*-$C_4H_{10} + NO_2 \rightarrow$ *s*-C_4H_9 + *trans*-HONO	4.75×10^{-11}	130.6	4.27×10^{-11}	129.4

6.3. Results and discussion

6.3.1. Reaction thermochemistry

6.3.1.1. Benchmarking

Table 6.2 defines the considered reactions for the H abstraction by the NO_2 radical resulting in the generation of three isomers of nitrous acids: *trans*-HONO, *cis*-HONO and *iso*-HNO_2.

The standard heat of formation ($\Delta_f H^o_{298}$) of *iso*-HNO_2 is -45.6 kJ mol^{-1}[144] and is thermally more stable than *trans*- and *cis*-HONO by almost 33.0 kJ mol^{-1}. Fourier transform spectroscopy confirmed the presence of *iso*-HNO_2 during nitric acid photolysis.[45] Intermolecular transformation of *iso*-HNO_2 to HONO or vice versa at low and intermediate temperatures is hindered in view of the sizable barrier (198.7–233.5 kJ mol^{-1}).[46]

Table 6.2. List of investigated reactions.

Reactants	**Products**			
	Radicals (R)	***trans*-HONO**	***cis*-HONO**	***iso*-HNO_2**
$CH_4 + NO_2$	CH_3	R1A	R1B	R1C
$C_2H_6 + NO_2$	C_2H_5	R2A	R2B	R2C
$C_3H_8 + NO_2$	*p*-C_3H_7	R3Aa	R3Ba	R3Ca
	s-C_3H_7	R3Ab	R3Bb	R3Cb
n-$C_4H_{10} + NO_2$	*p*-C_4H_9	R4Aa	R4Ba	R4Ca
	s-C_4H_9	R4Ab	R4Bb	R4Cb
iso-$C_4H_{10} + NO_2$	*p*-C_4H_9	R5Aa	R5Ba	R5Ca
	t-C_4H_9	R5Ab	R5Bb	R5Cb
$C_3H_6 + NO_2$	*v*-C_3H_5	R6Aa	R6Ba	
	a-C_3H_5	R6Ab	R6Bb	R6Cb
1-$C_4H_8 + NO_2$	*p*-C_4H_7	R7A	R7B	R7C
2-$C_4H_8 + NO_2$	*a*-C_4H_7	R8A	R8B	R8C
$C_2H_4 + NO_2$	*v*-C_2H_3	R9A	R9B	
$C_8H_{10} + NO_2$	*p*-C_8H_9	R10A	R10B	R10C
$C_8H_{10} + NO_2$	*b*-C_8H_9	R11A	R11B	R11C

To improve the discussion and illustration of the results, prefixes *p*, *s*, *t* and *b* precede the formed radicals to denote removal of a hydrogen atom from primary, secondary, tertiary and benzylic C–H bonds, respectively. Prefix *a* refers to an allylic hydrogen attached to the carbon adjacent to the sp^2 carbon and *v* signifies a vinylic hydrogen connected to sp^2 carbon atoms. Likewise, A, B and C represent *trans*-HONO, *cis*-HONO and *iso*-HNO_2 isomers, respectively, of the nitrous acid (nitryl hydride or hydrogen nitryl). Herein, we consider H abstraction reactions from methane, ethane, propane, *n*-butane, *iso*-butane, ethylene, propene, 1-butene, 2-butene and from the alkyl side chain in ethylbenzene.

Figure 6.1 depicts optimised transition structures of H abstraction from C_1-C_4 hydrocarbon and ethylbenzene with NO_2 generating *trans*-HONO. The optimised transition state geometries leading to the formation of *cis*-HONO and *iso*-HNO_2 are illustrated in Figure 6.2 and Figure 6.3, respectively.

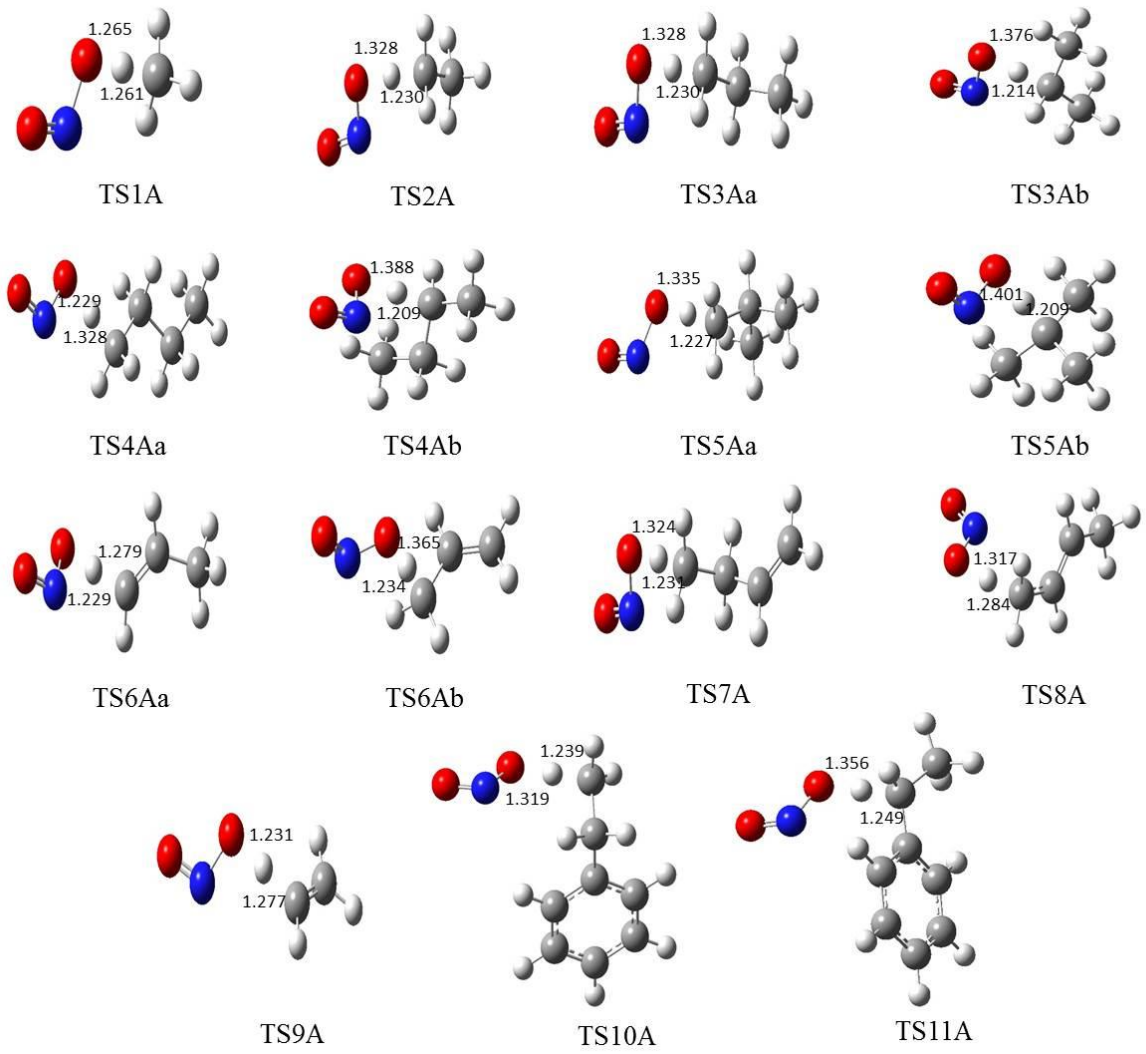

Figure 6.1. Optimised geometries of the transition states for the H abstraction reactions of the NO_2 radical with hydrocarbon forming *trans*-HONO. Distances are in Å. Molecule colours are hydrogen = white, carbon = grey, oxygen= red and nitrogen = blue.

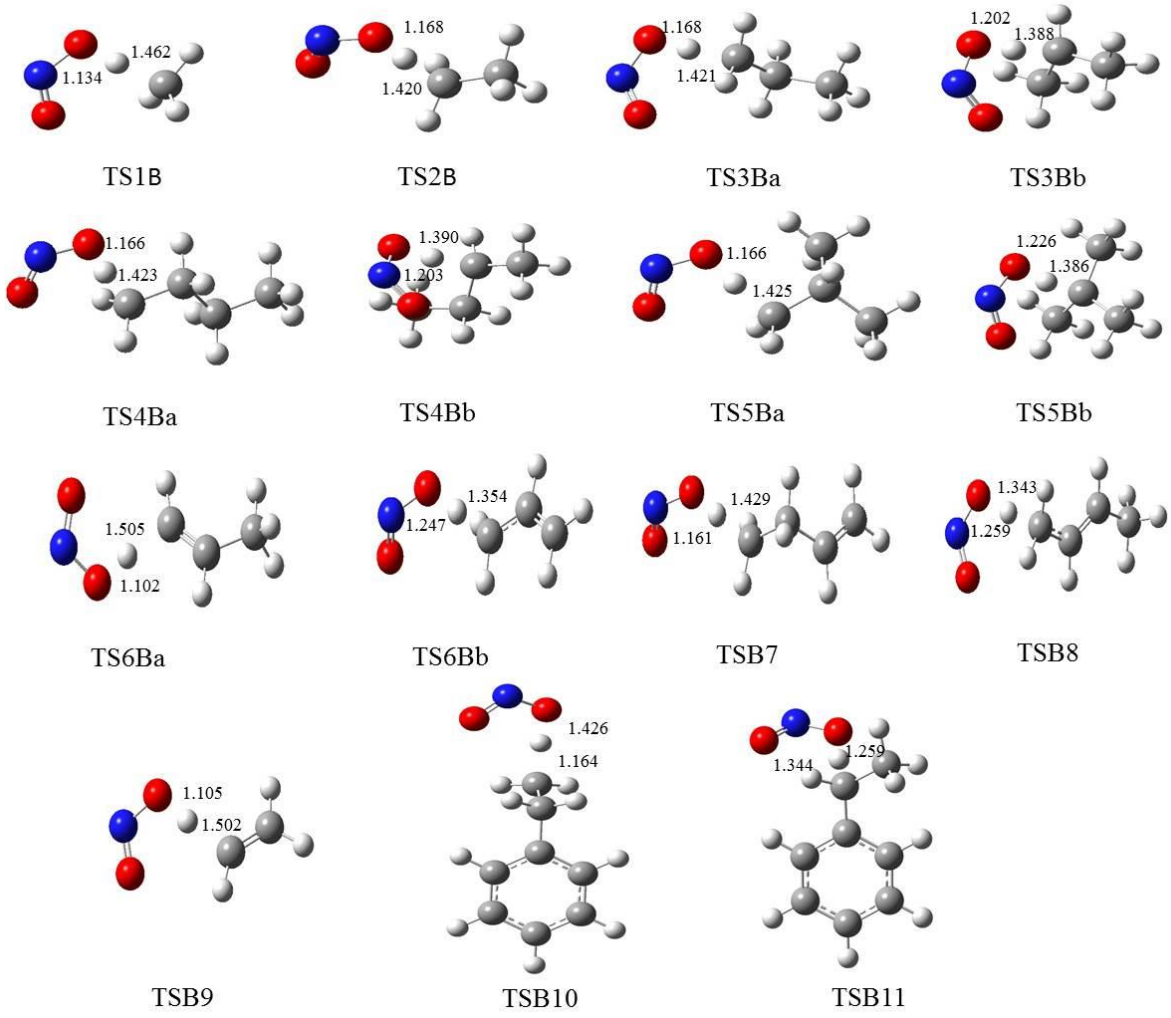

Figure 6.2. Optimised geometries of the transition states for the H abstraction reactions of the NO_2 radical with hydrocarbon forming *cis*-HONO. Distances are in Å. Molecule colours are hydrogen = white, carbon = grey, oxygen= red and nitrogen = blue.

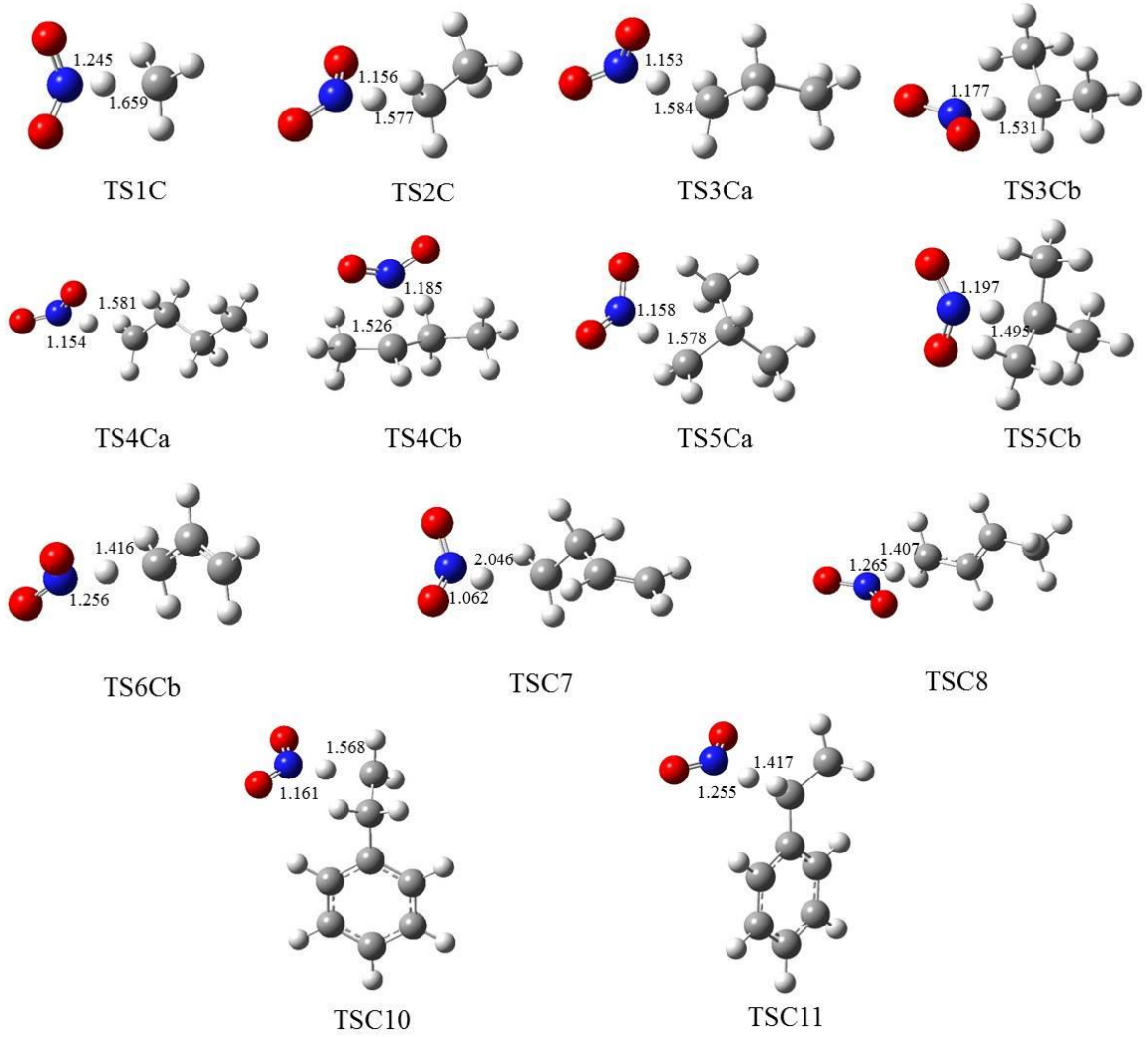

Figure 6.3. Optimised geometries of the transition states for the H abstraction reactions of the NO_2 radical with hydrocarbon forming *iso*-HNO_2. . Distances are in Å. Molecule colours are hydrogen = white, carbon = grey, oxygen= red and nitrogen = blue.

Table 6.3 contrasts the CBS-QB3 energy barrier ($\Delta^{\ddagger}E_0$ at 0 K) and reaction energy ($\Delta_r E_0$ at 0 K) of H abstraction from C_1–C_4 hydrocarbon cuts via NO_2 forming *trans*-HONO, *cis*-HONO and *iso*-HNO_2 with literature analogous values[31]. For *trans*-HNO_2, Chan et al.[31] reported $\Delta_r E_0$ for primary H removal in reactions CH_4 + NO_2 (R1A) and C_2H_6 + NO_2 (R2A) as 113.4 kJ mol^{-1} and 96.6 kJ mol^{-1}, respectively, at the BHandHLYP/6-311G**w level of theory. These values overestimate the analogous value of 112.1 kJ mol^{-1} and 95.8 kJ mol^{-1} computed based on the more accurate CBS-QB3 composite method utilized herein. Similarly, BHandHLYP/6-311G** estimated that the $\Delta_r E_0$ values for secondary H removal in reaction C_3H_8 + NO_2 (R3Ab) and tertiary H removal in reaction *i*-C_4H_{10} + NO_2 (R4Ab) overestimate the corresponding CBS-QB3 values by 0.8 kJ mol^{-1} and 4.2 kJ mol^{-1}, respectively. For reactions leading to the formation of *trans*-HONO isomers, we observed a mean unsigned error of 1.8 kJ mol^{-1} in $\Delta_r E_0$ values. Similarly, comparison of our calculated values with those from Chan et al.[31] for the reactions that formed *cis*-HONO and *iso*-HNO_2 exhibited a mean unsigned error of 5.5 kJ mol^{-1} and 2.5 kJ mol^{-1} in $\Delta_r E_{0,}$ respectively, as noted in Table 6.3.

Table 6.3. Comparison of CBS-QB3 calculated activation barriers ($\Delta^{\ddagger}E_0$) and reaction energies ($\Delta_r E_0$) of selected alkanes with Chan et al.[31] values (represented in italic font). Energy values are in kJ mol^{-1} at 0 K.

Reactant	Product (R)	*trans*-HONO			*cis*-HONO			*iso*-HNO_2		
		$\Delta^{\ddagger}E_0$	$\Delta_r E_0$	AD* $\Delta_r E_0$	$\Delta^{\ddagger}E_0$	$\Delta_r E_0$	AD* $\Delta_r E_0$	$\Delta^{\ddagger}E_0$	$\Delta_r E_0$	AD* $\Delta_r E_0$
$CH_4 + NO_2$	CH_3	158.3	112.1	1.3	132.3	113.8	3.3	142.8	145.7	1.7
		165.5	*113.4*		*141.5*	*110.5*		*152.5*	*147.4*	
$C_2H_6 + NO_2$	C_2H_5	140.7	95.8	0.8	112.1	97.9	4.2	119.3	129.3	1.7
		148.7	*96.6*		*124.7*	*93.7*		*133.5*	*131.0*	
$C_3H_8 + NO_2$	*s*-C_3H_7	128.9	84	0.8	94.9	85.7	5.5	101.3	117.6	0.4
		136.1	*83.2*		*111.7*	*80.2*		*118.8*	*117.2*	
i-C_4H_{10} + NO_2	*t*-C_4H_9	119.7	76.4	4.2	81.8	78.5	9.2	86.1	110.0	6.7
		127.7	*72.2*		*101.6*	*69.3*		*106.6*	*103.3*	
Mean absolute deviation				1.8			5.5			2.5

*AD = Absolute Deviation

Table 6.4 compares the calculated activation and reaction enthalpies of the H abstraction reaction of C_1–C_4 alkanes by NO_2 with the available literature data[31] and displays the reaction enthalpy mean unsigned error of 11.8 kJ mol^{-1}, 16.5 kJ mol^{-1} and 6.4 kJ mol^{-1} for *trans*-HONO, *cis*-HONO and *iso*-HNO_2, respectively. For the *trans*-HONO isomer, the activation enthalpy ($\Delta^{\ddagger}H^{o}_{298}$, i.e. at 298.15 K) of primary H abstraction in reaction $CH_4 + NO_2$ and in reaction $C_2H_6 + NO_2$ estimated by the BHandHLYP/6-311G** method equalled 152.0 kJ mol^{-1} and 134.0 kJ mol^{-1}, respectively. The corresponding calculated CBS-QB3 $\Delta^{\ddagger}H^{o}_{298}$ for reaction $CH_4 + NO_2$ equalled 154.6 kJ mol^{-1} whereas reaction $C_2H_6 + NO_2$ yielded $\Delta^{\ddagger}H^{o}_{298}$

values of 140.3 kJ mol^{-1}. Evidently, the values acquired from the BHandHLYP/6-311G**[31] level of theory underestimated the anticipated more accurate CBS-QB3 calculated values. The previous theoretical[31] $\Delta^{\ddagger}H^{o}_{298}$ value reported for secondary H atom removal for reaction $C_3H_8 + NO_2$ was 121.0 kJ mol^{-1}; a value that significantly underestimates the corresponding value of 129.4 kJ mol^{-1} computed herein. We observed a similar trend for the tertiary H atom removal for $\Delta^{\ddagger}H^{o}_{298}$ in reaction *i*-$C_4H_{10} + NO_2$ with 112.1 kJ mol^{-1} and 123.0 kJ mol^{-1} calculated by BHandHLYP/6-311G**[31] and CBS-QB3, respectively.

Table 6.4. Comparison of CBS-QB3 calculated standard activation enthalpies ($\Delta^{\ddagger}H^{o}_{298}$) and standard reaction enthalpies ($\Delta_rH^{o}_{298}$) of selected alkanes with available literature data[31] represented in italic font. All reported values are in kJ mol^{-1} at 298.15 K.

Reactant	Product (R)	*trans*-HONO			*cis*-HONO			*iso*-HNO_2		
		$\Delta^{\ddagger}H^{o}_{298}$	$\Delta_rH^{o}_{298}$	AD* $\Delta_rH^{o}_{298}$	$\Delta^{\ddagger}H^{o}_{298}$	$\Delta_rH^{o}_{298}$	AD* $\Delta_rH^{o}_{298}$	$\Delta^{\ddagger}H^{o}_{298}$	$\Delta_rH^{o}_{298}$	AD* $\Delta_rH^{o}_{298}$
$CH_4 + NO_2$	CH_3	154.6	113.8	8.8	130.2	115.5	13.5	138.2	147.0	3.4
		152.0	*105.0*		*130.2*	*102.0*		*144.1*	*143.6*	
$C_2H_6 + NO_2$	C_2H_5	140.3	98.3	10.9	111.7	100.0	15.6	118.4	131.5	5.5
		134.0	*87.4*		*111.3*	*84.4*		*123.1*	*126.0*	
$C_3H_8 + NO_2$	*s*-C_3H_7	129.4	86.5	12.6	94.9	88.2	17.2	101.6	119.7	7.1
		121.0	*73.9*		*97.4*	*71.0*		*107.5*	*112.6*	
i-C_4H_{10} + NO_2	*t*-C_4H_9	123.0	79.4	15.1	81.9	81.0	19.7	84.4	112.6	9.7
		112.1	*64.3*		*87.4*	*61.3*		*94.9*	*102.9*	
Mean absolute deviation				11.8			16.5			6.4

6.3.1.2. H abstraction by NO_2 leading to *trans*-HONO

Table 6.5 lists the thermochemical parameters of aliphatic C_1–C_4 and ethylbenzene producing their corresponding radicals + *trans*-HONO. The difference in $\Delta^{\ddagger}H^{o}_{298}$ for H abstraction from methane and ethane (154.6 kJ mol^{-1} versus 140.3 kJ mol^{-1} (Figure 6.2)) reflects a matching difference in their C-H bond dissociation enthalpy (BDH), i.e. 441.4 kJ mol^{-1} versus 425.9 kJ mol^{-1}[147]. This trend concurs with a higher exothermicity of reaction R2A with respect to reaction R1A, as illustrated in Table 6.5. Primary H abstraction in reactions R3Aa, R4Aa and R5Aa entail $\Delta^{\ddagger}H^{o}_{298}$ values in a narrow range, i.e. 137.8–139.9 kJ mol^{-1}. This trend is consistent with their very similar BDHs (426.0–428.8 kJ mol^{-1}). Calculated $\Delta_r H^{o}_{298}$ values for reactions R3Aa, R4a and R5Aa amount to 101.2 kJ $mol^{-1,}$ 99.1 kJ mol^{-1} and 79.4 kJ mol^{-1}, respectively, displaying a linear relationship with BDH values. This trend follows Evans-Polanyi plots similar to the one we observed in our previous study of H abstraction reactions of hydrocarbons + NH_2.[48] Abstraction of secondary H in reactions R3Ab and R4Ab acquire $\Delta^{\ddagger}H^{o}_{298}$ values of 129.4 kJ mol^{-1} and 126.8 kJ mol^{-1}, respectively, while tertiary H removal demands a $\Delta^{\ddagger}H^{o}_{298}$ value at 122.6 kJ mol^{-1}.

For propene, we considered abstraction of an H atom from vinylic (R6Aa) and allylic (R7Aa) sites. In R6Aa, the BDH of vinylic C–H site (466.9 kJ mol^{-1}) was substantially greater than the allylic C-H site in R6Ab (290.4 kJ mol^{-1}). Therefore, the $\Delta^{\ddagger}H^{o}_{298}$ of R6Aa notably surpassed that of R6Ab, i.e. 149.1 kJ mol^{-1} versus 119.7 kJ mol^{-1}. Allylic C-H bonds in 2-butene (357 kJ mol^{-1}) are weaker than the primary C-H bonds in 1-butene (412.0 kJ mol^{-1}). Intuitively, $\Delta^{\ddagger}H^{o}_{298}$ via TS7A (1-butene, R7A) and TS8A (2-butene, R8A) are 133.9 kJ mol^{-1} and 119.7 kJ mol^{-1}, respectively, above their separated reactants. The computed BDH for

ethylene's vinylic C–H attained a value of 464.9 kJ mol^{-1} with a calculated $\Delta^{\ddagger}H^{o}_{298}$ value at 156.7 kJ mol^{-1}.

For ethylbenzene, the primary H abstraction channel via transition state TS10A (ethylbenzene + NO_2) forming *trans*-HONO was accompanied by 150.4 kJ mol^{-1} of $\Delta^{\ddagger}H^{o}_{298}$ and 102.5 kJ mol^{-1} of $\Delta_r H^{o}_{298}$. This is owing to a lower benzylic C–H bond compared to the primary H atom in ethylbenzene in the corresponding $\Delta^{\ddagger}H^{o}_{298,}$ i.e. it attains a lower value of 126.8 kJ mol^{-1} (TS11A).

Table 6.5. Standard activation enthalpy ($\Delta^{\ddagger}H^{o}_{298}$), standard reaction enthalpy ($\Delta_r H^{o}_{298}$), activation barrier ($\Delta^{\ddagger}E_0$) and reaction barrier ($\Delta_r E_0$) of selected light aliphatic and aromatic hydrocarbon forming *trans*-HONO + R products. Enthalpy and energy values are in kJ mol^{-1} at 298.15 K and 0 K, respectively.

Reactants	Products (R)		*trans*-HONO			
			$\Delta^{\ddagger}H^{o}_{298}$	$\Delta_r H^{o}_{298}$	$\Delta^{\ddagger}E_0$	$\Delta_r E_0$
$CH_4 + NO_2$	CH_3	R1A	154.6	113.8	158.3	112.1
$C_2H_6 + NO_2$	C_2H_5	R2A	140.3	98.3	140.8	98.7
$C_3H_8 + NO_2$	*p*-C_3H_7	R3Aa	139.9	101.2	140.2	101.2
	s-C_3H_7	R3Ab	129.4	86.9	128.9	84.0
n-$C_4H_{10} + NO_2$	*p*-C_4H_9	R4Aa	137.8	99.1	139.4	83.6
	s-C_4H_9	R4Ab	126.8	87.4	126.4	97.0
i-$C_4H_{10} + NO_2$	*p*-C_4H_9	R5Aa	139.4	79.4	139.4	98.7
	t-C_4H_9	R5Ab	122.6	64.3	119.4	76.4
$C_3H_6 + NO_2$	*v*-C_3H_5	R6Aa	149.1	139.9	149.1	138.1
	a-C_3H_5	R6Ab	119.7	31.9	119.7	30.2
1-$C_4H_8 + NO_2$	*p*-C_4H_7	R7A	133.9	94.9	134.4	90.7
2-$C_4H_8 + NO_2$	*a*-C_4H_7	R8A	119.7	35.7	105.4	35.3
$C_2H_4 + NO_2$	*v*-C_2H_3	R9A	156.7	135.7	156.7	134.4
$C_8H_{10} + NO_2$	*p*-C_8H_9	R10A	150.4	102.5	150.7	100.8
$C_8H_{10} + NO_2$	*b*-C_8H_9	R11A	126.8	43.3	126.8	42.4

6.3.1.3. H abstraction by NO_2 leading to *cis*-HONO

Table 6.6 depicts the thermochemistry of the H abstraction of aliphatic C_1–C_4 hydrocarbons and aromatic ethylbenzene with NO_2 generating the *cis*-HONO isomer of nitrous acid and the respective hydrocarbon radicals. The standard heat of formation ($\Delta_f H^o_{298}$) of *trans*-HONO[49] and *cis*-HONO[50] are -79.4 kJ mol^{-1} and -76.9 kJ mol^{-1}, respectively. The *trans*-HONO structure is a more stable isomer than the *cis*-HONO adduct[44]. Accordingly, $\Delta^{\ddagger}E_0$ and $\Delta^{\ddagger}H^o_{298}$ should be lower for *trans*-HONO than *cis*-HONO; however, Tables 5 and 6 have shown the opposite trend. Chan et al.[31] explained this unpresented difference based on the five member ring transition state of *cis* configuration that induces a stabilisation effect. Similar to the *trans*-HONO product, the previous theoretically[31] $\Delta^{\ddagger}E_0$ values overestimated analogous values computed here. For example, in Chan et al.[31] $\Delta^{\ddagger}E_0$ values for reactions R1B and R2B were 141.5 kJ mol^{-1} and 124.7 kJ mol^{-1}, respectively, whereas our computed $\Delta^{\ddagger}E_0$ attained values of 132.3 kJ mol^{-1} and 112.1 kJ mol^{-1}, respectively. Abstraction of secondary H in propane (R3Bb) and tertiary H in *iso*-butane (R5Bb) show BHandHLYP/6-311G** $\Delta^{\ddagger}E_0$ values of 111.7 kJ mol^{-1} and 101.6 kJ mol^{-1}, respectively [31] These values clearly overshoot the analogous CBS-QB3 $\Delta^{\ddagger}E_0$ values by 16.8 kJ mol^{-1} and 19.8 kJ mol^{-1}, respectively. It can be inferred from Table 6.3 that $\Delta_r E_0$ of reactions R1B, R2B, R3Bb and R4Bb reported by Chan et al.[31] depart from our calculated values with a mean assigned error of 5.5 kJ mol^{-1}.

Overall, the $\Delta^{\ddagger}H^o_{298}$ values for H abstraction reaction with NO_2 leading to *cis*-HONO product were lower than *iso*-HNO_2 and *trans*-HONO. The difference in the current calculated $\Delta^{\ddagger}H^o_{298}$ from previous theoretical[31] estimates lie between 0.4 and 3.5 kJ mol^{-1} for reactions R1B, R2B and R3Bb. The $\Delta^{\ddagger}H^o_{298}$ for the removal of the secondary H atom in reaction R3Bb

in the present CBS-QB3 method (94.9 kJ mol^{-1}) displayed good agreement with the corresponding literature[31] $\Delta^{\ddagger}H^{o}_{298}$ estimation (97.4 kJ mol^{-1}). For reaction R5Bb, the theoretical[31] reported $\Delta^{\ddagger}H^{o}_{298}$ was lower than the analogous CBS-QB3 values by 6.5 kJ mol^{-1}. Owing to the narrow range of BDH for the relevant C-H sites, H abstraction in reactions R3Ba (110.5 kJ mol^{-1}), R4Ba (110.5 kJ mol^{-1}) and R5Ba (107.1 kJ mol^{-1}) proceeded via very similar values.

In the alkene family, H abstractions from propene occur via two channels: vinylic (R6Ba) and allylic (R6Bb) C-H sites. The $\Delta^{\ddagger}H^{o}_{298}$ of reaction R6Ba equalled 146.6 kJ mol^{-1}, which is higher by 59.7 kJ mol^{-1} than that of reaction R6Bb. The generation of primary *p*-C_4H_7 radicals in 1-butene (R7B) required more $\Delta^{\ddagger}H^{o}_{298}$ (105.0 kJ mol^{-1}) than $\Delta^{\ddagger}H^{o}_{298}$ (85.3 kJ mol^{-1}) of allylic *a*-C_4H_7 species in 2-butene (R8B). Similar to *trans*-HONO, the generation of *cis*-HONO (R9B) via abstraction of H from ethylene proceeded with the highest $\Delta^{\ddagger}H^{o}_{298}$ value (137.8 kcal mol^{-1}) among all of the investigated reactions. In the case of ethylbenzene, the primary and benzylic H abstraction corridor occurred via transition states TS10B and TS11B, and ensued with $\Delta^{\ddagger}H^{o}_{298}$ values of 124.3 kcal $mol^{-1}$and 89.0 kcal mol^{-1}, respectively.

Based on the exothermicity of each reaction reported in Tables 6.5 and 6.6, the allylic radical in propene and 2-butene formed the most stable radicals with a backward standard enthalpy barrier of 87.8 kJ mol^{-1} and 84.0 kJ mol^{-1}in R + *trans*-HONO products, respectively, and backward standard enthalpy barrier of 53.3 kJ mol^{-1} and 48.0 kJ mol^{-1} in R + *cis*-HONO products, respectively. This is because of the BDH values breaking C–H bonds in allylic propene (359.1 kJ mol^{-1}) and 2-butene (362.9 kJ mol^{-1}) versus the O-H site in *trans*-HONO (327.6 kJ mol^{-1}) and in *cis*-HONO (323.4 kcal mol^{-1}) being nearly similar and favouring the formation of *cis* and *trans* isomers. On the other hand, the BHD values of the rest of the

hydrocarbons (403.2–441.0 kJ mol^{-1}) were significantly stronger than the BDH of *trans*-HONO (327.6 kJ mol^{-1}) and *cis*-HONO (323.4 kJ mol^{-1}) and resulted in low exothermicity of the reactions. Owing to the significant difference in BDH values in the vinylic C-H site in propene (466.6 kJ mol^{-1}) and ethylene (462.8 kJ mol^{-1}) versus the O-H site in *trans*-HONO (327.6 kJ mol^{-1}) and in *cis*-HONO (323.4.0 kJ mol^{-1}), the least exothermic reactions were H abstraction from vinylic sites in propene and ethylene with reverse standard enthalpy barriers of 9.4 kJ mol^{-1} and 21.0 kJ mol^{-1}, respectively.

Table 6.6. Illustration of standard activation enthalpy ($\Delta^{\ddagger}H^{o}_{298}$), standard reaction enthalpy ($\Delta_r H^{o}_{298}$), activation barrier ($\Delta^{\ddagger}E_0$) and reaction barrier ($\Delta_r E_0$) of selected light aliphatic and aromatic hydrocarbon forming *cis*-HONO + R products. Enthalpy and energy values are in kJ mol^{-1} at 298.15 K and 0 K, respectively.

Reactant	Product (R)		*cis*-HONO			
			$\Delta^{\ddagger}H^{o}_{298}$	$\Delta_r H^{o}_{298}$	$\Delta^{\ddagger}E_0$	$\Delta_r E_0$
$CH_4 + NO_2$	CH_3	R1B	130.2	115.5	132.3	113.8
$C_2H_6 + NO_2$	C_2H_5	R2B	111.7	100.0	112.1	97.9
$C_3H_8 + NO_2$	*p*-C_3H_7	R3Ba	110.4	102.9	110.9	100.8
	s-C_3H_7	R3Bb	94.9	88.2	94.9	84.4
n-$C_4H_{10} + NO_2$	*p*-C_4H_9	R4Ba	110.5	100.8	110.5	98.7
	s-C_4H_9	R4Bb	92.4	89.5	68.9	86.9
i-$C_4H_{10} + NO_2$	*p*-C_4H_9	R5Ba	107.1	102.5	109.2	100.8
	t-C_4H_9	R5Bb	81.9	81.0	81.5	78.5
$C_3H_6 + NO_2$	*v*-C_3H_5	R6Ba	146.6	141.1	125.1	139.8
	a-C_3H_5	R6Bb	86.9	33.6	86.1	32.13
1-$C_4H_8 + NO_2$	*p*-C_4H_7	R7B	105.0	96.2	145.3	92.4
2-$C_4H_8 + NO_2$	*a*-C_4H_7	R8B	85.3	37.3	86.1	37.1
$C_2H_4 + NO_2$	*v*-C_2H_3	R9B	137.8	135.7	133.6	136.0
$C_8H_{10} + NO_2$	*p*-C_8H_9	R10B	124.3	104.2	124.3	102.1
$C_8H_{10} + NO_2$	*b*-C_8H_9	R11B	89.0	44.9	89.0	44.5

6.3.1.4. H abstraction by NO_2 leading to *iso*-HNO_2

Table 6.7 illustrates thermo-kinetic parameters of H abstraction of straight chain C_1–C_4 hydrocarbons and ethylbenzene with NO_2 generating *iso*-HNO_2. The $\Delta^{\ddagger}E_0$ and $\Delta^{\ddagger}H^{o}_{298}$ values of H abstraction reactions by NO_2 for R + *iso*-HNO_2 products were between those for the R + *trans*-HONO and R + *cis*-HONO. The $\Delta^{\ddagger}E_0$ and $\Delta^{\ddagger}H^{o}_{298}$ values of H abstraction by NO_2 for all the selected hydrocarbons forming R + *iso*-HNO_2 products were found to be lower than the corresponding $\Delta_r H^{o}_{298}$ and $\Delta_r E_0$ values except for the allylic C-H site in 2-butene (R8C) and the primary (R10C) and benzylic C-H sites (R11C) in ethylbenzene.

Table 6.7. Standard activation enthalpy ($\Delta^{\ddagger}H^{o}_{298}$), standard reaction enthalpy ($\Delta_r H^{o}_{298}$), activation barrier ($\Delta^{\ddagger}E_0$) and reaction barrier ($\Delta_r E_0$) of selected light aliphatic and aromatic hydrocarbon forming *iso*-HNO_2 + R products. Enthalpy and energy values are in kJ mol^{-1} at 298.15 K and 0 K, respectively.

Reactant	Product (R)		*iso*-HNO_2			
			$\Delta^{\ddagger}H^{o}_{298}$	$\Delta_r H^{o}_{298}$	$\Delta^{\ddagger}E_0$	$\Delta_r E_0$
$CH_4 + NO_2$	CH_3	RC1	138.2	147.0	142.8	145.7
$C_2H_6 + NO_2$	C_2H_5	RC2	118.4	131.5	119.3	129.4
$C_3H_8 + NO_2$	*p*-C_3H_7	R3Ca	119.3	134.4	119.3	132.3
	s-C_3H_7	R3Cb	101.6	119.7	101.2	117.6
n-$C_4H_{10} + NO_2$	*p*-C_4H_9	R4Ca	115.5	132.3	114.7	130.6
	s-C_4H_9	R4Cb	102.5	120.5	102.5	118.4
i-$C_4H_{10} + NO_2$	*p*-C_4H_9	R5Ca	118.0	134.0	118.4	132.3
	t-C_4H_9	R5Cb	84.8	112.6	86.1	110.4
$C_3H_6 + NO_2$	*a*-C_3H_5	R6Cb	84.4	65.1	84.0	63.8
1-$C_4H_8 + NO_2$	*p*-C_4H_7	R7C	115.5	127.7	113.8	124.3
2-$C_4H_8 + NO_2$	*a*-C_4H_7	R8C	83.6	70.1	84.4	68.8
$C_8H_{10} + NO_2$	*p*-C_8H_9	R10C	141.5	135.7	142.4	134.0
$C_8H_{10} + NO_2$	*b*-C_8H_9	R11C	124.3	76.4	124.3	75.6

Similar to *cis*- and *trans*-HONO isomer products, Chan et al.'s[31] $\Delta^{\ddagger}E_0$ values were higher than our calculated $\Delta^{\ddagger}E_0$ values by 9.7–20.5 kJ mol^{-1} for reactions illustrated in Table 6.3. For instance, Chan et al.[31] computed $\Delta^{\ddagger}E_0$ values for reactions R1C and R2C as being 152.5 kJ mol^{-1} and 133.5 kJ mol^{-1}, respectively, while our derived $\Delta^{\ddagger}E_0$ values were 142.8 kJ mol^{-1} and 119.3 kJ mol^{-1}, respectively. Our calculated $\Delta^{\ddagger}E_0$ values for reactions R3Cb and RC5 were 101.3 kJ mol^{-1} and 86.1 kJ mol^{-1}, respectively. These values are lower than the analogous available literature[31] values by 17.5 kJ mol^{-1} and 20.5 kJ mol^{-1}, respectively. The mean unsigned error underpinning $\Delta_r E_0$ for reactions R1C, R2C, R3Cb and R4Cb was 2.5 kJ mol^{-1} calculated in the present study at CBS-QB3 versus BHandHLYP/6-311G**.[31]

Similar to $\Delta^{\ddagger}E_0$, the CBS-QB3 $\Delta^{\ddagger}H^{o}_{298}$ for H abstraction reactions of hydrocarbons with NO_2 that result in *iso*-HNO_2 are lower than Chan et al.'s[31] evaluated $\Delta^{\ddagger}H^{o}_{298}$ values. The difference in the calculated $\Delta^{\ddagger}H^{o}_{298}$ from previous theoretical[31] values remains within 4.7–10.5 kJ mol^{-1} for reactions R1C, R2C, R3Cb and R5Cb as shown in Table 6.4. Reactions R1C, R2C and R3Cb displayed $\Delta^{\ddagger}H^{o}_{298}$ values of 138.2 kJ mol^{-1}, 118.4 kJ mol^{-1} and 101.6 kcal mol^{-1}, respectively. These values are in a close agreement with Chan et al.'s[31] estimated values of 144.1 kJ mol^{-1}, 123.1 kJ mol^{-1}, and 107.5 kJ mol^{-1}, respectively. Reaction R5Cb showed the least $\Delta^{\ddagger}H^{o}_{298}$ values of 86.1 kJ mol^{-1} in the alkane family.

In the alkene family, the title reaction of 1-butene (R7C) incurred the maximum $\Delta^{\ddagger}H^{o}_{298}$ value at 115.5 kJ mol^{-1} via the primary C-H site while H abstraction from 2-butene (R8C) acquired the least $\Delta^{\ddagger}H^{o}_{298}$ value of 83.6 kJ mol^{-1} via the allylic C-H sites. The generation of allylic *a*-C_4H_7 radical in propene (R6Cb) was found to occur through an enthalpy of activation at 84.4 kJ mol^{-1}. The formation of *iso*-HNO_2 during primary and benzylic H atom

abstraction from ethylbenzene by NO_2 proceeded with 141.5 kJ mol^{-1} and 124.3 kJ mol^{-1} of $\Delta^{\ddagger}H^{o}_{298}$, respectively.

Owing to a weaker N-H bond (294.4 kJ mol^{-1}) in *iso*-HNO_2 than the C-H bonds (378–466.2.0 kJ mol^{-1}) in selected hydrocarbons (RC1–R5Cb and RC7), we observed that the formed radicals for R + *iso*-HNO_2 products were very unstable and favoured the R–H + NO_2 via barrierless reversible reaction. The comparative stable radicals were formed in reactions R6Cb, R8 and R11 due to the competitive BDH of the allylic C–H bond in propene (359.3 kJ mol^{-1}) and 2-butene (363.0 kJ mol^{-1}), and the benzylic C–H site (359.1 kJ mol^{-1}) in ethylbenzene versus the N–H bond (294.4 kJ mol^{-1}) in *iso*-HNO_2.

6.3.2. Kinetic analysis

’Reaction rate constants were calculated for H abstraction C_1–C_4 hydrocarbons and ethylbenzene by the NO2 radical. Table 6.8 presents the Arrhenius parameters of H abstraction reactions generating *trans*-HONO, *cis*-HONO and *iso*-HNO_2 conformers over the temperature interval of 300–2000 K.

Table 6.8. Kinetic parameters for H abstraction atom by NO_2 radicals from aliphatic C_1-C_4 hydrocarbons and ethylbenzene forming *trans*-HONO, *cis*-HONO and *iso*-HNO_2. Reaction rate constants are fitted in the temperature range of 300–2000 K. Values of the Arrhenius parameters (A and E_a) are in units of $cm^3\ s^{-1}\ molecule^{-1}$ and $kJ\ mol^{-1}$, respectively.

	***trans*-HONO**			***cis*-HONO**			***iso*-HNO_2**	
	A	***E_a***		***A***	***E_a***		***A***	***E_a***
R1A	5.57×10^{-10}	158.8	R1B	8.97×10^{-11}	134.8	R1C	3.07×10^{-10}	160.4
R2A	1.01×10^{-10}	142.8	R2B	8.25×10^{-11}	113.8	R2C	1.68×10^{-11}	133.1
R3Aa	5.99×10^{-11}	142.0	R3Ba	5.09×10^{-11}	114.2	R3Ca	7.96×10^{-11}	144.9
R3Ab	1.82×10^{-11}	132.3	R3Bb	1.97×10^{-11}	97.9	R3Cb	8.82×10^{-11}	128.5
R4Aa	3.25×10^{-10}	142.8	R4Ba	9.99×10^{-11}	113.4	R4Ca	5.43×10^{-11}	144.5
R4Ab	4.75×10^{-11}	130.6	R4Bb	1.77×10^{-11}	106.3	R4Cb	2.60×10^{-11}	129.4
R5Aa	4.35×10^{-11}	141.5	R5Ba	1.36×10^{-10}	113.4	R5Ca	3.46×10^{-12}	140.3
R5Ab	1.59×10^{-11}	123.1	R5Bb	2.19×10^{-12}	79.0	R5Cb	1.62×10^{-10}	120.5
R6Aa	1.18×10^{-10}	147.8	R6Ba	2.45×10^{-10}	129.8			
R6Ab	2.21×10^{-11}	117.2	R6Bb	3.28×10^{-11}	84.8	R6Cb	2.17×10^{-11}	86.9
R7A	5.44×10^{-11}	135.2	R7B	1.32×10^{-10}	106.3	R7C	4.16×10^{-11}	142.0
R8A	1.35×10^{-13}	21.7	R8B	7.63×10^{-11}	24.5	R8C	1.23×10^{-11}	21.8
R9A	1.03×10^{-10}	37.2	R9B	9.40×10^{-11}	33.0			
R10A	3.62×10^{-11}	36.2	R10B	2.32×10^{-11}	29.7	R10C	2.49×10^{-12}	33.4
R11A	2.15×10^{-11}	31.3	R11B	9.38×10^{-12}	21.1	R11C	2.69×10^{-11}	30.3

Available literature kinetic parameters reported in Table 6.9 are limited for reactions R1A, R1B, R1C, R2A, R2B, R2C, R3Ab, R3Bb, R3Cb, R5Ab, R5Bb and R5Cb. For reaction R1A, Chan et al.[31] overestimated the reaction rate constant in reference to values reported by Yamaguchi et al.[30] Rate constants of reaction R1A from Chan et al.[31] are 21.5 and 3.2 times higher than those predicted by Yamaguchi et al.[30] at 600 K and 1100 K, respectively. At 1100 K, for reaction R1A, Chan et al.[31] estimated a rate constant value of 2.96×10^{-17} cm^3 $molecule^{-1}$ s^{-1} and Yamaguchi et al.[30] derived a rate constant of 9.31×10^{-19} cm^3 $molecule^{-1}$ s^{-1} while our calculated rate constant was 1.78×10^{-17} cm^3 $molecule^{-1}$ s^{-1}. Slack and Grillo[15] conducted shock tube experiments in a temperature range of 1300–1900 K and suggested a pre-exponential factor of 1.99×10^{-11} cm^3 $molecule^{-1}$ s^{-1} and an activation energy of 126.0 kJ mol^{-1} for the reaction of NO_2 + CH_4. Their proposed values constitute a sum of overall kinetic parameters producing *cis*-HONO and *trans*-HONO isomers.

Table 6.9. Comparison of calculated (CBS-QB3 at 300–2000 K) rate parameters (A and E_a) with Yamaguchi et al. (at 800 K) and Chen et al. (at 600–1100 K). Values of the Arrhenius parameters (A and E_a) are in units of cm^3 s^{-1} $molecule^{-1}$ and kcal mol^{-1}, respectively.

trans-HONO				*cis*-HONO				*iso*-HNO_2			
	A	E_a	k (1100)		A	E_a	k (1100 K)		A	E_a	k (1100 K)
R1A[a]	5.57×10^{-10}	158.8	1.78×10^{-17}	R1B[a]	8.97×10^{-11}	134.8	3.93×10^{-17}	R1C[a]	3.07×10^{-10}	160.4	7.82×10^{-18}
R1A[b]	3.49×10^{-10}	171.0	2.96×10^{-18}	R1B[b]	1.44×10^{-10}	147.8	1.50×10^{-17}	R1C[b]	1.58×10^{-09}	161.3	3.48×10^{-17}
R1A[c]	1.08×10^{-09}	192.4	9.32×10^{-19}								
R2A[a]	1.01×10^{-10}	142.8	1.78×10^{-17}	R2B[a]	8.25×10^{-11}	113.8	3.50×10^{-16}	R2C[a]	1.68×10^{-11}	133.1	8.53×10^{-18}
R2A[b]	9.47×10^{-11}	154.6	4.64×10^{-18}	R2B[b]	3.65×10^{-11}	160.6	2.50×10^{-17}	R2C[b]	2.66×10^{-10}	142.0	5.48×10^{-17}
R3Ab[a]	5.99×10^{-11}	142.0	1.03×10^{-17}	R3Bb[a]	5.09×10^{-11}	114.2	4.80×10^{-16}	R3Cb[a]	8.82×10^{-11}	128.5	7.59×10^{-17}
R3Ab[b]	2.32×10^{-11}	141.5	4.74×10^{-18}	R3Bb[b]	9.63×10^{-12}	118.4	2.40×10^{-17}	R3Cb[b]	4.98×10^{-11}	127.3	4.94×10^{-17}
R5Ab[a]	1.59×10^{-11}	123.0	2.13×10^{-17}	R5Bb`[a]	2.19×10^{-12}	79.0	4.02×10^{-16}	R5Cb[a]	1.62×10^{-10}	120.5	3.37×10^{-16}
R5Ab[b]	3.49×10^{-11}	131.4	2.47×10^{-17}	R5Bb`[b]	1.54×10^{-11}	106.3	1.20×10^{-16}	R5Cb[b]	4.65×10^{-10}	115.9	1.48×10^{-15}

[a]Current study at 300–2000 K, [b]Chan et al.[31] at 600–1100 K and [c]Yamaguchi et al. [30] at 800 K. Values of k(1100) are obtained by fitting the Arrhenius parameters.

Figure 6.4a shows comparison of Arrhenius plots for the total rate constant of reactions R1A and R1B (*trans*-HONO and *cis*-HONO) between calculated and available experimental and theoretical data. By comparing the kinetics summation of reactions R1A and R1B from Chan et al.[31] and Slack and Grillo,[15] we discovered the $k_{theoretical}/k_{experimental}$ ratio to reside between 0.28 and 0.78 at 800–1100 K. We observed good agreement between our calculated reaction rate constants for R1 (RIA + RIB) and the analogues values reported in the experimental study of Slack and Grillo.[15] Estimated $k_{calculated}/k_{experimental}$ ratio fell in the range 0.47–0.73 between 800 and 1100 K. Conversely, we observed higher reaction rate constants in the experimentally measured[15] rate constant at 400–500 K for the reaction R1 with $k_{calculated}/k_{experimental}$ ratios between 3.29 and 8.14. This produces a benchmark for our selected computational methodology for the H abstraction reactions from the investigated hydrocarbons by the NO_2 radical.

Owing to the lack of experimental values, we elected to compare our estimated reaction rate constants with the other theoretically derived values by Chen et al.[31] Figure 6.4b provides comparisons of Arrhenius plots for reaction R1B. Between 800 and 1100 K, our calculated reaction rate constants for the reaction R1B reside within 0.23–0.39 from values calculated by Chen et al.[31] Overall, comparison of the available literature data with the current CBS-QB3 measured rate constants for reactions R2A, R2B, R3A, R3Bb, R5Ab and R5Bb demonstrated that Chan et al.[31] rate constants were lower than our calculated rate constant values.

For channels producing *iso*-HNO_2, Chan et al.[31] calculated that reaction rates overestimated the current estimated reaction rates of primary H abstraction from methane (R1C), ethane (R2C) and *iso*-butane (R5Cb) within 4.27–4.44, 4.51–6.41 and 5.27–4.40, respectively, at

temperature intervals of 800–1100 K. For reaction R3Cb, we observed good agreement with Chan et al.[31] values (0.68–0.65) between 800 and 1100 K. Table 6.9 provides a detailed comparison between our calculated reaction rate constants and those reported by Chen at al.[31] and Yamaguchi et al.[30]

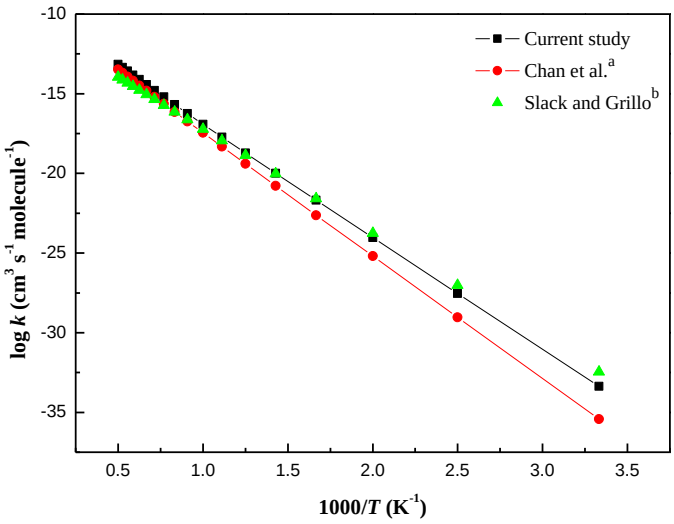

(a)

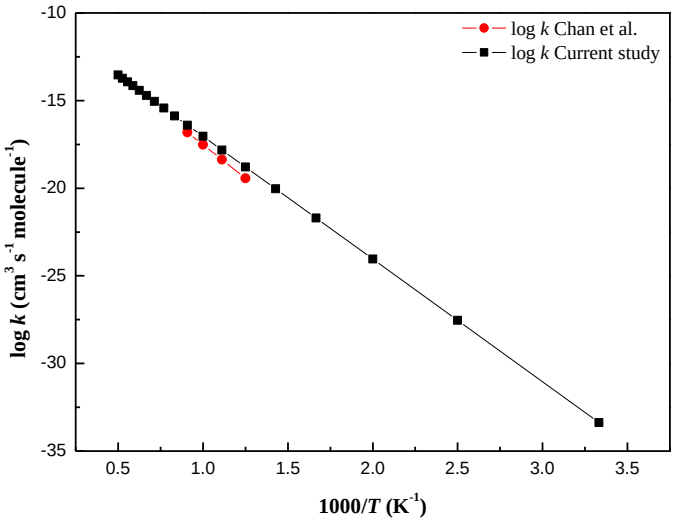

(b)

Figure 6.4. Arrhenius plot of the reaction rate constant for reaction R1 (a) and reaction R1B (b). [a] Chen et al.[31], [b] Slack and Grillo[15].

Having established an accuracy benchmark for the aforementioned reactions of alkanes with NO_2, we can now present rate coefficients of unreported H abstraction from aliphatic alkanes and alkenes in addition to ethylbenzene by NO_2 radical. Table 6.8 reports Arrhenius parameters for H abstraction from alkanes, alkenes and ethylbenzene producing the *trans-HONO, cis*-HONO, *iso*-HNO_2 channel isomers. Figure S6.1a–c in the Supplementary Information of Appendix III displays the Arrhenius plots of alkane + NO_2 forming R + HONO (*trans*-HONO, *cis*-HONO *and iso*-HNO_2). For *trans*-HONO, abstraction of a H atom from the primary C–H bond in alkanes (R2A, R3Aa, R4Aa and R5Aa) shows very comparable Arrhenius plots. The leading channel in the alkanes family is the removal of a H atom from a tertiary site in *iso*-butane (R5Ab) for the *trans*-HONO isomer. The reaction rate for the removal of H atoms from the secondary site (R3Cb and R4Cb) remained between the corresponding values of primary and tertiary sites reflecting the strength of the corresponding C-H sites.

Figure S6.2a–S6.2c (Appendix III-SI) portray Arrhenius plots for H abstraction from alkenes, namely ethylene, propene, 1-butene and 2-butene producing the *trans*-HONO, *cis*-HONO and *iso*-HNO_2 conformers, respectively. As expected from pertinent BDHs values in alkene, allylic H abstraction (R6Ab, R6Bb, R8A and R8B) was the dominant channel over the primary C–H bond in 1-butene (R7B) for both *trans*- and *cis*-HONO corridors. The least favourable channel was via the vinylic H abstraction in alkene (R6Aa, R6Ba, R9A and R9B). For the *iso*-HNO_2 in the alkene family (figure S6.2c), the H atom removal from the same allylic C-H sites in different compounds such as propene (R6Cb) and 2-butene (R8C)

remained the leading channels. Overall, the *cis*-configuration product in alkanes and alkenes proceeded with higher reaction rate constants than did the *iso*- and *trans*-conformers owing to lower activation energies. Figure S6.3 (Appendix III-SI) portrays the Arrhenius plot for reactions R10A, R10B, R10C, R11A, R11B and R11C of ethylbenzene + NO_2. Similar to aliphatic hydrocarbon, ethylbenzene reacted with NO_2 mainly via abstraction of *cis*-HONO + benzylic rather than *iso*-HNO_2/trans-HNO_2 + benzylic.

Overall, within the alkanes, abstraction of H by NO_2 from the tertiary C-H site of *iso*-butane remained the leading channel for *trans*-HONO (R5Ab) and *cis*-HONO (R5Bb) between a temperature interval of 300–900 K and between 300–2000 K formation, and *iso*-HNO_2 isomers from the abstraction of H from tertiary C-H bond of *iso*-butane was the dominant pathway. For the alkenes family, we observed that the rate constant for removal of H from the allylic sites of 2-butene (300–600 K) and propene (700–2000 K) resulting in *trans*-HONO was the most favourable. In the case of *cis*-HONO and *iso*-HNO_2, the removal of the allylic C-H site from propene showed higher reaction rate constants at a temperature interval of 300–2000 K. In summary, we found H abstraction reaction of NO_2 + R–H → *cis*-HONO + R remained the favourable mechanism.

To vindicate the different roles of H abstraction reactions from alkane and alkene by NO_2, we developed Evans-Polanyi plots shown in Figures 6.5a and 6.5b. These show that the higher H abstraction rate for NO_2 + R–H → *cis*-HONO + R described in the kinetic section corroborated with $\Delta^{\ddagger}H^{o}_{298}$ versus BDH for each corresponding reaction of alkane and alkene families. Furthermore, Figures 65a and 65b demonstrate linear correlations between activation $\Delta^{\ddagger}H^{o}_{298}$ and BDH for each group of hydrocarbons. The least square slope coefficients lie within the expected range for the Evans-Polanyi plots (0.0–1.0). The

literature has reported similar findings for H abstractions from hydrocarbons by HO_2 and NH_2 radicals.[48, 51] The developed Evans-Polanyi plots allow calculation of the $\Delta^{\ddagger}H^{o}_{298}$ for the reaction of NO_2 with other unreported hydrocarbons.

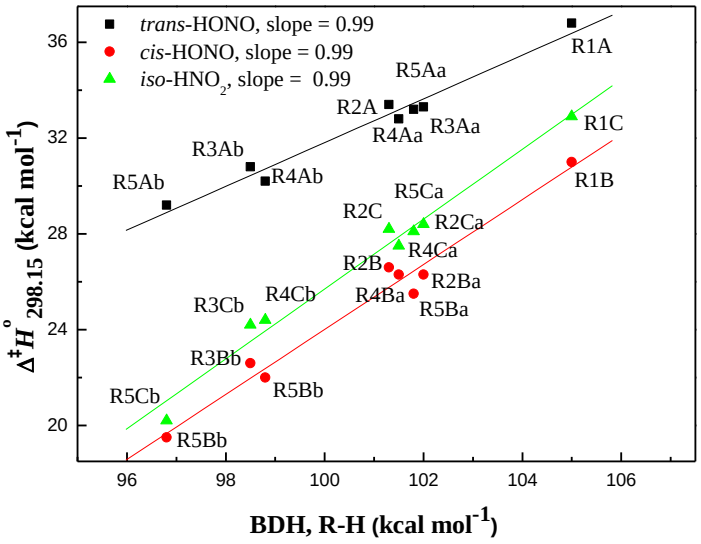

(a)

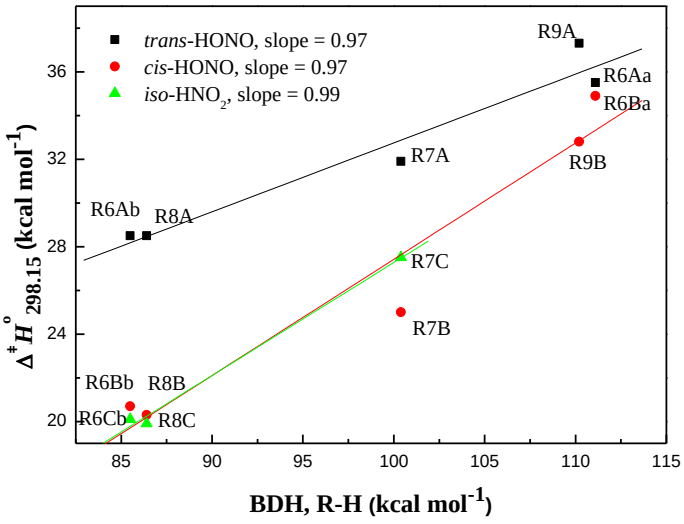

(b)

Figure 6.5. Evans-Polanyi plots for the H abstraction reaction of (a) NH_2 + R–H (alkane) and (b) NH_2 + R–H (alkene) forming *trans*-HONO, *cis*-HONO and *iso*-HNO_2 isomers.

6.4. Conclusions

The CBS-QB3 composite method was employed to predict the thermochemistry and kinetic parameters for H abstraction from a series of aliphatic hydrocarbon series, i.e. C_1–C_4 alkane and alkene by NO_2 radical. We utilised ethylbenzene as the representative model compound for alkyl benzenes. Three different isomers of nitrous acid formed with relative standard activation enthalpies in the order $\Delta^{\ddagger}H^{o}_{298}$ (*trans*-HONO) > $\Delta^{\ddagger}H^{o}_{298}$ (*iso*-HNO_2) $\Delta^{\ddagger}H^{o}_{298}$ (*cis*-HONO) for all selected reactions. In comparison to previous literature values, we observed a mean unsigned error of 0.42 kcal mol^{-1} in $\Delta_r E_0$ of primary, secondary and tertiary H abstraction from methane, propane and *iso*-butane. For H abstraction from methane producing *trans*-HONO (R1A) and *cis*-HONO (R1B), over a temperature range of 800–1100 K, the computed reaction rate constants (combined reaction rate constants from R1A and R1B) agreed with the available experimental measurements, i.e. $k_{calculated}/k_{experimental}$ ratio with a difference within factors of 0.47–0.73. Overall, the dominant channel was the formation of R + *cis*-HONO. Intuitively, estimated reaction rate constants follow the same order as for $\Delta^{\ddagger}H^{o}_{298}$ with higher reaction rates for R + *cis*-HONO products. While the *trans*-HONO isomer was more stable than *cis*-HONO and *iso*-HNO_2, reaction rate constants leading to formation of R + *trans*-HONO were significantly lower.

Appendix III: Supplementary Information

Figure S6.1. Arrhenius plots showing rate constant of H abstraction of C_1–C_4 alkane with NO_2 forming (a) *trans*-HONO, (b) *cis*-HONO and (c) *iso*-HNO_2 isomers.

Figure S6.2. Arrhenius plots showing rate constant of H abstraction of C_2–C_4 alkene with NO_2 forming (a) *trans*-HONO, (b) *cis*-HONO and (c) *iso*-HNO_2 isomers.

Figure S6.3. Arrhenius plots showing rate constant of H abstraction of ethylbenzene with NO_2 forming *trans*-HONO, *cis*-HONO, and *iso*-HNO

6.5. References

1. Borodkin, G. I.; Shubin, V. G., Nitrosonium Complexes of Organic Compounds. Structure and Reactivity. *Russ. Chem. Rev.* **2001**, *70*, 211-230.

2. Shiri, M., Dinitrogen Tetroxide: N_2O_4. *Synlett* **2006**, *2006*, 1789-1790.

3. Giamalva, D. H.; Kenion, G. B.; Church, D. F.; Pryor, W. A., Rates and Mechanisms of Reactions of Nitrogen Dioxide with Alkenes in Solution. *J. Am. Chem. Soc.* **1987**, *109*, 7059-7063.

4. Baldock, H.; Levy, N.; Scaife, C. W., 553. Addition of Dinitrogen Tetroxide to Olefins. Part V. Cyclohexene and the Octenes. *J. Chem. Soc.* **1949**, 2627-2633.

5. Brand, J.; Stevens, I., 123. Mechanism and Stereochemistry of the Addition of Nitrogen Dioxide to Olefins. *J. Chem. Soc.* **1958**, 629-638.

6. Pryor, W. A.; Lightsey, J. W.; Church, D. F., Reaction of Nitrogen Dioxide with Alkenes and Polyunsaturated Fatty Acids: Addition and Hydrogen-Abstraction Mechanisms. *J. Am. Chem. Soc.* **1982**, *104*, 6685-6692.

7. Augusto, O.; Bonini, M. G.; Amanso, A. M.; Linares, E.; Santos, C. C.; De Menezes, S. l. L., Nitrogen Dioxide and Carbonate Radical Anion: Two Emerging Radicals in Biology. *Free Radic. Biol. Med.* **2002**, *32*, 841-859.

8. Guan, Y.; Yang, B.; Qi, S.; Yi, C., Kinetic Modeling of the Free-Radical Process During the Initiated Thermal Cracking of Normal Alkanes with 1-Nitropropane as an Initiator. *Ind. Eng. Chem. Res.* **2011**, *50*, 9054-9062.

9. Rasmussen, C. L.; Rasmussen, A. E.; Glarborg, P., Sensitizing Effects of NO_x on CH_4 Oxidation at High Pressure. *Combust. Flame* **2008**, *154*, 529-545.

10. Pritchard, H., Thermal Decomposition of Isooctyl Nitrate. *Combust. Flame* **1989**, *75*, 415-416.

11. Clothier, P.; Pritchard, H.; Poirier, M.-A., Synergy between Additives in Stimulating Diesel-Fuel Ignition. *Combust. Flame* **1993**, *95*, 427-429.

12. Bowman, C. T., Fourteenth Symposium (International) on Combustionkinetics of Nitric Oxide Formation Incombustion Processes. *Symp. (Int.) Combust.* **1973**, *14*, 729-738.

13. Giménez-López, J.; Alzueta, M. U.; Rasmussen, C. T.; Marshall, P.; Glarborg, P., High Pressure Oxidation of C_2H_4/NO Mixtures. *P. Combust. Inst.* **2011**, *33*, 449-457.

14. Hori, M.; Matsunaga, N.; Marinov, N.; William, P.; Charles, W., An Experimental and Kinetic Calculation of the Promotion Effect of Hydrocarbons on the NO-NO_2 Conversion in a Flow Reactor. *Symp. (Int.) Combust.* **1998**, *27*, 389-396.

15. Slack, M.; Grillo, A., Shock Tube Investigation of Methane-Oxygen Ignition Sensitized by No 2. *Combusti. Flame* **1981**, *40*, 155-172.

16. Bendtsen, A. B.; Glarborg, P.; Dam-Johansen, K., Low Temperature Oxidation of Methane: The Influence of Nitrogen Oxides. *Combust. Sci. Technol.* **2000**, *151*, 31-71.

17. Han, L.-B.; Tsubota, S.; Haruta, M., Effect of the Addition of Nitrogen Dioxide on the Gas-Phase Partial Oxidation of Methane with Oxygen under Normal Pressures. *Chem. Lett.* **1995**, 931-932.

18. Otsuka, K.; Takahashi, R.; Amakawa, K.; Yamanaka, I., Partial Oxidation of Light Alkanes by NO_x in the Gas Phase. *Catal. Today* **1998**, *45*, 23-28.

19. Takemoto, T.; Tabata, K.; Teng, Y.; Nakayama, A.; Suzuki, E., The Effects of Reaction Pressures on the Production of Methanol through the Selective Oxidation of Methane in CH_4–O_2–NO_x (x = 1 or 2). *Appl. Catal., A.* **2001**, *205*, 51-59.

20. Konnov, A. A.; Zhu, J. N.; Bromly, J. H.; Zhang, D.-k., The Effect of NO and NO_2 on the Partial Oxidation of Methane: Experiments and Modeling. *Proc. Combust. Inst.* **2005**, *30*, 1093-1100.

21. Zalc, J. M.; Green, W. H.; Iglesia, E., NO_x -Mediated Homogeneous Pathways for the Synthesis of Formaldehyde from CH_4-O_2 Mixtures. *Ind. Eng. Chem. Res.* **2006**, *45*, 2677-2688.

22. Gersen, S.; Mokhov, A.; Darmeveil, J.; Levinsky, H.; Glarborg, P., Ignition-Promoting Effect of NO_2 on Methane, Ethane and Methane/Ethane Mixtures in a Rapid Compression Machine. *Proc. Combust. Inst.* **2011**, *33*, 433-440.

23. Chan, Y.; Barnes, F.; Bromly, J.; Konnov, A.; Zhang, D., The Differentiated Effect of NO and NO_2 in Promoting Methane Oxidation. *Proc. Combust. Inst.* **2011**, *33*, 441-447.

24. Oluwoye, I.; Dlugogorski, B. Z.; Gore, J.; Westmoreland, P. R.; Altarawneh, M., Enhanced Ignition of Biomass in Presence of NO_x. *Fire Saf. J.* **2017**, *91*, 235-242.

25. Pryor, W. A.; Lightsey, J. W., Mechanisms of Nitrogen Dioxide Reactions: Initiation of Lipid Peroxidation and the Production of Nitrous Acid. *Sci* **1981**, *214*, 435-437.

26. Sosnovsky, G., Free Radical Reactions in Preparative Organic Chemistry. **1964**, 255-269.

27. Fossey, J.; Lefort, D.; Sorba, J., Free Radicals in Organic Chemistry. *J. Am. Chem. Soc.* **1996**, *118*, 10678-10678.

28. Topchiev, A. V. e., *Nitration of Hydrocarbons and Other Organic Compounds*; Elsevier, 2013.

29. Tabata, K.; Teng, Y.; Yamaguchi, Y.; Sakurai, H.; Suzuki, E., Experimental Verification of Theoretically Calculated Transition Barriers of the Reactions in a Gaseous Selective Oxidation of CH_4−O_2−NO_2. *J. Phys. Chem. A.* **2000**, *104*, 2648-2654.

30. Yamaguchi, Y.; Teng, Y.; Shimomura, S.; Tabata, K.; Suzuki, E., Ab Initio Study for Selective Oxidation of Methane with NO_x (x = 1, 2). *J. Phys. Chem. A.* **1999**, *103*, 8272-8278.

31. Chan, W.-T.; Heck, S. M.; Pritchard, H. O., Reaction of Nitrogen Dioxide with Hydrocarbons and Its Influence on Spontaneous Ignition. A Computational Study. *PCCP* **2001**, *3*, 56-62.

32. M. J. Frisch, G. W. T., H. B. Schlegel, G. E. Scuseria, M. A. Robb, J. R. Cheeseman, G. Scalmani, V. Barone, B. Mennucci, G. A. Petersson, et al. , Gaussian 09, Revision A.1., Gaussian, Inc.:. Wallingford, CT, 2009.

33. Montgomery, J. A.; Frisch, M. J.; Ochterski, J. W.; Petersson, G. A., A Complete Basis Set Model Chemistry. Vi. Use of Density Functional Geometries and Frequencies. *J. Chem. Phys.* **1999**, *110*, 2822-2827.

34. Zhao, Y.; Truhlar, D. G., The M06 Suite of Density Functionals for Main Group Thermochemistry, Thermochemical Kinetics, Noncovalent Interactions, Excited States, and Transition Elements: Two New Functionals and Systematic Testing of Four M06-Class Functionals and 12 Other Functionals. *Theor. Chem. Acc.* **2008**, *120*, 215-241.

35. Mayer, P. M.; Parkinson, C. J.; Smith, D. M.; Radom, L., An Assessment of Theoretical Procedures for the Calculation of Reliable Free Radical Thermochemistry: A Recommended New Procedure. *J. Chem. Phys.* **1998**, *108*, 604-615.

36. Ahubelem, N.; Altarawneh, M.; Dlugogorski, B. Z., Dehydrohalogenation of Ethyl Halides. *Tetrahedron Lett.* **2014**, *55*, 4860-4868.

37. Vandeputte, A. G.; Sabbe, M. K.; Reyniers, M.-F.; Van Speybroeck, V.; Waroquier, M.; Marin, G. B., Theoretical Study of the Thermodynamics and Kinetics of Hydrogen Abstractions from Hydrocarbons. *J. Phys. Chem. A.* **2007**, *111*, 11771-11786.

38. Saeys, M.; Reyniers, M.-F.; Marin, G. B.; Van Speybroeck, V.; Waroquier, M., Ab Initio Calculations for Hydrocarbons: Enthalpy of Formation, Transition State Geometry, and Activation Energy for Radical Reactions. *J. Phys. Chem. A.* **2003**, *107*, 9147-9159.

39. Canneaux, S.; Bohr, F.; Henon, E., Kisthelp: A Program to Predict Thermodynamic Properties and Rate Constants from Quantum Chemistry Results†. *J. Comput. Chem.* **2014**, *35*, 82-93.

40. Truhlar, D. G.; Garrett, B. C.; Klippenstein, S. J., Current Status of Transition-State Theory. *J. Phys. Chem. A.* **1996**, *100*, 12771-12800.

41. Eckart, C., The Penetration of a Potential Barrier by Electrons. *Phys. Rev.* **1930**, *35*, 1303-1309.

42. Fernández-Ramos, A.; Ellingson, B. A.; Meana-Pañeda, R.; Marques, J. M.; Truhlar, D. G., Symmetry Numbers and Chemical Reaction Rates. *Theor. Chem. Acc.* **2007**, *118*, 813-826.

43. Van Speybroeck, V.; Gani, R.; Meier, R. J., The Calculation of Thermodynamic Properties of Molecules. *Chem. Soc. Rev.* **2010**, *39*, 1764-1779.

44. Asatryan, R.; Bozzelli, J. W.; Simmie, J. M., Thermochemistry for Enthalpies and Reaction Paths of Nitrous Acid Isomers. *Int. J. Chem. Kinet.* **2007**, *39*, 378-398.

45. Koch, T. G.; Sodeau, J. R., Photochemistry of Nitric Acid in Low-Temperature Matrixes. *J. Phys. Chem.* **1995**, *99*, 10824-10829.

46. Nguyen, M. T.; Sumathi, R.; Sengupta, D.; Peeters, J., Theoretical Analysis of Reactions Related to the HNO_2 Energy Surface: OH + NO and H + NO_2. *Chem. Phys.* **1998**, *230*, 1-11.

47. Luo, Y. R., *Handbook of Bond Dissociation Energies in Organic Compounds*; CRC Press, 2002.

48. Siddique, K.; Altarawneh, M. K.; Gore, J.; Westmoreland, P. R.; Dlugogorski, B. Z., Hydrogen Abstraction from Hydrocarbons by NH_2. *J. Phys. Chem. A* **2017**.

49. Gurvich, L. V.; Veyts, I. V.; Alcock, C. B., *Thermodynamic Properties of Individual Substances: Elements and Compounds*; Hemisphere Publishing: New York, 1991; Vol. 2.

50. Chase, M. W., Jr.,, Nist-Janaf Thermochemical Tables. In *J. Phys. Chem. Ref. Data*, , Vol. Monograph 9, pp 1-1951.

51. Aguilera-Iparraguirre, J.; Curran, H. J.; Klopper, W.; Simmie, J. M., Accurate Benchmark Calculation of the Reaction Barrier Height for Hydrogen Abstraction by the Hydroperoxyl Radical from Methane. Implications for C_nH_{2n}+2 Where $n = 2 \rightarrow 4$. *J. Phys. Chem. A.* **2008**, *112*, 7047-7054.

Chapter 7

Reduction of N_2O Emission with Catechol

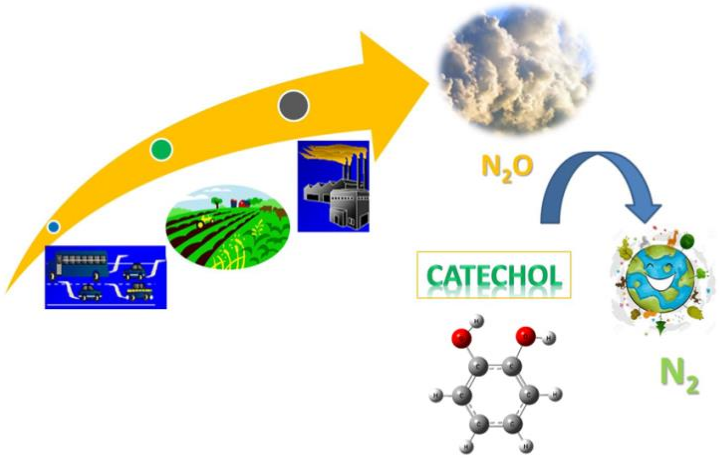

This chapter developed a systematic approach to the investigation of gas-phase reduction of N_2O using catechol. The interaction of N_2O with catechol has been studied using meta-Hybrid Density Functional Theory. The current chapter explores the plausible corridors for the diminution of N_2O into N_2 from those systems entailing the substantial concentration of N_2O.

7.0. Abstract

The NO_xOUT process affords a viable route for minimising the emission of NO_x. However, the generation of appreciable concentrations of N_2O as an unwanted by-product overshadows the overall merits of the NO_xOUT process. This contribution elucidates mechanistic reaction pathways into the conversion of N_2O to N_2 via bimolecular reaction of N_2O with catechol, a representative model compound for lignin constituent of biomass. Initial reactions of N_2O with catechol branch into three pathways: (i) 1,2-cycloaddition of N_2O to the C_6 ring; (ii) abstraction of an O atom from N_2O by catechol; and, (iii) concerted abstraction of the two H-hydroxyl atoms in catechol by N_2O. Opening transition structures in these pathways require the enthalpy of activation of 184.8, 257.1 and 281.5 kJ mol^{-1}, respectively. Reactions leading to the transformation of N_2O into N_2 along the 1,2-cycloaddition pathway characterise formation of a heteroatomic fused two-ring adduct, followed by elimination of N_2. The reaction of N_2O with cyclopenta-2,4-dienone, the major product from pathway (iii), proceeds similarly via 1,2-cycloaddition and transfer of an O atom from N_2O to the ring. Mechanistic and kinetic parameters developed in this study should assist in designing industrial processes for reduced emission of N_2O, by addition of biomass to N-rich substances, such as ammonium nitrate based blasting agents.

7.1. Introduction

Health and environmental concerns pertinent to the emission of nitrogen oxides (NO_x) from thermal operations have accelerated pioneering of several abatement technologies.[1] The selective catalytic reduction (SCR)[2-6] and selective non-catalytic reduction (SNCR) [7-12] processes constitute the most promising and effective approaches. NO_xOUT represents a particularly important implementation of SNCR. The NO_xOUT process applies urea as a reducing agent for NO_x, most notably in the narrow temperature window of 1173 to 1373 K. Merits of the NO_xOUT include the absence of heterogeneous catalysts and, hence, lower operating and capital costs.[13] Combustion chemistry of the NO_xOUT has been the subject of intense research over the last two decades.[14-16] The NO_xOUT process effectively reduces emissions of NO_x via transforming NO and NO_2 into N_2O and N_2. Most prominent reactions entail decomposition of N-agents into NH_2 fragments and subsequent bimolecular reactions of NH_2, HNCO and NCO with NO_2 and NO.

Generation of a significant amount of N_2O, and its emission into the atmosphere,[17-19] from the NO_xOUT process, overshadows its overall environmental merits. N_2O shares matching greenhouse effects with NO_x gases.[20-22] This challenge translates to re-optimising the NO_xOUT process to eliminate the formation of N_2O. Previous contributions aiming to improve performance of the NO_xOUT process have mainly targeted reducing emission of NO_x with minimal focus on formation of N_2O.[6, 23, 24] As the NO_xOUT process proceeds via a series of gas-phase reactions (i.e. in absence of heterogeneous catalysts), it is intuitively appealing that any modifications must not compromise this important advantage. A viable approach to consider is to assess the effect of introducing supplementary additives to urea formulations to supress the emission of N_2O.

We propose that hydroxylated benzenes have potential to reduce the emission of N_2O via a facile mechanism. Catechol or 1,2-hydroquinone (benzene-1,2-diol) appears as a major product from rupture of ether linkages in biomass constituents such as lignin[25-27]. Catechol also forms as a byproduct from the combustion of coal.[28, 29] In this contribution, we map out detailed reaction mechanisms for all plausible initial channels involved in the interaction between a catechol molecule and N_2O. The previous work indicates that unimolecular decomposition of *ortho*-semiquinone radical[30] and catechol[25] yields predominantly 1,2-benzoquinone that dissociates readily into CO and cyclopenta-2,4-dienone. Consequently, in the present chapter, we also investigate the plausible reduction of N_2O via its bimolecular reactions with cyclopenta-2,4-dienone. Developing an understanding of these pathways is instrumental in gaining an insight into potent N_2O abatement methodology and should pave the way for a rigorous experimental validation.

7.2. Computational details

Gaussian 09 suite of programs served to perform all structural optimisations and energy estimations.[31] We executed all calculations at the meta-hybrid DFT functional of M05-2X/6-311+G(d,p) level. M05-2X demonstrates optimum performance for general applications in thermochemical kinetics and non-covalent interactions.[32] In a previous study, we provided a kinetic and thermochemical assessment for the performance of M05-2X functional against analogous experimental measurements[33]. We report all energetic values throughout the discussion in this article on the *H*-scale at 298.15 K. The ChemRate[34] code facilitated calculations of reaction rate constants in the high-pressure limit according to the conventional transition state theory.

7.3. Results and Discussion

Reaction of N_2O with catechol branches into three initial corridors: (i) 1,2-cycloaddition to the C_6 ring in the catechol molecule producing a heteroatomic fused two-ring adduct; (ii) abstraction of an O atom from N_2O by the catechol ring leading to the formation of an epoxide intermediate; and, (iii) abstractions of the two H-hydroxyl atoms by N_2O forming HNNOH and 1,4-benzoquinone. Figures 7.1, 7.2 and 7.3 depict potential energy surfaces (PESs) for these three reactions and their subsequent steps for the three channels, respectively. All reactions in Figures 7.1-7.3 proceed as closed-shell pathways.

7.3.1. 1,2-cycloaddition to the C_6 ring in the catechol molecule

This pathway initiates via 1,2-cycloaddition of N_2O molecule to the catechol molecule in a mode similar to the addition of singlet oxygen to aromatic conjugated systems[35]. The initiation reaction forms the 1A intermediate after passing a barrier of 184.8 kJ mol^{-1}, through the transition state TS1A. The fused two-ring structure of 1A constitutes a stable intermediate with distances in N–N, N–O, C–N and C–O amounting to 1.21, 1.38, 1.5 and 1.50 Å, respectively. In the second reaction, a nitrogen molecule departs the 1A intermediate via a modest activation enthalpy of 81.9 kJ mol^{-1} associated with the transition structure TS2A. Expulsion of N_2 molecule through TS2A induces a 1,2-hydrogen shift affording the 2A molecule. The 2A intermediate and the N_2 molecule reside 212.8 kJ below the entrance channel.

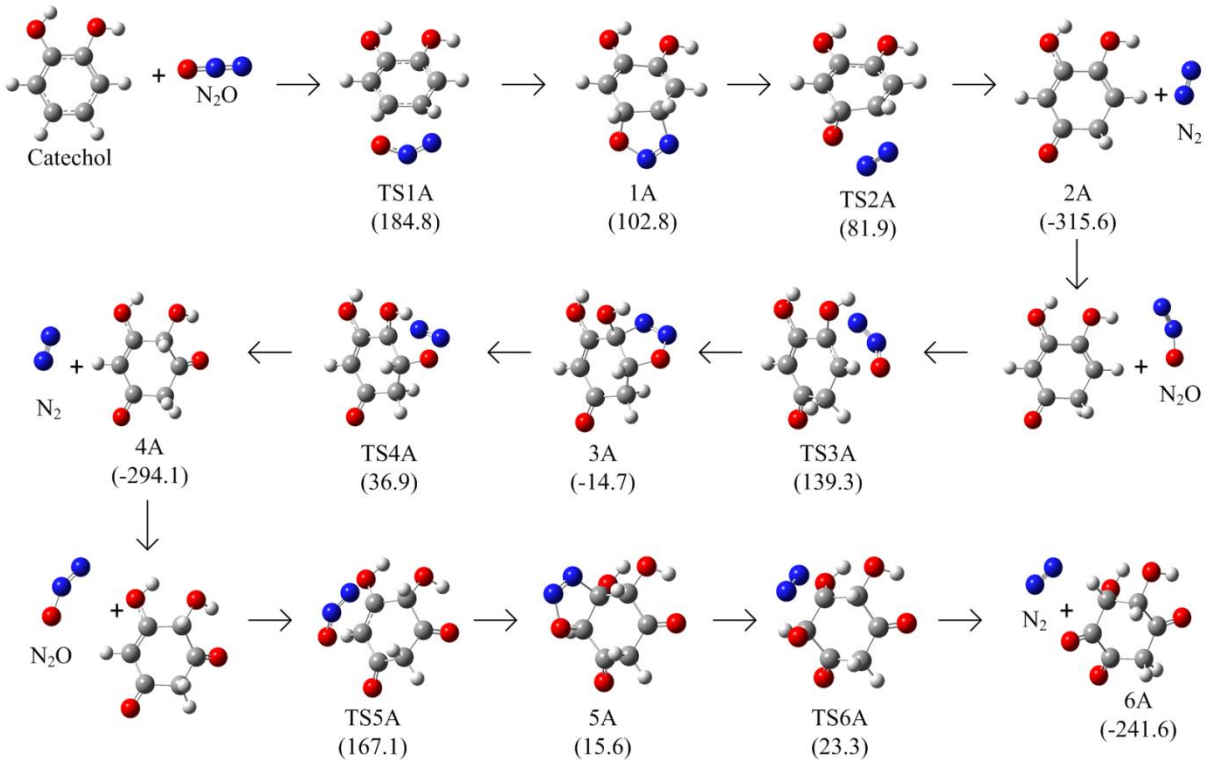

Figure 7.1. PES for the transformation of N_2O into N_2 initiated by 1,2-cycloaddition of N_2O to the π-conjugated system of catechol. Values of activation enthalpies are in kJ mol^{-1} and reaction enthalpies in kJ and are relative to isolated reactants in each step.

As Figure 7.1 depicts, subsequent addition of N_2O to 2A evolves in two similar steps, namely 1,2-cycloaddition (N_2O + 2A → 3A) and N_2 expulsion (2A → N_2 + 4A). Activation enthalpy for the second N_2O addition to the 2A molecule attains a value of 139.3 kJ mol^{-1}, i.e. lower by 45.5 kJ mol^{-1} when compared with the corresponding enthalpic barrier for the initial N_2O addition to the catechol molecule (TS1A). Likewise, unimolecular loss of N_2 from the 3A intermediate requires overcoming an enthalpic barrier of 36.9 kJ mol^{-1} (TS4A). Attack of N_2O molecule on a double bond in the 4A intermediates repeats the above-mentioned two-step process via similar enthalpic barriers and generates the oxygen rich compound 6A. Decomposition of 6A yields small oxygenated species, including CO, CO_2 and H_2CO. Intermediates 2A and 4A constitute stable compounds; i.e., they will live long enough to

undergo bimolecular reactions with N_2O. Overall, reactions in Figure 7.1 demonstrate that a catechol molecule transforms three N_2O molecules into N_2 through an overall activation enthalpy at 184.8 kJ mol^{-1}; i.e., the barrier of the first N_2O addition reaction.

7.3.2. Abstraction of O atom from N_2O by catechol

In the second plausible channel presented in Figure 7.2, a catechol molecule directly abstracts an O atom from N_2O through an activation enthalpy of 257.5 kJ mol^{-1} associated with the formation of TS1B. This reaction is highly exothermic by 91.9 kJ and generates the epoxide structure 1B and N_2. A 1,2-hydrogen shift stabilises the epoxide 1B adduct into the semiquinone intermediate 2B. This reaction necessitates 174.8 kJ mol^{-1} of activation enthalpy (TS2B). The 2B structure converts N_2O into N_2 via a trivial activation enthalpy of 7.3 kJ mol^{-1} (TS3B), in a very exothermic reaction of 217.8 kJ. A third conversion of N_2O by the 4B intermediate occurs analogously as portrayed in Figure 2.

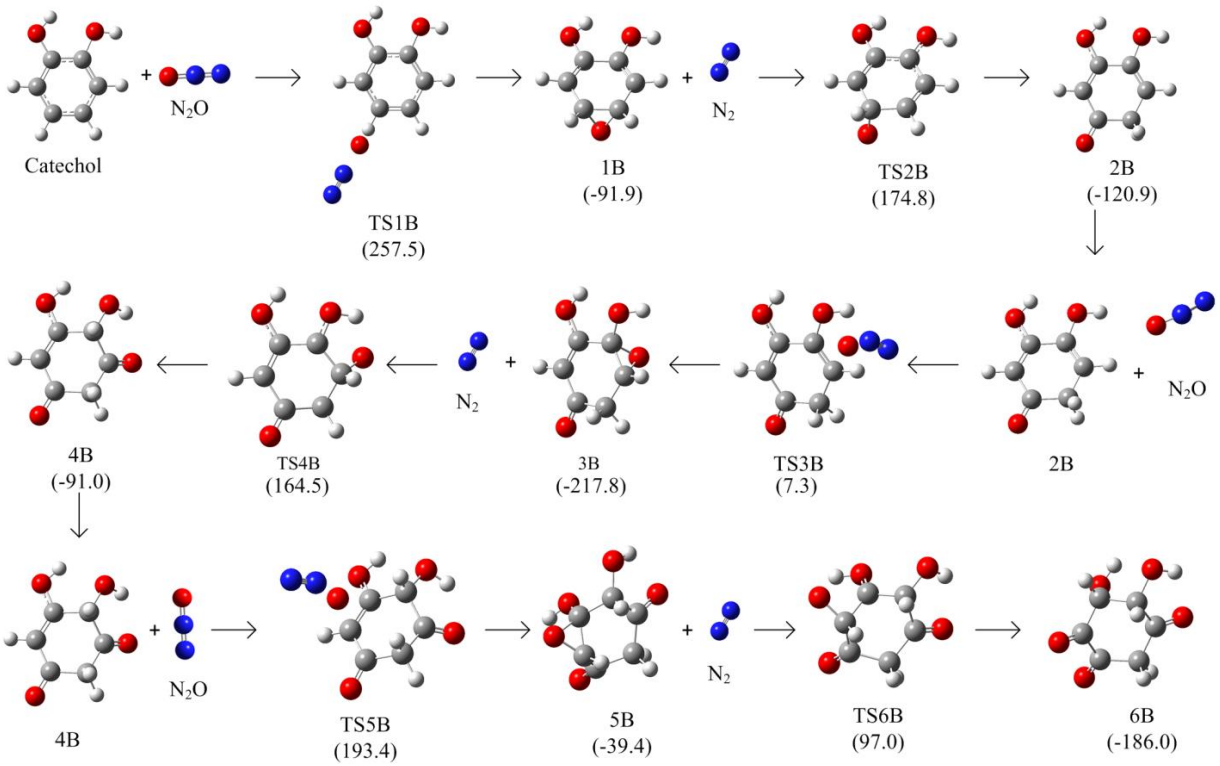

Figure 7.2. PES for the transformation of N_2O into N_2 via direct abstraction of O by the catechol molecule. Values of activation enthalpies are in kJ mol^{-1} and reaction enthalpies in kJ and are relative to isolated reactants in each step.

7.3.3. Concerted abstraction of two hydroxyl H atoms by N_2O

The third channel characterises concerted abstraction of the two H-hydroxyl atoms in the catechol molecule by O and the outer N atoms in N_2O, to form a molecule of HNNOH. Figure 7.3 shows the geometries of the nine-centred transition state of this reaction (TS1C). Formation of the HNNOH and the 1,2-benzoquinone (1C) moieties via TS1C incur endothermicity of 227.5 kJ and demands activation enthalpy of 281.5 kJ mol^{-1}. Expulsion of a CO molecule signifies the most plausible decomposition channel of 1C via an exceedingly high activation enthalpy of 406.7 kJ mol^{-1} (TS2C).

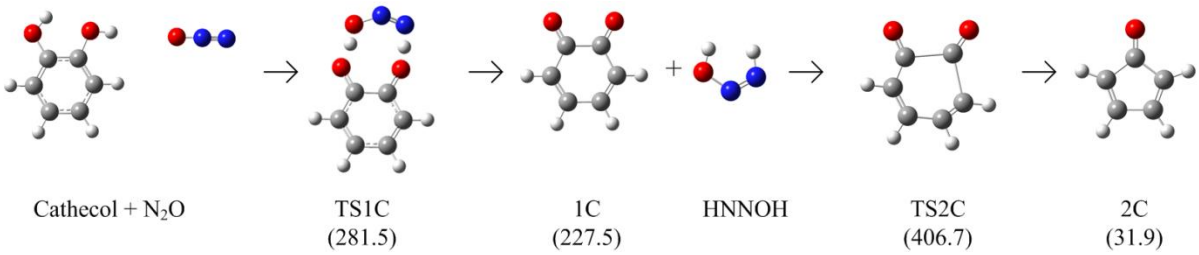

Figure 7.3. PES for the transformation of N_2O into N_2 initiated via abstraction of the two H-hydroxyl atoms by N_2O. Values of activation enthalpies are in kJ mol^{-1} and reaction enthalpies in kJ and are relative to isolated reactants in each step.

7.3.4. Reaction of N_2O with cyclopenta-2,4-dienone

In an analogy to pathways illustrated in Figures 7.1 and 7.2, cyclopenta-2,4-dienone (2C) reacts with N_2O via 1,2-cycloaddition and direct abstraction of O atoms from N_2O. Figure 7.4 presents the mechanism of N_2O reaction with the 2C adduct. The high enthalpic barrier of TS7C (262.5 kJ mol^{-1}) in reference to that of TS3C (102.3 kJ mol^{-1}) largely shut down the abstraction channel in preference to the addition channel. Subsequent reactions along the addition channel accord with mechanistic and energetic account shown in Figure 7.1 for the catechol + N_2O system.

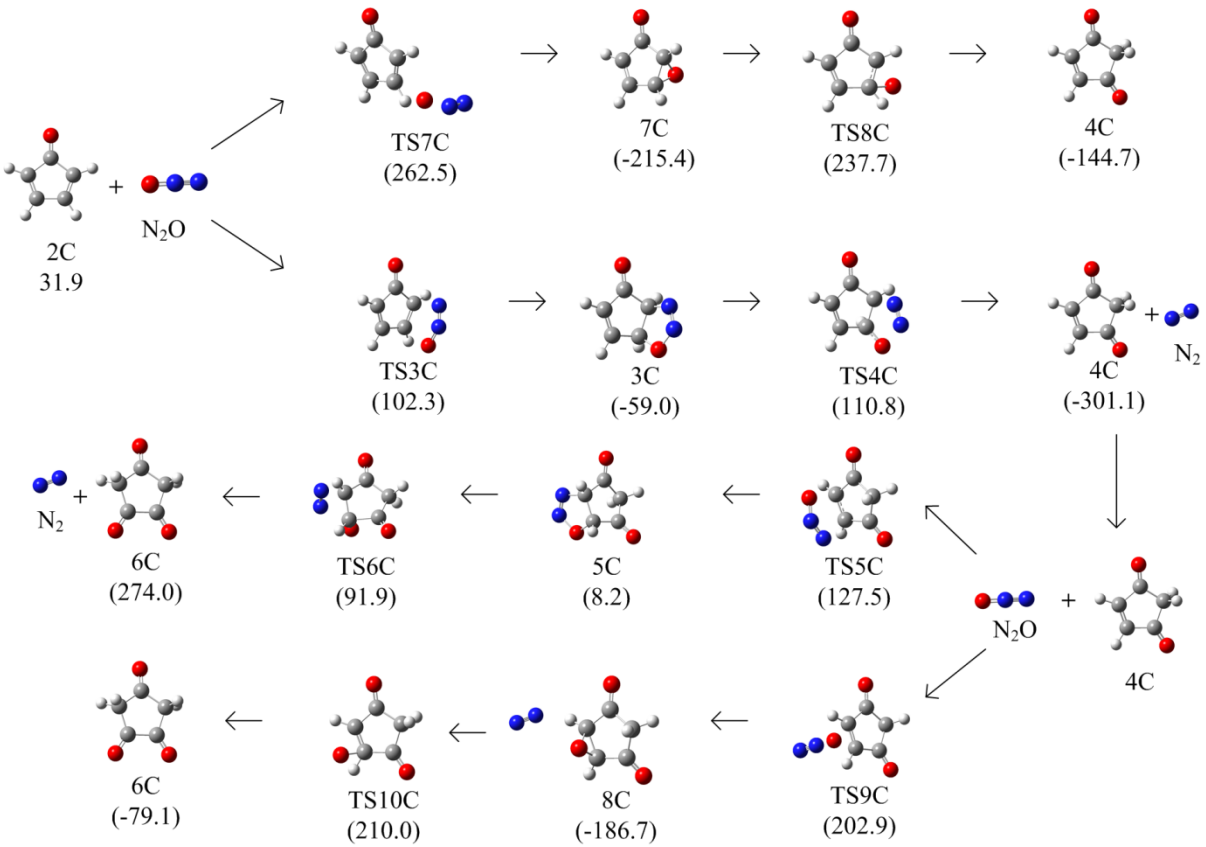

Figure 7.4. PES for transformation of N_2O into N_2 through reaction of N_2O with cyclopenta-2,4-dienone. Values of activation enthalpies are in kJ mol^{-1} and reaction enthalpies in kJ, and are relative to isolated reactants in each step.

7.3.5. Calculation of rate constants

Table 7.1 displays Arrhenius rate parameters for all considered reactions fitted over a temperature range from 300 to 2000 K. For unimolecular reactions, parameters are correspond to the high-pressure limit. The pathway leading to the formation of the 1A adduct largely predominates the other two initiation channels.

Table 7.1. Rate parameters between 300 and 2000 K. Values of Arrhenius parameter (A) are in units of s^{-1} T^n or cm^3 s^{-1} $molecule^{-1}$ T^n and values of E_a/R are in K; $k = A\ T^n \exp(-E_a/(R\ T))$.

Reactions	Transition state	A	n	E_a/R
Catechol + N_2O → 1A	TS1A	1.0×10^{-22}	2.45	22 100
1A → 2A + N_2	TS2A	1.58×10^{12}	0.5	10 200
2A + N_2O → 3A	TS3A	7.94×10^{-23}	2.4	16 600
3A → 4A + N_2	TS4A	3.16×10^{12}	0.3	4 800
4A + N_2O → 5A	TS5A	5.01×10^{-23}	2.6	19 900
5A → 6A + N_2	TS6A	3.16×10^{12}	0.3	3 100
Catechol + N_2O → 1B + N_2	TS1B	2.51×10^{-21}	3.1	30 800
1B → 2B	TS2B	6.31×10^{12}	0.3	21 300
2B + N_2O → 3B + N_2	TS3B	1.00×10^{-21}	2.8	700
3B → 4B	TS4B	6.31×10^{12}	0.1	20 100
4B + N_2O → 5B + N_2	TS5B	7.45×10^{-12}	2.9	23 100
5B → 6B	TS6B	2.00×10^{13}	0.02	12 000
Catechol + N_2O → 1C + HNNOH	TS1C	6.31×10^{-15}	3.2	33 300
1C → 2C + CO	TS2C	3.16×10^{-11}	0.6	17 100
2C + N_2O → 3C	TS3C	2.00×10^{-23}	2.7	12 100
2C + N_2O → 7C + N_2	TS7C	2.00×10^{-21}	3.1	31 400
3C → 4C + N_2	TS4C	5.01×10^{11}	0.9	13 600
7C → 4C	TS8C	2.00×10^{12}	0.4	33 300
4C + N_2O → 5C	TS5C	7.94×10^{-23}	2.5	15 200

$4C + N_2O \rightarrow 8C + N_2$	TS9C	2.51×10^{-21}	2.9	24 300
$5C \rightarrow 6C + N_2$	TS6C	1.58×10^{12}	0.6	11 400
$8C \rightarrow 6C$	TS10C	5.01×10^{12}	0.8	25 500

7.4. Conclusions

Optimising the NO_xOUT process remains an active area of research of fundamental and applied significance. Herein, we have proposed that introducing catechol as an additive has potential to minimise the emission of N_2O, via converting it to N_2 through modest energy requirements. We have shown that 1,2-cycloaddition of N_2O to catechol or its major decomposition products proceeds in a two-step process involving the addition of N_2O and unimolecular elimination of N_2. Twofold abstraction of the H-hydroxyl atoms from catechol by N_2O, as well as the direct formation of N_2 via abstraction of an O atom by catechol, are of minor importance in comparison with the 1,2-cycloaddition channel. We predict the cyclopenta-2,4-dienone to be a stable species that resist the oxidation by O_2 enabling its bimolecular reactions with N_2O. Plausible future research directions may include experimental verifications of the constructed mechanisms and investigation of reactions of N_2O with other benzene-substituted compounds.

7.5. References

1. Rayson, M. S.; Altarawneh, M.; Mackie, J. C.; Kennedy, E. M.; Dlugogorski, B. Z., Theoretical Study of the Ammonia−Hypochlorous Acid Reaction Mechanism. *J. Phys. Chem. A* **2010,** *114*, 2597-2606.

2. Shelef, M., Selective Catalytic Reduction of NO_x with N-Free Reductants. *Chem. Rev.* **1995,** *95*, 209-225.

3. Amiridis, M. D.; Zhang, T.; Farrauto, R. J., Selective Catalytic Reduction of Nitric Oxide by Hydrocarbons. *Appl. Catal., B* **1996,** *10*, 203-227.

4. Niksa, S.; Fujiwara, N., A Predictive Mechanism for Mercury Oxidation on Selective Catalytic Reduction Catalysts under Coal-Derived Flue Gas. *J. Air Waste Manage. Assoc.* **2005,** *55*, 1866-1875.

5. Baleta, J.; Vujanović, M.; Pachler, K.; Duić, N., Numerical Modeling of Urea Water Based Selective Catalytic Reduction for Mitigation of NOx from Transport Sector. *J. Clean. Prod.* **2015,** *88*, 280-288.

6. Liang, X.; Zhong, Z.; Jin, B.; Chen, X.; Li, W.; Wei, H.; Guo, H., Experimental Study of the Influence of Sodium Salts as Additive to NO_xOUT Process. *Korean J. Chem. Eng.* **2010,** *27*, 1483-1491.

7. Muzio, L. J.; Quartucy, G. C.; Cichanowicz, J. E., Overview and Status of Post-Combustion NO_x Control: SNCR, SCR and Hybrid Technologies. *Int. J. Environ. Pollut.* **2002,** *17*, 4-30.

8. Baltasar, J.; Carvalho, M. G.; Coelho, P.; Costa, M., Flue Gas Recirculation in a Gas-Fired Laboratory Furnace: Measurements and Modelling. *Fuel* **1997,** *76*, 919-929.

9. Lee, J. B.; Kim, S. D., Kinetics of NO_x Reduction by Urea Solution in a Pilot Scale Reactor. *J. Chem. Eng. Japan* **1996,** *29*, 620-626.

10. Wang, Q.; Wang, Q.; Cai, J., Experimental Study of Urea on SNCR Removal of NO_x. *J. Chem. Pharm. Res.* **2014,** *6*, 2541-2546.

11. Lee, S.; Park, K.; Park, J. W.; Kim, B. H., Characteristics of Reducing NO Using Urea and Alkaline Additives. *Combust. Flame* **2005,** *141*, 200-203.

12. Caton, J. A.; Narney, J. K.; Cariappa, H. C.; Laster, W. R., The Selective Non-Catalytic Reduction of Nitric Oxide Using Ammonia at up to 15% Oxygen. *Can. J. Chem. Eng.* **1995,** *73*, 345-350.

13. Tayyeb Javed, M.; Irfan, N.; Gibbs, B. M., Control of Combustion-Generated Nitrogen Oxides by Selective Non-Catalytic Reduction. *J. Environ. Manage.* **2007,** *83*, 251-289.

14. Glarborg, P.; Dam-Johansen, K.; Miller, J. A.; Kee, R. J.; Coltrin, M. E., Modeling the Thermal DeNO_x Process in Flow Reactors. Surface Effects and Nitrous Oxide Formation. *Int. J. Chem. Kinet.* **1994,** *26*, 421-436.

15. Bae, S. W.; Roh, S. A.; Kim, S. D., NO Removal by Reducing Agents and Additives in the Selective Non-Catalytic Reduction (SNCR) Process. *Chemosphere* **2006,** *65*, 170-175.

16. Skreiberg, O.; Kilpinen, P.; Glarborg, P., Ammonia Chemistry Below 1400 K Under Fuel-Rich Conditions in a Flow Reactor. *Combust. Flame* **2004,** *136*, 501-518.

17. Caton, J. A.; Siebers, D. L., Comparison of Nitric Oxide Removal by Cyanuric Acid and by Ammonia. *Combust. Sci. Technol.* **1989,** *65*, 277-293.

18. Gentemann, A. M.; Caton, J. A., Flow Reactor Experiments on the Selective Non-Catalytic Removal (SNCR) of Nitric Oxide Using a Urea-Water Solution. *VDI-Berichte* **2003,** *1750*, 497-502.

19. Mendoza-Covarrubias, C.; Romero, C. E.; Hernandez-Rosales, F.; Agarwal, H., N_2O Formation in Selective Non-catalytic NO_x Reduction Processes. *J. Envir. Protect.* **2011**, 1095-1100.

20. Lyon, R. K.; Kramlich, J. C.; Cole, J. A., Nitrous Oxide: Sources, Sampling, and Science Policy. *Environ. Sci. Technol.* **1989,** *23*, 392-393.

21. Muzio, L. J.; Kramlich, J. C., An Artifact in the Measurement of N_2O from Combustion Sources. *Geophys. Res. Lett.* **1988,** *15*, 1369-1372.

22. Wang, J.; Jia, L.; Anthony, E. J., Mechanism for N_2O Formation from NO at Ambient Temperature. *AICHE J.* **2003,** *49*, 277-282.

23. Zamansky, V. M.; Lissianski, V. V.; Maly, P. M.; Ho, L.; Rusli, D.; Gardiner, W. C., Reactions of Sodium Species in the Promoted SNCR Process. *Combust. Flame* **1999,** *117*, 821-831.

24. Yang, W. J.; Zhou, J. H.; Zhou, Z. J.; Lu, Z. M.; Wang, Z. H.; Liu, J. Z.; Cen, K. F., Characteristics of Sodium Compounds on NO Reduction at High Temperature in NO_x Control Technologies. *Fuel Process. Technol.* **2008,** *89*, 1317-1323.

25. Altarawneh, M.; Dlugogorski, B. Z.; Kennedy, E. M.; Mackie, J. C., Theoretical Study of Unimolecular Decomposition of Catechol. *J. Phys. Chem. A* **2010,** *114*,1060-1067.

26. Dellinger, B.; Pryor, W. A.; Cueto, R.; Squadrito, G. L.; Hegde, V.; Deutsch, W. A., Role of Free Radicals in the Toxicity of Airborne Fine Particulate Matter. *Chem. Res. Toxicol.* **2001,** *14*, 1371-1377.

27. Dorrestijn, E.; Laarhoven, L. J. J.; Arends, I. W. C. E.; Mulder, P., The Occurrence and Reactivity of Phenoxyl Linkages in Lignin and Low Rank Coal. *J. Anal. Appl. Pyrolysis* **2000,** *54*, 153-192.

28. Hatcher, P. G.; Clifford, D. J., The Organic Geochemistry of Coal: From Plant Materials to Coal. *OrGeo* **1997,** *27*, 251-274.

29. Wornat, M. J.; Ledesma, E. B.; Marsh, N. D., Polycyclic Aromatic Hydrocarbons from the Pyrolysis of Catechol (ortho-dihydroxybenzene), a Model Fuel Representative of Entities in Tobacco, Coal, and Lignin. *Fuel* **2001,** *80*, 1711-1726.

30. Altarawneh, M.; Dlugogorski, B. Z.; Kennedy, E. M.; Mackie, J. C., Thermochemical Properties and Decomposition Pathways of Three Isomeric Semiquinone Radicals. *J. Phys. Chem. A* **2010,** *114*, 1098-1108.

31. Frisch, M. J.; Trucks,G. W.; Schlegel, H. B.; Scuseria, G. E.; Robb, M. A.; Cheeseman, J. R.; Scalmani,G.; Barone,V.; Mennucci, B.; Petersson, G. A.; et al. , Gaussian 09, revision A.1; Gaussian, Inc.: Wallingford, CT, 2009.

32. Zhao, Y.; Schultz, N. E.; Truhlar, D. G., Design of Density Functionals by Combining the Method of Constraint Satisfaction with Parametrization for Thermochemistry, Thermochemical Kinetics, and Noncovalent Interactions. *J. Chem. Theory. Comput.* **2006,** *2*, 364-382.

33. Altarawneh, M.; Dlugogorski, B. Z., A Mechanistic and Kinetic Study on the Formation of PBDD/Fs from PBDEs. *Environ. Sci. Technol.* **2013,** *47*, 5118-5127.

34. Mokrushin, V.; Bedanov, V.; Tsang, W.; Zachariah, M.; Knyazev, V. *ChemRate*, NIST Gaithersburg: MD, USA, 2002.

35. Bobrowski, M.; Liwo, A.; Ołdziej, S.; Jeziorek, D.; Ossowski, T., CAS MCSCF/CAS MCQDPT2 Study of the Mechanism of Singlet Oxygen Addition to 1,3-Butadiene and Benzene. *J. Am. Chem. Soc.* **2000,** *122*, 8112-8119.

Chapter 8

Decomposition of Ammonium Nitrate: A Mechanistic study.

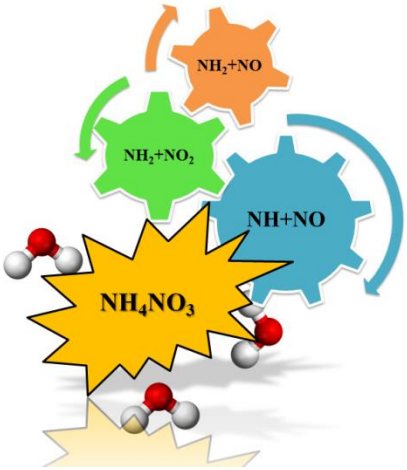

This chapter underpins the effect of reaction medium on the cracking routes of the Ammonium Nitrate especially those occurring in emulsion explosives. The interaction of amidogen radical with nitrogen oxide prevailing under NO_xOUT and DeNO_x technologies remains the focus underlying this chapter.

8.0. Abstract

In this section, we theoretically account for reactions prevailing during the thermal decomposition of ammonium nitrate (AN) both in the gas phase and solutions form. Herein, we model aqueous phase reactions based on the solvation model and explicitly added water molecules. Water may induce a catalysing role via predicted lower activation enthalpies about analogous gas phase reactions, i.e. by 7.6–44.5 kJ mol^{-1}. Reactions between NH_2 radical and NO_x species lead to the generation of nitrogen molecules through modest activation enthalpies. These reactions represent the core of the thermal $DeNO_x$ process. By observing the effect of explicit water molecules, we noticed that there is an interaction between transition structures and water molecules. It leads to differences in enthalpy values computed with the solvation model and the explicitly added water molecules. Results obtained in this study should be a mechanistic frame in the pursuit to minimise NO_x emission from AN-based emulsion explosives.

8.1. Introduction

Ammonium nitrate (AN) serves as an essential raw ingredient in the fertiliser, materials industry and finds its application as a main and cheap ingredient in emulsion explosives.[1-3] AN in its pure form is stable and safe at the lower range of temperature [4-5]. A heating solid form of AN produces a mixture of NH_3, HNO_3 and NH_4NO_3.[6] AN readily decomposes at a temperature higher than its melting point.[7] Decomposition of AN accounts for the hazardous phenomena such as NO_x plume in mines.[4, 8-10] Owing to the applications and implications mentioned above, decomposition of AN in the three phases has been the subject of intensive research.

Early studies on the decomposition of AN revealed that degradation of AN readily occurs at temperatures higher than 443 K, yielding nitrous oxides and water as primary products[11]. At all temperatures, AN decomposition is governed by its endothermic dissociation into ammonia and nitric acid. An intermolecular proton transfer instigates this process. Subject to the experimental conditions, this reaction consumes all of the AN at about 523 to 593 K. With the increase in temperature from 473 to 563 K, the chemical reaction amid nitric acid and ammonia indicated to be ionic with the generation of NO_2^+. To the best of knowledge, thermal decomposition of AN is acid catalysed. [12-16] Above 563 K, the dominant mechanism constitutes the hemolysis reaction of nitric acid producing nitrogen dioxide and hydroxyl radicals.[17-18] On the oxidative side, a bimolecular reaction of AN competes with the reaction between ammonium and nitrate ions and afford the formation of nitrogen and nitrous oxide. The latter serves as an intermediate for the generation of nitrogen (N_2) from the breakdown of AN.[8, 19-22]

Literature analysis[17] revealed the ionic mechanism for the decomposition of ammonium nitrate at temperatures below 573 K that is displaced by a rate controlling homolysis of nitric acid at higher temperatures. In the lower limit of temperature, activation energy constantly varies from 118 kJ to 193 kJ at high temperatures. It is not decisive; the change of E_a will bring a change of mechanism. Confined ammonium nitrate can undergo rapid, self-accelerating decomposition at temperatures of 533–553 K[23]; however, this phenomenon occurs at a much lower temperature if contaminants are present, such as pyrite. [24] The rate of decomposition also increases significantly in the presence of carbon black. [25] Impurities such as inorganic acid and organic oil which act to catalyse the decomposition of AN and trigger auto-ignition and explosion.[26]

Theoretically, Irikura[27] addressed the gas-phase decomposition of AN into ammonia and nitric acid. Alavi and Donald[28] reported structural parameters, vibrational modes, and binding energies for the proton transfer in a gaseous phase AN molecule. Very recently, Satefania et al. [29] mapped out potential energy surfaces for prominent reactions encountered during the gas-phase degradation of AN. Nguyen and co-workers[30] theoretically explored the system of nitric acid–ammonia system concurrently considering the solvation effect of water.

Decomposition of AN in explosive emulsions could be viewed to occur simultaneously in gas and liquid phases, in which pathways leading to NO_x and N_2 formation are a crucial set of reactions. To this end, the focus of this study is two-fold: firstly, to report mechanistic and kinetic parameters accounting for all reactions leading to the formation of nitrogen molecules from thermal decomposition of AN in gas and aqueous phases; and secondly, to observe any plausible catalysing effect of water molecules on the decomposition of AN.

8.2. Computational details

We carried out all structural optimisations and energy calculations using the Gaussian 09 suite of programs.[31] We report the optimised geometries and zero-point vibrational energies (ZPVE) by employing two theoretical approaches, CBS-QB3[32-33] and M05-2X/6-311+G(d,p).[34] M05-2X functional; i.e., new hybrid meta exchange-correlation functional is reported to exhibit optimum performance for general applications in thermochemical kinetics and noncovalent interactions.[34] Energetic-values throughout the discussion reported on the *H*-scale at 298.15 K. To simulate the effect of bulk water on the enthalpic trends, a continuum solvation model density-polarisable continuum model (SMD-PCM)[35-36] deployed in all reactions. We also assess the effect of adding explicit water molecules on the enthalpy of activations for selected reactions. Calculations of reaction rate constants at the high-pressure limit were performed with the aid of the ChemRate code.[37]

8.3. Results and discussion

The decomposition reaction of AN in the gas phase is initiated by dissociation into ammonia and nitric acids with an estimated barrier of 86.9 kJ mol^{-1} calculated by the CBS-QB3 method. Decomposition of nitric acid into hydroxyl and nitrogen dioxide requires an endothermicity of 202.9 kJ mol^{-1} (CBS-QB3). The produced hydroxyl radical can then react with ammonia, passing through a trivial barrier of 11.3 kJ mol^{-1} at the CBS-QB3 method to produce NH_2 and H_2O. This NH_2 radical constitutes the primary carrier for the so-called thermal DeNO_x process [38-39] which converts NO_x species into N_2. Thus, we present energies for all subsequent reactions using four different theoretical methods, corresponding to CBS-

QB3 in the gas phase (1), CBS-QB3 with the SMD-PCM model (2), M05-2X in the gas phase (3) and M05-2X along with the SMD-PCM model (4).

8.3.1. Reaction between NH_2 and NO_2

Figure 8.1 illustrates the potential energy surface of the reactions between NH_2 and NO_2. These reactants can associate to form NH_2NO_2 or H_2NONO. Formation of NH_2NO_2 is more exothermic by 88.6 kJ mol^{-1} compared to that of H_2NONO, calculated at CBS-QB3. Calculated exothermicity for the formation of H_2NONO amounts to 123.1 and 121.0 kJ mol^{-1}, computed at CBS-QB3 and M05-2X methods, respectively. These two values agree satisfactorily with conforming values reported by Mebel et al.[40] at 119.3 and 143.2 kJ mol^{-1} using the QCISD(T)+ZPC (119.3 kJ mol^{-1}) and G2(PU) levels (143.2 kJ mol^{-1}), correspondingly. Intramolecular migration of one of the two hydrogen atoms to NH_2 in NH_2NO_2 to the oxygen atom forms $NHNO_2H$ through a barrier of 160.9 kJ mol^{-1} at the CBS-QB3 method. $NHNO_2H$ can branch into three distinct pathways. The first channel characterises the formation of $NN(OH)_2$ via a barrier of 214.6 kJ mol^{-1} (CBS-QB3) through the transition structure (TS3). The second channel signifies the barrierless dissociation of $NHNO_2H$ into NHNO and OH. The enthalpic barrier associated with TS3 is 21.4 kJ mol^{-1} (CBS-QB3) higher than the reaction enthalpy of the second channel. The third channel resembles the most favourable initial exit channel for $NHNO_2H$ through a barrier of 130.6 kJ mol^{-1} (CBS-QB3). This channel results in the formation of N_2O and H_2O. Unimolecular decomposition of $NN(OH)_2$ into a nitrogen molecule and two hydroxyl radicals proceeds with a negligible exothermicity of 21.0 kJ mol^{-1} (CBS-QB3).

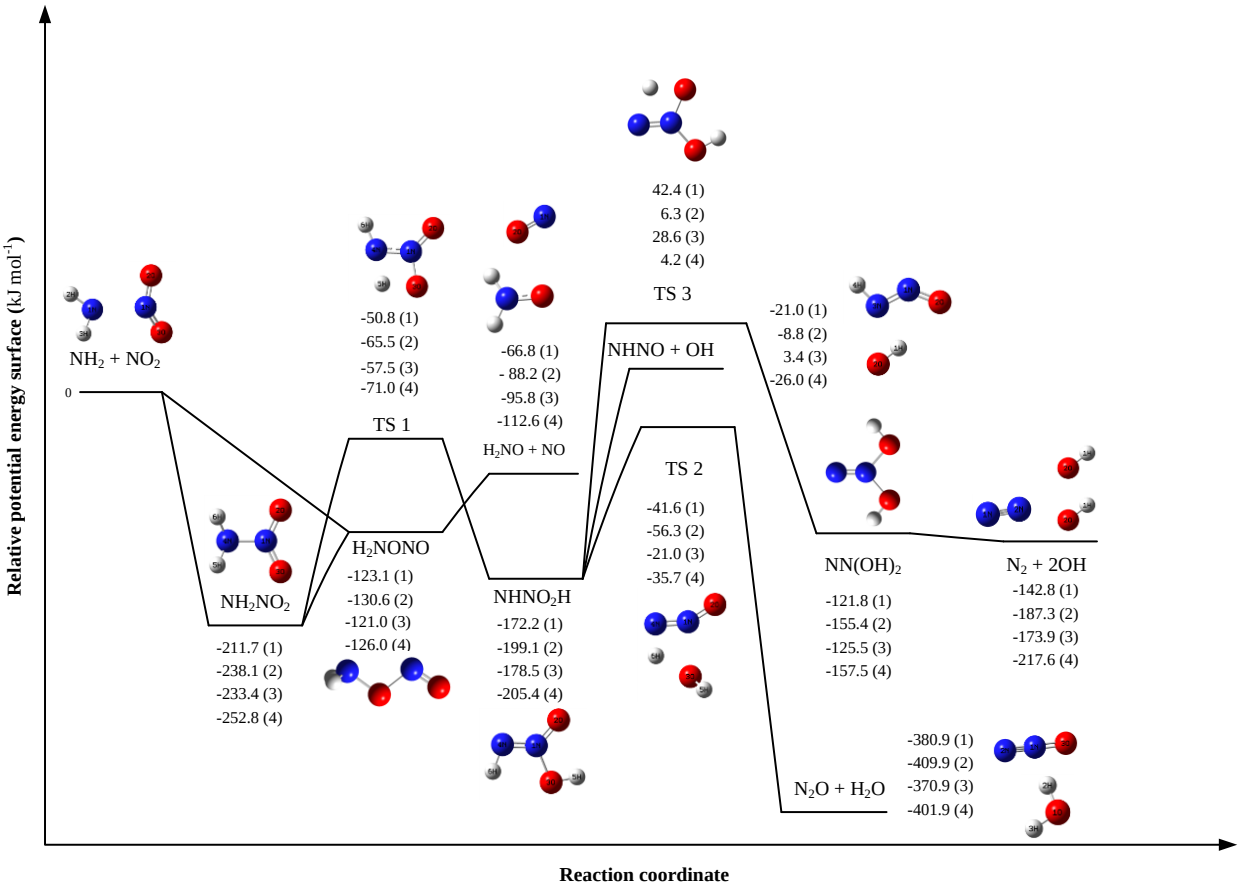

Figure 8.1. Potential energy surfaces of reactions involved in the reactions of NH_2 and NO_2. (1), (2), (3) and (4) refer to CBS-QB3 in the gas phase (1), CBS-QB3 SMD-PCM model (2), M05-2X in the gas phase (3) and M05-2X SMD-PCM model (4). Values (in kJ mol^{-1}) are relative to the initial reactants of NH_2 and NO_2.

As shown in Figure 8.1, analogous enthalpic values based on the solvation model that simulates the effect of bulk water, are lower. It indicates that water assists the reactions involved in the addition of NH_2 and NO_2. The enthalpic deviation between gas-phase and solvation models stretches between 7.6 to 44.5 kJ mol^{-1} (CBS-QB3) and 5.0 to 5.9 kJ mol^{-1} (M05-2X/6-311+G(d,p). Values derived by the M05-2X/6-311+G(d,p) method predicted lower energies by 2.1–31.1 kJ mol^{-1} and 2.1–30.2 kJ mol^{-1} for the gas-phase and the solvation models (in reference to corresponding values calculated at the CBS-QB3 level).

8.3.2. Reaction between NH_2 and NO

Figure 8.2 portrays the potential energy surface for the bimolecular reaction NH_2 and NO. Association of NH_2 and NO results in the formation of NH_2NO without encountering an intrinsic barrier and produces an excess enthalpy of 193.6 kJ mol^{-1} (CBS-QB3). This value is higher by 18.1 kJ mol^{-1} (CBS-QB3) in comparison to the corresponding formation of NH_2NO_2 from bimolecular reactions of NH_2 and NO_2. Hydrogen shifts from nitrogen to an oxygen atom in NH_2NO forms HNNOH via a barrier of 133.6 kJ mol^{-1} (TS4) at the CBS-QB3 method. Three dissociation reactions stemming from HNNOH afford N_2 + H + OH, N_2O + H_2, and N_2 + H_2O. Expulsion of a hydrogen molecule from HNNOH produces N_2O via a barrier of 203.3 kJ mol^{-1} (CBS-QB3), as characterised by the transition structure (TS5) calculated using CBS-QB3. This barrier is noticeably lower than the corresponding hindrance obtained at the M05-2X/6-311+G(d,p) level of theory; i.e. 232.7 kJ mol^{-1}. Formation of N_2 + H_2O requires an enthalpic barrier of 93.2 kJ mol^{-1} (TS6), computed from the CBS-QB3 method. As deduced from Figure 8.2, the overall reaction of NH_2 and NO results in the formation of N_2 + H_2O in a significant well depth of 517.9 kJ mol^{-1} (CBS-QB3). An energetic trend for the simulated water bulk phase via the solvation model is lower by 6.7-30.2 kJ mol^{-1} (CBS-QB3) than corresponding values obtained for the gas-phase reactions.

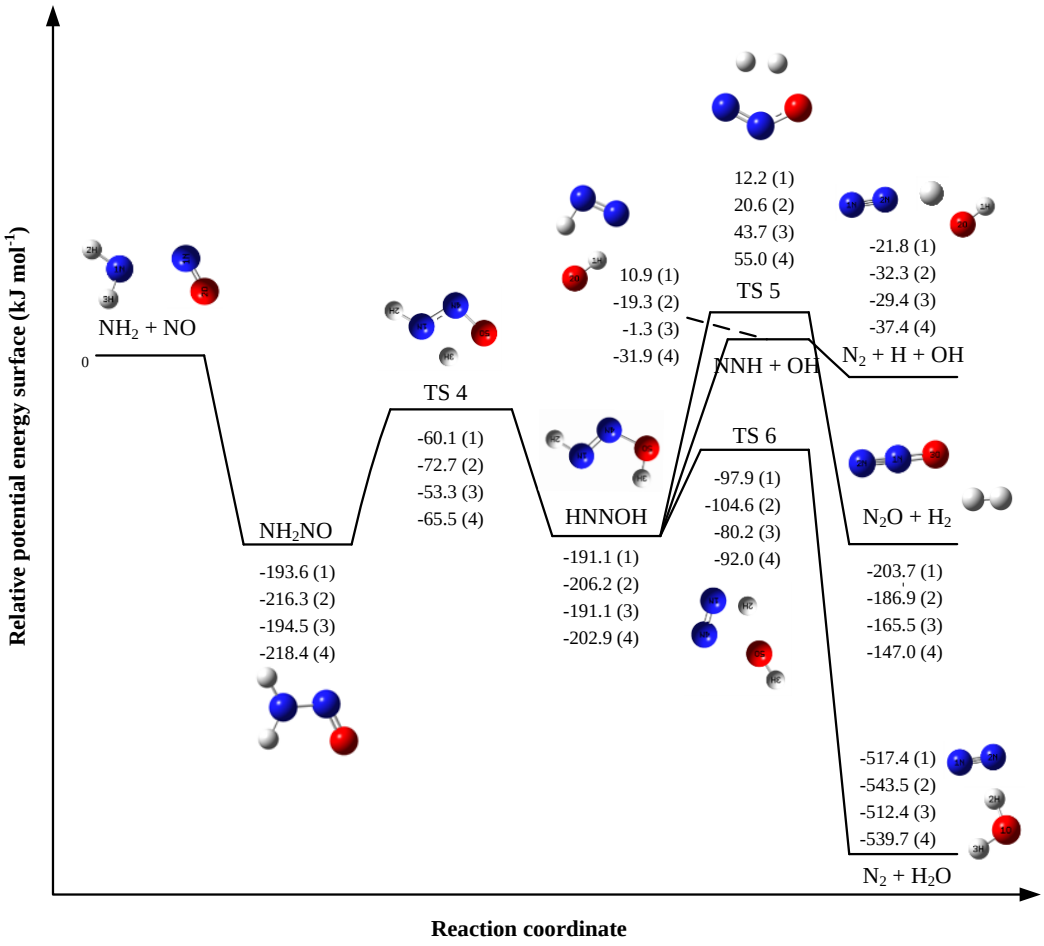

Figure 8.2. Potential energy surfaces of molecules involved in the reactions of NH_2 and NO. (1), (2), (3) and (4) refer to CBS-QB3 in the gas phase (1), CBS-QB3 SMD-PCM model (2), M05-2X in the gas phase (3) and M05-2X SMD-PCM model (4). Values (in kJ mol^{-1}) are relative to the initial reactants of NH_2 and NO.

8.3.3. Reaction between NH and NO, as well as other additional reactions

From figure 8.3, we can see, schematically, the response of NH and NO, initiated by their barrierless addition to forming HNNO. This reaction step is highly exothermic by 407.0 kJ mol^{-1} (CBS-QB3) and 417.9 kJ mol^{-1} (M05-2X/6-311+G(d,p)). H-N bond scission in HNNO proceeds through barriers of 122.6 kJ mol^{-1} and 132.7 kJ mol^{-1} at the CBS-QB3 and M05-2X

levels, leading to the formation of N_2O and H. The hydrogen atom can then abstract the oxygen atom from N_2O to form OH and N_2 after passing the barrier of 76.9 kJ mol^{-1} (CBS-QB3). This reaction is predicted to be highly energetic by 257.0 kJ mol^{-1} and 286.4 kJ mol^{-1} at the CBS-QB3 and M05-2X/6-311+G(d,p) levels.

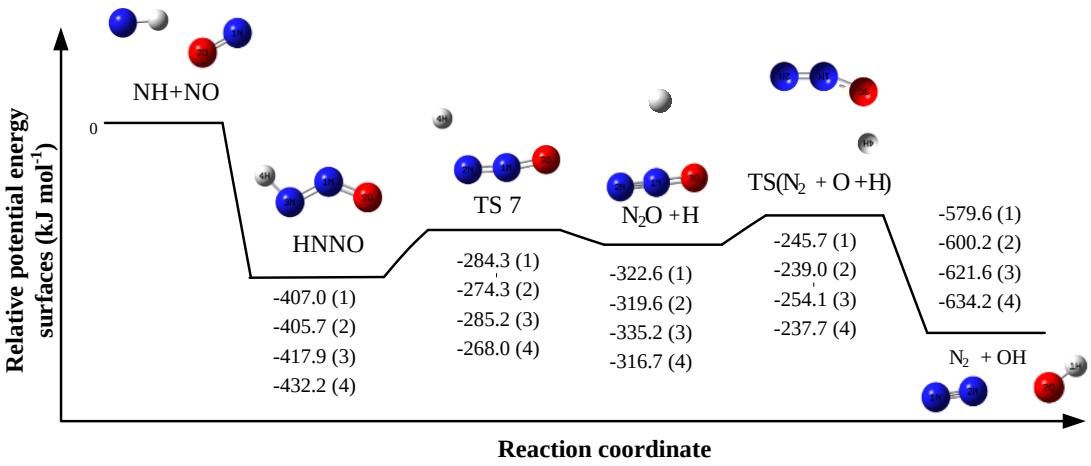

Figure 8.3. Potential energy surfaces of molecules involved in the reactions of NH and NO. (1), (2), (3) and (4) refer to CBS-QB3 in the gas phase (1), CBS-QB3 SMD-PCM model (2), M05-2X in the gas phase (3) and M05-2X SMD-PCM model (4). Values (in kJ mol^{-1}) are relative to the initial reactants of NH and NO.

Table 8.1 enlists reaction and activation enthalpies for other critical corridors encountered during the decomposition of AN. Fragmentation of AN is commenced by dissociation into nitric acid and ammonia passing a barrier of 86.9 kJ mol^{-1} and 88.2 kJ mol^{-1}, calculated at CBS-QB3 and M05-2X levels of theory, respectively. NO_2 reacts with hydroxyl radicals in three competing reactions to form HNO_3, HOONO, as well as NO and HO_2. Formation of HNO_3 is the most plausible channel with an exothermicity of 202.9 kJ mol^{-1}. Generation of NO and HO_2 is predicted to be a rather negligible channel encountered within NO_2 + OH.

The reaction of OH with NH_3 produces NH_2 and NH radicals. The latter are prominent intermediates leading to N_2, which subsequently reacts with C_xH_y radicals to produce NO_x [41].

Table 8.1. Additional reactions involved during the decomposition of ammonium nitrate.

Reactions	Enthalpy (kJ mol^{-1})				Enthalpy of activation (kJ mol^{-1})			
	(1)	(2)	(3)	(4)	(1)	(2)	(3)	(4)
$NH_4NO_3 \rightarrow NH_3 + HNO_3$	-37.0		-25.2		86.9		88.2	
$NO_2 + OH \rightarrow HNO_3$	-202.9	-206.6	-195.7	-200.8				
$NO_2 + OH \rightarrow HOONO$	-79.0	-78.1	-49.6	-50.0				
$NO_2 + OH \rightarrow NO + HO_2$	33.6	22.3	26.0	14.3	-14.3	-33.6	0.84	-34.0
$NH_3 + OH \rightarrow NH_2 + H_2O$	-49.6	-60.1	-42.0	-55.9	11.3	11.8	10.9	-15.5
$NH_2 + OH \rightarrow NH + H_2O$	62.6	56.7	25.9	22.5	0.8	1.0	6.0	6.0

Note: (1), (2), (3) and (4) refer to CBS-QB3 in the gas phase (1), CBS-QB3 SMD-PCM model (2), M05-2X in the gas phase (3) and M05-2X SMD-PCM model (4).

8.3.4. Effect of the addition of explicit water molecules

In order to estimate a plausible catalysing role of water in the decomposition of AN in solutions, we explore the impact of introducing a water molecule between the dissociated NH_4^+ and NO_3^- ions while surrounded by three water molecules. The final equilibrium configuration reveals that there are two concurrent hydrogen transfers (hydrogen number 3 to oxygen number 10; and hydrogen number 12 to oxygen number 7) as shown in Scheme 1.

Scheme 1:

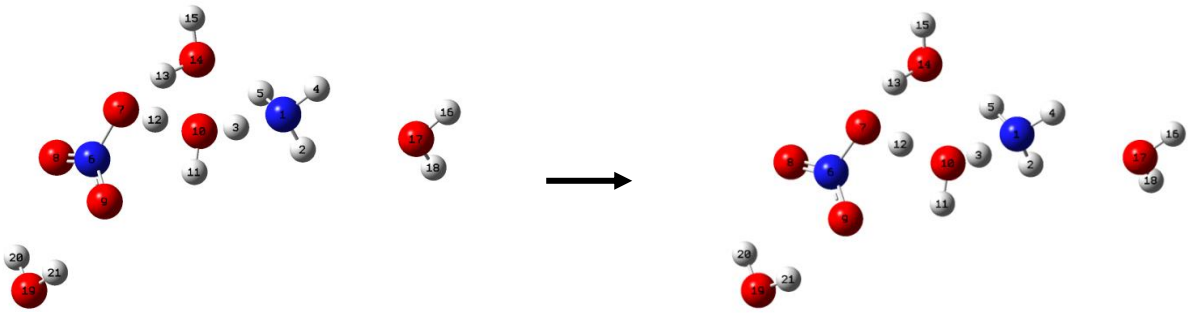

Initial structure Optimised structure

Scheme 1 shows that water molecules facilitate the conversion of the dissociated ammonium and nitrate ions into NH_3 and HNO_3. The final configuration is more stable than the initial structure by 216.7 kJ mol^{-1} at CBS-QB3 method.

To illustrate the effect of the addition of water to the PESs shown in Figures 8.1–8.3, we have calculated the reaction and activation enthalpies for selected reactions while adding three explicit water molecules. Table 8.2 compares enthalpies of activation for three cases, gas-phase, solvation model and three added explicit water molecules. It was anticipated that the energies computed with the addition of explicit water molecules to be in relative agreement with corresponding values acquired with the solvation method. The results, however, seem to indicate that the energies calculated with three added water molecules were significantly lower compared to those simulated using both the solvation model and gas phase system.

Table 8.2. Enthalpies of activation of selected reactions based on three approaches; namely three explicit water molecules, the solvation model and gas phase system. All values are at a CBS-QB3 level based on gaseous phase separated three water molecules and separated reactants.

Transition States	Reaction	Activation Enthalpies (kJ mol^{-1})		
		3 Water Molecules	Solvation	Gas
$NHNO_2$ + H	$NH_2NO_2 \rightarrow NHNO_2H$	176.4	172.6	160.9
N_2O + OH + H	$NHNO_2H \rightarrow N_2O + H_2O$	29.8	142.8	160.6
HNNO + H	$NH_2NO \rightarrow HNNOH$	84.0	143.6	133.6
N_2 + OH + H	$HNNOH \rightarrow N_2 + H_2O$	26.9	101.6	93.2

The significant difference in values of activation enthalpies indicates that there is a profound interaction between transition state and water molecules. For instance, during the simulation of the transition state for the reaction $HNNOH \rightarrow N_2 + H_2O$ with the three added water molecules, one water molecule tends to attract the hydrogen from transition state to form H_3O^+ (hydrogen number 2 to oxygen number 13), as illustrated in Scheme 2.

Scheme 2:

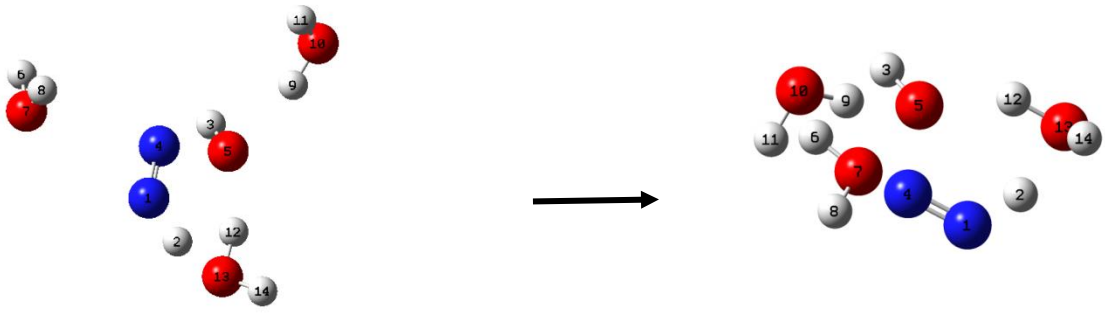

Initial structure Optimised structure

The noticeable difference in values of enthalpies of activation prompted us to assume that strong interaction exists between water molecules and structures of products and reactants. This variation is not accounted for when considering separated water molecules as reactants. We conducted the optimisation of each reactant and product with three surrounded water molecules, with the aim to underpin the noticeable difference of reaction enthalpies obtained from the three models. Results of this comparison are summarised in Table 8.3. As given in Table 3, the three set of values are within 10.9–33.6 kJ mol^{-1}. The quite small differences in these values could suggest that there are similar interactions between reactants and products with water molecules. Therefore, by integrating the effect of water for both reactants and products, the enthalpies of activation are close to the values obtained with the solvation model and gas phase.

Table 8.3. The comparison of the energy of the reaction between explicit water addition and gas phase.

Transition States	Reaction	Energy of reaction (kJ mol^{-1})		
		Explicit water	Solvation	Gas phase
$NHNO_2$ + H	$NH_2NO_2 \rightarrow NHNO_2H$	74.8	39.1	39.5
N_2O + OH + H	$NHNO_2H \rightarrow N_2O + H_2O$	-221.8	-210.8	-208.7
HNNO + H	$NH_2NO \rightarrow HNNOH$	22.3	10.1	2.5
N_2 + OH + H	$HNNOH \rightarrow N_2 + H_2O$	-348.6	337.3	-326.3

8.4. Kinetic data

In Table 8.4, we assemble fitted reaction rate constants for prominent reactions in the gas phase. Kinetic experiments have been carried out to measure the reaction rate of the constant of $NH_3 + OH \rightarrow NH_2 + H_2O$, calculated as 1.5×10^{-13} to 1.7×10^{-13} cm^3/molecule s at 300 K [42-44]. Our prediction of this rate constant is in good agreement with the experimental value, within a factor of 3.5.

Table 4. Arrhenius parameters for the calculation of the rate constants of the reactions in the decomposition of ammonium nitrate (temperature range 300–2000 K).

Reactions	*log A* (s^{-1} or s^{-1} cm^3.$molecule^{-1}$)	$\Delta E/R$ (kJ mol^{-1}.K)	*n*
$NH_2NO_2 \rightarrow NHNO_2H$	12.7	29.1	1
$N_2 + 2OH \rightarrow NN(OH)_2$	-20.4	100.3	2.3
$NHNO_2H \rightarrow NN(OH)_2$	11.8	108.8	0.5
$NHNO_2H \rightarrow N_2O + H_2O$	11.8	66.5	0.6
$HNNOH \rightarrow NH_2NO$	11.8	66.7	0.5
$HNNOH \rightarrow N_2O + H_2$	10.7	102.5	0.8
$HNNOH \rightarrow N_2 + H_2O$	11.9	47.6	0.8
$ONNH \rightarrow N_2O + H$	10.5	62.1	1.0
$H + N_2O \rightarrow N_2 + OH$	-12.9	39.1	1.0
$OH + NH_2 \rightarrow NH + H_2O$	-18.8	1.2	1.9
$NH_3 + OH \rightarrow NH_2 + H_2O$	-20.5	5.9	0

[a]Rate constants, defined by $k = AT^n \exp(-\Delta E/RT)$

8.5. Conclusions

Ammonium nitrate decomposition has been investigated employing various computational approaches. Modelled reactions of NH_2 with NO_x species present a mechanistic version for the $DeNO_x$ process. To account for the effect of bulk water on kinetic and thermochemical parameters, we thoroughly compared energies computed for gas-phase reactions with analogous values from the solvation model. The solvation model predicted lower energies compared to those in the gas phase, indicating that water poses a catalysing role in the thermal decomposition of AN-based emulsion explosives. Results obtained from the gas-phase and the solvation models differ in the range of 7.6–44.5 kJ mol^{-1} at the CBS-QB3 theoretical level. Overall, calculations using the M05-2X method provided energies in close agreement with the CBS-QB3 method.

8.6. References

1. Venpin, W. K. P. F.; Kennedy, E. M.; Mackie, J. C.; Dlugogorski, B. Z., Trapping of Nitric Oxide, Generated During Sensitization of Ammonium Nitrate Emulsion Explosive, by Aromatic Nitroso Sulfonates. *Ind. Eng. Chem. Res.* **2013**, *52*, 10561-10568.

2. Rayson, M. S.; Mackie, J. C.; Kennedy, E. M.; Dlugogorski, B. Z., Experimental Study of Decomposition of Aqueous Nitrosyl Thiocyanate. *Inorg. Chem.* **2011**, *50*, 7440-7452.

3. Rayson, M. S.; Mackie, J. C.; Kennedy, E. M.; Dlugogorski, B. Z., Accurate Rate Constants for Decomposition of Aqueous Nitrous Acid. *Inorg. Chem.* **2012**, *51*, 2178-2185.

4. Sun, J.; Sun, Z.; Wang, Q.; Ding, H.; Wang, T.; Jiang, C., Catalytic Effects of Inorganic Acids on the Decomposition of Ammonium Nitrate. *J. Hazard. Mater.* **2005**, *127*, 204-210.

5. Gunawan, R.; Freij, S.; Zhang, D.-k.; Beach, F.; Littlefair, M., A Mechanistic Study into the Reactions of Ammonium Nitrate with Pyrite. *Chem. Eng. Sci.* **2006**, *61*, 5781-5790.

6. Chien, W.-M.; Chandra, D.; Lau, K. H.; Hildenbrand, D. L.; Helmy, A. M., The Vaporization of NH_4NO_3. *J. Chem. Thermodyn.* **2010**, *42*, 846-851.

7. Szabó, Z. G.; Trompler, J.; Hollós-Rokosinyi, E., A New Gas Volumetric Determination of the Nitrate Ion. *Anal. Chim. Acta* **1978**, *100*, 495-501.

8. Keenan, A. G.; Notz, K.; Franco, N. B., Synergistic Catalysis of Ammonium Nitrate Decomposition. *J. Am. Chem. Soc.* **1969**, *91*, 3168-3171.

9. Duh, Y.-S.; Lee, C.; Hsu, C.-C.; Hwang, D.-R.; Kao, C.-S., Chemical Incompatibility of Nitrocompounds. *J. Hazard. Mater.* **1997**, *53*, 183-194.

10. Li X- R., K. H., Study on Reactivity of Ammonium Nitrate Contaminated by Sodium Dichloroisocyanurate. *Sci. Tech. Energetic Materials* **2005**, *66*, 431-435.

11. Rosser, W. A.; Inami, S. H.; Wise, H., The Kinetics of Decomposition of Liquid Ammonium Nitrate. *J. Phys. Chem.* **1963**, *67*, 1753-1757.

12. Dana, A. G.; Shter, G. E.; Grader, G. S., Thermal Analysis of Aqueous Urea Ammonium Nitrate Alternative Fuel. *R. Soc. Chem. Adv.* **2014**, *4*, 34836-34848.

13. Xu, Z.; Liu, D.; Hu, Y.; Ye, Z.; Wei, Y., Infuence of Iron Ion on Thermal Behavior of Ammonium Nitrate and Emulsion Explosives. *Cent. Eur. J. Energetic Mater.* **2010**, *7*, 77-93.

14. Rosser, W. A.; Inami, S. H.; Wise, H., The Kinetics of Decomposition of Liquid Ammonium Nitrate. *J. Phys. Chem.* **1963**, *67*, 1753-1757.

15. Oommen, C.; Jain, S. R., Ammonium Nitrate: A Promising Rocket Propellant Oxidizer. *J. Hazard. Mater.* **1999**, *67*, 253-281.

16. Vyazovkin, S.; Clawson, J. S.; Wight, C. A., Thermal Dissociation Kinetics of Solid and Liquid Ammonium Nitrate. *Chem. Mater.* **2001**, *13*, 960-966.

17. Brower, K. R.; Oxley, J. C.; Tewari, M., Evidence for Homolytic Decomposition of Ammonium Nitrate at High Temperature. *J. Phys. Chem.* **1989**, *93*, 4029-4033.

18. Oxley, J. C.; Kaushik, S. M.; Gilson, N. S., Thermal Decomposition of Ammonium Nitrate-Based Composites. *Thermochim. Acta* **1989**, *153*, 269-286.

19. MacNeil, J. H.; Zhang, H.-T.; Berseth, P.; Trogler, W. C., Catalytic Decomposition of Ammonium Nitrate in Superheated Aqueous Solutions. *J. Am. Chem. Soc.* **1997**, *119*, 9738-9744.

20. Hörold, S.; Tacke, T.; Vorlop, K. D., Catalytical Removal of Nitrate and Nitrite from Drinking Water: 1. Screening for Hydrogenation Catalysts and Influence of Reaction Conditions on Activity and Selectivity. *Environ. Technol.* **1993**, *14*, 931-939.

21. Prüsse, U.; Hähnlein, M.; Daum, J.; Vorlop, K.-D., Improving the Catalytic Nitrate Reduction. *Catal. Today* **2000**, *55*, 79-90.

22. Kamal, F.; Weimin, C.; Yann, B.; Charles, K., In *45th Aiaa/Asme/Sae/Asee Joint Propulsion Conference & Exhibit*, American Institute of Aeronautics and Astronautics: 2009.

23. Feick, G.; Hainer, R. M., On the Thermal Decomposition of Ammonium Nitrate. Steady-State Reaction Temperatures and Reaction Rate. *J. Amer. Chem. Soc.* **1954**, *76*, 5860-5863.

24. Gunawan, R.; Zhang, D., Thermal Stability and Kinetics of Decomposition of Ammonium Nitrate in the Presence of Pyrite. *J. Hazard. Mater.* **2009**, *165*, 751-758.

25. Lurie, B. A.; Lianshen, C., Kinetics and Mechanism of Thermal Decomposition of Ammonium Nitrate Powder under the Action of Carbon Black. *Combust. Explos. Shock Waves* **2000**, *36*.

26. Chaturvedi, S.; Dave, P. N., Review on Thermal Decomposition of Ammonium Nitrate. *J. Energ. Mater.* **2013**, *31*, 1-26.

27. Irikura, K. K., Thermochemistry of Ammonium Nitrate, NH_4NO_3, in the Gas Phase. *J. Phys. Chem. A* **2010**, *114*, 11651-11653.

28. Alavi, S.; Thompson, D. L., Theoretical Study of Proton Transfer in Ammonium Nitrate Clusters. *J. Chem. Phys.* **2002**, *117*, 2599-2608.

29. Cagnina, S.; Rotureau, P.; Fayet, G.; Adamo, C., The Ammonium Nitrate and its Mechanism of Decomposition in the Gas Phase: A Theoretical Study and a DFT Benchmark. *PCCP* **2013**, *15*, 10849-10858.

30. Nguyen, M.-T.; Jamka, A. J.; Cazar, R. A.; Tao, F.-M., Structure and Stability of the Nitric Acid–Ammonia Complex in the Gas Phase and in Water. *J. Chem. Phys.* **1997**, *106*, 8710-8717.

31. Frisch, M. J.; Trucks, G. W.; Schlegel, H. B.; Scuseria, G. E.; Robb, M. A.; Cheeseman, J. R.; Scalmani, G.; Barone, V.; Mennucci, B.; Petersson, G. A. et al. *Gaussian 09*, revision A.1.; Gaussian, Inc.: Wallingford, CT, 2009.

34. Zhao, Y.; Schultz, N. E.; Truhlar, D. G., Design of Density Functionals by Combining the Method of Constraint Satisfaction with Parametrisation for Thermochemistry, Thermochemical Kinetics, and Noncovalent Interactions. *J Chem Theory Comput* **2005**, *2006*, 364-382.

35. Scalmani, G.; Frisch, M. J., Continuous Surface Charge Polarizable Continuum Models of Solvation. I. General Formalism. *J. Chem. Phys.* **2010**, *132*, 114110.

36. Marenich, A. V.; Cramer, C. J.; Truhlar, D. G., Universal Solvation Model Based on Solute Electron Density and on a Continuum Model of the Solvent Defined by the Bulk Dielectric Constant and Atomic Surface Tensions. *J. Phys. Chem. B* **2009**, *113*, 6378-6396.

37. Mokrushin, V.; Bedanov, V.; Tsang, W.; Zachariah, M.; Knyazev, V. *Chemrate*, NIST Gaithersburg: MD, USA, 2002.

38. Rota, R.; Antos, D.; Zanoelo, É. F.; Morbidelli, M., Experimental and Modeling Analysis of the Noxout Process. *Chem. Eng. Sci.* **2002**, *57*, 27-38.

39. Tayyeb Javed, M.; Irfan, N.; Gibbs, B. M., Control of Combustion-Generated Nitrogen Oxides by Selective Non-Catalytic Reduction. *J. Environ. Manage.* **2007**, *83*, 251-289.

40. Mebel, A. M.; Hsu, C.-C.; Lin, M. C.; Morokuma, K., An Ab Initio Molecular Orbital Study of Potential Energy Surface of the NH_2 + NO_2 Reaction. *J. Chem. Phys.* **1995**, *103*, 5640-5649.

41. Khan, A. A.; de Jong, W.; Jansens, P. J.; Spliethoff, H., Biomass Combustion in Fluidized Bed Boilers: Potential Problems and Remedies. *Fuel Process. Technol.* **2009**, *90*, 21-50.

42. A. Silver, J.; E. Kolb, C., Rate Constant for the Reaction NH_3 + OH → NH_2 + H_2O over a Wide Temperature Range. *Chem. Phys. Lett.* **1980**, *75*, 191-195.

43. Bulatov, V. P.; Ioffe, A. A.; Lozovsky, V. A.; Sarkisov, O. M., On the Reaction of the NH_2 Radical with NO at 295–620 K. *Chem. Phys. Lett.* **1989**, *161*, 141-146.

44. Atakan, B.; Jacobs, A.; Wahl, M.; Weller, R.; Wolfrum, J., Kinetic Measurements and Product Branching Ratio for the Reaction NH_2+NO at 294–1027 K. *Chem. Phys. Lett.* **1989**, *155*, 609-613.

Chapter 9

> Mitigation of NO_x using a biomass surrogate (catechol) as a reburn fuel.

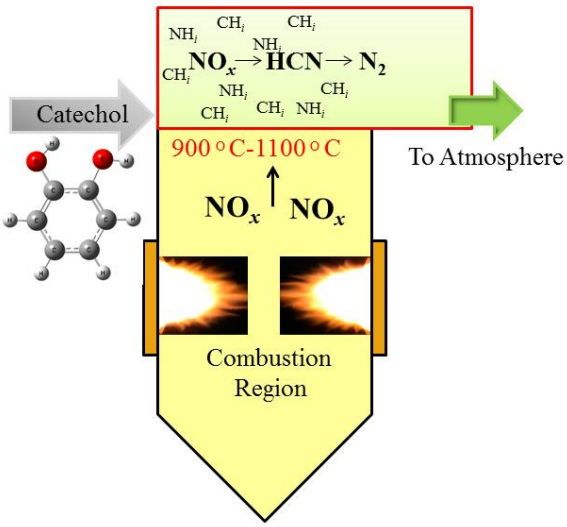

This chapter investigates the thermal interaction of catechol—used as a biomass-modelled fuel—with NO_x. It investigates the profiles of selected gaseous hydrocarbon and nitrogenous species, as well as the ability of catechol to reduce NO at high temperatures under fuel-rich conditions.

9.0. Abstract

This chapter investigates the effectiveness of a biomass surrogate in reducing nitric oxide (NO) under conditions relevant to reburning processes. The study applied flow reactor experiments for the reduction of NO using catechol, a model compound of lignin biomass, under fuel rich conditions covering a temperature range of 400–1200 °C, pressure of 1 atm, residence time of 2 s, fuel equivalence ratio of 1.25 and initial NO concentration of 600 ppm. Fourier transform infrared (FTIR) spectroscopy, NO_x chemiluminescence analysis and gas chromatography provided the necessary gaseous product profiles. Identification and quantification of catechol conversion under pure oxygen and NO_x oxidative atmospheres were performed by triple quad gas chromatography and mass spectrometry (GC-QQQMS). The only N-containing products observed were hydrogen cyanide (HCN) and N_2. The presence of NO_x promoted the decomposition of catechol at a lower temperature. Furthermore, the maximum reduction efficiency of NO (81 %) was achieved at 900 °C, apparently consuming the oxidative fragments of catechol and converting them into N_2 via the HCN reactive corridor. These findings will assist in understanding the reactions of hydroxylated aromatic compounds and developing kinetic models in the presence of NO_x, as well as the interaction of biomass residue in NO_x-laden atmospheres.

9.1. Introduction

Combustion processes emit sulfur dioxide (SO_2), carbon monoxide (CO), unburnt hydrocarbons and nitrogen oxides (NO_x = NO and NO_2) as their main pollutants. Emissions of NO_x contribute significantly to stratospheric ozone depletion, the greenhouse effect, acid rain and photochemical smog, imposing major threats to the environment and human health. The estimated emissions of NO_x from stationary and mobile combustion systems amount to 19×10^9 kg N/y, while biomass combustion emits 12×10^9 kg N/y. Concentrations of NO_x are approximately 800 ppm in the emissions of untreated combustion systems (e.g., in power plants), and approximately 500 ppm in emissions resulting from the decomposition of nitrate oxidisers used in mining operations.[1-8] However, as a direct result of various strict socio-technical regulations, NO_x control technologies have become increasingly more sophisticated.

Existing NO_x mitigation technologies include low-NO_x burners, reburning, air and fuel staging, selective catalytic reduction (SCR) and selective non-catalytic reduction (SNCR). These abatement methods have been widely used in combustion processes to meet environmental pollution regulations.[9-10] Among these mitigation techniques, the fuel reburning method is considered more effective and economical. In reburning technology, a reburning fuel (functioning as a reducing agent) is added into the exit of the primary combustion zone, reducing NO_x into N_2 in the reburning zone (fuel-rich region). In the burnout region, excess oxygen oxidises the CO, H_2 and unburnt hydrocarbons escaping the reburning region. NO_x reduction efficiency of 50–85 % can generally be achieved in reburning technology.[11-19]

Natural gas, biomass and coal are potential sources of reburning fuel. Spliethoff et al. studied the NO_x mitigation efficiency (~80 %) of the pyrolysis gases produced from coal as a reburn fuel in an entrained flow.[20] Similarly, in commercial boilers, coal has been employed as a reburn fuel, resulting in 70 % reductions in NO_x.[21-22] In particular, biomass fuels have been identified as better reburning energy sources due to their sustainable carbon nature, low CO_2 emissions, and low levels of sulfur and other toxic contents, compared to coal.[23-24] Previous literature employed biomass (wood, poplar, cornstalk, rice husk and wheat straw) to reduce NO_x, and up to 70 % overall reduction efficiency was observed.[25-27] For example, Han et al. [28] conducted an experimental study of the advanced reburning (AR) technique. The authors co-injected sodium carbonate with a nitrogen agent using biomass (15–20 %) as a reburning fuel, achieving 85–92 % NO_x reduction. Accordingly, it is essential to understand the fundamental factors that sustain the thermal decomposition of biomass and coal in reactive NO_x environments, particularly in terms of conversion efficiency.

The current experimental investigation is based on the reduction of NO_x using catechol as a reburn modelled fuel of coal and biomass. Catechol is main structural chemical species of coal, tobacco smoke, biomass tars and lignin (a major component of wood). Catechol is an appropriate choice of model compound for the investigation of NO_x mitigation as it also contains polyphenolic compounds. Furthermore, catechol's relevancy is further strengthened by the demonstrated similarity between polyaromatic hydrocarbons (PAH) product distributions from the pyrolysis of catechol and coal volatiles.[29-32] The literature contains various studies on the thermal decomposition and oxidation products of catechol. In thermal and oxidative environments in the temperature range of 500–1000 °C, the predominant carbon compounds identified are CO, CO_2, acetylene, 1,3-butadiene, phenol, benzene,

vinylacetylene, ethylene, methane, cyclopentadiene, styrene and phenylacetylene, with ethane, propyne, propadiene, propylene and toluene emerging as the minor products.[29, 32-36]

Herein, we present experimental aspects of the high-temperature reduction of NO_x (especially NO) through its co-pyrolysis/co-oxidation with catechol. This is used as model for the oxygenated compounds present in real biomass and coal fuel. The chapter aims to provide insights into the interactions of biomass and NO_x that occur during thermal energy recovery from biofuels, and in fuel reburning technology utilising herbaceous, woody and/or chaff biomass as the secondary reburn fuel. In addition, it can also help describe the effect of NO_x introduced by ammonium nitrate explosives on the ignition of lignocellulosic materials in open-cut mines.

9.2. Applied methodologies

9.2.1. Materials and experimental apparatus

Catechol, a solid white to faintly beige powder was purchased from Sigma Aldrich (purity > 99.0 %). Figure 9.1 shows a graphical representation of the experimental rig. It was comprised of a catechol vaporiser and an isothermal tubular reactor (12.7 mm OD, 10.0 mm ID, 960 mm length) linked with a sampling train to trap and analyse reaction products as well as unreacted catechol. A reactor tube (high-grade quartz, H. Baumbach & Co. Ltd., USA) was placed in the centre of the electrically-heated horizontal (500 mm heated length) 3-zone laboratory-scale furnace (supplied by Lebec, Australia). Each zone had its own temperature controller (Udian708, Australia, accuracy of 0.2 %). Also, external thermocouples were

placed inside the high purity quartz cylinders (9.5 mm OD) from both ends of the reactor tube. They facilitated the continuous monitoring of temperature during the course of the reaction and assured the quick flow of reactants and products through the annular space, thereby reducing the chance of reaction in low-temperature regions. Furthermore, the inlet of the reactor tube was connected with a feed assembly (vaporiser) and the exit of the reactor was attached to a product collection system.

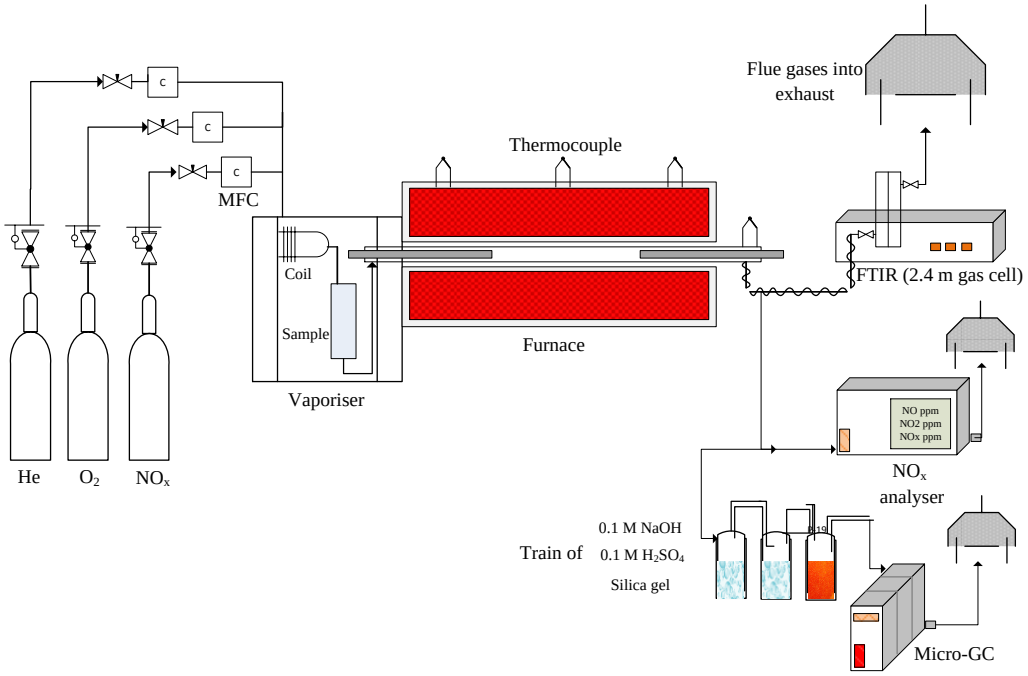

Figure 9.1. Schematic representation of the experimental setup.

The gases were led to the reactor through calibrated mass flow controllers in three separate streams; helium gas, oxygen gas (3 %, balanced in helium) and NO_x gas (840 ppm, balanced in helium). The flow rates of the gases (helium, oxygen, and NO_x) were adjusted through thermal mass flow controllers for each reaction temperature, for the predefined volume of reaction region and residence time (2 s), using Charles' law. The annular volume of the reactor tube (4–5 %) makes a negligible contribution to the overall system. Catechol

oxidative (O_2/NO_x) experiments are carried out by loading catechol particles (60 mg) into a quartz tube fixed within the vaporiser in a constant-temperature oven held at 80 °C, for slight vaporisation of the catechol. Clean glass wool was placed at the inlet and outlet points of the vaporiser tube to hold the reactant and for the uniform mixing of the catechol with carrier gases prior to entering the reaction zone. The combined flowing stream of gases provides 0.1 mole % of catechol into the reactor. The use of helium gas (99.999 % purity, BOC) as a primary carrier gas allowed the quantitative measurement of N_2 generation. The concentrations of NO and NO_2 were kept constant at 600 ppm and 20 ppm, respectively, i.e., there was a total of 620 ppm NO_x in the reaction zone, which is similar to that of real combustion systems.[37] The concentration of NO_x (620 ppm) was maintained by adjusting the oxygen flow rate (fuel-oxygen equivalence ratio, ϕ = 1.25) for fuel-rich conditions using the stoichiometry equation E9.1. The experiments were conducted over a wide range of temperatures (400–1200 °C) at ambient pressure.

$$C_6H_6O_2 + 6.5O_2 \rightarrow 6CO_2 + 3H_2O \qquad \text{R9.1}$$

9.2.2. Product sampling and analyses

Gaseous product analyses comprised of three stages: 1) A chemiluminescence NO_x analyser (Thermo-Scientific model 42*i*-HL) monitored the concentration of NO; 2) Fourier transform infrared spectroscopy (FTIR, Perkin Elmer) recorded the spectrum of gaseous product species exiting the tubular reactor. The products were kept in a gaseous state when exiting the reactor by an electrically-heated transfer line maintained at 150 ^oC (3.17 mm ID × 300 mm) that was linked to the sampling cell of the FTIR compartment. The spectrometer averaged 16 accumulated scans per spectrum at 1 cm^{-1} resolution. The gas sample cell was maintained at

150 ^{o}C to avoid any condensation of the product species. The QASoft database enabled semi-quantification of the species by their characteristic IR bands. 3) Micro-GC (Agilent 490 micro-gas chromatography, 20 m Molsieve-5A column, heated injection) quantified the formation of N_2. Three inline impingers (0.1 M H_2SO_4, 0.1 NaOH and orange silica gel) were used to protect the GC column from contaminants such as ammonia and H_2O.

The conversion of the catechol sample at each temperature was determined using GC-QQQMS (Rxi-5Sil MS, 15 m length column). During the experimental run, the reactor exit was connected to a dichloromethane (DCM) solvent trap placed inside a sodium chloride/ice bath, which aided in capturing unreacted catechol. For selected experiments (400 °C, 600 °C and 800 °C), we introduced biphenyl-D10 into the solvent trap at a concentration of 2 ppm before the experimental run. Furthermore, after the completion of experimental runs, we spiked 2 ppm of benzene-^{13}C into the collected samples. Later, the products were concentrated to a final volume of 1 ml in a rotary evaporator. Before injecting the sample into the GC-QQQMS, the concentrated samples were diluted to save the column from saturation and to achieve accurate results within the range of the calibration curve. Development of a calibration curve for the known sample of catechol (2–10 ppm) allowed accurate quantification. Deuterated biphenyl (D10) and benzene-^{13}C were recovered at 87–94 % and 98–99 %, respectively, for the selected temperatures. The detailed method used to analyse the catechol is given in Chapter 3.

9.3. Results and discussion

9.3.1. Sensitisation of catechol oxidation in the presence of NO_x

It has been extensively reported that small amounts of NO_x can alter the oxidation chemistry of burning fuels. The literature reports numerous studies on such interactions of fuel and NO_x, particularly on C_1–C_2 hydrocarbons[38-42], while fewer studies exist for CO[43-45] and CH_2O.[46-47] The sensitisation of hydrocarbons is attributed to the reactions of NO_x with H_2, O_2, CH_2O, CH_4 and C_2H_6. The presence of a radical pool (H/O/OH/HO_2) and hydrocarbon radicals can cause NO and NO_2 to form through recycling processes, such as the decomposition of nitrous acid. Consequently, the recycled NO and NO_2 enhance the oxidation of hydrocarbons via chain propagation radicals (OH and CH_3) such as $NO_2 + CH_3 \leftrightarrow NO + CH_3O$ and $NO + CH_3OO \leftrightarrow NO_2 + CH_3O$.[45]

Gersen et al.[39] studied the sensitisation effects of NO_x on methane, ethane and their blends at temperatures of 627–777 °C and pressures of 25–50 bar. They observed an enhanced oxidation of a methane gas blend, even with small amounts of NO_x. Ramussen et al.[45] carried out experiments in high-pressure laminar flow reactor for a methane and NO_x system at distinct pressure conditions of 20, 50, and 100 bar, and a temperature range of 327–627 °C. The results demonstrated a significant decrease in the initiation temperature of reaction upon addition of NO_x, and a similar effect was observed with increasing pressure. Sivaramakrishnan et al.[48] conducted a shock tube study where dilute methane-ethane mixtures enhanced oxidation in the presence of NO_x at high pressure (~50 bar) and temperatures of 727–1227 ^oC. Recently, Oluwoye et al.[49] studied the premature ignition of morpholine as a biomass-modelled compound, particularly the sensitising effect of NO_x that can cause fires in the timber industry and in underground coal mining. They conducted the experiments in a laminar flow reactor under constant pressure, fuel rich conditions, a

residence time of 1 s and a temperature range of 300–1100 °C. They observed a 150 ^{o}C reduction in the ignition temperature of morpholine when NO_x (620 ppm) was present.

The literature has reported many aspects of the thermal and oxidative decomposition of catechol.[33, 50] The decomposition of catechol starts through hydroxyl H migration to a neighbouring *ortho*-carbon-containing H atom. Figure 9.2 illustrates the conversion of catechol under an oxidative NO_x atmosphere. At 400 °C, the conversion of catechol appears more readily under NO_x oxidative environment than in a pure oxidation condition. It is anticipated that the formation of organic nitrites and nitrates reduces the oxidative temperature of catechol. The findings are consistent with Oluwoye et al.[49] (promotion of morpholine ignition due to NO_x) and with other fuels discussed in the literature.[45, 51-52] Further investigations are required (beyond the scope of this chapter) to determine the interaction mechanism of NO_x and catechol, with specific focus on the potential for premature ignition, as catechol is a potent source of toxic polychlorinated dibenzo-*p*-dioxins and dibenzofurans (PCDD/Fs) and their N-analogous compounds.[36] The conversion of catechol is calculated using equation E9.2. Relative to clean oxidation conditions, the initial NO concentration (600 ppm) increases the catechol conversion percentage to between approximately 10 % (at 400 °C) to 35 % (at 700 °C).

$$X = \frac{\text{Catechol}_{\text{inlet}} - \text{Catechol}_{\text{outlet}}}{\text{Catechol}_{\text{inlet}}} \times 100 \qquad \text{E9.2}$$

We will discuss the nitration of phenol, which is a similar hydroxylated benzene entity with one less hydroxyl group attached to benzene, compared to catechol. Berndt and Boge[53] studied the gas-phase reaction of OH radicals with phenol. They observed the maximum yield of catechol via phenol oxidation (OH + O_2) with a small amount of nitrophenol (from the oxidation of phenol) in

the presence of NO_2. Nitrophenol generation is thought to take place through the formation of a phenoxy radical intermediate and subsequent reaction with NO_2.[54] However, Bertho et al.[55] reported that the phenyl nitrite (C_6H_5O–NO) bond dissociation energy amounts to 88.2 kJ mol^{-1}, suggesting that R–NO is highly thermally unstable.

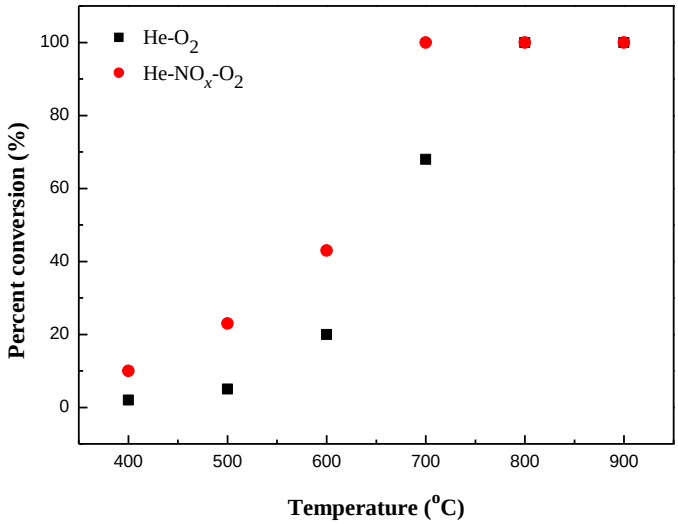

Figure 9.2. Conversion profiles of catechol in He-O_2 and He-NO_x-O_2 atmospheres with a residence time of 2 s and equivalence ratio of 1.25.

9.3.2. Formation of gaseous products

Figures 9.3a and 9.3b show the typical FTIR spectra (with the identified species) of products at the exit stream of the reactor for the case of catechol decomposition in pure oxygen, and in the NO_x oxidative condition. The characteristic IR bands used to quantify methane, acetylene, ethylene, formaldehyde, hydrogen cyanide, carbon monoxide and carbon dioxide were 3019—3011 cm^{-1}, 729 cm^{-1}, 950 cm^{-1}, 1747—1743 cm^{-1}, 712 cm^{-1}, 2171—2157 cm^{-1} and 2420—2207 cm^{-1}, respectively. The concentration of NO was monitored via NO_x analyser.

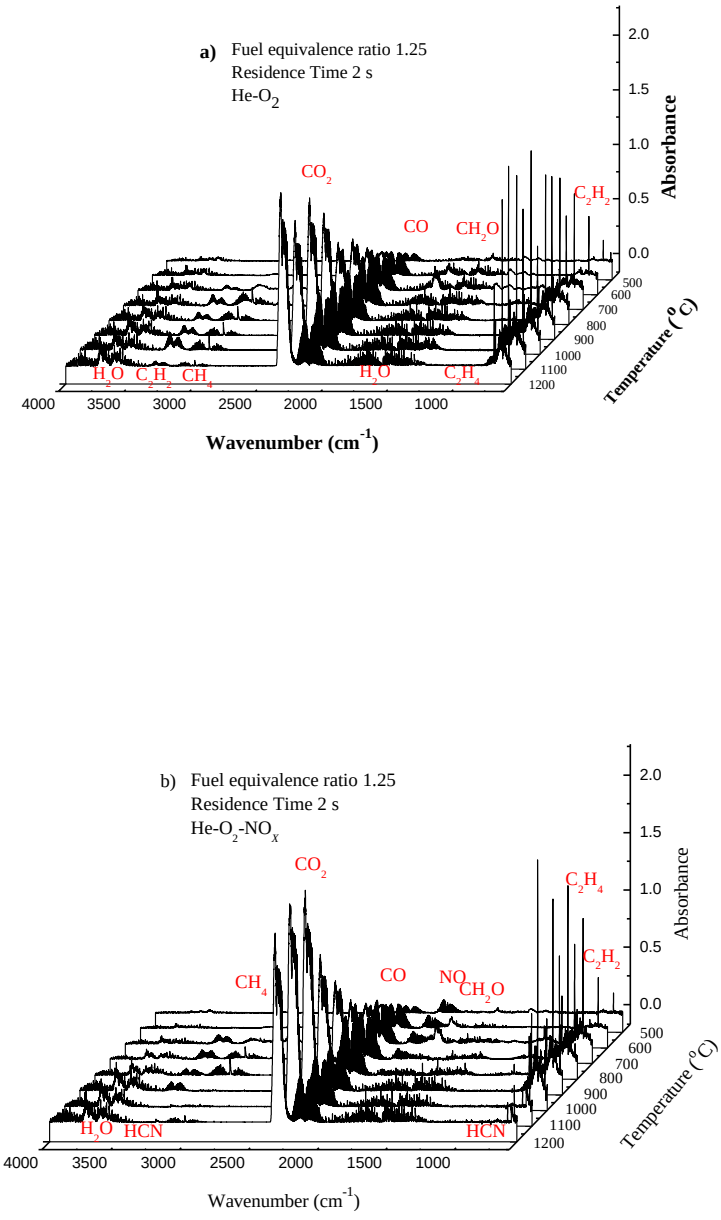

Figure 9.3. Annotated IR spectra of product species during decomposition of catechol in a) $He–O_2$ and b) $He–O_2–NO_x$ environments over a temperature range of 500–1200 ^oC.

In a catechol-O_2-NO_x system, the reaction chemistry of NO_x is based on the interaction of hydrocarbon fragments that form via pyrolysis and oxidative decomposition of catechol. Formation of hydrocarbon radicals and fragments is dependent on the thermal and oxidative decomposition of catechol, and the later process produces radicals (CH_i) at a lower

temperature than the former decomposition process. Increases in temperature produce more CH_i radicals and result in more interactions with NO. Subsequently, this leads to increases in intermediate nitrogenous species (HCN) that are finally converted into nitrogen.[14]

With the decomposition of catechol, below 600 °C, we did not observe the formation of hydrocarbons in the He-O_2 system, nor any nitrogenated species and hydrocarbons in the He-NO_x-O_2 environment, for except CO and CO_2. Figures 9.4a and 9.4b depict the concentrations of selected species produced from the decomposition of catechol under the fuel rich condition (ϕ = 1.25). The formation of C_1–C_2 hydrocarbons increased with temperature. The major product of catechol oxidation (He-O_2) in the fuel rich condition was CO, which peaked at 1000 °C. The contributions of identified species of hydrocarbons started from 700 °C, reaching their respective peaks at 800 °C, with the major species appearing to be ethylene followed by methane, acetylene and formaldehyde. For oxidation of catechol in the NO_x atmosphere, Figure 9.4b shows the early formation of hydrocarbons (ethylene and formaldehyde) starting from 600 °C, which shows the sensitising role of NO_x on catechol conversion. Additionally, the presence of NO_x reduced the concentration of hydrocarbons, which is consistent with a study of morpholine + NO_x.[49] Again, the major product was CO, which reached a maximum value at 900 °C, earlier than what we observed in the case of clean oxidation of catechol (peak at 1000 ^oC). Overall, more CO was formed under the NO_x oxidative environment than with the pure oxidation of catechol. At higher temperatures, CO was mostly converted into CO_2. For instance, in He-O_2, the level of CO started decreasing from its peak value and converted to CO_2 above 1000 ^oC. A similar trend was observed for He-NO_x-O_2 system—the concentration of CO_2 increased above 900 ^oC while the level of CO decreased. The peak concentration of HCN under NO_x-laden atmosphere appeared at 800 °C and followed a decreasing trend up to 1200 °C due to the fast

oxidation reactions of HCN. The formation of HCN was linked to the interaction of NO and hydrocarbon radicals, which is well covered in the literature.[56-57]

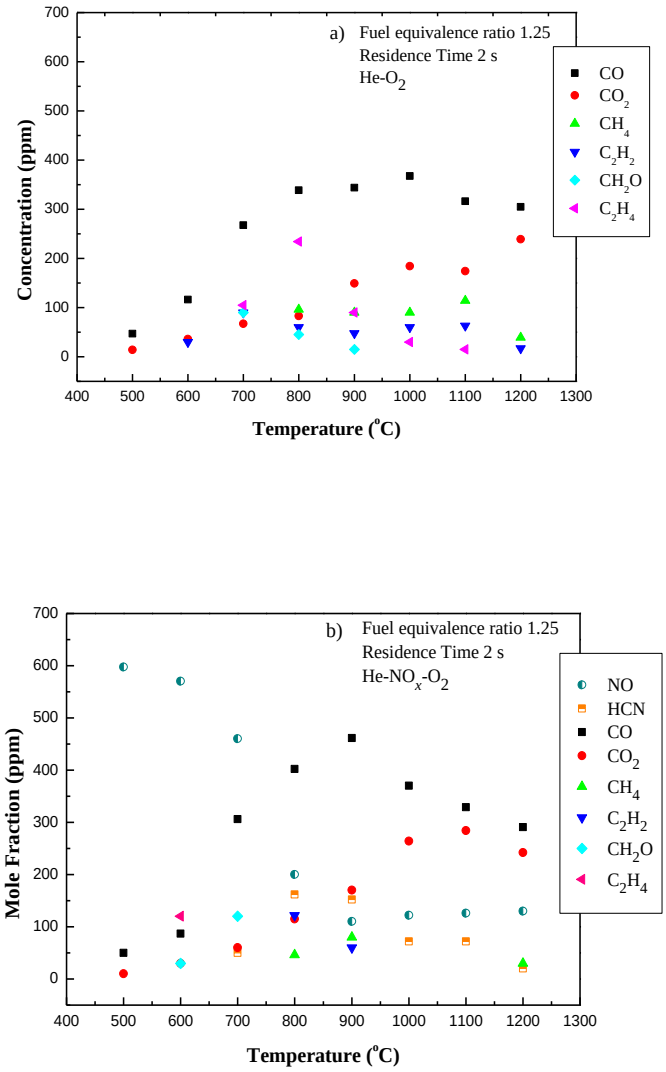

Figure 9.4. Concentration profiles of selected product species identified during the decomposition of catechol under a) oxidative and b) NO_x oxidative atmospheres with a residence time of 2 s and fuel equivalence ratio (ϕ) of 1.25. The initial concentration of NO was 600 ppm.

9.3.3. Reduction of NO with catechol oxidative fragments.

The reduction efficiency of NO was defined according to E9.3:

$$\eta = \frac{NO_{inlet} - NO_{outlet}}{NO_{inlet}} \times 100 \qquad \text{E9.3}$$

Increases in temperature promote catechol decomposition and oxidation products, which increases NO mitigation efficiency. Figure 9.5 depicts that above 800 °C, products of catechol under the fuel rich condition (ϕ =1.25) are enough to reduce NO, and peaks at 81 % (at 900 °C) for τ = 2 s, after which NO reduction decreases to 78 % due to the activity of the reduction mechanism at higher temperatures.[14] At a temperature range of 800–1200 °C, the percentage of NO converted into N_2 was 25–39 %, and the nitrogen balance remained within 72–81 %, based on NO, N_2 and HCN present in the system as outlined in table 9.1. The concentration of NO in the vaporiser and at the inlet of the reactor are the same.

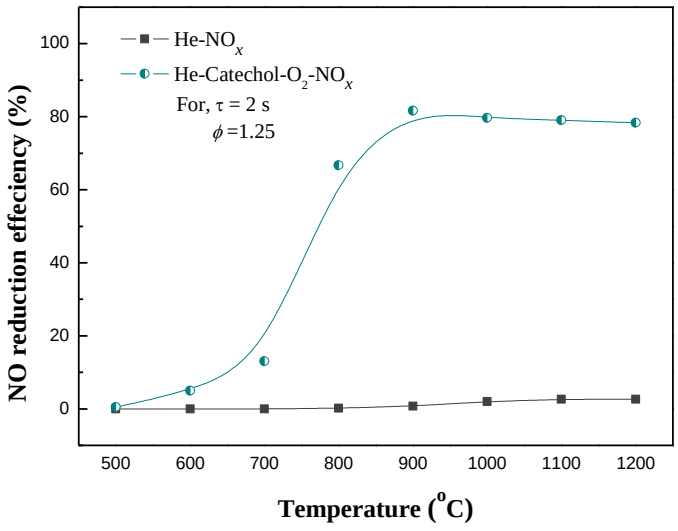

Figure 9.5. Reduction efficiency of NO_x for He–Catechol–O_2–NO_x vs. He–NO_x as a function of temperature for ϕ =1.25.

Table 9.1. Nitrogen balance of the identified gaseous N-containing species around the reactor.

Temperature °C	Initial NO ppm	Final NO ppm	N_2 ppm	HCN ppm	N-Balance %
800	600	200	125.0	162	81.3
900	600	110	194.8	152	76.1
1000	600	122	234.7	72	71.5
1100	600	126	236.4	72	72.4
1200	600	130	284.2	20	72.3

While we did not observe the formation of ammonia (NH_3) at the studied experimental temperatures of 400–1200 °C, its formation is very plausible. We anticipate the formation of small amounts of NH_3 and subsequent oxidation into an amidogen radical (NH_2) intermediate via reaction R9.1. The amidogen radical is very selective in the reduction of NO into nitrogen and NHH through reactions R9.2 and R9.3, respectively. The overall reaction chemistry is self-sustaining if the reactions of NH_2 and NO regenerate O and OH radical pools to convert more NH_3 into NH_2 radicals.[58] Wendt considered reaction R9.2 as a crucial pathway for NO_x destruction.[59]

$$NH_3 + OH/O \rightleftharpoons NH_2 + H_2O/OH \quad \text{R9.1}$$

$$NH_2 + NO \rightleftharpoons N_2 + H_2O \quad \text{R9.2}$$

$$NH_2 + NO \rightleftharpoons NNH + OH \quad \text{R9.3}$$

Nitrogenated species formed from the interaction of hydrocarbon with NO_x, particularly in reburning, are HCN, HCNO, and NH_3; these species are also able to regenerate NO through the oxidative process. The chemistry involved in NO-reburning is quite complex and still needs both experimental and computational investigations, particularly at moderate temperatures. Figure 9.4b shows and confirms the reaction of NO with hydrocarbon radicals that increases the concentration of HCN through reaction R9.4 according to temperature, and subsequent oxidises into N_2 following reaction R9.5. Reaction R9.4 primarily depends on the concentration of hydrocarbons.

$NO + C_xH_y \rightarrow HCN + \ldots..$ R9.4

$HCN + O/OH \rightarrow N_2 + \ldots..$ R9.5

Chan et al.[60] elucidated that the end product of the interaction of hydrocarbon and NO is HCN sourced from the potent CN and HCNO intermediates. HCN consumes OH and O radicals via the following subset of reactions:

$HCN + OH \rightarrow HOCN + H$ R9.6

$HCN + OH \rightarrow HNCO + H$ R9.7

$HCN + O \rightarrow NCO + H$ R9.8

$HCN + O \rightarrow NH + CO$ R9.10

$NH + NO \rightarrow N_2 + O$ R9.11

The efficiency of the hydrocarbon interaction with NO_x depends on the temperature profiles of the chemical species (N-compounds, carbon monoxide, and hydrocarbons) as well as the process conditions (temperature, pressure, time and stoichiometry).[57, 61-62]

9.3.4. Further literature comparison

The literature reports several reburning additive fuels, such as natural gas,[63] fuel oil,[64] biomass,[65-66] coal,[67] polymers,[68] pulverised coal[16] and bio gas.[69] At high temperature reburning (above 1300 °C), surrogates of fossil fuels, for example methane,[41] ethylene,[70] acetylene[71] and mixtures of small hydrocarbons,[48] have been employed for the reduction of NO; while for low temperature reburning, C_1–C_4 hydrocarbons have been tested.[56, 72-73] The reduction efficiency of NO using biomass has been addressed in detail in Chapter 2. The present content compares the effects of hydrocarbons on NO mitigation that are pertinent to fuel reburning conditions.

Figure 9.6 summarises the results of NO reduction efficiency by different hydrocarbons at nearly the same equivalence ratios.[13, 56, 74-76] For linear hydrocarbons, propane and ethane show maximum reduction efficiency at 1000 °C and ϕ = 1.51. Among the aromatic hydrocarbons, phenol shows matching performance with catechol at 1200 ^{o}C (~79 % NO reduction), while benzene is able to reduce only 50 % of the NO. The NO mitigation performance of morpholine is achieved at a relatively lower temperature (above 80 % at 800 °C) as compared to catechol that had maximum NO reduction at 900 °C. The variation in NO reduction is attributed to the different activities of HCCO and CH_i radicals released from hydrocarbons.[77]

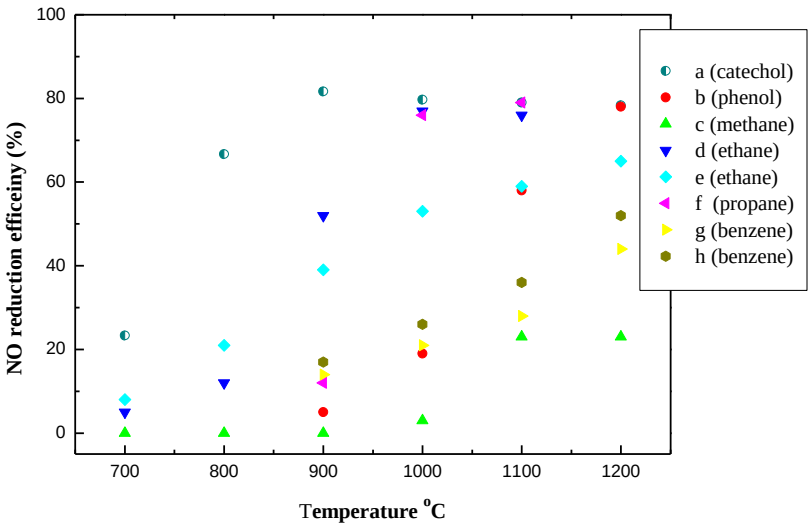

Figure 9.6. Reduction efficiency as a function of temperature at similar equivalence ratios according to various studies: a) this study, catechol, ϕ = 1.25, b) Liu et al.[78], phenol, ϕ = 1.35; c) Glaborg et al.[79], methane, ϕ = 1.16; d) Lecomte et al.[80], ethane, ϕ = 1.51; e) Glaborg et al.[79], ethane ϕ = 1.35; f) Dagaut et al.[56], propane, ϕ = 1.51; g) Zhang et al.[77], benzene, ϕ = 1.51; h) Zhang et al.[77], benzene, ϕ = 1.

9.4. Conclusion

The current chapter experimentally investigated the reduction of NO_x using catechol under a fuel-rich condition with a residence time of 2 s and temperature range of 400–1200 °C. Flow reactor experiments were performed for the oxidation of catechol with and without NO_x. At similar temperatures, more decomposition products were noted under the NO_x atmosphere compared to clean catechol oxidation. We observed maximum NO reduction at 900 °C, which is a similar temperature to that used in practical reburning technology, suggesting biomass is a viable fuel source for NO_x mitigation. Catechol shows better performance at temperature range 700–900 °C while above 900 °C, there is almost no effect compared to conventional hydrocarbon fuels used as reburn fuel (e.g., ethane and propane). The two OH groups attached to the catechol aromatic ring may have allowed NO reduction at lower temperatures, especially in fuel-rich conditions.

9.5. References

1. Muzio, L.; Quartucy, G., Implementing NO_x Control: Research to Application. *Prog. Energy Combust. Sci.* **1997**, *23*, 233-266.

2. Skalska, K.; Miller, J. S.; Ledakowicz, S., Trends in NO_x Abatement: A Review. *Sci. Total Environ.* **2010**, *408*, 3976-3989.

3. Gómez-García, M. A.; Pitchon, V.; Kiennemann, A., Pollution by Nitrogen Oxides: An Approach to Nox Abatement by Using Sorbing Catalytic Materials. *Environ. Int.* **2005**, *31*, 445-467.

4. Dvořák, R.; Chlápek, P.; Jecha, D.; Puchýř, R.; Stehlík, P., New Approach to Common Removal of Dioxins and NO_x as a Contribution to Environmental Protection. *J. Clean. Prod.* **2010**, *18*, 881-888.

5. Bowman, C. T., Kinetics of Pollutant Formation and Destruction in Combustion. *Prog. Energy Combust. Sci.* **1975**, *1*, 33-45.

6. Attalla, M. I.; Day, S. J.; Lange, T.; Lilley, W.; Morgan, S., NO_x Emissions from Blasting Operations in Open-Cut Coal Mining. *Atmospheric Environ.* **2008**, *42*, 7874-7883.

7. Chaturvedi, S.; Dave, P. N., Review on Thermal Decomposition of Ammonium Nitrate. *J. Energ. Mater.* **2013**, *31*, 1-26.

8. Oluwoye, I.; Dlugogorski, B. Z.; Gore, J.; Vyazovkin, S.; Boyron, O.; Altarawneh, M., Thermal Reduction of NO_x with Recycled Plastics. *Environ. Sci. Technol.* **2017**, *51*, 7714-7722.

9. Zhuang, H.; Niu, Y.; Gong, Y.; Zhang, Y.; Zhang, Y.; Hui, S., Influence of Biomass Reburning on NO_x Reductions During Pulverized Coal Combustion. *Energy & Fuels* **2017**, *31*, 5597-5602.

10. Mahmoudi, S.; Baeyens, J.; Seville, J. P. K., NO_x Formation and Selective Non-Catalytic Reduction (SNCR) in a Fluidized Bed Combustor of Biomass. *Biomass Bioenergy.* **2010**, *34*, 1393-1409.

11. Smoot, L. D.; Hill, S. C.; Xu, H., NO_x Control through Reburning1this Mini-Review Paper Was Presented, Together with a Series of Other Review Papers, at the Tenth Annual Technical Conference of the Advanced Combustion Engineering Research Center, Held in Salt Lake City, Utah, in March 1997.1. *Prog. Energy Combust. Sci.* **1998**, *24*, 385-408.

12. Prada, L.; Miller, J. A., Reburning Using Several Hydrocarbon Fuels: A Kinetic Modeling Study. *Combust. Sci. Technol.* **1998**, *132*, 225-250.

13. Glarborg, P.; Alzueta, M. U.; Dam-Johansen, K.; Miller, J. A., Kinetic Modeling of Hydrocarbon/Nitric Oxide Interactions in a Flow Reactor. *Combust. Flame* **1998**, *115*, 1-27.

14. Alzueta, M. U.; Glarborg, P.; Dam-Johansen, K., Low Temperature Interactions between Hydrocarbons and Nitric Oxide: An Experimental Study. *Combust. Flame* **1997**, *109*, 25-36.

15. Pratapas, J.; Bluestein, J., Natural Gas Reburn: Cost Effective NO_x Control; Reburning Natural Gas in Coal-Fired Boilers Is Proving to Be an Effective Strategy for Regulatory Compliance in Non-Attainment Areas. *Power Eng.* **1994**, *98*, 47-51.

16. Spliethoff, H.; Greul, U.; Rüdiger, H.; Hein, K. R. G., Basic Effects on NO_x Emissions in Air Staging and Reburning at a Bench-Scale Test Facility. *Fuel* **1996**, *75*, 560-564.

17. Luan, T.; Wang, X.; Hao, Y.; Cheng, L., Control of NO Emission During Coal Reburning. *Appl. Energy* **2009**, *86*, 1783-1787.

18. Rüdiger, H.; Kicherer, A.; Greul, U.; Spliethoff, H.; Hein, K. R. G., Investigations in Combined Combustion of Biomass and Coal in Power Plant Technology. *Energy Fuels* **1996**, *10*, 789-796.

19. Maly, P.; Zamansky, V.; Ho, L.; Payne, R., Alternative Fuel Reburning. *Fuel* **1999**, *78*, 327-334.

20. Spliethoff, H.; Greul, U.; Rüdiger, H.; Magel, H. C.; Schnell, U.; Hein, K. R. G.; Li, C. Z.; Nelson, P. F., NO_x Reduction Using Coal Pyrolysis Gas as Reburn Fuel: Effects of Pyrolysis Gas Composition. *Coal Sci. Technol.* **1995**, *24*, 1775-1778.

21. Li, S.; Xu, T.; Zhou, Q.; Tan, H.; Hui, S.; Hu, H., Optimization of Coal Reburning in a 1mw Tangentially Fired Furnace. *Fuel* **2007**, *86*, 1169-1175.

22. Zarnitz, R.; Pisupati, S., Identification of Significant Factors in Reburning with Coal Volatiles. *Environ. Sci. Technol.* **2008**, *42*, 2004-2008.

23. Saidur, R.; Abdelaziz, E. A.; Demirbas, A.; Hossain, M. S.; Mekhilef, S., A Review on Biomass as a Fuel for Boilers. *Renew. Sustainable Energy Rev.* **2011**, *15*, 2262-2289.

24. Duan, L.; Duan, Y.; Zhao, C.; Anthony, E. J., NO Emission During Co-Firing Coal and Biomass in an Oxy-Fuel Circulating Fluidized Bed Combustor. *Fuel* **2015**, *150*, 8-13.

25. Harding, N. S.; Adams, B. R., Biomass as a Reburning Fuel: A Specialized Cofiring Application. *Biomass Bioenergy* **2000**, *19*, 429-445.

26. Luan, J.; Sun, R.; Wu, S.; Lu, J.; Yao, N., Experimental Studies on Reburning of Biomasses for Reducing NO_x in a Drop Tube Furnace. *Energy Fuels* **2009**, *23*, 1412-1421.

27. Lu, P.; Wang, Y.; Huang, Z.; Lu, F.; Liu, Y., Study on NO Reduction and Its Heterogeneous Mechanism through Biomass Reburning in an Entrained Flow Reactor. *Energy Fuels* **2011**, *25*, 2956-2962.

28. Han, K.; Niu, S.; Lu, C., Experimental Study on Biomass Advanced Reburning for Nitrogen Oxides Reduction. *Process Saf. Environ. Prot.* **2010**, *88*, 425-430.

29. Lomnicki, S.; Truong, H.; Dellinger, B., Mechanisms of Product Formation from the Pyrolytic Thermal Degradation of Catechol. *Chemosphere* **2008**, *73*, 629-633.

30. Soltes, E. J.; Milne, T. A., *Pyrolysis Oils from Biomass*; American Chemical Society, 1988; Vol. 376, p 372.

31. Lee, S., *Alternative Fuels*; CRC Press, 1996.

32. Wornat, M. J.; Ledesma, E. B.; Marsh, N. D., Polycyclic Aromatic Hydrocarbons from the Pyrolysis of Catechol (*ortho*-Dihydroxybenzene), a Model Fuel Representative of Entities in Tobacco, Coal, and Lignin. *Fuel* **2001**, *80*, 1711-1726.

33. Thomas, S.; Ledesma, E. B.; Wornat, M. J., The Effects of Oxygen on the Yields of the Thermal Decomposition Products of Catechol under Pyrolysis and Fuel-Rich Oxidation Conditions. *Fuel* **2007**, *86*, 2581-2595.

34. Ledesma, E. B.; Marsh, N. D.; Sandrowitz, A. K.; Wornat, M. J., An Experimental Study on the Thermal Decomposition of Catechol. *Proc. Comb. Inst.* **2002**, *29*, 2299-2306.

35. Marsh, N. D.; Ledesma, E. B.; Sandrowitz, A. K.; Wornat, M. J., Yields of Polycyclic Aromatic Hydrocarbons from the Pyrolysis of Catechol [*ortho*-Dihydroxybenzene]: Temperature and Residence Time Effects. *Energy Fuels* **2004**, *18*, 209-217.

36. Altarawneh, M.; Dlugogorski, B. Z.; Kennedy, E. M.; Mackie, J. C., Theoretical Study of Unimolecular Decomposition of Catechol. *J. Phys. Chem. A.* **2010**, *114*, 1060-1067.

37. Yanfeng, G.; Shenghua, L.; Hejun, G.; Tiegang, H.; Longbao, Z., A New Diesel Oxygenate Additive and Its Effects on Engine Combustion and Emissions. *Appl. Therm. Eng.* **2007**, *27*, 202-207.

38. Hori, M.; Matsunaga, N.; Marinov, N.; William, P.; Charles, W., An Experimental and Kinetic Calculation of the Promotion Effect of Hydrocarbons on the NO-NO_2 Conversion in a Flow Reactor. *Symp. Int. Combust.* **1998**, *27*, 389-396.

39. Gersen, S.; Mokhov, A. V.; Darmeveil, J. H.; Levinsky, H. B.; Glarborg, P., Ignition-Promoting Effect of NO_2 on Methane, Ethane and Methane/Ethane Mixtures in a Rapid Compression Machine. *Proc. Comb. Inst.* **2011**, *33*, 433-440.

40. Konnov, A. A.; Zhu, J. N.; Bromly, J. H.; Zhang, D.-k., The Effect of NO and NO_2 on the Partial Oxidation of Methane: Experiments and Modeling. *Proc. Comb. Inst.* **2005**, *30*, 1093-1100.

41. Dagaut, P.; Nicolle, A., Experimental Study and Detailed Kinetic Modeling of the Effect of Exhaust Gas on Fuel Combustion: Mutual Sensitization of the Oxidation of Nitric Oxide and Methane over Extended Temperature and Pressure Ranges. *Combust. Flame* **2005**, *140*, 161-171.

42. Dagaut, P.; Mathieu, O.; Nicolle, A.; Dayma, G., Experimental Study and Detailed Kinetic Modeling of the Mutual Sensitization of the Oxidation of Nitric Oxide, Ethylene, and Ethane. *Combust. Sci. Technol.* **2005**, *177*, 1767-1791.

43. Roesler, J. F.; Yetter, R. A.; Dryer, F. L., Kinetic Interactions of CO, NO_x, and HCl Emissions in Postcombustion Gases. *Combust. Flame* **1995**, *100*, 495-504.

44. Glarborg, P.; Kubel, D.; Kristensen, P. G.; Hansen, J.; Dam-Johansen, K., Interactions of CO, NO_x and H_2O under Post-Flame Conditions. *Combust. Sci. Technol.* **1995**, *110-111*, 461-485.

45. Rasmussen, C. L.; Hansen, J.; Marshall, P.; Glarborg, P., Experimental Measurements and Kinetic Modeling of $CO/H_2/O_2$/Nox Conversion at High Pressure. *Int. J. Chem. Kinet.* **2008**, *40*, 454-480.

46. Glarborg, P.; Alzueta, M. U.; Kjærgaard, K.; Dam-Johansen, K., Oxidation of Formaldehyde and Its Interaction with Nitric Oxide in a Flow Reactor. *Combust. Flame* **2003**, *132*, 629-638.

47. Li, J.; Zhao, Z.; Kazakov, A.; Chaos, M.; Dryer, F. L.; Scire, J. J., A Comprehensive Kinetic Mechanism for CO, CH_2O, and CH_3OH Combustion. *Int. J. Chem. Kinet.* **2007**, *39*, 109-136.

48. Sivaramakrishnan, R.; Brezinsky, K.; Dayma, G.; Dagaut, P., High Pressure Effects on the Mutual Sensitization of the Oxidation of NO and CH_4-C_2H_6 Blends. *Phys. Chem. Chem. Phys.* **2007**, *9*, 4230-4244.

49. Oluwoye, I.; Dlugogorski, B. Z.; Gore, J.; Westmoreland, P. R.; Altarawneh, M., Enhanced Ignition of Biomass in Presence of Nox. *Fire Saf. J.* **2017**, *91*, 235-242.

50. Ledesma, E. B.; Marsh, N. D.; Sandrowitz, A. K.; Wornat, M. J., An Experimental Study on the Thermal Decomposition of Catechol. *Proceedings of the Combustion Institute* **2002**, *29*, 2299-2306.

51. Bendtsen, A. B.; Glarborg, P.; Dam-Johansen, K. I. M., Low Temperature Oxidation of Methane: The Influence of Nitrogen Oxides. *Combust. Sci. Technol.* **2000**, *151*, 31-71.

52. Bromly, J. H.; Barnes, F. J.; Mandyczewsky, R.; Edwards, T. J.; Haynes, B. S., An Experimental Investigation of the Mutually Sensitised Oxidation of Nitric Oxide and *n*-Butane. *Symp. Int. Comb.* **1992**, *24*, 899-907.

53. Berndt, T.; Boge, O., Gas-Phase Reaction of Oh Radicals with Phenol. *Phys. Chem. Chem. Phys.* **2003**, *5*, 342-350.

54. Carter, W. P. L., A Detailed Mechanism for the Gas-Phase Atmospheric Reactions of Organic Compounds. *Atmospheric Environ.* **1990**, *24*, 481-518.

55. Boyd, A.; Noziere, B.; Lesclaux, R., Kinetics and Thermochemistry of the Reversible Combination Reactions of the Allyl and Benzyl Radicals with NO. *J. Phys. Chem.* **1995**, *99*, 10815-10823.

56. Dagaut, P.; Luche, J.; Cathonnet, M., Reduction of NO by Propane in a JSR at 1atm: Experimental and Kinetic Modeling. *Fuel* **2001**, *80*, 979-986.

57. Dagaut, P.; Lecomte, F., Experiments and Kinetic Modeling Study of NO-Reburning by Gases from Biomass Pyrolysis in a JSR. *Energy Fuels* **2003**, *17*, 608-613.

58. Tayyeb Javed, M.; Irfan, N.; Gibbs, B. M., Control of Combustion-Generated Nitrogen Oxides by Selective Non-Catalytic Reduction. *J. Environ. Manage.* **2007**, *83*, 251-289.

59. Wendt, J. O. L., Mechanisms Governing the Formation and Destruction of NO_x and Other Nitrogenous Species in Low NO_x Coal Combustion Systems1. *Combust. Sci. and Tech.* **1995**, *108*, 323-344.

60. Chen, W.-Y.; Lester, T.; Babcock, L. *Formation and Destruction of Nitrogen Oxides in Coal Combustion.[Reburning]*; Louisiana State Univ., Baton Rouge, LA (United States): 1988.

61. Miller, J. A.; Bowman, C. T., Mechanism and Modeling of Nitrogen Chemistry in Combustion. *Prog. Energy Combust. Sci.* **1989**, *15*, 287-338.

62. Kilpinen, P.; Glarborg, P.; Hupa, M., Reburning Chemistry: A Kinetic Modeling Study. *Ind. Eng. Chem. Res.* **1992**, *31*, 1477-1490.

63. Bilbao, R.; Millera, A.; Alzueta, M. U.; Prada, L., Evaluation of the Use of Different Hydrocarbon Fuels for Gas Reburning. *Fuel* **1997**, *76*, 1401-1407.

64. Kicherer, A.; Spliethoff, H.; Maier, H.; Hein, K. R. G., The Effect of Different Reburning Fuels on NO_x-Reduction. *Fuel* **1994**, *73*, 1443-1446.

65. Shu, Y.; Zhang, F.; Wang, H.; Zhu, J.; Tian, G.; Zhang, C.; Cui, Y.; Huang, J., An Experimental Study of No Reduction by Biomass Reburning and the Characterization of Its Pyrolysis Gases. *Fuel* **2015**, *139*, 321-327.

66. Do, H.-S.; Bunman, Y.; Gao, S.; Xu, G., Reduction of NO by Biomass Pyrolysis Products in an Experimental Drop-Tube. *Energy & Fuels* **2017**, *31*, 4499-4506.

67. Liu, H.; Hampartsoumian, E.; Gibbs, B. M., Evaluation of the Optimal Fuel Characteristics for Efficient No Reduction by Coal Reburning. *Fuel* **1997**, *76*, 985-993.

68. Nimmo, W.; Singh, S.; Gibbs, B. M.; Williams, P. T., The Evaluation of Waste Tyre Pulverised Fuel for NO_x Reduction by Reburning. *Fuel* **2008**, *87*, 2893-2900.

69. Zhi-lin, F.; Jun, Z.; Chang-dong, S.; Xiao-feng, L.; Yi-qian, X., Experimental Study of NO reduction through Reburning of Biogas. *Energy Fuels* **2006**, *20*, 579-582.

70. Dagaut, P.; Lecomte, F.; Chevailler, S.; Cathonnet, M., The Reduction of NO by Ethylene in a Jet-Stirred Reactor at 1 Atm: Experimental and Kinetic Modelling. *Combust. Flame* **1999**, *119*, 494-504.

71. Dagaut, P.; Lecomte, F.; Chevailler, S.; Cathonnet, M., Experimental and Kinetic Modeling of Nitric Oxide Reduction by Acetylene in an Atmospheric Pressure Jet-Stirred Reactor. *Fuel* **1999**, *78*, 1245-1252.

72. Dagaut, P.; Luche, J.; Cathonnet, M., Experimental and Kinetic Modeling of the Reduction of NO by Propene at 1 Atm. *Combust. Flame* **2000**, *121*, 651-661.

73. Dagaut, P.; Luche, J.; Cathonnet, M., The Kinetics of C_1 to C_4 Hydrocarbons/NO Interactions in Relation with Reburning. *Proc. Comb. Inst.* **2000**, *28*, 2459-2465.

74. Liu, C.-y.; Zhang, C.-s.; Yin, R.-h., A Study on NO Reduction by Biomass Tar-Using Phenol as a Model Compound of Tar from Updraft Biomass Gasification. *Environ. Prog. Sustain. Energy.* **2015**, *34*, 47-53.

75. Lecomte, F.; Dagaut, P.; Chevailler, S.; Cathonnet, M., NO-Reduction by Ethane in a JSR at Atmospheric Pressure: Experimental and Kinetic Modeling. *Combust. Sci. Technol.* **2000**, *150*, 181-203.

76. Zhang, R.-Z.; Liu, C.-Y.; Yin, R.-H.; Duan, J.; Luo, Y.-H., Experimental and Kinetic Study of the NO-Reduction by Tar Formed from Biomass Gasification, Using Benzene as a Tar Model Component. *Fuel Process. Technol.* **2011**, *92*, 132-138.

77. Zhang, R.-Z.; Liu, C.-Y.; Yin, R.-H.; Duan, J.; Luo, Y.-H., Experimental and Kinetic Study of the NO-Reduction by Tar Formed from Biomass Gasification, Using Benzene as a Tar Model Component. *Fuel Process. Technol.* **2011**, *92*, 132-138.

78. Liu, C.-y.; Zhang, C.-s.; Yin, R.-h., A Study on NO Reduction by Biomass Tar-Using Phenol as a Model Compound of Tar from Updraft Biomass Gasification. *Environmental Progress & Sustainable Energy* **2015**, *34*, 47-53.

79. Glarborg, P.; Alzueta, M. U.; Dam-Johansen, K.; Miller, J. A., Kinetic Modeling of Hydrocarbon/Nitric Oxide Interactions in a Flow Reactor. *Combust. Flame* **1998**, *115*, 1-27.

80. Lecomte, F.; Dagaut, P.; Chevailler, S.; Cathonnet, M., NO-Reduction by Ethane in a JSR at Atmospheric Pressure: Experimental and Kinetic Modeling. *CST* **2000**, *150*, 181-203.

Chapter 10

Conclusion and Recommendations

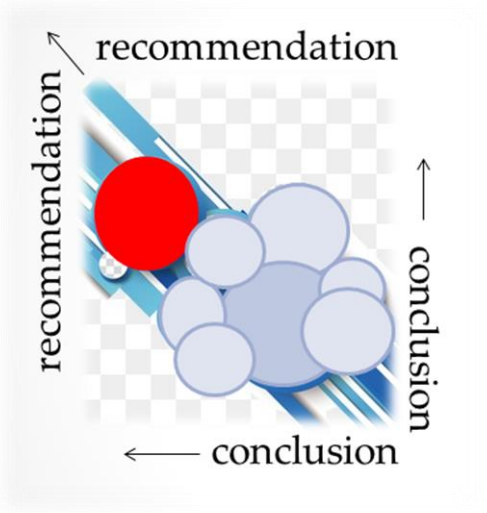

This chapter highlights concluding remarks of the dissertation and sets out some noteworthy directions for future potential work in line with the findings presented in the thesis.

10.1. Conclusion

Significant discrepancies exist in the literature regarding the kinetics and mechanisms pertinent to H abstraction from hydrocarbons by NH_2 radicals. To resolve these disagreements, we studied H abstraction reactions for a wide range of saturated and unsaturated hydrocarbons and estimated relevant thermo-kinetic parameters of these biomolecular gas-phase reactions using the CBS-QB3 method. We considered the tunnelling effects and accounted for hindered rotors in our estimation of the reaction rate constants based on the conventional transition state theory. The removal of H from methane displayed a reasonable agreement with the available experimental measurements at 300–500 K with the ratio of $k_{calculated}/k_{experimental}$ equalling 0.3–2.5, while in the 1600–2000 K temperature window, the calculated reaction rate constants showed the ratio of $k_{calculated}/k_{experimental}$ equalling 1.1–1.4. For ethane, the abstraction of H reached a ratio of $k_{calculated}/k_{experimental}$ equal to 0.10–1.2 and 1.3–1.5 across the temperature windows of available experimental measurements, i.e. 300–900 K and 1500–2000 K, respectively. Overall, the average ratio of $k_{calculated}$ /$k_{experimental}$ for methane + NH_2, ethane + NH_2 and *n*-butane + NH_2 remained within 1.1–1.5, increasing to 2.6 for propane, within the temperature windows of the experimental measurements. We presented generalised parameters for the studied reactions of hydrocarbon (C_1–C_4) species, and fewer C_5 hydrocarbons of 2-methylbutane, 2-methyl-1-butene, 3-methyl-1-butene, 3-methyl-2-butene and 3-methyl-1-butyne with NH_2 from different C-H bond types, per one abstractable H atom. We observed the mean unsigned error of CBS-QB3 measurements as 3.7 kJ mol^{-1} when comparing CBS-QB3 computed standard enthalpy of reactions ($\Delta_r H^o_{298}$) with the available experimental analogous $\Delta_r H^o_{298}$ values of alkanes. Evans-Polanyi plots for studied reactions showed that the bond dissociation enthalpies correlated linearly with the

standard enthalpy of activation ($\Delta^{\ddagger}H^{o}_{298}$), which should be helpful in determining the $\Delta^{\ddagger}H^{o}_{298}$ of the hydrocarbons not yet studied.

We deployed the CBS-QB3 computational method to develop thermochemical and kinetic parameters of H removal from the alkyl side chains in alkylbenzenes (methylbenzene, ethylbenzene and *n*-propylbenzene) as well as the attachment of NH_2 at the four plausible sites of the phenyl ring in toluene and ethylbenzene. Computation of kinetic parameters was performed based on the conventional transition state theory with the inclusion of a one-dimensional Eckart barrier and hindered-rotor treatment for harmonic oscillators. We observed that the abstraction of the benzylic H atom in toluene was the only favourable reaction corridor at all temperatures. A similar trend was observed for ethylbenzene and *n*-propylbenzene. We noticed an increase in the kinetic importance of the primary H removal in ethylbenzene with increasing temperatures with the maximum contribution reported as 28.3 % at the high end of the considered temperature region (2000 K). The sum of the contribution from the four addition pathways in toluene and ethylbenzene within a temperature range of 300–2000 K peaked at 2.4 % and 9.3 %, respectively. This indicates the dominance of the H abstraction reactions from the side chain of alkylbenzenes over the addition of NH_2 at the aromatic ring in alkylbenzenes. Moreover, the comparison of primary H abstraction reactions for the reaction rate constants of ethylbenzene and *n*-propylbenzene with those of the analogous sites in alkanes revealed a minimal effect of the aromatic ring. Accordingly, H removal from primary and secondary C-H sites in alkanes and alkylbenzenes by NH_2 radicals proceeded via similar values of $\Delta^{\ddagger}H^{o}_{298}$ and $\Delta_r H^{o}_{298}$.

A considerable ambiguity exists for the kinetics of the reaction of nitrogen dioxide (NO_2) with hydrocarbons, particularly in low-temperature combustion systems. The accurate CBS-

QB3 method was utilised to calculate the thermochemistry and reaction kinetics parameters of H abstraction from C_1–C_4 hydrocarbons and ethylbenzene by NO_2 radicals. Arrhenius rate parameters were estimated based on conventional transition state theory at the high-pressure limit while accounting for Eckart's tunnelling. Based on $\Delta^{\ddagger}H^{o}_{298}$ values, we found that the formation of *cis*-HONO (via H abstraction by NO_2) was the sole feasible channel compared to the competing potential formation of *iso*-HNO_2 and *trans*-HONO isomers. In comparison with previous literature values for C_1–C_4 alkanes, mean unsigned errors in reaction energies ($\Delta_r E_0$) for the generation of *trans*-HONO, *cis*-HONO and *iso*-HNO_2 via H abstraction from primary, secondary and tertiary H abstraction from methane, propane and *iso*-butane amounted to 1.8 kJ mol^{-1}, 5.5 kJ mol^{-1} and 2.5 kJ mol^{-1}, respectively. For the abstraction of H from methane by NO_2 radical forming *cis*-HONO and *trans*-HONO, the comparison of the computed reaction rate (CBS-QB3) showed good agreement with the available experimental measurements, i.e. $k_{calculated}/k_{experimental}$ ratio of around 0.47–0.73 over the temperature range of 800–1100 K. All considered reactions of hydrocarbons with NO_2 systematically indicated that the dominant product was *cis*-HONO + R. Evans-Polanyi plots for alkanes and alkenes showed an apparent linear trend between bond dissociation enthalpies and values of $\Delta^{\ddagger}H^{o}_{298}$.

The formation of side products such as nitrous oxide (N_2O) in the NO_xOUT process requires re-optimisation of the NO_x mitigation technique. Herein, we suggested the addition of catechol as an active molecular scavenger of N_2O. Structural and energy computations were performed at the meta-hybrid DFT functional of M05-2X with the basis set 6-311+G(d,p). The plausible reaction routes of N_2O with catechol split into three initial pathways: (i) 1,2-cycloaddition to the catechol chemical species, which resulted in a heteroatomic fused two-ring adduct followed by removal of N_2 molecule via 1,2-hydrogen shift; (ii) abstraction of an O atom from N_2O by the catechol ring leading to the formation of an epoxide intermediate

and N_2 molecule and (iii) abstractions of the two H-hydroxyl atoms by N_2O forming HNNOH and 1,4-benzoquinone. The standard activation barriers associated with routes (i), (ii) and (iii) were 184.8 kJ mol^{-1}, 257.5 kJ mol^{-1} and 281.5 kJ mol^{-1}, respectively. Accordingly, pathways (ii) and (iii) were of minor significance compared to pathway (i), i.e. 1,2-cycloaddition of N_2O into catechol molecule.

The gas phase decomposition of ammonium nitrate (AN) is well reported in the literature compared to its decomposition in the condensed phase. Therefore, the role of the reaction medium on the mechanism of AN decomposition requires further scrutiny. We theoretically accounted for reactions prevailing during the thermal decomposition of AN both in the gas phase and in an aqueous medium. We simulated the aqueous phase reactions by employing a PCM solvation model with the CBS-QB3 method as well as via the addition of explicit water molecules. Both approaches were executed at the CBS-QB3 level of theory. Energies estimated with the inclusion of three water molecules were notably smaller compared to those evaluated from both a solvation model and a pure gas phase system. By observing the effect of explicit water molecules, we noticed that there was an interaction between transition structures and water molecules. Overall, we showed that water molecules exhibited a profound effect by reducing activation enthalpies when contrasted with analogous gas phase reactions, i.e. by 1.8–10.6 kcal mol^{-1}. Many kinetic experiments have been performed to measure the reaction rate constant of $NH_3 + OH \rightarrow NH_2 + H_2O$, calculated as 1.5×10^{-13} to 1.7×10^{-13} cm^3/molecule s at 300 K. Our prediction of reaction rate constant for the reaction ($NH_3 + OH \rightarrow NH_2 + H_2O$) is within a factor of 3.5 from the rather limited analogous experimental values.

10.2. Recommendations

Reactive hydrocarbon free radicals and oxygenated carbon-centred free radicals are produced in several NO_x-containing environments such as atmospheric oxidation and low-temperature combustion systems. In addition to the pure hydrocarbon species investigated in our work, it would be insightful to study reactions of oxygenated hydrocarbon (aldehydes, ketones and alcohols) and higher aromatic hydrocarbons with NO_x and NO_2 radicals. Along the same line of interest, tracing the fate of NO_x and NO_2 during the combustion of transportation fuels requires accurate reaction rate constants for the interaction of the two title radicals with alkyl benzenes; the latter signifies an important group of hydrocarbons in commercial diesel and gasoline fractions. Biomass structural entities entail various attached functional groups (halogens, – OH and – CH_3), and thus it would be instrumental to explore the effect of these functional groups on the kinetics of NH_2/NO_2 reactions with structural surrogates that mimic biomass constituents. Obtained NH_2 rate parameters in the present study could be utilised to improve the accuracy of kinetics models of NH_2-containing species such as ethylamine, morpholine and acetamide, i.e. the commonly deployed N-surrogate species.

We have studied the mechanistic routes for the reduction of N_2O by catechol. As catechol is generally regarded as a good structural representative of hydroxylated aromatic compounds in biomass, it is intuitive to contrast the N_2O/NO reduction efficiencies with other plausible biomass compound representatives such as anisole and furfural.

Herein, we studied the unimolecular decomposition of AN as an isolated molecule. However, a more accurate representation of AN could be attained by deploying an extended periodic model of AN based on its unit cell. Figure 10.1 depicts the unit cell of AN and its Miller index termination along 100 directions. Prominent steps to investigate within a solid

model of AN includes intramolecular H transfer, direct formation of NH_3/NH_2 and emission of NO_x. Likewise, the interaction of AN with hydrocarbon fuels is an important reaction in emulsion based explosives. Utilising the extended real model of AN would facilitate investigating the initial step of the reaction between hydrocarbon fuel oils and AN. Solid-state quantum chemistry codes enable explanation for solvation models. Hence, the effect of water solvent medium on thermal decomposition of AN could be described more rigorously.

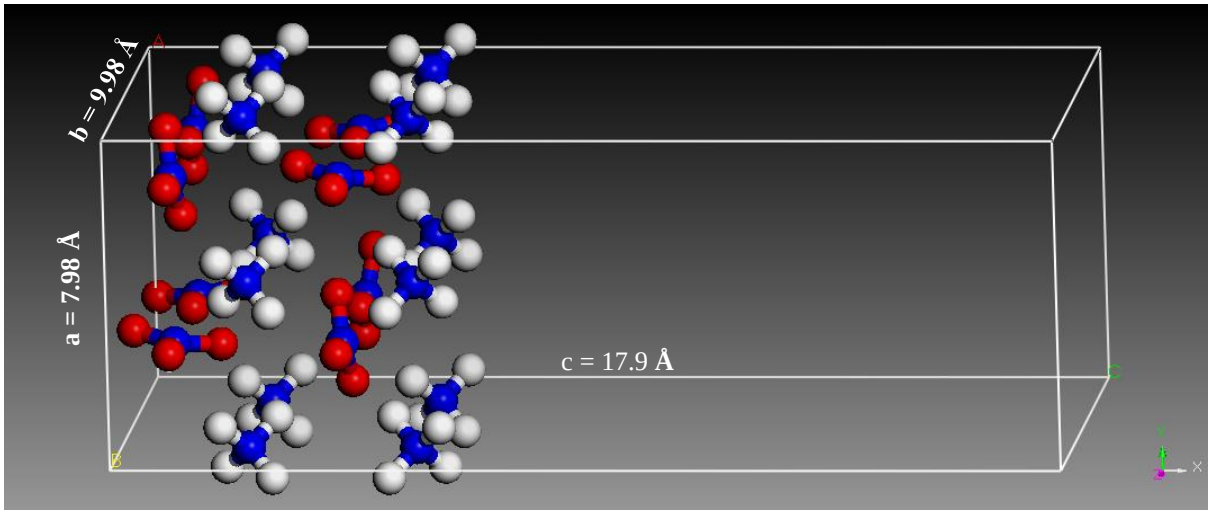

Figure 10.1. Ammonium nitrate unit cell showing 100 directions. Molecule colours are hydrogen = white, oxygen= red and nitrogen = blue.

Finally, we observed a substantial reduction of NO_x through co-oxidation of catechol, with the generation of hydrogen cyanide confirmed via FTIR and formation of nitrogen verified by μ-GC. Further confirmation of interactions between catechol and NO_x, necessitates identification and quantitative measurements of nitro- and nitroso-adducts via robust experimental techniques. This would be instrumental to construct a robust kinetics model for the reaction of NO_x by catechol. The underlying aim is to understand the factors (operational conditions and involved species) that influence nitrogen transformation during co-oxidation

of catechol with NO_x. The effect of fuel equivalency ratios on the reduction efficiency requires a thorough investigation. In addition to catechol, many candidates could be tested for their efficiency in converting NO_x into nitrogen, which includes real biomass samples, various polymers and mixtures of salts/hydrocarbons.

Chapter 11

Supplementary Document

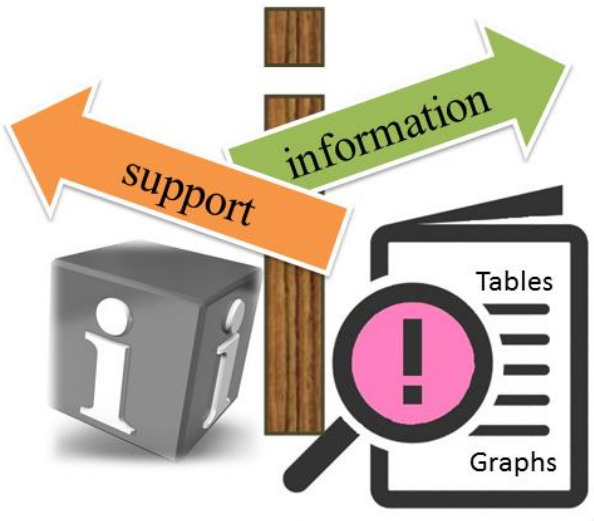

This chapter reports the essential supplementary information for chapter 4, chapter 5 and chapter 6 related to this thesis.

Appendix I: Supplementary Information for Chapter 4

Table S4.1. Comparison of standard activation enthalpy ($\Delta^{\ddagger}H^{o}_{298}$) and standard enthalpy change of reaction ($\Delta_r H^{o}_{298}$) using CBS-QB3, CBS-APNO and G4 method at 298.15 K. All units are in kJ mol^{-1}

	CBS-QB3		G4		CBS-APNO	
Reactions	$\Delta_r H^{o}_{298}$	$\Delta^{\ddagger}H^{o}_{298}$	$\Delta_r H^{o}_{298}$	$\Delta^{\ddagger}H^{o}_{298}$	$\Delta_r H^{o}_{298}$	$\Delta^{\ddagger}H^{o}_{298}$
R1	-9.4	50.1	-9.4	55.2	-10.1	48.1
R2	-24.8	37.3	-25.4	42.0	-25.3	35.6
R3a	-21.8	35.1	-23.4	40.8	-22.5	35.8
R3b	-36.4	26.9	-37.2	30.5	-36.5	24.9
R4b	-35.4	25.1	-37.3	27.5		
R5b	-43.7	18.8	-44.9	18.4		
R6	-41.2	18.2	-43.1	19.1		
R7a	16.4	44.3	16.8	47.9		
R7b	-90.0	19.7	-87.7	23.4		
R8	-28.4	31.0	-32.7	31.7		
R9	-87.2	23.2	-84.7	26.2		
R12	12.5	49.6	13.5	54.5		
R16	-89.8	12.5	-89.0	12.7		
Mean unsigned error of $\Delta_r H^{o}_{298}$ and $\Delta^{\ddagger}H^{o}_{298}$ between CBS-QB3 and G4 method 1.48 kJ mol^{-1} and 2.94 kJ mol^{-1}						

Table S4.2. Comparison of calculated bond dissociation enthalpies (BDH) of C-H bond associated with hydrocarbons with the literature values.

Hydrocarbon			Calculated BDH (kJ mol^{-1})	Literature (kJ mol^{-1})	Unsigned Error (kJ mol^{-1})
methane	$CH_4 \rightarrow H + p\text{-}CH_3$	R1	440.9	439.3[1]	1.6
ethane	$C_2H_6 \rightarrow H + p\text{-}C_2H_5$	R2	425.4	420.5[2]	4.9
propane	$C_3H_8 \rightarrow H + p\text{-}C_3H_7$	R3a	428.4	422.2[3]	6.2
	$C_3H_8 \rightarrow H + s\text{-}C_3H_7$	R3b	413.9	410.5[4]	3.4
n-butane	$n\text{-}C_4H_{10} \rightarrow p\text{-}C_4H_9 + H$	R4a	426.4	421.3[5]	5.1
	$n\text{-}C_4H_{10} \rightarrow s\text{-}C_4H_9 + H$	R4b	414.8	411.1[6]	3.7
i-butane	$i\text{-}C_4H_{10} \rightarrow p\text{-}C_4H_9 + H$	R5a	427.9	419.2[7]	8.7
	$i\text{-}C_4H_{10} \rightarrow t\text{-}C_4H_9 + H$	R5b	406.6	400.4[3]	6.2
2-methylbutane	$C_5H_{12} \rightarrow t\text{-}C_5H_{11} + H$	R6	409.3	400.8[8]	8.5
propene	$C_3H_6 \rightarrow v\text{-}C_3H_5 + H$	R7a	466.6	464.8[8]	1.8
	$C_3H_6 \rightarrow a\text{-}C_3H_5 + H$	R7b	359.3	368.6[3]	9.3
1-butene	$1\text{-}C_4H_8 \rightarrow p\text{-}C_4H_7 + H$	R8	421.8	410.5[9]	11.3
2-butene	$2\text{-}C_4H_8 \rightarrow a\text{-}C_4H_7 + H$	R9	363.0	355.8[10]	7.2
2-methyl-1-butene	$C_5H_{10} \rightarrow a\text{-}C_5H_9 + H$	R10	358.8	347.1[10]	11.7
3-methyl-1-butene	$C_5H_{10} \rightarrow p\text{-}C_5H_9 + H$	R11a	428.0	NA	
	$C_5H_{10} \rightarrow a\text{-}C_5H_9 + H$	R11b	345.3	332.6[11]	12.7
ethylene	$C_2H_4 \rightarrow v\text{-}C_2H_3 + H$	R12	462.7	465.3[12]	2.6
3-methyl-2-butene	$C_5H_{10} \rightarrow a\text{-}C_5H_9 + H$	R13	365.3	352.4[10]	12.9
1-butyne	$1\text{-}C_4H_6 \rightarrow s\text{-}C_4H_5 + H$	R14	365.2	355.6[13]	9.6

2-butyne	2-$C_4H_6 \rightarrow p$-$C_4H_5 + H$	R15	377.0	379.5[14]	2.5
3-methyl-1-butene	$C_5H_8 \rightarrow t$-$C_5H_7 + NH_3$	R16	356.9	345.2[15]	11.7
			Mean Unsigned Error		7.1

1. Dobis, O.; Benson, S. W., Analysis of Flow Dynamics in a New, Very Low Pressure Reactor. Application to the Reaction: Cl + CH_4⇌ HCl + CH_3. *Int. J. Chem. Kinet.* **1987**, *19*, 691-708.
2. Dobis, O.; Benson, S. W., Temperature Coefficients of Rates of Ethyl Radical Reactions with HBr and Br in the 228−368 K Temperature Range at Millitorr Pressures. *J. Phys. Chem. A.* **1997**, *101*, 6030-6042.
3. Tsang, W., Heats of Formation of Organic Free Radicals by Kinetic Methods. In *Energetics of Organic Free Radicals*, Martinho Simões, J. A.; Greenberg, A.; Liebman, J. F., Eds. Springer Netherlands: Dordrecht, **1996**; pp 22-58.
4. Russell, J. J.; Seetula, J. A.; Gutman, D., Kinetics and Thermochemistry of CH_3, C_2H_5, and *i*-C_3H_7. Study of the Equilibrium R + HBr . ⇌. R-H + Br. *J. Am. Chem. Soc.* **1988**, *110*, 3092-3099.
5. Walker, J. A.; Tsang, W., Single-Pulse Shock Tube Studies on the Thermal Decomposition of *n*-Butyl Phenyl Ether, *n* -Pentylbenzene, and Phenetole and the Heat of Formation of Phenoxy and Benzyl Radicals. *J. Phys. Chem.* **1990**, *94*, 3324-3327.
6. Seakins, P.; Pilling, M.; Niiranen, J.; Gutman, D.; Krasnoperov, L., Kinetics and Thermochemistry of R+ HBr ⇄ RH + Br Reactions: Determinations of the Heat of Formation of C_2H_5, *i*-C_3H_7, sec-C_4H_9, and *t*-C_4H_9. *J. Phys. Chem.* **1992**, *96*, 9847-9855.
7. Benson, S. W., Thermochemistry and Kinetics of Sulfur-Containing Molecules and Radicals. *Chem. Rev.* **1978**, *78*, 23-43.
8. Tsang, W., Shock Tube Studies on the Stability of Polyatomic Molecules and the Determination of Bond Energies. In *Energetics of Stable Molecules and Reactive Intermediates*, Minas da Piedade, M. E., Ed. Springer Netherlands: Dordrecht, **1999**; pp 323-352.
9. Schultz, J. C.; Houle, F. A.; Beauchamp, J. L., Photoelectron Spectroscopy of Isomeric C_4H_7 Radicals. Implications for the Thermochemistry and Structures of the Radicals and Their Corresponding Carbonium Ions. *J. Am. Chem. Soc.* **1984**, *106*, 7336-7347.
10. Denisov, E. D., TG., *Handbook of Antioxidants*; CRC Press: London-New York. 2000, *88*, 19.
11. Egger, K. W.; Jola, M., The Kinetics of the Gas-Phase Isomerization of 1,*trans*-3,*trans*-5-Heptatriene into the *cis*-5-isomer Catalyzed by Nitric Oxide and the Stabilization Energy in the Pentadienyl Radical. *Int. J. Chem. Kinet.* **1970**, *2*, 265-280.
12. Berkowitz, J.; Ellison, G. B.; Gutman, D., Three Methods to Measure RH Bond Energies. *J. Phys. Chem* **1994**, *98*, 2744-2765.
13. Nguyen, T. T.; King, K. D., Kinetics of Decomposition and Interconversion of 3-Methylbut-1-yne and 3-Methylbuta-1,2-diene. Resonance Stabilization Energies of Propargylic Radicals. *J. Phys. Chem.* **1981**, *85*, 3130-3136.
14. Tsang, W., Thermal Stability of Intermediate Sized Acetylenic Compounds and the Heats of Formation of Propargyl Radicals. *Int. J. Chem. Kinet.* **1978**, *10*, 687-711.
15. Lossing, F. P; Traeger, J. C, Free Radicals by Mass Spectrometry XlVI. Heats of Formation of $C_5H_7$and C_5H_9 Radicals and Cations. *Int. J. Mass Spectrom. Ion Phys.* **1976**, *19*, 9-22

Table S4.3. Calculated energies, vibrational frequencies and moments of inertia for the VTST calculations for Reaction R3b.

	s (amu)										
MEPs	-0.25	-0.20	-0.15	-0.10	-0.05	0.00	0.05	0.100	0.15	0.20	0.25
E (0 K) ha	-174.635374	-174.635307	-174.635352	-174.635253	-174.635147	-174.635180	-174.635479	-174.636086	-174.637071	-174.638614	-174.640154
Moment of inertia (au)	238.08478 438.17128 609.35956	238.28867 435.23657 606.52539	238.56726 432.53473 604.01341	238.80960 430.78673 602.43843	239.07009 429.06617 600.86986	239.34351 427.45359 599.44005	239.62320 426.07511 598.30609	239.91912 424.68819 597.17680	240.24402 423.15915 595.90953	239.69875 425.99135 596.08816	240.03858 424.14142 594.67189
Vibrational frequencies (cm^{-1})	88.6905i	302.9124i	690.8752i	1047.8626i	1310.8017i	1502.5764i	1630.4013i	1682.5521i	1659.1929i	1549.4160i	1355.0745i
	69.5771	68.8006	67.2232	65.8074	64.3634	62.8117	61.2028	59.9050	58.9937	37.5410	33.3541
	60.2	75.8	94.4	107.0	117.4	126.5	134.6	140.7	144.8	142.0	142.0
	117.9	125.2	141.6	152.5	160.8	167.7	173.2	176.8	178.7	163.7	160.0
	220.2	219.4	217.9	216.5	214.9	212.9	210.4	207.6	204.3	189.8	185.3
	276.1	267.9	260.0	255.5	252.0	248.6	245.1	241.7	238.0	237.9	234.0
	370.1	367.0	364.3	363.6	363.8	364.4	365.5	366.7	367.9	365.3	366.1

	599.3	614.4	630.6	595.9	563.1	540.9	527.0	520.4	519.5	487.1	495.7
	646.7	646.9	631.6	642.4	650.0	655.2	657.4	656.2	651.2	626.9	623.1
	831.3	847.2	845.9	760.9	726.0	710.8	700.3	691.4	682.3	734.2	717.2
	873.9	873.4	863.8	867.5	869.1	869.6	869.3	868.1	865.4	863.8	857.2
	925.7	926.8	928.0	912.2	913.7	917.2	918.6	916.8	912.2	911.6	908.9
	945.6	948.3	951.1	928.9	929.6	930.4	931.1	931.8	932.5	932.5	933.1
	1087.9	1092.9	957.7	952.6	953.3	953.6	953.4	952.8	951.8	948.6	946.9
	1165.1	1157.5	1099.8	1105.1	1109.5	1113.5	1117.0	1119.6	1121.7	1121.1	1122.4
	1192.4	1192.3	1168.7	1164.3	1161.7	1159.3	1156.9	1154.4	1151.8	1165.6	1165.5
	1326.7	1276.6	1192.6	1191.6	1190.6	1189.4	1188.0	1186.8	1185.6	1186.7	1185.5
	1373.4	1331.5	1337.3	1341.4	1345.0	1348.4	1351.6	1354.4	1356.8	1335.8	1341.3
	1389.1	1393.6	1396.6	1397.8	1393.9	1384.0	1374.6	1366.8	1360.9	1361.8	1360.9
	1409.2	1416.3	1415.6	1405.1	1398.6	1399.4	1400.1	1400.7	1401.4	1403.4	1403.2
	1417.7	1417.2	1424.4	1417.2	1416.4	1415.9	1415.4	1415.0	1414.7	1414.5	1414.3
	1488.5	1487.9	1430.3	1442.9	1455.5	1468.8	1479.0	1481.0	1480.7	1479.4	1478.6
	1493.2	1490.5	1487.1	1486.5	1485.9	1485.5	1485.6	1485.7	1485.3	1481.7	1480.9

	1502.8	1492.6	1491.9	1491.3	1491.0	1491.7	1497.2	1496.3	1495.5	1492.7	1491.9
	1505.6	1503.5	1501.3	1500.2	1499.2	1498.3	1498.1	1499.9	1498.8	1497.5	1496.7
	1540.5	1508.8	1504.5	1503.6	1502.8	1501.9	1500.9	1514.5	1536.0	1552.1	1575.6
	1708.0	1544.3	1545.3	1547.8	1550.8	1554.6	1559.6	1565.6	1573.1	1584.2	1593.9
	3006.5	3005.3	3003.3	3001.3	2999.1	2996.6	2993.6	2990.4	2987.0	2982.4	2978.6
	3010.6	3009.4	3007.4	3005.4	3003.3	3000.8	2997.9	2994.7	2991.2	2987.2	2983.6
	3035.2	3037.2	3040.4	3042.9	3045.1	3047.0	3048.2	3048.5	3048.1	3047.6	3046.3
	3059.1	3057.9	3056.2	3054.9	3053.6	3052.4	3051.0	3049.7	3048.3	3053.5	3052.9
	3065.9	3064.8	3063.4	3062.6	3062.3	3062.7	3064.1	3066.6	3069.8	3071.0	3074.4
	3082.3	3082.9	3083.7	3084.3	3084.9	3085.4	3085.9	3086.3	3086.5	3088.8	3089.2
	3085.8	3086.6	3087.7	3088.7	3089.6	3090.5	3091.6	3092.7	3094.1	3098.9	3099.8
	3351.1	3354.2	3358.8	3363.1	3367.5	3372.6	3378.5	3384.9	3392.2	3400.1	3408.6
	3441.3	3444.4	3449.0	3453.1	3457.4	3462.2	3467.8	3474.0	3480.8	3488.3	3496.1

s: represent minimum energy pathways (MEPs)

Table S4.4. TST and VTST rate coefficient for Reactions R3a and R3b. Units are in cm^3 $molecule^{-1}$ s^{-1}.

	R3b		
T K	k^{TST}	k^{VTST}	k^{TST}/k^{VTST}
300	1.50×10^{-17}	1.21×10^{-17}	1.23
400	5.41×10^{-16}	4.48×10^{-16}	1.21
500	4.65×10^{-15}	3.90×10^{-15}	1.19
600	1.95×10^{-14}	1.65×10^{-14}	1.18
700	5.44×10^{-14}	4.64×10^{-14}	1.17
800	1.17×10^{-13}	1.00×10^{-13}	1.17
900	2.13×10^{-13}	1.83×10^{-13}	1.16
1000	3.44×10^{-13}	2.97×10^{-13}	1.16
1100	5.08×10^{-13}	4.40×10^{-13}	1.16
1200	7.04×10^{-13}	6.10×10^{-13}	1.15
1300	9.28×10^{-13}	8.06×10^{-13}	1.15
1400	1.18×10^{-12}	1.02×10^{-12}	1.15
1500	1.44×10^{-12}	1.26×10^{-12}	1.15
1600	1.73×10^{-12}	1.50×10^{-12}	1.15
1700	2.02×10^{-12}	1.76×10^{-12}	1.15
1800	2.33×10^{-12}	2.03×10^{-12}	1.15
1900	2.64×10^{-12}	2.31×10^{-12}	1.14
2000	2.96×10^{-12}	2.58×10^{-12}	1.14

Table S4.5. Comparison of experimental and calculated (at CBS-QB3 level) standard enthalpy of reaction ($\Delta_r H^o_{298}$). The table presents the values of standard activation enthalpy ($\Delta^{\ddagger} H^o_{298}$) and standard enthalpy change of reaction ($\Delta_r H^o_{298}$) at 298.15 K. All units are in kJ mol^{-1}

Reaction	$\Delta_r H^o_{298}$ [a]	$\Delta_r H^o_{298}$ [b]	Unsigned error ($\Delta_r H^o_{298}$)	$\Delta^{\ddagger} H^o_{298}$ [c]
R1	-10.9	-9.4	1.5	50.1
R2	-26.8	-24.8	2.0	37.3
R3a	-29.2	-21.8	7.4	40.8
R3b	-36.8	-36.4	0.4	26.9
R4a				34.5
R4b				25.1
R5a	-30.9	-22.2	8.7	35.1
R5b	-45.9	-43.7	2.2	18.8
Mean unsigned error			3.7	
R6				18.2
R7a				44.3
R7b				19.7
R8				31.0
R9				23.2
R10				13.8
R11a				33.6

R11b				11.2
R12				49.6
R13				22.7
R14				16.7
R15				27.2
R16				15.2

[a] Experimental standard enthalpy change of reaction at 298.15 K from reference 22.

[b] Calculated standard enthalpy change of reaction using CBS-QB3 method at 298.15 K (present work).

[c] Standard enthalpy of activation calculated at CBS-QB3 level at 298.15 K

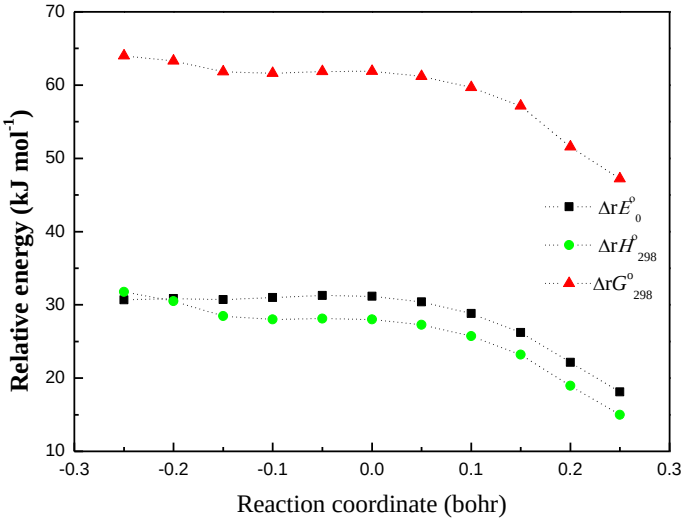

Figure S4.1. Energy profiles of the MEPs along R3b.

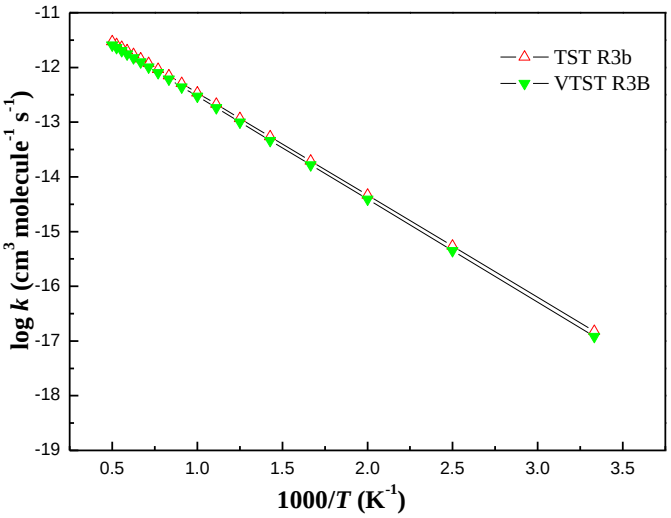

Figure S4.2. Comparison of rate constants for Reaction R3b for TST and VTST formalisms, calculated at the CBS-QB3 level of theory and for the temperature range of 300–2000 K.

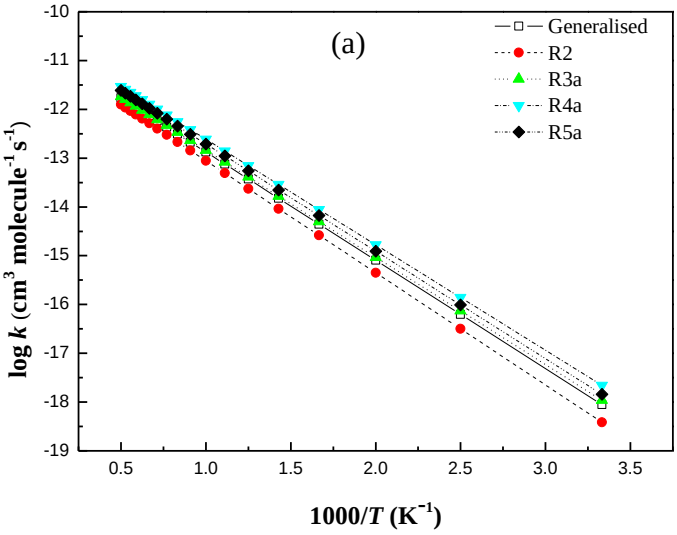
(a)
Generalised
R2
R3a
R4a
R5a
log k (cm3 molecule-1 s-1)
1000/T (K-1)

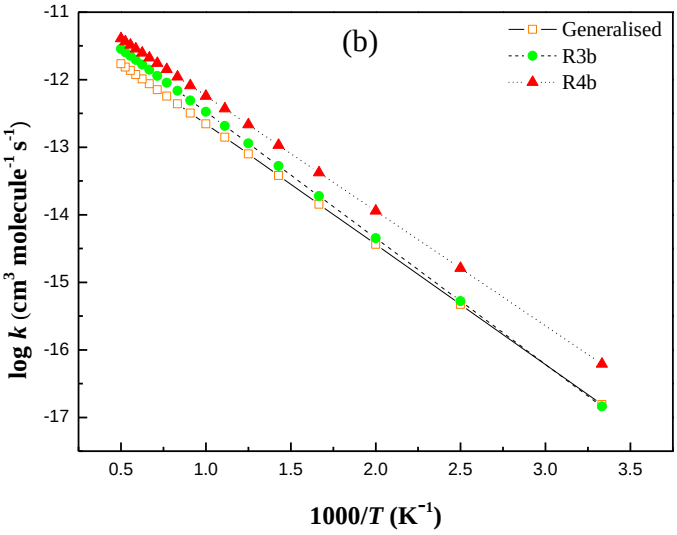
(b)
Generalised
R3b
R4b
log k (cm3 molecule-1 s-1)
1000/T (K-1)

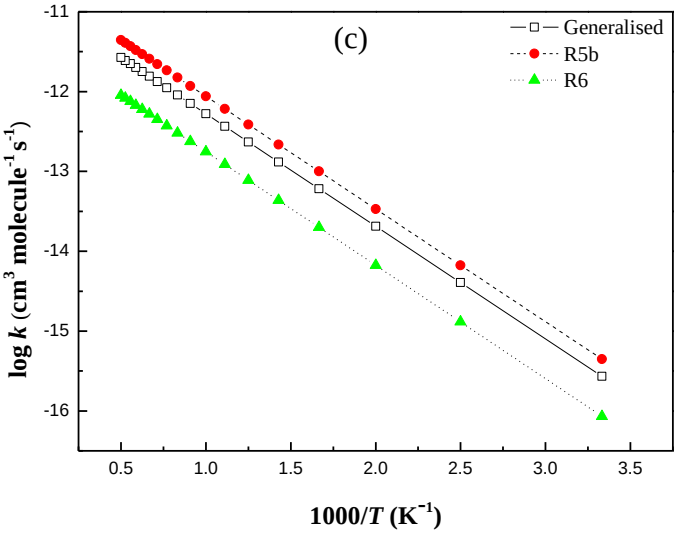
(c)
Generalised
R5b
R6
log k (cm3 molecule-1 s-1)
1000/T (K-1)
-11
-12
-13
-14
-15
-16
0.5
1.0
1.5
2.0
2.5
3.0
3.5

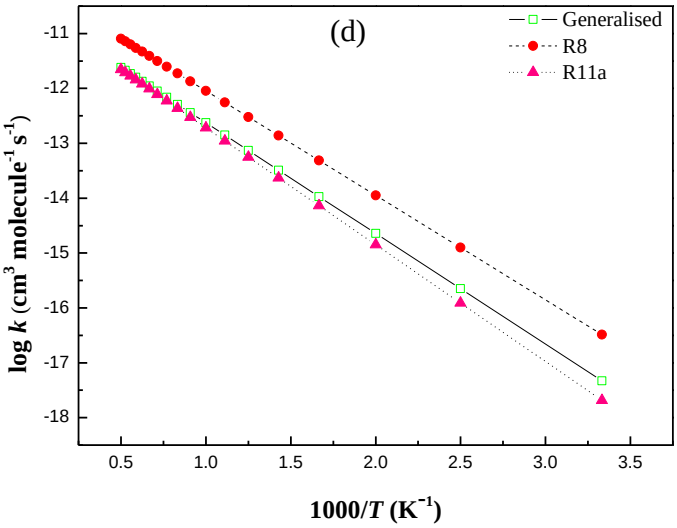
(d)
Generalised
R8
R11a
log k (cm3 molecule-1 s-1)
1000/T (K-1)
-11
-12
-13
-14
-15
-16
-17
-18
0.5
1.0
1.5
2.0
2.5
3.0
3.5

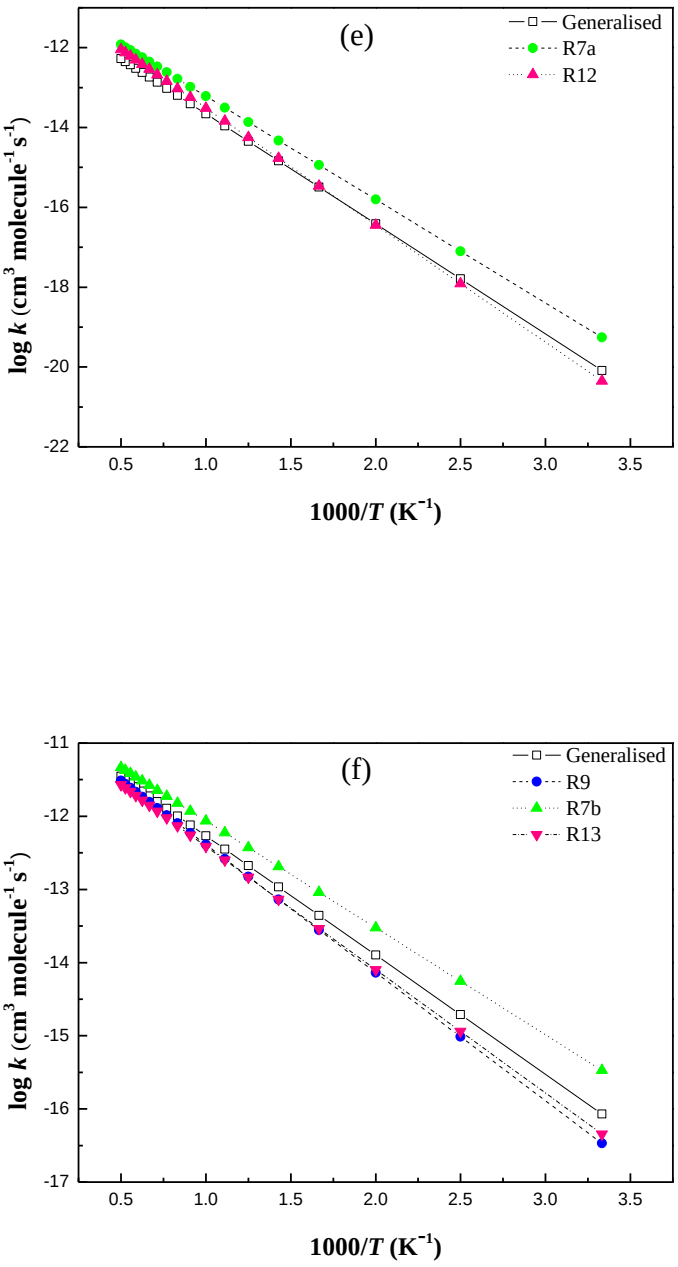

Figure S4.3. Comparison of the Arrhenius plots of the rate constant for (a) primary H abstraction from alkanes (b) secondary H abstraction from alkanes (c) tertiary H abstraction from alkanes (d) primary H abstraction from alkenes (e) vinylic H abstraction from alkenes and (f) allylic H abstraction from alkenes by NH_2 with the corresponding Arrhenius plot of the generalised rate parameters, per one abstractable H atom, fitted between 300 and 2000 K.

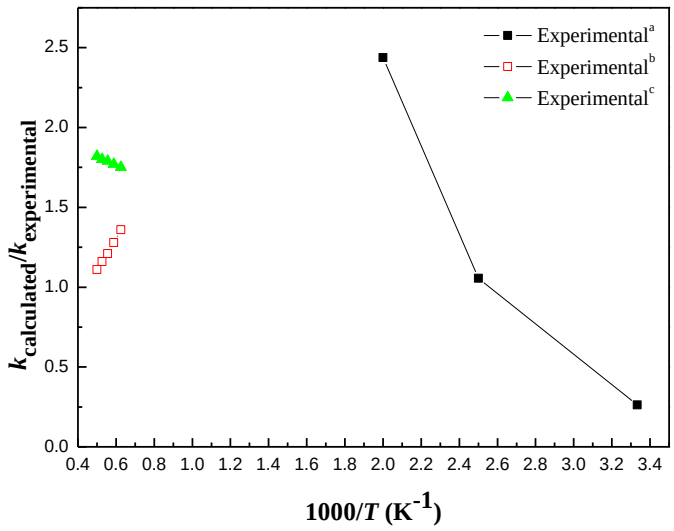

Figure S4.4. Ratio of calculated to experimental rate constants for Reaction R1 in the temperature windows of available experimental measurements. The experimental values are from Refs [a]17, [b]22, and [c]16.

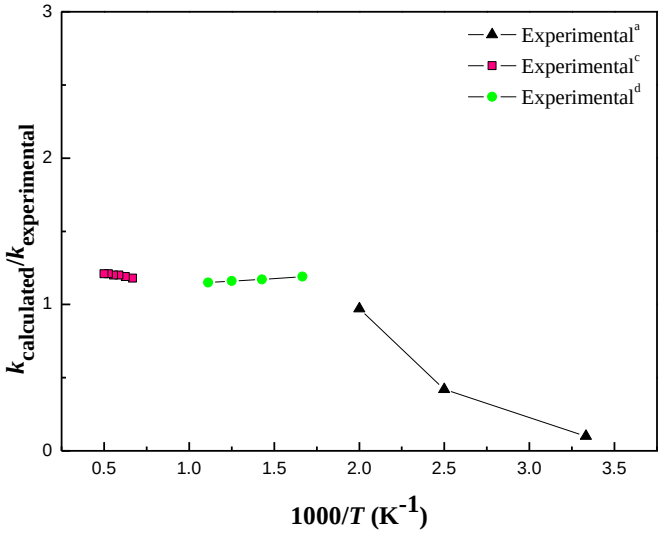

Figure S4.5. Ratio of calculated to experimental rate constants for Reaction R2 in the temperature windows of available experimental measurements. The experimental values are from Refs [a]17, [d]14, and [c]16.

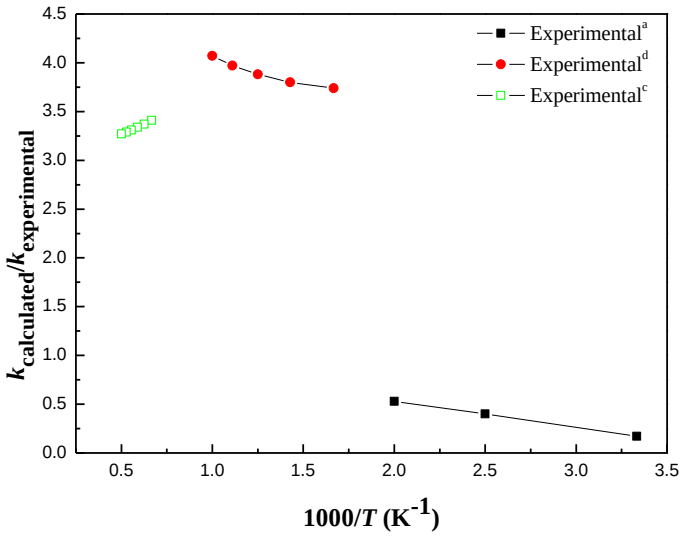

Figure S4.6. Ratio of calculated to experimental rate constants for Reaction R3 in the temperature windows of available experimental measurements. The experimental values are from Refs [a]17, [d]14,and [c]16.

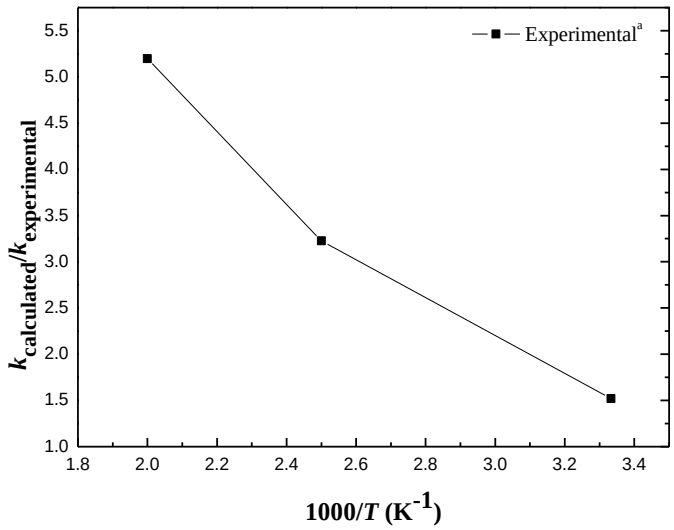

Figure S4.7. Ratio of calculated to experimental rate constants for Reaction R4 in the temperature windows of available experimental measurements. The experimental values are from Ref [c]17.

Appendix II: Supplementary Information for Chapter 5

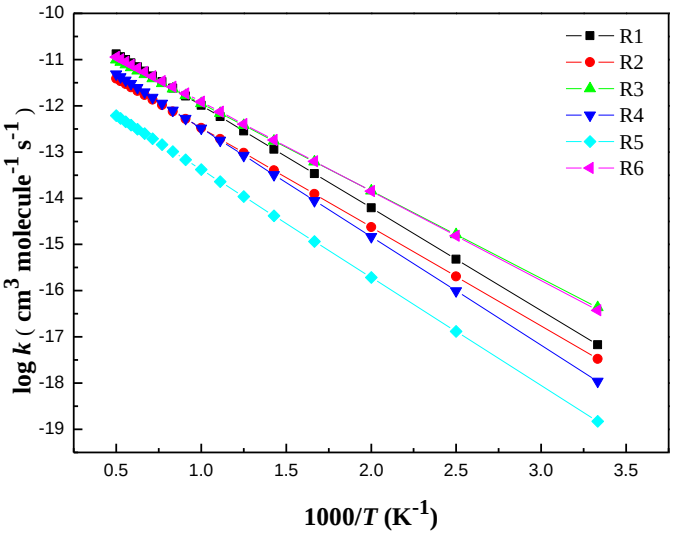

Figure S5.1. Arrhenius plots for the rate constant for H abstraction reactions from the alkyl side chain in alkylbenzenes by NH_2.

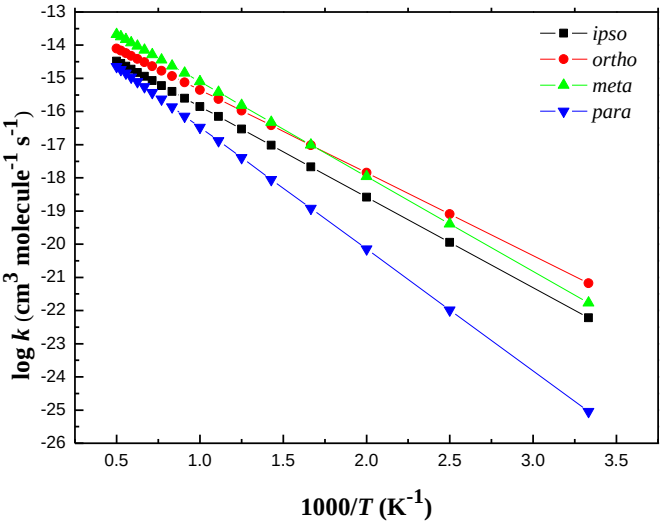

Figure S5.2. Arrhenius plots for the rate constant for addition reactions of NH_2 to toluene.

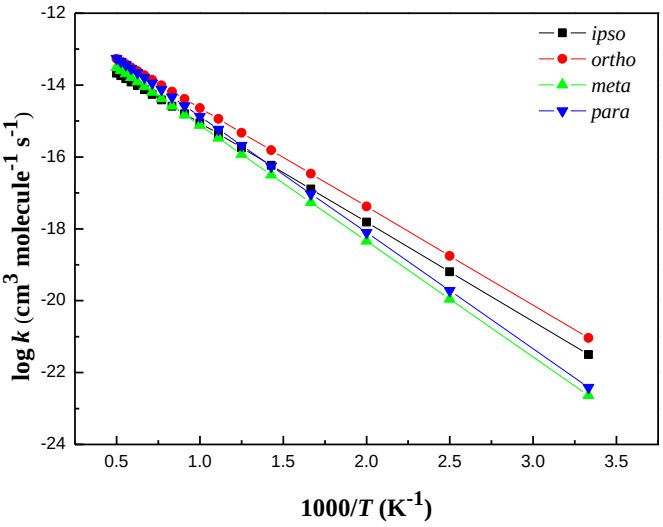

Figure S5.3. Arrhenius plots for the rate constant for the addition reactions of NH_2 to ethylbenzene.

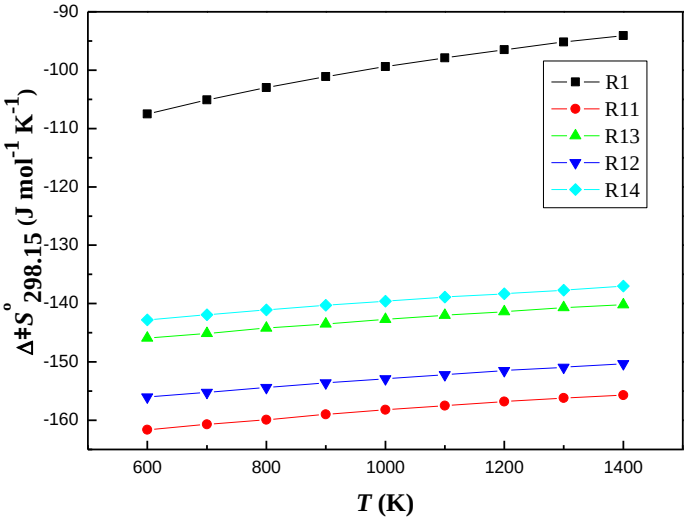

Figure S5.4. $\Delta^{\ddagger}S_{298}$ values for the abstraction and addition reactions of NH_2 with toluene (R1, R11, R12, R13 and R14) over temperature interval of 600–1400 K.

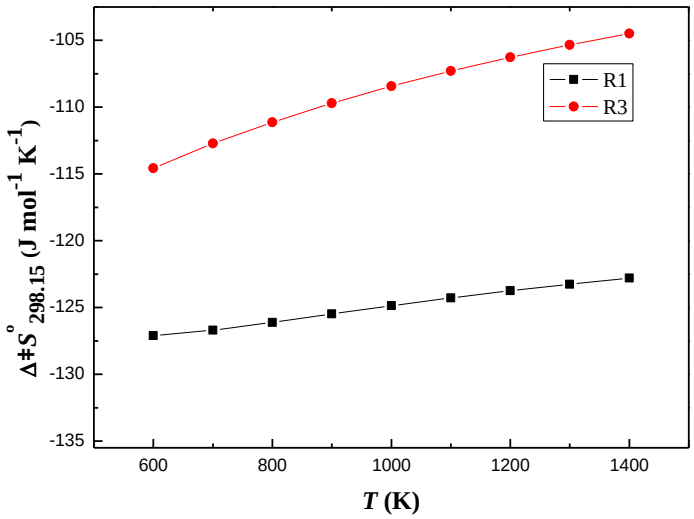

Figure S5.5. $\Delta^{\ddagger}S_{298}$ values for benzylic H abstraction reactions from toluene (R1) and ethylbenzene (R3) by NH_2 over temperature interval of 600–1400 K.

Cartesian coordinates

TS1

C	-1.73587900	-1.19123600	-0.24307500
C	-2.38466500	0.02462600	-0.45805000
C	-1.71690000	1.21755600	-0.18407500
C	-0.41319200	1.19380300	0.29949800
C	0.25374600	-0.02166400	0.52493100
C	-0.43286700	-1.21389800	0.24068200
H	-2.24858700	-2.12361200	-0.45244700
H	-3.40144900	0.04189500	-0.83357300
H	-2.21518600	2.16744400	-0.34403200
H	0.09817900	2.12689200	0.51458200
H	0.06632000	-2.16360500	0.40242400
C	1.65286200	-0.04701300	1.00132800
H	1.91402900	-0.93500800	1.57888300
H	2.41669800	-0.16666500	0.01499000
H	1.96520400	0.86234500	1.51434800
H	4.08105000	0.41205900	-0.59239400
N	3.30727200	-0.09101900	-1.04353300
H	2.83420800	0.64234700	-1.58547900

TS2

C	0.13543000	-0.54322900	0.36326500
C	0.30270000	0.82705500	0.60003300
C	1.50554900	1.45951100	0.29536500
C	2.56344300	0.73383100	-0.25027700
C	2.40877100	-0.62910100	-0.49006300
C	1.20381300	-1.25960800	-0.18435800
H	-0.52085500	1.39932000	1.01360400
H	1.61848700	2.52081900	0.48864800
H	3.50087900	1.22632500	-0.48340700
H	3.22673500	-1.20391000	-0.91060800
H	1.09331600	-2.32390700	-0.36866700
C	-1.17986000	-1.22738100	0.67396300
H	-1.55428100	-0.88710900	1.64547900
H	-1.00624500	-2.30707400	0.77646700
C	-2.25386600	-1.00044600	-0.37998500
H	-1.92072100	-1.16179000	-1.40562800
H	-3.19195600	-1.52011900	-0.17557500
H	-2.58417000	0.25951900	-0.29450000
H	-2.36628600	1.83122700	-1.11113100
N	-2.93325700	1.51043200	-0.31878700
H	-3.87798900	1.42988300	-0.71083800

TS3

C	0.03213700	0.05754500	0.33956100
C	-0.55815000	1.05424300	-0.45298700
C	-1.91310100	1.00869300	-0.77126500
C	-2.71075500	-0.03556400	-0.30915700
C	-2.14017900	-1.03583500	0.47800000
C	-0.78831200	-0.98818800	0.79634600
H	0.04140600	1.87920000	-0.81961300
H	-2.34744100	1.79414200	-1.38018600
H	-3.76562500	-0.06921500	-0.55681200
H	-2.75161800	-1.85223600	0.84637800
H	-0.35200600	-1.77100100	1.40853400
C	1.48454300	0.04841300	0.67140200
H	2.03495800	-0.73706700	-0.11274200
H	1.66413300	-0.48475600	1.60917600
C	2.25170800	1.36072800	0.61880700
H	1.82467900	2.09908400	1.30639600
H	3.29484900	1.20496700	0.90437000
H	2.24748400	1.80112700	-0.38175900
H	3.42128800	-0.83591300	-1.37895800
N	2.68050300	-1.49759600	-1.11649600
H	1.97701800	-1.36536200	-1.85355600

TS4

C	-2.73633500	-1.20493600	-0.39600400
C	-1.48412700	-1.20029900	0.21411100
C	-0.83879200	0.00151700	0.52530800
C	-1.48484800	1.20140100	0.20824100
C	-2.73706600	1.20231300	-0.40187800
C	-3.36739600	-0.00225200	-0.70664200
H	-3.22170500	-2.14768400	-0.62378000
H	-1.00310200	-2.14226200	0.45959900
H	-1.00437100	2.14483400	0.44911000
H	-3.22300100	2.14364500	-0.63425200
H	-4.34390000	-0.00370100	-1.17764300
C	0.53662000	0.00349200	1.15386100
H	0.64755900	0.88348600	1.79590300
H	0.64772100	-0.87264100	1.80114200
C	1.67681900	0.00048500	0.10507000
H	1.55608200	-0.87852600	-0.53758200
H	1.55583800	0.87560000	-0.54284200
C	3.05451900	0.00255900	0.73203900
H	3.29236600	-0.89502600	1.30707200
H	3.98828700	0.00030200	-0.17916600
H	3.29207100	0.90356700	1.30181700
N	4.76346400	-0.00324400	-1.22352800
H	4.38023000	-0.81245100	-1.72511200
H	4.37531400	0.79788900	-1.73421100

TS5

C	2.22636200	1.20588900	0.34899900
C	0.92216800	0.84938200	0.68521100
C	0.43317700	-0.43092100	0.39937800
C	1.28644300	-1.34306800	-0.23000300
C	2.59143200	-0.98978200	-0.56774100
C	3.06599400	0.28738400	-0.27850100
H	2.58861700	2.20135900	0.58191700
H	0.27019500	1.57162700	1.16489900
H	0.92683100	-2.34328400	-0.45204300
H	3.23828500	-1.71376100	-1.05122700
H	4.08226500	0.56366300	-0.53638800
C	-0.99153500	-0.81150500	0.74081600
H	-1.04439800	-1.89643300	0.90948700
H	-1.28590500	-0.34095300	1.68547400
C	-2.00864400	-0.43703700	-0.33406900
H	-2.00924700	0.84710200	-0.34278400
H	-1.67649900	-0.72553300	-1.33468200
C	-3.43872000	-0.84773200	-0.04334500
H	-3.78724500	-0.42470400	0.90378100
H	-4.12065600	-0.51682900	-0.83118700

H	-3.52894500	-1.93922500	0.03123300
N	-2.02092500	2.17376100	-0.42337700
H	-2.81990900	2.30171200	-1.05479900
H	-1.20696000	2.30326800	-1.03450700

TS6

C	2.63607000	0.80043400	-0.71243200
C	1.26119800	0.87387100	-0.89930400
C	0.38675600	-0.00101300	-0.23287700
C	0.94671700	-0.95042200	0.63634400
C	2.32415800	-1.02707700	0.82250200
C	3.17576300	-0.15320300	0.15042700
H	3.28901900	1.48610500	-1.24117600
H	0.84904800	1.62068400	-1.57021700
H	0.30446500	-1.64028000	1.17064700
H	2.73353000	-1.77248100	1.49564700
H	4.24822400	-0.21374200	0.29690200
C	-1.08261900	0.13520300	-0.43434600
H	-1.43142100	1.03765900	0.33967700
H	-1.29812700	0.59275100	-1.40536200
C	-1.97036400	-1.08055900	-0.19213400
H	-1.60168900	-1.91675900	-0.80030100
H	-1.88652800	-1.40740700	0.84997400
C	-3.44368400	-0.82518300	-0.52213100
H	-3.57147900	-0.54849300	-1.57306700
H	-4.05139800	-1.71415600	-0.33580900
H	-3.84704400	-0.01105500	0.08680800
N	-1.99234000	2.02366000	1.19962100
H	-2.82745100	2.27897000	0.65874500
H	-2.36674900	1.41027800	1.93388700

TS7

C	0.15750000	1.03253600	0.31127100
H	0.09007600	1.05496400	1.40124200
H	1.11113600	0.18101500	0.05841800
H	0.51165300	1.98743700	-0.07992100
C	-1.06936400	0.47502900	-0.38178000
H	-1.90153000	1.18449100	-0.26270300
H	-0.88129800	0.41334800	-1.45955700
C	-1.48841000	-0.90057800	0.14688600
H	-2.37497300	-1.27217800	-0.37362100
H	-0.68356800	-1.62676900	0.00908200
H	-1.72346800	-0.85569800	1.21514800
N	2.13823300	-0.59232300	-0.15798700
H	2.75361900	0.06565400	-0.64915300
H	2.53236700	-0.62792700	0.78871200

TS8

C	0.00000000	0.00000000	0.00000000
H	1.09797612	0.00000000	0.00000000
H	-0.32769542	1.04307182	0.00000000
H	-0.32826526	-0.45598701	-0.93885371
C	-0.54309252	-0.76056794	1.19418706
H	-0.35029573	-0.24653772	2.13971317
H	-1.81600993	-0.73006890	1.05837830
C	-0.18487758	-2.23293204	1.25172981
H	0.90176523	-2.37053903	1.32795790
H	-0.63903327	-2.72774076	2.11445873
H	-0.51917227	-2.75444469	0.34982208
H	-3.37068152	-1.04728048	1.93096890
N	-3.14683991	-0.64530240	1.01319826
H	-3.25488792	0.36396456	1.16719603

TS9

C	0.00000000	0.00000000	0.00000000
H	1.09447476	0.00000000	0.00000000
H	-0.33035670	1.04221904	0.00000000
H	-0.33072177	-0.45332489	0.94008511
C	-0.55155638	-0.75954864	-1.20914547
H	-1.64766316	-0.71323096	-1.20213657
H	-0.22633609	-0.27215147	-2.13391611
C	-0.11378952	-2.22931080	-1.24833948
H	-0.44032742	-2.72996605	-0.32360489
H	0.98174656	-2.28270476	-1.24551825
C	-0.65367227	-2.99010059	-2.44193978
H	-0.15902901	-2.38929826	-3.48707759
H	-0.31408594	-4.02401261	-2.51813437
H	-1.73610307	-2.92194883	-2.57054595
H	0.80062553	-2.68843005	-4.97107944
N	0.30043433	-1.87566924	-4.59409346
H	-0.56424762	-1.84941788	-5.14588702

TS10

C	0.00000000	0.00000000	0.00000000
H	1.09476806	0.00000000	0.00000000
H	-0.33139967	1.04170456	0.00000000
H	-0.33903812	-0.46343157	0.92961930
C	-0.55191953	-0.75754023	-1.21119405
H	-1.64760915	-0.71342019	-1.20517421
H	-0.23496466	-0.25598038	-2.13829788
C	-0.11508511	-2.21130653	-1.26863671

H	-0.57043156	-2.70955386	-0.17887455
H	0.96951074	-2.32067510	-1.16578100
C	-0.67032112	-3.02785285	-2.41928259
H	-0.32620591	-2.63287667	-3.38395812
H	-0.35473761	-4.07328517	-2.36403233
H	-1.76455597	-3.00419867	-2.43204780
H	-1.41330916	-4.15220395	0.52261857
N	-1.00997184	-3.30345969	0.93539703
H	-0.11198750	-3.62676309	1.31294072

TS11

C	-1.38880900	-1.20823500	-0.19202300
C	-2.10780100	-0.03061400	0.02363500
C	-1.43031500	1.19997900	0.03046000
C	-0.06442700	1.25242700	-0.14980500
C	0.72113400	0.05656300	-0.27531700
C	-0.01521400	-1.16821900	-0.37567400
H	-1.90887300	-2.15896000	-0.23794700
H	-3.18242900	-0.06222400	0.15977700
H	-1.99017300	2.12017500	0.15910000
H	0.45014300	2.20708700	-0.15651500
H	0.53073000	-2.08320500	-0.58380900
C	2.08709000	0.15095300	-0.92454000
H	2.66861100	-0.75724700	-0.75313700
H	1.98003500	0.28601500	-2.00589200
H	2.64779100	0.99207900	-0.51714500
H	1.57307300	-1.14245100	1.64546100
N	1.41297000	-0.12792300	1.61965800
H	0.53035200	-0.02293700	2.13208600

TS12

C	-1.56108000	-1.12752300	0.38930700
C	-2.00707800	0.09766100	-0.11116000
C	-1.09780800	0.99347400	-0.65293300
C	0.29815900	0.71690200	-0.62306300
C	0.73536500	-0.58408600	-0.20092800
C	-0.19805500	-1.45822200	0.32898000
H	-2.26892400	-1.83588900	0.80445000
H	-3.06466600	0.33681000	-0.09968700
H	-1.44100900	1.92786300	-1.08363700
H	0.94673600	1.27054700	-1.29161900
H	0.12999000	-2.42767400	0.69076400
C	2.19950200	-0.90797200	-0.26651800
H	2.40922700	-1.91354400	0.10311600
H	2.57722500	-0.83612100	-1.29219300
H	2.75993200	-0.18395500	0.33417000

H	0.37505800	1.48386000	1.64406300
N	0.97882400	1.86452000	0.90676700
H	0.51062900	2.74506100	0.66110100

TS13

C	0.32407800	1.76263900	0.15912700
C	1.36224000	1.03207300	-0.38045200
C	1.17488000	-0.34860700	-0.69547400
C	-0.14956200	-0.87219500	-0.61110300
C	-1.19326200	-0.13690900	-0.06024900
C	-0.94357800	1.18653700	0.33436500
H	0.47967900	2.80067800	0.43299600
H	2.33979800	1.47638200	-0.52259900
H	1.87089900	-0.81524500	-1.38037000
H	-0.33515400	-1.88136900	-0.96579800
H	-1.74855900	1.78015500	0.75513500
C	-2.56784800	-0.74067800	0.10565200
H	-2.73755500	-1.05510000	1.14121700
H	-3.35190200	-0.02265300	-0.14827600
H	-2.69541400	-1.61954100	-0.52994800
H	1.58792100	-0.85398800	1.59581900
N	2.12204300	-1.27211200	0.82554600
H	1.69429600	-2.20169500	0.73180300

TS14

C	-0.72824900	-1.17044500	-0.56324100
C	-1.44013900	0.06188800	-0.62274300
C	-0.67316300	1.26105700	-0.49267100
C	0.65733600	1.20902400	-0.14102400
C	1.32932900	-0.02095800	0.02935200
C	0.61031100	-1.20133300	-0.20156200
H	-1.25103000	-2.09539600	-0.78153700
H	-2.36686000	0.10410700	-1.17972600
H	-1.16866800	2.21534100	-0.62593100
H	1.21172000	2.13372800	-0.01115300
H	1.11967300	-2.15656200	-0.12042200
C	2.77951100	-0.05176900	0.43694400
H	3.21484500	-1.04218200	0.28886000
H	3.37027600	0.66809000	-0.13736400
H	2.90014800	0.20700200	1.49527500
H	-1.73920800	0.03267800	1.74427300
N	-2.52512500	0.04891000	1.08442900
H	-2.82463600	-0.93396700	1.06639900

TS15

C	-1.38880900	-1.20823500	-0.19202300
C	-2.10780100	-0.03061400	0.02363500
C	-1.43031500	1.19997900	0.03046000
C	-0.06442700	1.25242700	-0.14980500
C	0.72113400	0.05656300	-0.27531700
C	-0.01521400	-1.16821900	-0.37567400
H	-1.90887300	-2.15896000	-0.23794700
H	-3.18242900	-0.06222400	0.15977700
H	-1.99017300	2.12017500	0.15910000
H	0.45014300	2.20708700	-0.15651500
H	0.53073000	-2.08320500	-0.58380900
C	2.08709000	0.15095300	-0.92454000
H	2.66861100	-0.75724700	-0.75313700
H	1.98003500	0.28601500	-2.00589200
H	2.64779100	0.99207900	-0.51714500
H	1.57307300	-1.14245100	1.64546100
N	1.41297000	-0.12792300	1.61965800
H	0.53035200	-0.02293700	2.13208600

TS16

C	1.64379200	-1.45615100	-0.32178400
C	2.26140800	-0.46872400	0.44928200
C	1.52371400	0.61379800	0.90312000
C	0.16254400	0.77833200	0.51767600
C	-0.48951000	-0.29187400	-0.18480000
C	0.27543000	-1.36082700	-0.62023400
H	2.21389500	-2.30868300	-0.67297500
H	3.30951700	-0.56033500	0.71182100
H	1.98653600	1.36392600	1.53525800
H	-0.45601300	1.45030200	1.09989000
H	-0.19937600	-2.15113900	-1.19366700
C	-1.96148400	-0.18009500	-0.48640000
H	-2.23229600	-0.92207800	-1.24369400
H	-2.13947500	0.80804800	-0.92489600
H	0.86646400	1.69866300	-1.57575800
N	0.24851700	2.19699700	-0.92557100
H	0.88789400	2.85292800	-0.46089900
C	-2.86374600	-0.36426000	0.74691300
H	-2.64243600	0.37670100	1.51976500
H	-3.91664200	-0.25258500	0.47381300
H	-2.73057200	-1.35591500	1.18769500

TS17

C	1.35527800	1.63424600	0.04951700
C	2.01618900	0.53823900	-0.48809200
C	1.31701500	-0.68466100	-0.69091800

C	-0.10295300	-0.68231200	-0.51221600
C	-0.76219600	0.41134200	0.01455400
C	-0.01226500	1.57374000	0.31020500
H	1.90006300	2.55131300	0.24651500
H	3.07099600	0.59766900	-0.73219400
H	1.73872700	-1.41983300	-1.36410300
H	-0.64277000	-1.58907200	-0.75245500
H	-0.51947800	2.44025600	0.72278300
C	-2.25916800	0.43165200	0.27436100
H	-2.41674500	0.62563100	1.34253200
H	-2.68385300	1.29969900	-0.24398500
H	1.59443900	-1.22005400	1.61642900
N	1.95292900	-1.81372400	0.85990200
H	2.95067200	-1.56890900	0.83487600
C	-3.03892100	-0.82150500	-0.12562700
H	-2.69141500	-1.70450600	0.41728600
H	-4.10078300	-0.69287100	0.09789900
H	-2.94822900	-1.02770000	-1.19560200

TS18

C	-0.99215200	-1.15460000	-0.62943100
C	-1.91403800	-0.07101300	-0.59504100
C	-1.36658400	1.23821500	-0.41891600
C	-0.03568400	1.40494600	-0.11349400
C	0.85460000	0.30907900	-0.03457400
C	0.34652500	-0.96618100	-0.31083000
H	-1.35035500	-2.14624700	-0.88434000
H	-2.85579100	-0.16732700	-1.11917400
H	-2.02779000	2.09444500	-0.47947500
H	0.35152100	2.40603600	0.05354300
H	1.00810100	-1.82413800	-0.30369400
C	2.30390300	0.56548800	0.32889000
H	2.66461300	1.40630100	-0.27583000
H	2.34249200	0.92127200	1.36707400
H	-2.10268600	-0.27748500	1.77338100
N	-2.90667800	-0.36658300	1.14176800
H	-3.02932800	-1.38470500	1.07518400
C	3.26691400	-0.61313600	0.17281000
H	4.28358300	-0.30707800	0.43094200
H	2.99931200	-1.44600200	0.82864500
H	3.28217100	-0.98578200	-0.85511700

Table S5.1. Thermodynamic data for each species appearing in this study. Values of heat capacity and entropy are in J mol^{-1} K^{-1} and energy values in kJ mol^{-1}.

1. Toluene

Temperature (K)	Standart heat capacity	Standard entropy	Standard enthalpy of formation	Standard Gibbs energy of formation
300	103.9	327.9	50.0	120.8
400	140.3	362.8	43.4	145.4
500	172.0	397.6	38.1	171.6
600	198.0	431.4	33.9	198.7
700	219.2	463.5	30.6	226.4
800	236.6	494.0	28.2	254.6
900	251.0	522.7	26.4	283.0
1000	263.1	549.8	25.3	311.5
1100	273.5	575.4	24.6	340.2
1200	282.3	599.5	24.3	369.0
1300	289.9	622.4	24.4	397.6
1400	296.4	644.2	24.6	426.4
1500	302.1	664.8	25.1	455.0
1600	307.0	684.5	25.7	483.7
1700	311.2	703.2	26.5	512.3
1800	315.0	721.1	27.2	540.8
1900	318.2	738.2	28.1	569.4
2000	321.2	754.6	28.9	597.8

2. Benzyl radical (R1`)

Temperature (K)	Heat capacity	Standard entropy	Standard enthalpy of formation	Gibbs energy of formation
300	105.3	324.3	207.2	109.9
400	139.8	359.4	219.5	75.7
500	168.6	393.8	235.0	38.1
600	191.6	426.7	253.0	-3.0
700	210.2	457.6	273.1	-47.2
800	225.4	486.7	294.9	-94.4
900	238.1	514.0	318.1	-144.5
1000	249.0	539.7	342.5	-197.2
1100	258.2	563.9	367.9	-252.4
1200	266.1	586.7	394.1	-309.9
1300	273.0	608.3	421.1	-369.7
1400	279.0	628.7	448.7	-431.5
1500	284.2	648.1	476.8	-495.4
1600	288.7	666.6	505.5	-561.1
1700	292.7	684.3	534.6	-628.7
1800	296.2	701.1	564.0	-698.0
1900	299.2	717.2	593.8	-768.9
2000	302.0	732.6	623.8	-841.4

3. Ethylbenzene

Temperature (K)	Heat capacity	Standard entropy	Standard enthalpy of formation	Gibbs energy of formation
300	125.9	364.5	29.6	130.3
400	167.7	406.5	21.6	165.1
500	204.5	448.0	15.1	201.7
600	235.2	488.1	9.9	239.5
700	260.5	526.3	5.9	278.2
800	281.6	562.5	2.9	317.3
900	299.5	596.7	0.9	356.7
1000	314.7	629.1	-0.4	396.3
1100	327.7	659.7	-0.9	436.0
1200	339.0	688.7	-1.0	475.7
1300	348.6	716.2	-0.5	515.4
1400	357.1	742.4	0.2	555.1
1500	364.4	767.3	1.3	594.7
1600	370.7	791.0	2.6	634.2
1700	376.3	813.7	4.1	673.6
1800	381.2	835.3	5.7	713.0
1900	385.5	856.0	489.0	7.4
2000	389.3	875.9	527.8	9.1

4. 1-phenyl-2-ethyl (R2`)

Temperature (K)	Heat capacity	Standard entropy	Standard enthalpy of formation	Gibbs energy of formation
300	129.6	373.5	234.4	312.8
400	169.2	416.3	228.2	339.9
500	203.3	457.8	223.1	368.4
600	231.2	497.5	219.1	397.8
700	253.9	534.9	216.0	427.9
800	272.7	570.0	213.7	458.3
900	288.6	603.1	212.2	489.0
1000	302.1	634.2	211.3	519.8
1100	313.7	663.6	210.9	550.7
1200	323.6	691.3	210.9	581.6
1300	332.3	717.5	211.3	612.4
1400	339.8	742.4	212.0	643.3
1500	346.3	766.1	212.9	674.0
1600	352.0	788.7	214.0	704.7
1700	357.0	810.1	215.2	735.4
1800	361.4	830.7	216.5	765.9
1900	365.2	850.3	217.9	796.4
2000	368.7	869.1	219.3	826.8

5. 1-phenyl-1-ethyl (R3`)

Temperature (K)	Heat capacity	Standard Entropy	Standard enthalpy of formation	Gibbs energy of formation
300	127.3	364.2	173.6	254.7
400	167.0	406.3	167.1	282.8
500	201.3	447.4	161.8	312.3
600	229.4	486.7	157.6	342.8
700	252.5	523.8	154.4	374.0
800	271.6	558.8	152.0	405.5
900	287.7	591.8	150.3	437.3
1000	301.4	622.8	149.3	469.2
1100	313.1	652.1	148.9	501.3
1200	323.2	679.8	148.9	533.3
1300	332.0	706.0	149.2	565.3
1400	339.5	730.9	149.9	597.3
1500	346.1	754.6	150.8	629.2
1600	351.8	777.1	151.9	661.1
1700	356.9	798.6	153.0	692.9
1800	361.3	819.1	154.3	724.6
1900	365.2	838.7	155.7	756.3
2000	368.6	857.5	157.1	787.8

6. *n*-Propylbenzene

Temperature (K)	Heat capacity	Standard entropy	Standard enthalpy of formation	Gibbs energy of formation
300	146.6	396.7	7.1	139.0
400	194.9	445.5	-2.4	184.5
500	237.9	493.7	-10.2	232.2
600	273.8	540.4	-16.3	281.2
700	303.6	584.9	-20.9	331.2
800	328.6	627.1	-24.3	381.8
900	349.7	667.1	-26.4	432.7
1000	367.7	704.9	-27.6	483.7
1100	383.2	740.7	-28.0	534.9
1200	396.5	774.6	-27.7	586.1
1300	408.0	806.8	-26.8	637.2
1400	418.0	837.4	-25.5	688.2
1500	426.6	866.6	-23.9	739.1
1600	434.2	894.3	-21.9	789.9
1700	440.8	920.9	-19.8	840.6
1800	446.6	946.2	-17.5	891.2
1900	451.7	970.5	-15.1	941.6
2000	456.3	993.8	-12.6	991.9

7. 1-phenyl-3-propyl (R4`)

Temperature (K)	Heat capacity	Standard Entropy	Standard enthalpy of formation	Gibbs energy of formation
300	150.5	406.6	0.3	319.0
400	196.7	456.3	17.4	356.7
500	236.9	504.6	39.1	396.1
600	270.0	550.9	64.7	436.7
700	297.2	594.6	93.6	478.0
800	319.8	635.8	125.3	519.8
900	338.9	674.6	159.2	561.8
1000	355.1	711.2	195.1	603.9
1100	369.1	745.7	232.7	646.2
1200	381.2	778.3	271.7	688.4
1300	391.6	809.3	311.9	730.5
1400	400.6	838.6	353.2	772.6
1500	408.5	866.5	395.5	814.6
1600	415.4	893.1	438.5	856.5
1700	421.4	918.5	482.3	898.3
1800	426.7	942.7	191.2	939.9
1900	431.4	965.9	193.3	981.5
2000	435.5	988.2	195.4	1022.9

8. 1-phenyl-2-propyl (R5`)

Temperature (K)	Heat capacity	Standard entropy	Standard enthalpy of formation	Gibbs energy of formation
300	149.9	412.4	204.6	312.3
400	195.5	461.9	196.8	349.3
500	235.6	509.9	190.4	388.3
600	268.9	555.9	185.4	428.3
700	296.4	599.5	181.6	469.1
800	319.3	640.6	178.9	510.4
900	338.6	679.4	177.2	551.9
1000	355.1	715.9	176.3	593.6
1100	369.2	750.4	176.1	635.4
1200	381.4	783.1	176.5	677.1
1300	391.9	814.1	177.4	718.8
1400	401.0	843.4	178.6	760.4
1500	408.9	871.4	180.1	801.9
1600	415.8	898.0	181.9	843.3
1700	421.8	923.4	183.8	884.6
1800	427.1	947.6	185.8	925.7
1900	431.7	970.9	188.0	966.8
2000	435.9	993.1	190.1	1007.7

9. 1-phenyl-1-propyl (R6`)

Temperature (K)	Heat capacity	Standard entropy	Standard enthalpy of formation	Gibbs energy of formation
300	147.5	398.2	147.5	259.4
400	193.9	447.1	139.5	298.0
500	234.4	494.8	133.0	338.4
600	267.9	540.6	127.8	380.0
700	295.5	584.1	124.0	422.3
800	318.5	625.1	121.2	465.1
900	337.8	663.7	119.4	508.2
1000	354.4	700.2	118.4	551.5
1100	368.5	734.7	118.2	594.8
1200	380.7	767.3	118.5	638.1
1300	391.2	798.2	119.3	681.4
1400	400.4	827.5	120.5	724.6
1500	408.3	855.4	121.9	767.7
1600	415.2	882.0	123.6	810.7
1700	421.3	907.3	125.5	853.6
1800	426.6	931.6	127.5	896.3
1900	431.3	954.8	129.6	939.0
2000	435.5	977.0	131.7	981.5

10. Amine Radical

Temperature (K)	Heat capacity	Standard entropy	Standard enthalpy of formation	Gibbs energy of formation
300	33.6	204.5	190.4	129.1
400	34.3	214.3	193.8	108.1
500	35.4	222.0	197.3	86.3
600	36.6	228.6	200.9	63.8
700	37.9	234.3	204.6	40.6
800	39.3	239.5	208.5	16.9
900	40.6	244.2	212.5	-7.3
1000	42.0	248.5	216.6	-31.9
1100	43.3	252.6	220.9	-57.0
1200	44.5	256.4	225.3	-82.4
1300	45.7	260.0	229.8	-108.2
1400	46.7	263.4	234.4	-134.4
1500	47.6	266.7	239.1	-160.9
1600	48.5	269.8	243.9	-187.7
1700	49.3	272.7	248.8	-214.9
1800	50.0	275.6	253.8	-242.3
1900	50.6	278.3	258.8	-270.0
2000	51.2	280.9	263.9	-297.9

11. Ammonia

Temperature (K)	Heat capacity	Standard entropy	Standard enthalpy of formation	Gibbs energy of formation
300	34.9	211.3	-49.4	-112.8
400	37.4	221.7	-45.8	-134.5
500	40.5	230.4	-41.9	-157.1
600	43.5	238.0	-37.7	-180.5
700	46.5	244.9	-33.2	-204.7
800	49.3	251.3	-28.4	-229.5
900	52.0	257.3	-23.4	-254.9
1000	54.6	262.9	-18.0	-281.0
1100	56.9	268.2	-12.5	-307.5
1200	59.1	273.3	-6.7	-334.6
1300	61.1	278.1	-0.6	-362.2
1400	63.0	282.7	5.6	-390.2
1500	64.6	287.1	11.9	-418.7
1600	66.2	291.3	18.5	-447.6
1700	67.5	295.4	25.2	-477.0
1800	68.7	299.3	32.0	-506.7
1900	69.8	303.0	38.9	-536.8
2000	70.8	306.6	46.0	-567.3

Table S2. Calculated standard reaction enthalpies of Reaction R1-R6. All values in italic are experimental standard heat of formation of individual species from the cited literature and in unit of kJ mol^{-1}.

Reactions	**Calculated from literature[a]** $\Delta_r H^o_{298}$
$C_6H_5CH_3 + NH_2 = C_6H_5CH_2 + NH_3$ *(50.1)*[1] *+ (186.2)*[2] *(207.0)*[3] *+ (-45.9)*[2]	-75.3
$C_6H_5CH_2CH_3 + NH_2 = C_6H_5CH_2CH_2 + NH_3$ *(29.8)*[4] *+ (186.2)*[2] *(234.8)*[5] *+ (-45.9)*[2]	-27.1
$C_6H_5CH_2CH_3 + NH_2 = C_6H_5CHCH_3 + NH_3$ *(29.8)*[4] *+ (186.2)*[2] *(173.9)*[6] *+ (-45.9)*[2]	-88.0
$C_6H_5CH_2CH_2CH_3 + NH_2 = C_6H_5CH_2CH_2CH_2 + NH_3$ *(7.8)*[7] *+ (186.2)*[2] *(210.0)*[8] *+ (-45.9)*[2]	-29.9
$C_6H_5CH_2CH_2CH_3 + NH_2 = C_6H_5CH_2CHCH_3 + NH_3$ *(7.8)*[7] *+ (186.2)*[2] *(205.4)*[8] *+ (-45.9)*[2]	-34.5
$C_6H_5CH_2CH_2CH_3 + NH_2 = C_6H_5CHCH_2CH_3 + NH_3$ *(7.8)*[7] *+ (186.2)*[2] *(147.8)*[8] *+ (-45.9)*[2]	-92.1

[a]Standard reaction enthalpies of R1-R6 based on the experimental standard heat of formation of the species involved in each reaction.

References

1. Roux, M. V.; Temprado, M.; Chickos, J. S.; Nagano, Y., Critically Evaluated Thermochemical Properties of Polycyclic Aromatic Hydrocarbons. *J. Phys. Chem. Ref. Data* **2008**, *37*, 1855-1996.

2. Ruscic, B.; Boggs, J. E.; Burcat, A.; Császár, A. G.; Demaison, J.; Janoschek, R.; Martin, J. M.; Morton, M. L.; Rossi, M. J.; Stanton, J. F., IUPAC Critical Evaluation of Thermochemical Properties of Selected Radicals. Part I. *J. Phys. Chem. Ref. Data* **2005**, 34, 573-656.

3. Tsang, W., Heats of Formation of Organic Free Radicals by Kinetic Methods. In *Energetics of Organic Free Radicals*, Springer: **1996**; pp 22-58.

4. Prosen, E. J. J., W.H.; Rossini, F.D., Heats of Combustion and Formation at 25°C of the Alkylbenzenes through $C_{10}H_{14}$, and of the Higher Normal Monoalkylbenzenes, J. Res. NBS, 1946, 36, 455-461.

5. Luo, Y. R., *Handbook of Bond Dissociation Energies in Organic Compounds*; CRC Press, 2002.

6. Metcalfe, W.; Dooley, S.; Dryer, F., Comprehensive Detailed Chemical Kinetic Modeling Study of Toluene Oxidation. *Energy & Fuels* **2011**, *25*, 4915-4936.

7. Prosen, E.; Johnson, W.; Rossini, F., Heats of Combustion and Formation at 25°C of the Alkylbenzenes through $C_{10}H_{14}$, and of the Higher Normal Monoalkylbenzenes. *J. Res. Natl. Bur. Stand.* **1946**, 36, 455-461.

8. Dagaut, P.; Ristori, A.; El Bakali, A.; Cathonnet, M., Experimental and Kinetic Modeling Study of the Oxidation of *n*-Propylbenzene. *Fuel* **2002**, *81*, 173-184.

Appendix III: Supplementary Information for Chapter 6

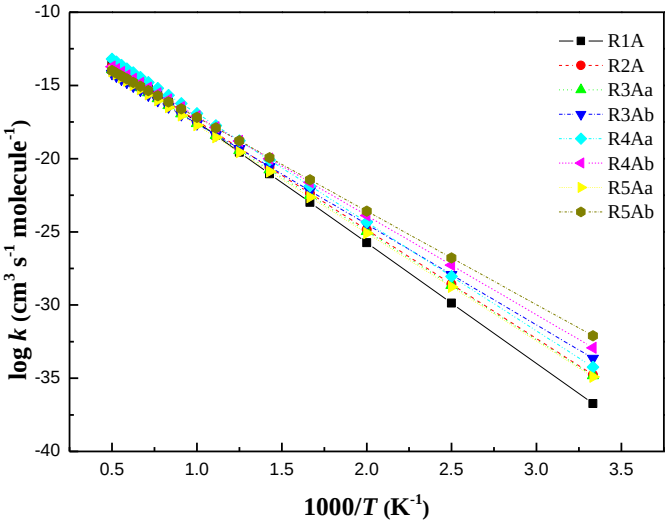

(a)

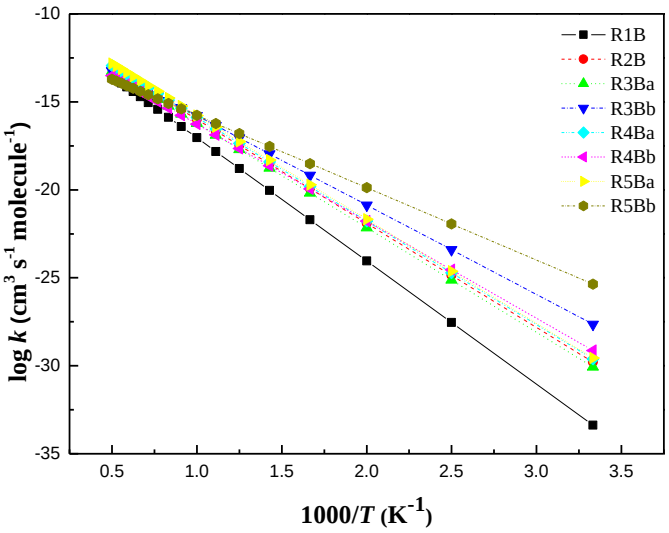

(b)

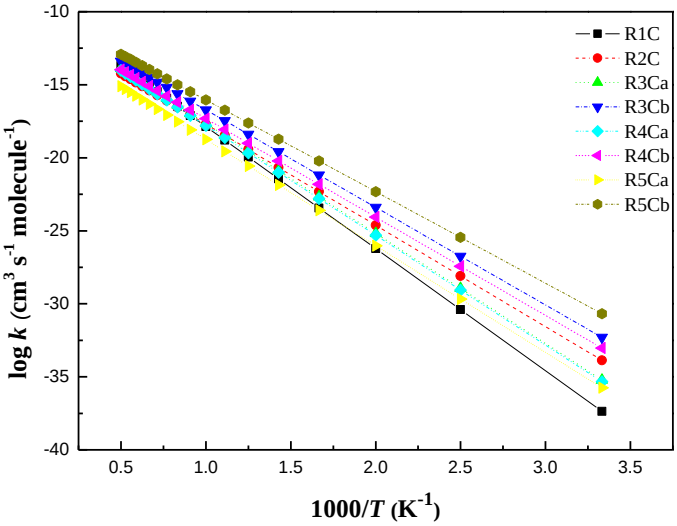

(c)

Figure S6.1. Arrhenius plots showing rate constant of H abstraction of C_1–C_4 alkane with NO_2 forming (a) *trans*-HONO, (b) *cis*-HONO and (c) *iso*-HNO_2 isomers.

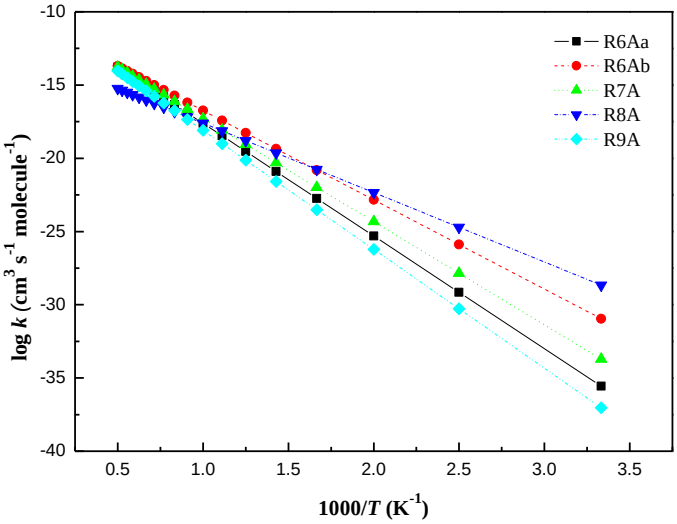
R6Aa
R6Ab
R7A
R8A
R9A
log k (cm3 s-1 molecule-1)
1000/T (K-1)
-10
-15
-20
-25
-30
-35
-40
0.5
1.0
1.5
2.0
2.5
3.0
3.5

(a)

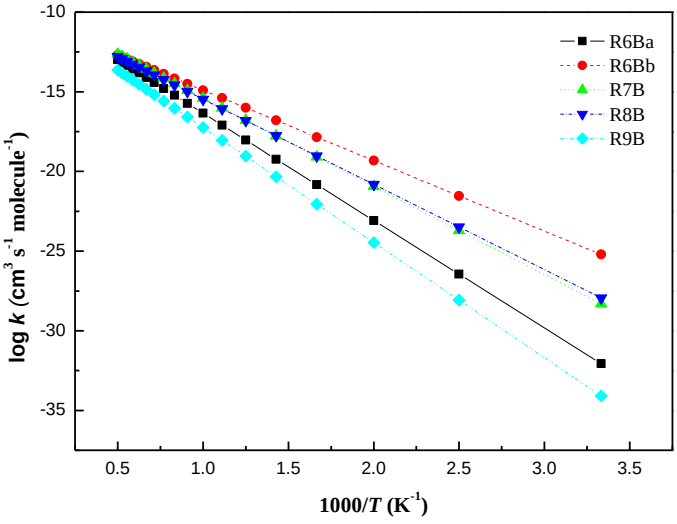
R6Ba
R6Bb
R7B
R8B
R9B
log k (cm3 s-1 molecule-1)
1000/T (K-1)
-10
-15
-20
-25
-30
-35
0.5
1.0
1.5
2.0
2.5
3.0
3.5

(b)

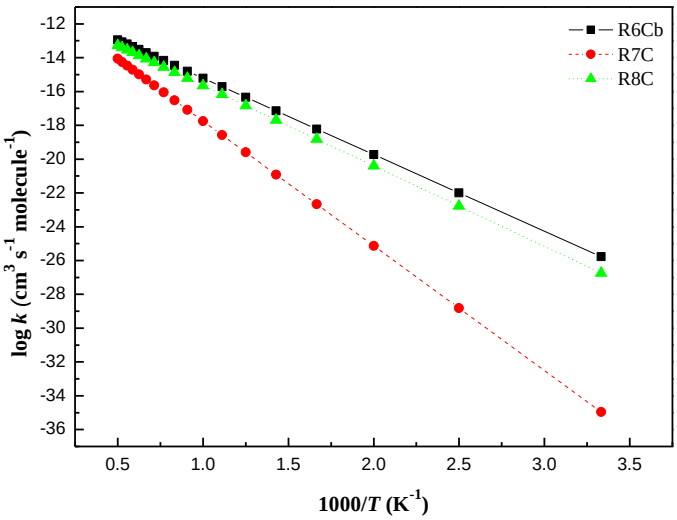

(c)

Figure S6.2. Arrhenius plots showing rate constant of H abstraction of C_2–C_4 alkene with NO_2 forming (a) *trans*-HONO, (b) *cis*-HONO and (c) *iso*-HNO_2 isomers.

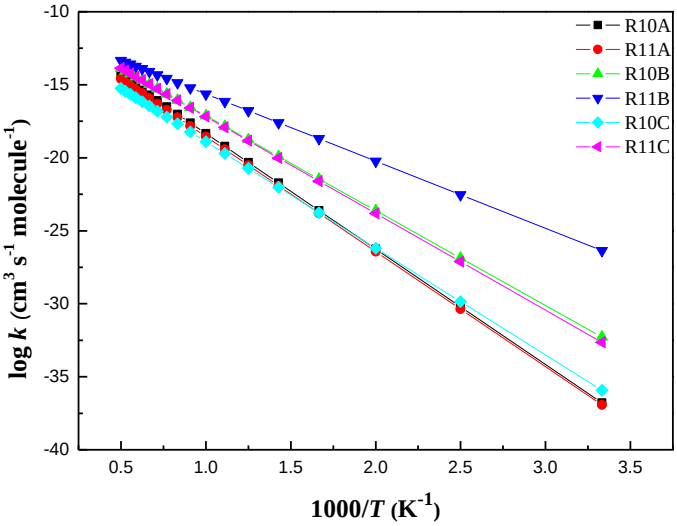

Figure S6.3. Arrhenius plots showing rate constant of H abstraction of ethylbenzene with NO_2 forming *trans*-HONO, *cis*-HONO, and *iso*-HNO